Experimental and Numerical Investigations on the Momentum Balance Applied to Hydraulic Structures

Sebastian Müller

Vollständiger Abdruck der von der Fakultät für Bauingenieurwesen und Umweltwissenschaften der Universität der Bundeswehr München zur Erlangung des akademischen Grades eines

Doktor-Ingenieurs (Dr.-Ing.)

genehmigten Dissertation.

Gutachter/Gutachterin

1. Prof. Dr.-Ing. habil. Andreas Malcherek
2. Prof. Dr.-Ing. Philipp Epple
3. Prof. Dr.-Ing. habil. Günter Wozniak

Die Dissertation wurde am 16. März 2023 bei der Universität der Bundeswehr München eingereicht und durch die Fakultät für Bauingenieurwesen und Umweltwissenschaften am 20. Oktober 2023 angenommen. Die mündliche Prüfung fand am 24. November 2023 statt.

Acknowledgements

This doctoral thesis came into existence during my employment as a research associate at the professorship of Hydromechanics and Hydraulic Engineering at the Bundeswehr University Munich.
During my doctorate, I started doing triathlons - a sport that bewitched me as a physical balance to my mental efforts. Since so many similarities can be found, the doctorate and triathlon almost fused into a single experience for me with maxims to act upon. First: It is not sufficient to be excellent at biking or running when you can not swim or drown in the water. You have to train different skills so that one's deficiencies do not affect one's assets to reach the finish line. This is in accordance with a doctorate, where it is not enough to perform excellently in conducting experiments, simulating, or programming when being incapable of putting findings on paper or expressing oneself succinctly. Second: A doctorate and triathlons also strengthen mental resilience. At the start, it is not helpful to think about the project en bloc. It is better to divide the big task into many subtasks to complete. Again, this can be completely transferred to a doctorate. One may not see the doctorate as a single task to work on but as to divide it into many subtasks, and step by step, the finish line gets closer. Third: Just hang in there and get it done. When I get off my bike, exhausted, being aware of running 10 kilometers now, it is just a matter of keeping going - I came too far to quit.
But even though a doctorate is an individual achievement, many people coached me and cheered me on so I was able to meet my biggest challenge so far.

In the first place, I have to thank my doctoral supervisor Prof. Andreas Malcherek for first challenging and later promoting me in my scientific development. I have never met a person before who is that deeply immersed in so many fields of science. He taught me the perception to spot loose (scientific) ends and the usage of tools to tie them together.

I thank my second supervisor, Prof. Philipp Epple, for his valuable contributions and vivid and concise comments, letting some sudden insights fall into place to complete my hydromechanical jigsaw.

With the lectures of Prof. Günter Wozniak in my diploma program at the Chemnitz University of Technology, I initially got in contact with hydromechanics. Therefore, I am very grateful to him that he accompanied my scientific development, critically reviewing the publications I contributed as well as my thesis as my third supervisor.

I also thank Ivo for all the fruitful discussions and his expedient advice plus the sporty challenges I tried to compete in.

Analogously to triathlon, a doctorate also needs people in the background who keep everything running. For having a walk-over in the cooperation for all the practical tasks, I thank the team of the laboratory: Brigitte, Frank, Hans-Peter, Jürgen, Marcus, Martin, Michael, and Yvonne. My thesis benefited from their practical solutions and advice.

It is said that pictures are the language of engineers. Therefore, I express my gratitude to Karina and Julia for translating my work into catchy pictures.

I also say thank you to my doctoral companion Johanna for all the plain and unbiased discussions.

Her different perspectives made her a valuable comrade on the road to the Ph.D.

I am very grateful for Hermann proofreading the whole thesis in record time. His view from the outside revealed some ambiguities and mental leaps to revise, making this thesis a neater piece of work.

My long-time companion Sandra I owe a debt of gratitude for her understanding and unquestionable confidence in me.

Last but not least, I have to say thank you from the bottom of my heart to my parents Brigitte and Wolfgang. You paved my way to the point where I now am and almost ingenuously believed in me.

Abstract

The Bernoulli principle is the state-of-the-art method for practical calculations in hydraulics, like the pressure difference of flows through hydraulic structures. Therefore, the energy of a specific fluid particle must be considered at different times. It means that the Bernoulli principle is only valid when applied to a single streamline (and when additional restrictions are considered). However, almost every hydraulic textbook applies the Bernoulli principle to the whole cross-section for simple applicability, disregarding the restrictions. This strong simplification is accompanied by a significant deviation of the calculated result from the empirical result. To bridge the gap between calculation and measurement, correction coefficients are introduced that are specifically determined for every hydraulic structure. In the end, erroneously applying the Bernoulli principle and introducing a proper correction coefficient yields a result that is acceptably close to the measurement.
This is the common approach to calculations in hydraulics. However, there are approaches capable of correctly predicting the empirical results without artificial correction coefficients, like the state-of-the-art method employed for numerical simulations. In fluid dynamics, the momentum-based Navier-Stokes equations are solved (among others) for any kind of flow and yield results with a very high agreement to measurements. Momentum-based approaches for analytical calculations are already reported by the literature but the theories are often presented as ideal solutions, not detailed up to applicability or blended with the Bernoulli principle.
Based on Newton's fundamental laws of motion, a straightforward momentum-based and applicable alternative to the established method is presented. The presented approach is aided by numerical simulations accounting for physical coefficients that occur due to the substitution of integral by averaged expressions. In this case, the coefficients are physically well-defined but not for the correction of a faultily applied approach. The derived integral momentum balance requires knowledge of the pressure and velocity distributions which can be obtained by numerical simulations. With the subsequent parametrizations of the coefficients, the approach can be applied by simple analytical formulas.

The momentum-based approach is applied to the sudden contraction, the sudden expansion, and the metering orifice as a combination of a contraction and an expansion. Due to the application of the same approach, similarities in the flow behavior of the hydraulic structures are identified. As a result, parametrizations of some coefficients are also valid for additional structures than they were defined for. The numerical simulations are performed with ANSYS based on the finite volume method and solving the Reynolds-Averaged Navier Stokes equations. The kω-SST turbulence model is employed, which shows the best performance for all investigated hydraulic structures compared with literature numbers and own experiments. The evaluation of the numerical simulations and the comparison with the theory and the reference data is performed with MATLAB.
The results obtained with the proposed approach show a very high correlation between the experimental data and the literature numbers. The derived momentum-based formulas in combination with

the numerically obtained coefficients also confirm empirical parametrizations. In addition, the flow rate through a metering orifice can be predicted with the momentum-based approach as precisely as by applying the Bernoulli principle with the empirical correction coefficient. Consequentially, the proposed approach is applicable to various hydraulic structures and does not require extensive empirical investigations but yields a very high agreement to the measurements.

Kurzfassung

Die Bernoulli-Gleichung gilt als der aktuelle Stand der Technik für analytische Berechnungen in der Fluidtechnik, wie beispielsweise für die Druckdifferenz oder den Durchfluss durch hydraulische Bauteile. Dazu ist die Energie ein und desselben Fluidpartikels zu verschiedenen Zeitpunkten zu bilanzieren. Dies bedeutet, dass die Bernoulli-Gleichung nur bei Anwendung auf eine einzelne Stromlinie Gültigkeit besitzt (zusätzlich gelten weitere Einschränkungen). Jedoch wird die Bernoulli-Gleichung in der Literatur zur einfacheren Anwendung fast immer auf die gesamte Querschnittsfläche bezogen, ungeachtet der Einschränkungen. Diese starken Vereinfachungen gehen einher mit einer erheblichen Abweichung zwischen berechnetem und beobachtetem Ergebnis. Um diese Abweichung zu überbrücken werden speziell für jedes hydraulische Bauteil ermittelte Korrekturbeiwerte eingeführt. Somit liefert die falsch angewandte Theorie zusammen mit einem geeigneten Korrekturbeiwert eine akzeptable Übereinstimmung mit Messergebnissen.
Dies ist die standardgemäße Vorgehensweise bei hydraulischen Berechnungen. Jedoch gibt es auch Ansätze, mit denen die experimentellen Ergebnisse ohne die Einführung von künstlichen Korrekturbeiwerten korrekt berechnet werden können. Einer dieser Ansätze wird bei numerischen Simulationen eingesetzt. In der Strömungsmechanik werden unter anderem die auf der Impulserhaltung basierenden Navier-Stokes-Gleichungen für jede Art von Strömungen gelöst, womit man Ergebnisse erhält, die sehr hohe Übereinstimmung mit den entsprechenden Messergebnissen zeigen. Impuls-basierte Ansätze sind in der Literatur bereits bekannt, aber die Theorien werden oft als ideale bzw. idealisierte Lösungen präsentiert und daher nicht bis zur praktischen Anwendung ausgeführt oder vermengt mit der Bernoulli-Gleichung.
Auf Grundlage von Newtons Bewegungsgleichungen wird eine direkte impulsbasierte und praktisch anwendbare Alternative für den bekannten Ansatz präsentiert. Der gezeigte Ansatz ist durch numerische Simulationen gestützt, wodurch physikalische Koeffizienten ermittelt werden können die aus der Ersetzung von integralen durch gemittelte Ausdrücke entstehen. Hierbei sind die Koeffizienten physikalisch fundiert und nicht zur Korrektur eines falsch angewandten Ansatzes. Der beschriebene Ansatz der integralen Impulserhaltung setzt Kenntnisse über die Druck- und Geschwindigkeitsverteilungen voraus, die durch die numerischen Simulationen ermittelt werden können. Die daraus folgenden Parametrisierungen der Koeffizienten liefern einfache analytische Formeln die auf den vorgestellten Ansatz anwendbar sind.

Dieser Ansatz wird auf die plötzliche Verengung, die plötzliche Aufweitung und die Messblende angewandt, die eine Kombination einer plötzlichen Verengung gefolgt von einer Aufweitung darstellt. Durch Anwendung des gleichen Ansatzes auf die genannten hydraulischen Bauteile können Gemeinsamkeiten in deren Strömungsbeeinflussung identifiziert werden. Infolgedessen sind auch Parametrisierungen einiger Koeffizienten für andere Bauteile gültig und anwendbar als nur für das, wofür diese

Koeffizienten ursprünglich definiert wurden.
Die numerischen Simulationen werden mit Hilfe von ANSYS vorgenommen, basierend auf der Methode der Finiten Volumen und Lösung der Reynolds-gemittelten Navier-Stokes-Gleichungen. Zur Modellierung der Turbulenz kommt das kω-SST Turbulenzmodell zum Einsatz, welches die beste Leistungsfähigkeit und Übereinstimmung mit eigenen Messungen sowie Daten aus der Literatur zeigt. Die Auswertung der numerischen Simulationen und der Vergleich des neuen Ansatzes mit Referenzwerten wird mittels MATLAB vorgenommen.
Die mit dem vorgestellten Ansatz erzielten Ergebnisse zeigen eine sehr gute Übereinstimmung mit den eigenen experimentellen und in der Literatur vorgestellten Ergebnissen. Der hergeleitete impulsbasierte Ansatz in Kombination mit den numerisch ermittelten Koeffizienten bestätigt zudem empirisch gefundene Zusammenhänge physikalisch. Weiterhin kann der Durchfluss durch eine Messblende so genau berechnet werden, wie bei Anwendung des etablierten Ansatzes der Bernoulli-Gleichung mit empirischen Korrekturbeiwerten. Schlussendlich ist der vorgestellte Ansatz anwendbar auf eine Vielzahl von hydraulischen Strukturen, benötigt dabei keine experimentellen Untersuchungen im Vorfeld und erzielt dennoch eine hohe Übereinstimmung mit Messergebnissen.

Contents

1 No Flow Without Momentum / Introduction

1.1 The Bernoulli Principle is Not Enough

Why do aircraft fly? This simple question was recently readdressed in the Scientific American in 2020 [1] and puzzles many engineers and scientists up to date. The present work is not coping with this research issue and, therefore, does not give a response to this big question. But the question serves as a tangible explanation to describe the motivation of this work.

What keeps aircraft in the air still can not be explained satisfactorily by a single theory. Figure 1.1 shows the main principles of how aerodynamic lift is produced. The most common explanation states that lift is produced due to a high-pressure zone at the bottom surface and a low-pressure zone at the top surface of an airfoil, shown on the left side of Fig. 1.1. The accepted assertion is that the different pressure zones occur due to the air molecules passing the lower and upper airfoil surfaces with different velocities. Within the same period, the air molecules at the upper airfoil surface have to cover more distance due to the curved surface than the ones at the lower airfoil surface. Therefore, the literature postulates that two neighboring air molecules parting ways around the airfoil meet again at the airfoil's trailing edge (rear end). This assumption serves as the justification that the flow velocity over the upward-facing airfoil surface must be higher and, consequently, the pressure lower, considering the Bernoulli principle. Although the flow velocity is actually higher, no physical law enforces the two neighboring air molecules parting ways around the airfoil to meet again at the trailing edge. This assumption is also debunked by experiments shown by Babinsky [2]. In this case, a better (but still incomplete) explanation for the origin of lift is obtained by considering the curvature of the streamlines around an airfoil, detailed in Ref. [2] and fused to an all-encompassing approach to explain lift in Epple et al. [3].

However, the common explanation of the production of lift based on different pressure zones completely collapses when aircraft fly inverted or (mostly military) with flat or uniformly thick airfoils. Disregarding the effect of the wing's angle of attack, Newton's third law of motion is consulted for a reasonable explanation, which states that the angled airfoil causes a downward movement of the air molecules resulting in an upturned reacting force of the airfoil as shown on the right side of Fig. 1.1.

Eventually, both theories combined add up to a feasible explanation of how aircraft fly. But straightforward and one-way causations explaining lift are misleading and oversimplify the problem since there is no easy cause-and-effect relation between the flow field and the pressure distribution - due to a coupled system of partial differential equations to be solved jointly, see Epple et al. [3]. The authors also identify a major gap in the explanation of lift which is the imbalance of equations and the number of unknowns. The Bernoulli principle (as a scalar equation) and the Newton principle (as a vectorial equation) give one more unknown variable than the number of equations. Therefore, the principle of mass conservation is always required to resolve the equation system, which is almost never mentioned, according to Ref. [3]. Despite the incompletely revealed enigma of aerodynamic lift, aircraft fly indeed.

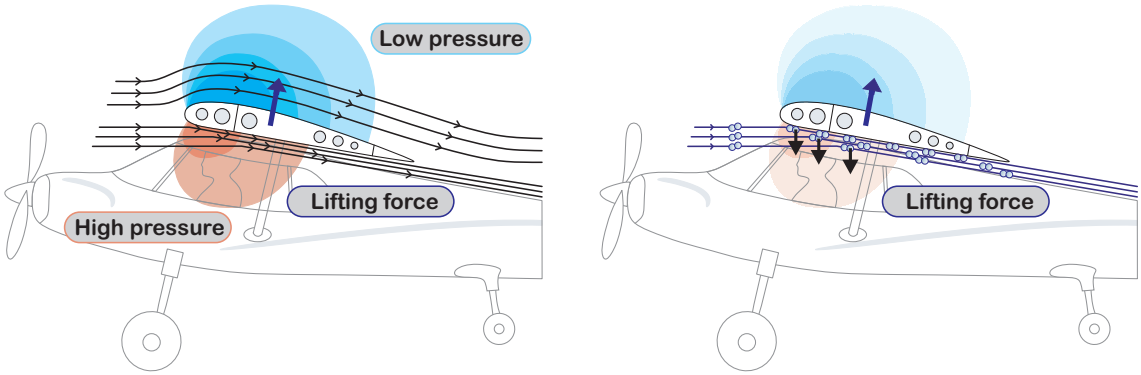

Figure 1.1: Illustration of the flow around an airfoil, following Ref. [1]. The Bernoulli principle is shown on the left and the Newton principle on the right side.

But just because a theory or a technical application works somehow does not necessarily mean that the problem behind is fully explored.
To draw the link to the scope of the present work: even the textbook theories of state-of-the-art hydraulic structures are not covering the physical principles coherently and in full detail. The accepted general consensus is that almost every hydraulic problem can be described by the Bernoulli principle. It can be employed for calculating the pressure loss or flow velocity of any flow structure - except for the sudden expansion. In this case, the momentum-based Borda-Carnot equation must be employed for correct results. Another application where literature defines applying an alternative theory is the calculation of supporting forces of pipe bearings. Here, the momentum balance is accepted as the state-of-the-art method as well. In addition to the described inconsistencies, the application of the Bernoulli principle generally results in gaps between a predicted and a measured result (e.g. the pressure loss of flows through an orifice). In consequence, these gaps are bridged by empirically determined correction coefficients. Therefore, the Bernoulli principle is accompanied by an enormous number of textbooks addressing only correction coefficients for every hydraulic structure to be applied to the theory making it work. In other words: how do hydraulics work? Is there one theory covering all general phenomena and problems and a second theory required for special cases, in analogy to when aircraft fly inverted? And why are empirical coefficients mandatory to obtain the correct result?
To explore these questions in detail, a short outline of the beginning of hydraulics is presented now.

Daniel Bernoulli is considered the founder of hydraulics as we know and use it. He was the first researcher who intensively studied flows and the flow characteristics of different hydraulic structures. Daniel Bernoulli's book 'Hydrodynamica' [4] is known to large extent and contains geometrical descriptions of the observed effects occurring in the conducted experiments, see Fig. 1.2 showing the sketch of a weight force-induced fountain. In the 18th century, Daniel Bernoulli established a calculation method applicable to all hydraulic structures based on the conservation of energy. With the assumption of constant total energy, this principle is simply balancing the internal, kinetic, and potential energy between two points within a flow. Referred to the volume of a fluid element, the energy balance turns into a pressure balance, which is called the Bernoulli principle. Since then, hydraulic calculations primarily rely on the Bernoulli principle, which is discussed in detail in Chap. 1.6. But Daniel Bernoulli already recognized a discrepancy between the predicted and the empirical results, which is bridged by introducing empirical correction coefficients. These correction coefficients represent the factor obtained by dividing the empirical result by the predicted result of test cases. In the end, tabular values

or parametrizations of the correction coefficient are multiplied by the predicted result of the Bernoulli principle, which then yields the more or less correct empirical result.
Ever since significant discrepancies have been occurring between theory and experiment, correction coefficients are implemented to ensure the applicability of a theory. Although these correction coefficients were investigated with great effort, the physical principles behind them have never been questioned to the same extent. It is not unusual that different authors propose different correction coefficient values or parametrizations for the same hydraulic phenomena.
Since Bernoulli's work, giant leaps have been accomplished in hydraulics and fluid engineering in the last century. For one thing, the methodology of employing correction coefficients is state-of-the-art for practical applications. Then again, Computational Fluid Dynamics (CFD) simulations evolved into a powerful and easily operated tool to simulate flows and consequently optimize the design of hydraulic and aerodynamic structures. The described dichotomy between hydraulics and fluid mechanics (CFD) exactly represents the gist of the matter. For analytic calculations, the Bernoulli principle together with application-specific correction coefficients is used and accepted. On the contrary, it is accepted that CFD simulations employ the principle of momentum conservation and yield correct solutions for (almost) every flow. But most importantly, CFD does not require any empirical coefficient, except for the turbulence model if employed. With this contradiction, the present discussion refers back to the beginning and the 'enigma of aerodynamic lift' [1]. One can use and support (correct) a theory to make it work. But at some point, it fails to explain an observed phenomenon, so another theory must be employed (Newton's law of motion for flat airfoils). In analogy, the loss coefficient for every hydraulic structure is obtained empirically - except for the sudden expansion. In this case, the application of the momentum balance yields the correct and physically derived loss coefficient. This indicates that the standard theory is not covering physics completely. That is why, to the author's belief, it all should come down to a single theory capable of predicting the observation without knowing the result in advance.

Initially, A. Malcherek questioned the duality of the two existing approaches, namely the Bernoulli principle and the momentum balance, and why to apply the approaches almost arbitrarily to different hydraulic problems. This ambiguity resulted in the publication presenting a new outflow theory based on the momentum balance, Malcherek [5]. Applicating the momentum balance to weirs [6] and sluice

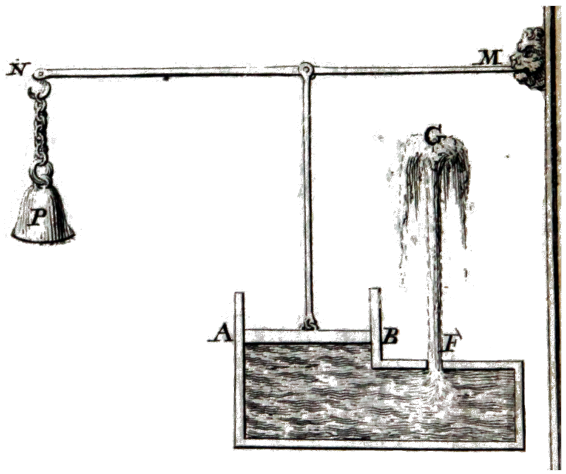

Figure 1.2: Figure 47 of Daniel Bernoulli's Hydrodynamica showing a weight force-induced fountain

gates [7], it turned out that the momentum balance appears to be more suitable - because universally applicable - and a more physically intuitive approach than the Bernoulli principle. In consequence, the preceding research of A. Malcherek gave the green light for the present investigations.
On this account, an approach for hydraulic calculations based on the momentum balance is presented, starting with the basic fluid dynamics in Chap. 1.2 and the derivation of the integral momentum balance in Chap. 1.3. The first fundamental benefit of the proposed approach of connecting theory and numerical simulation is presented in Chap. 1.4. Chapter 1.5 shows how the integral momentum balance can be broken down to practical applicability. It is also shown that, as a major benefit, the geometrical shape of the hydraulic structure is automatically considered by deducing the momentum balance. The Bernoulli principle is derived in Chapter 1.6, including a discussion of its deficiencies and simplifications.
The proposed approach includes the momentum balance, which requires well-defined physical coefficients to substitute integral by average expressions. These coefficients directly result from analyzing the specific flow field and can be obtained by numerical simulations which is a strong differentiation from the empirical correction coefficient. Ultimately, evaluating these coefficients directly leads to a better comprehension of the flow and its phenomena. The numerical model is described in Chap. 2.
Chapter 3 contains the application of the integral momentum balance to hydraulic structures such as the sudden contraction, the sudden expansion, and the metering orifice. It is found that all structures can be described by a very similar theory. In addition, the theory for the metering orifice is a combination of the sudden contraction and the sudden expansion. But the theory based on the Bernoulli principle considers these three related flow structures as independent of each other and with fundamentally different correction coefficients. A comparison of the results obtained by the proposed approach with the results obtained by the Bernoulli principle is also provided.
Eventually, the momentum-based approach is wrapped up in Chap. 4, highlighting its advantages concisely and followed by an outlook on further investigations and applications.

1.2 Basic Models to Describe a Flow

The equations to describe flows can be derived from two different perspectives, represented by the two rows in Fig. 1.3. In the end, both perspectives result in the same, but a different perspective often turns out to be beneficial for comprehension and simplification.

Figure 1.3 shows a flow field of a fluid system represented by the streamlines. Since it is often unpractical or simply impossible to consider and estimate all impacts acting on a whole system, the observation is limited to the relevant parts of this system. Within a finite region of this flow, a closed volume can be defined as the so-called control volume, represented by Ω. A control volume is an open system that solely contains relevant impacts for the present investigation. Therefore, an appropriately chosen control volume is required. The surface of the control volume is represented by $\partial\Omega$.
As shown on the left-hand side of the figure, the control volume can be defined as fixed in space, so the fluid moves through the control volume. Another approach is to define the control volume as moving with the flow, which means that the very same fluid molecules always stay within the control volume. This is shown on the right-hand side of Fig. 1.3. In this case, no mass flows cross the control volume surface of a control volume moving with the flow. This is an important finding when applying the fundamental physical principles to the fluid within the control volume, as shown in the following chapters.
The application of the fundamental physical principles to a finite control volume, as shown in the top

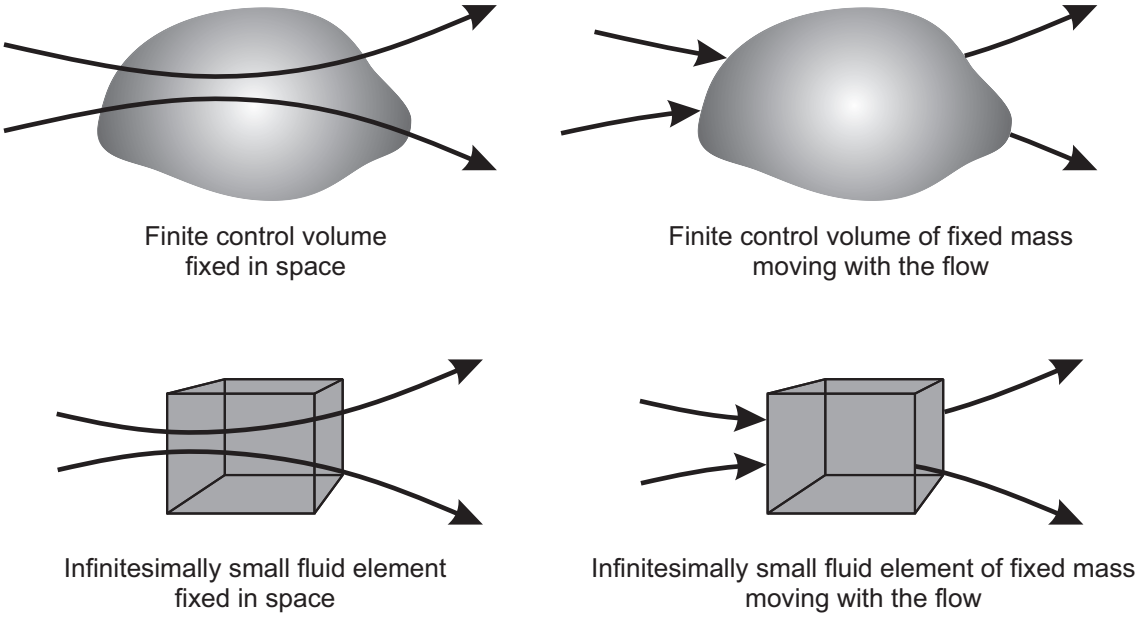

Figure 1.3: Conservation and non-conservation form of a finite and an infinitesimally small volume, following the illustration of Anderson [8]

row in Fig. 1.3, yields the flow equations in integral form. This form is used to obtain the momentum balance for hydraulics.

For both methods, it is also possible to shrink the control volume to an infinitesimally small fluid element $d\Omega$, which still contains a sufficient number of fluid molecules to be considered a continuous medium. This is represented by the bottom row in Fig. 1.3. In analogy to the integral form, the infinitesimal fluid element can also be defined as fixed in space or moving with the flow. The application of the fundamental physical principles to an infinitesimally small fluid element yields the flow equations in partial differential equation form. This form is used to obtain the momentum balance for numerics - also known as the Navier-Stokes equations.

Despite the method applied to derive the flow equations, the equations obtained from a fluid element fixed in space are in conservation form (left-hand side of Fig. 1.3). Contrarily, the equations obtained from a fluid element moving with the flow are in non-conservation form (right-hand side of Fig. 1.3). In general, it is irrelevant which form to apply. Just for special cases such as the simulation of shock waves, instabilities or numerical faults may occur in case the wrong form is applied. In the present work, solely control volumes fixed in space are employed, which means the flow equations are used in the conservation form.

1.3 Why the Integral Momentum Balance is a More Suitable Approach

In this chapter, the momentum balance will be derived in integral form. Based on the integral form, the differential form is derived in Chap. 1.4. The integral form is used for hydraulic calculations, whereas the differential form is used for computational fluid dynamics (CFD) calculations. Therefore, numerics and hydraulic formulas are now based on the same foundation, namely Newton's fundamental laws of motion.

The momentum balance as a conservation law is physically based on Newton's second law of motion [9], which states that the change of a body's motion is proportional to the motive force F acting on the body with the mass m. Nowadays, motion is known to us as momentum I. This law is cast into Eq. (1.1), where the motive force F is the net force or resulting force.

$$\frac{dI}{dt} = F \tag{1.1}$$

Newton also worked out that forces are vectors possessing a direction and magnitude. In a more general way, Eq. (1.1) can be expressed as

$$\frac{d\,(m\vec{v})}{dt} = \sum_i \vec{F}_i \tag{1.2}$$

with the product of mass m and velocity v as the linear momentum I of a system. Here, the net force F is substituted by the sum of all forces $\sum \vec{F}_i$ interacting with the mass. Physically speaking: the change of momentum of a body equals all forces interacting with the body. Applying the product rule of derivation for $d(m\vec{v})/dt = m\ d\vec{v}/dt + \vec{v}\ dm/dt$ to Eq. (1.2) yields

$$\frac{d\,(m\vec{v})}{dt} = m\frac{d\vec{v}}{dt} + \vec{v}\frac{dm}{dt} \tag{1.3}$$

noting that $dm/dt = 0$ due to the assumption of an incompressible fluid. More generally, the left side of Eq. (1.3) can be expressed as

$$m\frac{d\vec{v}}{dt} = \frac{d}{dt}\int\limits_{sys} \varrho\ \vec{v}\ dV \tag{1.4}$$

with $m = \int\limits_{sys} \varrho\ dV$ as the integral of the density over the considered closed system's volume V. But mass does not cross the boundaries of closed systems, whereas a control volume allows mass to cross its boundaries. With the aid of the Reynolds transport theorem, the system formulation of Eq. (1.4) is transformed into the control volume formulation for a moving system.

$$\frac{d}{dt}\int\limits_{sys} \varrho\ \vec{v}\ dV = \frac{d}{dt}\int\limits_{\Omega} \varrho\ \vec{v}\ dV + \int\limits_{\partial\Omega} \varrho\ \vec{v}\,(\vec{v}_r \cdot \vec{n})\ dA \tag{1.5}$$

Here, $\vec{v}_r$ represents the relative fluid velocity in relation to the surface of the control volume (represented by $\partial\Omega$) and $\vec{v}$ the fluid velocity in relation to an inertial coordinate system. The normal unit vector $\vec{n}$ is oriented in the normal direction to the control surface element dA and facing outward of the control volume per definition. For a control volume that is not in motion of deforming, the relative fluid velocity $\vec{v}_r$ is equal to the fluid velocity $\vec{v}$ and Eq. (1.5) yields:

$$\frac{d}{dt}\int\limits_{sys} \varrho\ \vec{v}\ dV = \frac{d}{dt}\int\limits_{\Omega} \varrho\ \vec{v}\ dV + \int\limits_{\partial\Omega} \varrho\ \vec{v}\,(\vec{v} \cdot \vec{n})\ dA \tag{1.6}$$

For a control volume fixed in space and of constant volume, the order of integration and differentiation is irrelevant. Mathematically, this means that the time derivative $(\frac{d}{dt})$ on the right-hand side can be moved inside the integral but must then be changed to a partial derivative $(\frac{\partial}{\partial t})$. The conversion to a partial derivative is mandatory because the density ϱ and the velocity $\vec{v}$ can also be dependent on other variables like the position within the control volume. This results in

$$\frac{d}{dt}\int\limits_{sys} \varrho\ \vec{v}\ dV = \int\limits_{\Omega} \frac{\partial \varrho\ \vec{v}}{\partial t}\ dV + \int\limits_{\partial\Omega} \varrho\ \vec{v}\,(\vec{v}\cdot\vec{n})\ dA \tag{1.7}$$

being also valid for moving control volumes, see Ref. [10] for further details. Thereby, the change of momentum $d\vec{I}/dt$ is completely detailed, so the sum of forces representing the right side of Eq. (1.2) must be examined and quantified.

$$\frac{d\vec{I}}{dt} = \int\limits_{\Omega} \frac{\partial \varrho\ \vec{v}}{\partial t}\ dV + \int\limits_{\partial\Omega} \varrho\ \vec{v}\,(\vec{v}\cdot\vec{n})\ dA = \sum_i \vec{F}_i. \tag{1.8}$$

Equation (1.2) also states that the momentum of a mass (or more precisely: a fluid element) changes when forces are applied to it. The forces acting on a fluid element with the mass m can be divided into:

1. Body forces $\vec{F}_b$ that act on the whole fluid element like gravity, Coriolis force, electric, and magnetic forces as examples
2. Surface forces $\vec{F}_s$ that can be seen as contact forces acting on the surface of the fluid element, which are tangential forces and normal forces.

Therefore, the sum of forces of Eq. (1.8) is substituted by the sum of the body forces and the surface forces.

$$\int\limits_{\Omega} \frac{\partial \varrho\ \vec{v}}{\partial t}\ dV + \int\limits_{\partial\Omega} \varrho\ \vec{v}\,(\vec{v}\cdot\vec{n})\ dA = \sum_i \vec{F}_{b,i} + \sum_i \vec{F}_{s,i}, \tag{1.9}$$

Body forces can be determined by a volume integral on every differential portion of the entire fluid element dV. The gravitational force $\vec{F}_g$ is of superordinate importance for the present investigations, whereas other effects can be neglected in good approximation. It is assumed that only gravity contributes to body forces, which is named the net body force ($\sum \vec{F}_{b,i} \simeq \vec{F}_g$). To account for $\vec{F}_b$ of the whole fluid element, the density ϱ must be integrated over the fluid element's volume V:

$$\sum_i \vec{F}_{b,i} \simeq \vec{F}_g = \int\limits_{V} \varrho\ \vec{g}\ dV = m\ \vec{g} \tag{1.10}$$

In Eq. (1.10), the density ϱ is assumed constant over the whole fluid element and $\vec{g}$ is the gravitational acceleration vector defined pointing in the z-direction. Hence, the z-component of $\vec{g}$ has a negative value when the z-axis is oriented in the opposite direction to the gravitational acceleration.

Surface forces $\vec{F}_{s,i}$ exerted on the surface of a fluid element are the result of pressure and shear stresses that are induced by a flow with velocity gradients. The integral surface forces $\vec{F}_s$ acting on the surface of a fluid element A can be expressed as

$$\vec{F}_s = \int\limits_{A} \boldsymbol{\sigma}\ \vec{n}\ dA \tag{1.11}$$

The normal unit vector $\vec{n}$ is oriented in the normal direction to the surface element dA and facing outward of the fluid element. The stress tensor $\boldsymbol{\sigma}$ contains all stresses that are exerted on the surface of the fluid element. Due to symmetry reasons, the stress tensor is symmetric: $\sigma_{ij} = \sigma_{ji}$, where i and j are the tensor indices. For detailed proof of the symmetry of the stress tensor, see Ref. [11].

By convention, the first index of the stress tensor's component indicates the normal direction of the specific plane. For example, z represents a xy-plane. The second index indicates the direction the stress acts on the surface. Hence, σ_{zy} represents the stress acting on a xy-plane in the y-direction. The stresses acting on the surfaces of the fluid element are shown in Fig. 1.4.

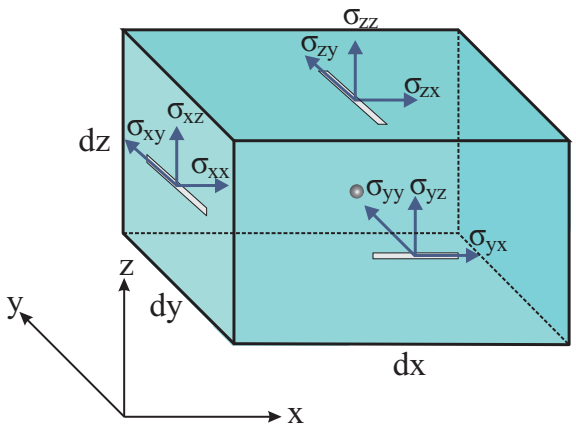

Figure 1.4: Stresses exerted on a fluid element

In detailed notation, the stress tensor $\boldsymbol{\sigma}$ reads: $\boldsymbol{\sigma} = \sigma_{ij} = \begin{bmatrix} \sigma_{xx} & \sigma_{yx} & \sigma_{zx} \\ \sigma_{xy} & \sigma_{yy} & \sigma_{zy} \\ \sigma_{xz} & \sigma_{yz} & \sigma_{zz} \end{bmatrix}$

The components of the stress tensor's main diagonal are the normal stresses $\sigma_{xx}, \sigma_{yy}, \sigma_{zz}$, whereas the components off-diagonal represent the stresses acting tangentially to the surface, called shear stresses. It shall be mentioned that shear stresses entirely result from viscous stresses. Normal stresses result from pressure and viscous stresses since pressure can only act in the normal direction on surfaces. Therefore, the stresses σ_{ij} of the stress tensor $\boldsymbol{\sigma}$ can be split into normal and tangential stresses

$$\boldsymbol{\sigma} = \sigma_{ij} = \begin{bmatrix} -p+\tau_{xx} & \tau_{yx} & \tau_{zx} \\ \tau_{xy} & -p+\tau_{yy} & \tau_{zy} \\ \tau_{xz} & \tau_{yz} & -p+\tau_{zz} \end{bmatrix} = \underbrace{\begin{bmatrix} -p & 0 & 0 \\ 0 & -p & 0 \\ 0 & 0 & -p \end{bmatrix}}_{\mathbf{p}} + \underbrace{\begin{bmatrix} \tau_{xx} & \tau_{yx} & \tau_{zx} \\ \tau_{xy} & \tau_{yy} & \tau_{zy} \\ \tau_{xz} & \tau_{yz} & \tau_{zz} \end{bmatrix}}_{\boldsymbol{\tau}}$$

as a sum of pressure p and viscous stresses τ_{ij} with $\boldsymbol{\tau}$ as the viscous stress tensor and $\mathbf{p}$ as the pressure tensor. The pressure p is uniform in every direction and is defined as a compressive stress. This results in a negative sign because of the sign convention. Tensile stresses are normal stresses with a positive sign as per sign convention. Reminiscing higher mathematics, the inner product of a second-order tensor and first-order tensor (vector) yields a vector. With regard to Eq. (1.11), the inner product of the stress tensor $\boldsymbol{\sigma}$ and the normal unit vector $\vec{n}$ returns a vector whose components represent the stresses on the surface element and whose direction is the direction of the resulting surface force.

Now the stress tensor $\boldsymbol{\sigma}$ can be detailed by considering all stresses on a small fluid element. Figure 1.5 shows the stresses only in the x-direction for better clearness. As a reference point, the center of the fluid element (grey-shaded circle) is used, which enjoys the advantage that the following description is valid for control volumes and infinitesimally small fluid elements as well. Regarding all stresses in

a spatial direction, only the gradient of the stress causes the net force on a (differential) fluid element surface. At the surface to the left of the center point, the gradient of the stress $\partial p/\partial x$ and $\partial \tau_{xx}/\partial x$ represents the share over one surface $1/2\,dx$ analogously for the surface to the right with the inverse sign representing the second share.

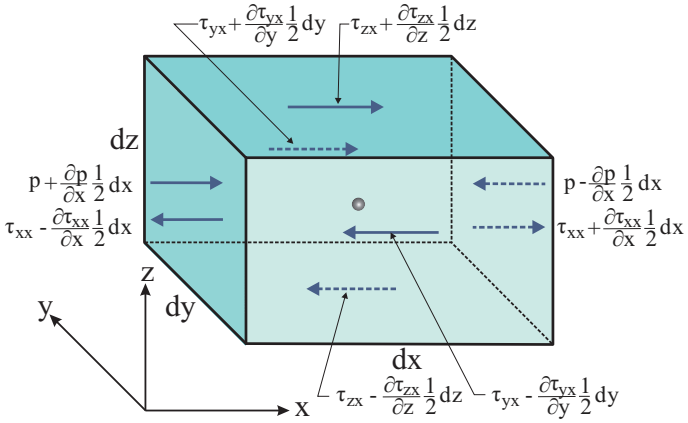

Figure 1.5: Stresses in x-direction exerted on a fluid element. Only the stress gradients cause a net force on the element.

As an example, the stress σ_{xx} on the surface $dy\,dz$ consists of shares of the right surface $\left(p - \frac{\partial p}{\partial x}\frac{1}{2}dx + \tau_{xx} + \frac{\partial \tau_{xx}}{\partial x}\frac{1}{2}dx\right) dy\,dz$ and of the left surface $\left(p + \frac{\partial p}{\partial x}\frac{1}{2}dx + \tau_{xx} - \frac{\partial \tau_{xx}}{\partial x}\frac{1}{2}dx\right) dy\,dz$ (see Fig. 1.5). Subtracting the forces of both surfaces results in the net force induced by surfaces normal to the x-direction $\frac{\partial \sigma_{xx}}{\partial x}dx\,dy\,dz = \left(-\frac{\partial p}{\partial x}dx + \frac{\partial \tau_{xx}}{\partial x}dx\right) dy\,dz$. Summing up all the remaining stress shares in the x-direction and multiplying by the respective surface area gives

$$dF_{s,x} = \left(\frac{\partial \sigma_{xx}}{\partial x} + \frac{\partial \sigma_{yx}}{\partial y} + \frac{\partial \sigma_{zx}}{\partial z}\right) dx\,dy\,dz = \left(-\frac{\partial p}{\partial x} + \frac{\partial \tau_{xx}}{\partial x} + \frac{\partial \tau_{yx}}{\partial y} + \frac{\partial \tau_{zx}}{\partial z}\right) dx\,dy\,dz \tag{1.12}$$

The surface forces in the y- and z-direction are derived accordingly. Consequently, the force is proportional to the fluid element's volume. As mentioned previously, the normal stresses on the tensor's main diagonal comprise pressure and viscous stresses, whereas the off-diagonal components solely result from viscous stresses. All elements of the viscous stress tensor's first row are given in Eq. (1.12). Consequently, the elements of the second row of $\boldsymbol{\tau}$ represent the y-direction and the elements of the third row the z-direction. The summation of the stress tensor's derivatives in all spatial directions is the mathematical definition of the divergence ($div\,\boldsymbol{\tau}$). In addition, the derivatives of pressure in all three spatial directions represent the mathematical expression of the pressure gradient ($grad\,p$). Therefore, the vectorial surface force can be written in short:

$$d\vec{F}_s = (-grad\,p + div\,\boldsymbol{\tau})\,dx\,dy\,dz \tag{1.13}$$

To obtain a solvable set of equations, substitutes with known variables must be found for the components of the viscous stress tensor $\boldsymbol{\tau}$. Therefore, rheology must be employed. Since all investigations in this thesis are based on isothermal Newtonian fluids, the following considerations focus on Newtonian fluids with constant fluid parameters, like the dynamic viscosity μ and the kinematic viscosity ν for an incompressible fluid. Applying this assumption to the viscous stress tensor $\boldsymbol{\tau}$, viscous stresses can be expressed with the aid of the strain rates $\boldsymbol{\varepsilon}$ by

$$\boldsymbol{\tau} = 2\,\mu\,\boldsymbol{\varepsilon} \tag{1.14}$$

as shown by Kundu [12]. For a compressible Newtonian fluid, the term $\xi\,(div\,\vec{v})$ would add to the main diagonal elements of the viscous stress tensor

$$\tau_{ii} = \xi\,(div\,\vec{v}) + 2\,\mu\,\varepsilon_{ii} \tag{1.15}$$

which was already obtained by Stokes [13] in 1845 with the hypothesis that $\xi + \frac{2}{3}\mu = 0$. This is called the Stokes hypothesis and is still found to be accurate for many applications. However, for the present investigations the strain rate tensor $\boldsymbol{\varepsilon}$ is introduced for incompressible fluids (see Ref. [12]) as

$$\boldsymbol{\varepsilon} = \begin{bmatrix} \frac{\partial u}{\partial x} & \frac{1}{2}\left(\frac{\partial u}{\partial y} + \frac{\partial v}{\partial x}\right) & \frac{1}{2}\left(\frac{\partial u}{\partial z} + \frac{\partial w}{\partial x}\right) \\ \frac{1}{2}\left(\frac{\partial v}{\partial x} + \frac{\partial u}{\partial y}\right) & \frac{\partial v}{\partial y} & \frac{1}{2}\left(\frac{\partial v}{\partial z} + \frac{\partial w}{\partial y}\right) \\ \frac{1}{2}\left(\frac{\partial w}{\partial x} + \frac{\partial u}{\partial z}\right) & \frac{1}{2}\left(\frac{\partial w}{\partial y} + \frac{\partial v}{\partial z}\right) & \frac{\partial w}{\partial z} \end{bmatrix}.$$

Introducing $\boldsymbol{\varepsilon}$ to Eq. (1.14), the viscous stress tensor $\boldsymbol{\tau}$ gives

$$\boldsymbol{\tau} = \begin{bmatrix} 2\mu\frac{\partial u}{\partial x} & \mu\left(\frac{\partial u}{\partial y} + \frac{\partial v}{\partial x}\right) & \mu\left(\frac{\partial u}{\partial z} + \frac{\partial w}{\partial x}\right) \\ \mu\left(\frac{\partial v}{\partial x} + \frac{\partial u}{\partial y}\right) & 2\mu\frac{\partial v}{\partial y} & \mu\left(\frac{\partial v}{\partial z} + \frac{\partial w}{\partial y}\right) \\ \mu\left(\frac{\partial w}{\partial x} + \frac{\partial u}{\partial z}\right) & \mu\left(\frac{\partial w}{\partial y} + \frac{\partial v}{\partial z}\right) & 2\mu\frac{\partial w}{\partial z} \end{bmatrix} \tag{1.16}$$

solely comprising velocity gradients $\partial u_i/\partial x_j$ and the dynamic viscosity μ. Introducing the respective elements of $\boldsymbol{\tau}$ as per Eq. (1.16) into Eq. (1.12) gives

$$dF_{s,x} = \left(-\frac{\partial p}{\partial x} + 2\,\mu\frac{\partial}{\partial x}\frac{\partial u}{\partial x} + \mu\frac{\partial}{\partial y}\left(\frac{\partial v}{\partial x} + \frac{\partial u}{\partial y}\right) + \mu\frac{\partial}{\partial z}\left(\frac{\partial w}{\partial x} + \frac{\partial u}{\partial z}\right)\right) dx\,dy\,dz \tag{1.17}$$

The velocity components of fluids are continuous functions of the spatial directions, which mathematically means that the order of differentiation can be changed arbitrarily:

$$\frac{\partial}{\partial y}\frac{\partial v}{\partial x} = \frac{\partial}{\partial x}\frac{\partial v}{\partial y}. \tag{1.18}$$

In addition, the following rearrangement of the second-order derivative of Eq. (1.17)

$$2\,\mu\frac{\partial^2 u}{\partial x^2} = \mu\frac{\partial^2 u}{\partial x^2} + \mu\frac{\partial}{\partial x}\frac{\partial u}{\partial x} \tag{1.19}$$

proves beneficial for incompressible flow since the continuity equation is revealed to be set to zero as subsequently shown. Rearrangement of the viscous stress terms of Eq. (1.17) in due consideration of the formulations as per Eq. (1.18) and Eq. (1.19) yields

$$dF_{s,x} = \left(-\frac{\partial p}{\partial x} + \mu\left(\frac{\partial^2 u}{\partial x^2} + \frac{\partial}{\partial x}\frac{\partial u}{\partial x} + \frac{\partial}{\partial x}\frac{\partial v}{\partial y} + \frac{\partial^2 u}{\partial y^2} + \frac{\partial}{\partial x}\frac{\partial w}{\partial z} + \frac{\partial^2 u}{\partial z^2}\right)\right) dx\,dy\,dz$$

$$dF_{s,x} = \left(-\frac{\partial p}{\partial x} + \mu\left(\frac{\partial}{\partial x}\left(\frac{\partial u}{\partial x} + \frac{\partial v}{\partial y} + \frac{\partial w}{\partial z}\right) + \frac{\partial^2 u}{\partial x^2} + \frac{\partial^2 u}{\partial y^2} + \frac{\partial^2 u}{\partial z^2}\right)\right) dx\,dy\,dz \tag{1.20}$$

Since the fluid is assumed incompressible, the term $\frac{\partial u}{\partial x} + \frac{\partial v}{\partial y} + \frac{\partial w}{\partial z}$ representing the continuity equation is equal to zero. The remaining velocity derivatives can be written compendiously by the Laplacian operator or the squared Nabla operator ∇^2:

$$dF_{s,x} = \left(-\frac{\partial p}{\partial x} + \mu \nabla^2 \, u \right) dx \, dy \, dz \tag{1.21}$$

which is equal to

$$dF_{s,x} = \left(-\frac{\partial p}{\partial x} + \mu \, div \, (grad \; u) \right) dx \, dy \, dz \tag{1.22}$$

For all three spatial directions, the surface force is therefore given by

$$d\vec{F}_s = \left(-grad \, p + \mu \, div \, (grad \, \vec{v}) \right) dx \, dy \, dz \tag{1.23}$$

Since the off-diagonal elements of the pressure tensor are zero, the divergence of the pressure tensor $div \, \mathbf{p}$ is equal to the pressure gradient $grad \, p$. As a result, the integral form of Eq. (1.23) combined for all directions yields

$$\int\limits_{\Omega} div \, \boldsymbol{\sigma} \, d\Omega = - \int\limits_{\Omega} div \, \mathbf{p} \, d\Omega + \int\limits_{\Omega} \mu \, div \; (grad \, \vec{v}) \; d\Omega \tag{1.24}$$

with $d\Omega = dx \, dy \, dz$. Applying the divergence (or Gauss) theorem to the volume integrals results in area integrals to be multiplied by the normal unit vector $\vec{n}$ of the respective surface. The pressure tensor $\mathbf{p}$ can be replaced by the pressure p because the values of the pressure tensor's main diagonal are equal to the uniform pressure p. Therefore, Eq. (1.24) gives

$$\int\limits_{\partial\Omega} \boldsymbol{\sigma} \vec{n} \, dA = - \int\limits_{\partial\Omega} p \, \vec{n} \, dA + \int\limits_{\partial\Omega} \mu \; (grad \, \vec{v}) \, \vec{n} \, dA = \sum_i \vec{F}_s \tag{1.25}$$

representing the sum of the surface forces. At this point, it shall be mentioned that surface forces $\vec{F}_s$ can also be induced by flow machines (pumps, turbines, etc.). Physically speaking, flow machines can be seen as additional surface forces that add or take the momentum from the flow. This means the impact of flow machines on the flow can be considered by an additional surface force term $\vec{F}_{add}$. This is important to consider when the control volume comprises a flow machine. Equation (1.9), together with Eq. (1.10) and Eq. (1.25), gives the integral momentum balance for incompressible fluids

$$\int\limits_{\Omega} \frac{\partial \varrho \, \vec{v}}{\partial t} \, dV + \int\limits_{\partial\Omega} \varrho \, \vec{v} \, (\vec{v} \cdot \vec{n}) \; dA = \int\limits_{\Omega} \varrho \, \vec{g} \, dV - \int\limits_{\partial\Omega} p \, \vec{n} \, dA + \int\limits_{\partial\Omega} \mu \; (grad \, \vec{v}) \, \vec{n} \, dA + \sum_i \vec{F}_{add}. \tag{1.26}$$

Equation (1.26) represents the physical foundation of the present work. Derived from fundamental laws of motion, Eq. (1.26) serves as the basis for the derivation of the Navier-Stokes equations, demonstrated in the following chapter, plus for the application to analytical hydraulic calculations as shown in Chap. 1.5.

1.4 From Integral to Differential - the Navier-Stokes Equations

The Navier-Stokes equations have been derived by Navier [14] in 1821 and represent the cornerstone for hydrodynamics and flow simulations. The Navier-Stokes equations comprise the momentum equations in all three spatial directions. It was the first time fluid viscosity effects have been considered formally in contrast to the equations of the fluid motion introduced by Euler [15] in 1757. The so-called Euler equations originally comprise the continuity and the momentum equations for inviscid flow. By definition, an inviscid flow neglects viscosity and mass diffusion, resulting in limited applicability of the Euler equations in fluid dynamics.
However, Stokes' contribution leading to the association with the Navier-Stokes equations refers to the investigation of viscous effects by examining pendulum motions. Stokes calculated cases of motion regarding oscillating spheres and cylinders and investigated the deviation from ideal fluids to viscous (real) fluids [16]. Stokes identified frictional effects as the main reason for the recognized deviation. But the author also addressed other effects, such as the discontinuity of flows causing instabilities that lead to turbulent wakes. In a subsequent publication [13, p. 298], Stokes concluded that the Navier-Stokes equations and the continuity equation "[...] apply to the determination of the motion of water in pipes and canals, to the calculation of the effect of friction on the motions of tides and waves, and such questions". Finally, Stokes obtained a high agreement of the experimental data of the oscillation experiments with the results of the later so-called Navier-Stokes equations. Stokes' focus on a practical application of Navier's equations reasons that Stokes is nowadays also associated with the Navier-Stokes equations.

In the following, the derivation of the Navier-Stokes equations from the integral momentum balance is demonstrated.
Converting the area integrals back into volume integrals with the aid of the divergence theorem and substituting the left side by the integral expression as per Eq. (1.7), Eq. (1.26) yields

$$\int_\Omega \frac{\partial\, \varrho\, \vec{v}}{\partial t} dV + \int_\Omega \varrho\; div\,(\vec{v} \otimes \vec{v})\; dV = \int_\Omega \varrho\; \vec{g}\, dV - \int_\Omega grad\, p\; dV + \int_\Omega \mu\, div\;(grad\, \vec{v})\; dV \tag{1.27}$$

with $\otimes$ as the dyadic or tensor product. Additional forces $\vec{F}_{add}$ are neglected. Here, the pressure gradient is introduced instead of the divergence, as explained before Eq. (1.24). Now, the control volume is thought to approach zero sizes meaning the integrals cease. Applying the product rule of calculus to the differential of the left side of Eq. (1.27) results in

$$\varrho \frac{\partial \vec{v}}{\partial t} + \vec{v} \frac{\partial \varrho}{\partial t} = \varrho\; \vec{g} - \varrho\; div\,(\vec{v} \otimes \vec{v}) - grad\, p + \mu\, div\;(grad\, \vec{v}) \tag{1.28}$$

In due consideration of constant density $(\partial \varrho / \partial t = 0)$, Eq. (1.28) divided by ϱ gives

$$\frac{\partial \vec{v}}{\partial t} = \vec{g} - div\,(\vec{v} \otimes \vec{v}) - \frac{1}{\varrho}\, grad\, p + \nu\, div\;(grad\, \vec{v}) \tag{1.29}$$

with $\nu = \mu / \varrho$ as the kinematic viscosity. The tensor product of the velocity $\vec{v} \otimes \vec{v}$ is a velocity matrix. With a little rearrangement of Eq. (1.29), the Navier-Stokes-equations in conservation form are obtained in the concise vectorial notation.

$$\begin{aligned}\frac{\partial \vec{v}}{\partial t} + div\,(\vec{v} \otimes \vec{v}) &= \vec{g} - \frac{1}{\varrho}\, grad\, p + \nu\, div\ (grad\, \vec{v}) \\ \frac{\partial \vec{v}}{\partial t} + \nabla \cdot (\vec{v} \otimes \vec{v}) &= \vec{g} - \frac{1}{\varrho}\, \nabla\, p + \nu\, \nabla^2\, \vec{v}\end{aligned} \tag{1.30}$$

Here, the Nabla operator with the multiplication sign ($\nabla\cdot$) indicates the divergence, whereas the Nabla operator without the multiplication sign indicates the gradient. Equation (1.30) applied to a Cartesian coordinate system yields

$$\begin{aligned}\frac{\partial u}{\partial t} + \frac{\partial u^2}{\partial x} + \frac{\partial u\, v}{\partial y} + \frac{\partial u\, w}{\partial z} &= g_x - \frac{1}{\varrho}\frac{\partial p}{\partial x} + \nu \left(\frac{\partial^2 u}{\partial x^2} + \frac{\partial^2 u}{\partial y^2} + \frac{\partial^2 u}{\partial z^2}\right) \\ \frac{\partial v}{\partial t} + \frac{\partial u\, v}{\partial x} + \frac{\partial v^2}{\partial y} + \frac{\partial v\, w}{\partial z} &= g_y - \frac{1}{\varrho}\frac{\partial p}{\partial y} + \nu \left(\frac{\partial^2 v}{\partial x^2} + \frac{\partial^2 v}{\partial y^2} + \frac{\partial^2 v}{\partial z^2}\right) \\ \frac{\partial w}{\partial t} + \frac{\partial u\, w}{\partial x} + \frac{\partial v\, w}{\partial y} + \frac{\partial w^2}{\partial z} &= g_z - \frac{1}{\varrho}\frac{\partial p}{\partial z} + \nu \left(\frac{\partial^2 w}{\partial x^2} + \frac{\partial^2 w}{\partial y^2} + \frac{\partial^2 w}{\partial z^2}\right)\end{aligned} \tag{1.31}$$

and reveals that the Equations (1.31) comprise four unknowns (p, u, v, and w). For a solution independent of one of the unknowns, an additional equation must be employed, which is the continuity equation:

$$\frac{\partial \varrho}{\partial t} + \nabla \cdot (\varrho\, \vec{v}) = 0 \tag{1.32}$$

The continuity equation is given in conservation form since the fluid element is fixed in space.

A more prevalent shape of the Navier-Stokes-Equations is obtained by deriving the left side of Eq. (1.2) for an infinitesimal fluid element moving with the flow, which represents the non-conservation form. In this case, solely the left sides of Eq. (1.31) are changing. A compendious derivation is given by Anderson [8]. Recalling Eq. (1.2), the velocity change per time rate of a moving fluid element is a function of time t and the location $x,\ y,\ z$, which is the mathematical definition of the substantial derivative, indicated by D/Dt. The assumption of an incompressible fluid ($Dm/Dt = 0$) yields

$$m \frac{D\vec{v}}{Dt} = \sum_i \vec{F}_i \tag{1.33}$$

For an infinitesimally small fluid element whose volume approaches zero, Eq. (1.33) is divided by the volume, which gives the density ϱ on the left-hand side and the force per volume on the right-hand side. By the definition of the substantial derivative, the left-hand side of Eq. (1.33) can be expressed by

$$\varrho \frac{D\vec{v}}{Dt} = \varrho \left(\frac{\partial \vec{v}}{\partial t} + \frac{dx}{dt}\frac{\partial \vec{v}}{\partial x} + \frac{dy}{dt}\frac{\partial \vec{v}}{\partial y} + \frac{dz}{dt}\frac{\partial \vec{v}}{\partial z}\right) = \varrho \left(\frac{\partial \vec{v}}{\partial t} + (\vec{v} \cdot \nabla)\, \vec{v}\right) \tag{1.34}$$

with $dx/dt = u$, $dy/dt = v$, and $dz/dt = w$. The partial differential of the right-hand side of Eq. (1.34) is the local acceleration that vanishes for steady flow conditions. The divergence term represents the so-called convective acceleration that affects the fluid element moving through flow regions of spatial velocity changes such as orifices, expansions, or contractions. With Eq. (1.34) reduced by ϱ and used in Eq. (1.31) as the substitute for the left sides, the Navier-Stokes-Equations in the non-conservation

form are obtained.

$$\begin{aligned}
\frac{\partial u}{\partial t} + u\frac{\partial u}{\partial x} + v\frac{\partial u}{\partial y} + w\frac{\partial u}{\partial z} &= g_x - \frac{1}{\varrho}\frac{\partial p}{\partial x} + \nu\left(\frac{\partial^2 u}{\partial x^2} + \frac{\partial^2 u}{\partial y^2} + \frac{\partial^2 u}{\partial z^2}\right) \\
\frac{\partial v}{\partial t} + u\frac{\partial v}{\partial x} + v\frac{\partial v}{\partial y} + w\frac{\partial v}{\partial z} &= g_y - \frac{1}{\varrho}\frac{\partial p}{\partial y} + \nu\left(\frac{\partial^2 v}{\partial x^2} + \frac{\partial^2 v}{\partial y^2} + \frac{\partial^2 v}{\partial z^2}\right) \\
\frac{\partial w}{\partial t} + u\frac{\partial w}{\partial x} + v\frac{\partial w}{\partial y} + w\frac{\partial w}{\partial z} &= g_z - \frac{1}{\varrho}\frac{\partial p}{\partial z} + \nu\left(\frac{\partial^2 w}{\partial x^2} + \frac{\partial^2 w}{\partial y^2} + \frac{\partial^2 w}{\partial z^2}\right)
\end{aligned} \tag{1.35}$$

The direct conversion of the left-hand sides of the Navier-Stokes-Equations from conservation to non-conservation form is given in detail in Ref. [8]. However, for a solvable set of equations, the continuity equation in the non-conservation form must be employed in addition.

$$\frac{D\varrho}{Dt} + \varrho\nabla\cdot\vec{v} = 0 \tag{1.36}$$

Ultimately, this short derivation of the Navier-Stokes equations from the integral momentum balance shows the close relation of both approaches. In the following, the integral momentum balance is simplified to be employed for practical applications.

1.5 Breaking Down the Integral Momentum Balance for Practical Hydraulics

The integral momentum balance, as per Eq. (1.26), yields the exact solution of the flow variables of a specific control volume. But the vectorial formulation of the momentum balance contains a time derivative ($\partial/\partial t$) and additionally requires integration over the whole control volume Ω or the control volume's surface $\partial\Omega$. Therefore, Eq. (1.26) is limitedly suitable for practical hydraulics and concise hydraulic formulas.

For a practical application of the integral momentum balance to hydraulics, the flow must be stationary or assumed stationary in good approximation. This results in the time derivative equalling zero, so the whole term is canceled. Normally, the momentum of the flow in the flow direction is the important object of the calculation. Therefore, Eq. (1.26) is multiplied by the normal unit vector in the flow direction $\vec{n}_v$ via the dot product, which results in the scalar momentum equation in the flow direction. Additional forces are not considered for the sake of a lucid and applicable simplification. Applying the described modifications to Eq. (1.26) gives

$$\int_{\partial\Omega} \varrho\,\vec{v}\;(\vec{v}\cdot\vec{n})\;\vec{n}_v\,dA = \int_{\Omega} \varrho\,\vec{g}\cdot\vec{n}_v\,dV - \int_{\partial\Omega} p\,\vec{n}\cdot\vec{n}_v\,dA + \int_{\partial\Omega} \mu\;(grad\,\vec{v})\,\vec{n}\cdot\vec{n}_v\,dA. \tag{1.37}$$

The integrals physically mean that the velocity and pressure distributions over the (open) surface of the control volume must be known since all practical flows are not uniformly distributed over the inlets and outlets of a control volume. The open boundaries of the control volume should be placed in regions where the flow is fully (re-)developed. This means that the pressure can be assumed constant over the surface, and the integral expression can be expressed by the sum of the pressure forces of all open boundaries i: $\sum_i\; p_i\,\vec{n_i}\cdot\vec{n}_v\,A_i$, leading to:

$$\int\limits_{\partial\Omega} \varrho\, \vec{v}\ (\vec{v}\cdot\vec{n})\ \vec{n}_v\, dA = \int\limits_{\Omega} \varrho\, \vec{g}\cdot\vec{n}_v\, dV - \sum_i p_i\, \vec{n_i}\cdot\vec{n}_v\, A_i + \int\limits_{\partial\Omega} \mu\ (grad\,\vec{v})\,\vec{n}\cdot\vec{n}_v\, dA. \tag{1.38}$$

Nevertheless, the velocity distribution diverges considerably from a constant value over the control surface, whether the surface is placed in a fully or non-fully developed flow region. Therefore, an integration coefficient must be introduced to avoid the integral velocity formulation but consider the non-uniform velocity distribution. Boussinesq [17] was the first who proposed an equation to substitute the integral of the velocity over a cross-section by the mean velocity. This coefficient β is named the momentum coefficient in the following. In the literature, β is often named the momentum correction coefficient. But in the proper sense, β is no correction coefficient since the momentum coefficient is exactly substituting the integral expression. The preface of Boussinesq's book [17, pp. VII-IX] contains considerations on a coefficient that takes into account the fluid's inertia and, more importantly, the inhomogeneity of the velocities in different sections. Boussinesq also proposes analytical equations to calculate the coefficient for rectangular and semicircular channel flow. This means that Boussinesq found out that the velocity distribution is dependent on the viscosity μ (ν) and the wall roughness ks. Boussinesq defines the coefficient β as a sum of the value for an ideal homogeneous velocity distribution (unity) plus its deviation from the ideal value due to the viscosity (named internal friction by Boussinesq) and the wall roughness (named external friction by Boussinesq). Numerical flow simulations of different liquids in circular pipes at the same Reynolds number indicate that the momentum coefficient β is indeed dependent on the viscosity and the wall roughness. But the wall roughness exhibits a superior impact on β, so the effect of the viscosity can be neglected in good approximation for practical liquid flows.

In the second chapter of Ref. [17, p. 66], Boussinesq derives the equation to calculate the momentum coefficient directly by theoretically examining fluid particles on a streamline. The author proposes an approach to substitute the local velocities or velocity distributions v of a specific area A by the mean velocity Q/A over the full cross-section with Q representing the volumetric flow rate. Therefore, the required coefficient β is introduced, accounting for the ratio of the area integral of the squared velocity to the squared mean velocity times the area, which leads to:

$$\beta = \int\limits_A \frac{v^2}{\left(\frac{Q}{A}\right)^2}\, \frac{dA}{A}, \tag{1.39}$$

or formulated alternatively:

$$\int\limits_A v^2\, dA = \beta\, \left(\frac{Q}{A}\right)^2\, A. \tag{1.40}$$

Therefore, the integration coefficient β is obtained by setting the exact integral flux term of Eq. (1.38) equal to the flux term based on the average velocity Q/A over the inlet or outlet of the control volume. Practically speaking, β represents a value defining the mean deviation of the velocity at every area element of the cross-section dA from the average velocity of this cross-section.

Idelchik proposed the following purely empirical formulation to evaluate the momentum coefficient in Ref. [18, p. 115]

$$\beta = \frac{(2\,q+1)^2\,(q+1)}{4\,q^2\,(q+2)} \tag{1.41}$$

with q as a variable ranging from 1 to ∞. The velocity profile corresponds to a triangle for $q = 1$ but to a rectangle for $q = \infty$. Idelchik proposes to perform experimental investigations if the velocity profile (or the value of q) is unknown. For $q = 6$, a very high correlation to the momentum coefficient β of fully developed turbulent pipe flow can be obtained.
Nowadays, the velocity distribution can be obtained precisely with the aid of numerical simulations. Therefore, the integral velocity can be substituted by the mean velocity multiplied by the well-defined momentum coefficient β for every open boundary i. With $\vec{v}\ \vec{n}_v = v$ where v is the velocity in flow direction and $\vec{v}\ \vec{n}$ only accounting for the right direction of the velocity, the vectorial momentum flux term ultimately turns into a scalar one, so Eq. (1.40) can be applied. Equation (1.40) used in Eq. (1.38) now gives

$$\sum_i \varrho\ \beta_i\ v_i\ \vec{v}_i \cdot \vec{n}_i\ A_i = \int_\Omega \varrho\ \vec{g} \cdot \vec{n}_v\ dV - \sum_i p_i\ \vec{n}_i \cdot \vec{n}_v\ A_i + \int_{\partial\Omega} \mu\ (grad\,\vec{v})\ \vec{n} \cdot \vec{n}_v\ dA. \tag{1.42}$$

Here, the integral momentum flux term is replaced by a sum of the averaged momentum fluxes of all open boundaries analogously to the pressure force term. Since the flow is considered incompressible, the integral of the density ϱ over the volume Ω can be replaced by the constant mass of the considered control volume m (see Eq. (1.10)), which reduces Eq. (1.42) to

$$\sum_i \varrho\ \beta_i\ v_i\ \vec{v}_i \cdot \vec{n}_i\ A_i = m\ \vec{g} \cdot \vec{n}_v - \sum_i p_i\ \vec{n}_i \cdot \vec{n}_v\ A_i + \int_{\partial\Omega} \mu\ (grad\,\vec{v})\ \vec{n} \cdot \vec{n}_v\ dA. \tag{1.43}$$

But Eq. (1.43) is still not analytically evaluable since all spatial velocity derivatives must be known to obtain a result for the viscous stress term. Therefore, a multitude of investigations have been made in the 19th century to obtain a suitable analytical expression for viscous stresses. Finally, the Weisbach equation [19] became accepted in hydraulics and is used to merge the viscous stresses into one simple expression called the friction force F_F

$$F_F = \varrho\ \lambda\ A\ \frac{L\ Q^2}{d_{Hyd}\ 2\ A^2} \tag{1.44}$$

with λ as the friction factor, L as the length where friction occurs, and d_{Hyd} as the hydraulic diameter. Since the derivatives $\partial u_i / \partial x_j$ account for the correct sign of the viscous stresses, the sign of the friction force must be defined by convention: Friction is always counteracting the direction of motion and, therefore, diminishes the momentum of a flow which means the sign must be negative.

$$\int_{\partial\Omega} \mu\ (grad\,\vec{v})\ \ \vec{n} \cdot \vec{n}_v\ dA := -\varrho\ \lambda\ A\ \frac{L\ Q^2}{d_{Hyd}\ 2\ A^2} = -F_F \tag{1.45}$$

Colebrook [20] and Colebrook and White [21] investigated the correlation of the wall roughness ks, the Reynolds number Re, and the frictional pressure loss. The outcome is the so-called Colebrook-White equation which can be applied to smooth and rough surfaces to calculate λ iteratively.
Using Eq. (1.45) in Eq. (1.43) with the momentum flux term flipped to the right side gives

$$0 = m\ \vec{g} \cdot \vec{n}_v - \sum_i \varrho\ \beta_i\ v_i\ \vec{v}_i \cdot \vec{n}_i\ A_i - \sum_i p_i\ \vec{n}_i \cdot \vec{n}_v\ A_i - F_F. \tag{1.46}$$

This is the final formula straightforwardly applicable to hydraulic structures.
As an example: For a horizontal pipe flow in the positive x-direction with one inlet and one outlet, the

normal unit vectors give $\vec{n}_1 = [-1;\ 0]$ at the inlet side, $\vec{n}_2 = [1;\ 0]$ at the outlet side and $\vec{n}_v = [1;\ 0]$ in the flow direction. In consequence, for a flow through a horizontal pipe with no flow obstructions, Eq. (1.46) simplifies to

$$0 = \varrho\ \beta_1 \frac{Q_1^2}{A_1} - \varrho\ \beta_2 \frac{Q_2^2}{A_2} + p_1\ A_1 - p_2\ A_2 - F_F \tag{1.47}$$

1.6 How the Bernoulli Principle is Abused

In contrast to the integral momentum balance, the principle of the conservation of energy (or energy balance) can be derived from the first law of thermodynamics. But to the author's conviction, in a cumbersome way compared with the momentum balance. However, the energy balance can be straightforwardly derived from the momentum balance as well, which will be shown in this paragraph. Therefore, some assumptions and simplifications have to be made so the energy balance can be seen as a special case of the general momentum balance. It leads Epple et al. [3, p. 5] to the conclusion that "the Bernoulli equation is basically only half of the momentum or complete Euler equation" since it provides no information in the normal direction to the streamlines.

Resuming Eq. (1.37) for a control volume moving with the fluid flow, no mass enters or leaves the control volume. This means that the momentum flux term gives zero. Assuming a flow without additional forces $\vec{F}_{add}$ and applying the substitution of the frictional force as per Eq. (1.45), the change of momentum $d\vec{I}/dt$ for a fluid of constant density can be expressed as

$$\frac{m\, d\vec{v}}{dt} = m\vec{g} - \int\limits_{\partial\Omega} p\ \vec{n}\ dA - \vec{F}_F. \tag{1.48}$$

Equation (1.48) is now multiplied by the velocity of the system's center of gravity $\vec{v} = d\vec{x}/dt$. To express $\vec{v}$ on the left side of Eq. (1.48) as a time derivative, the velocity must be integrated. Therefore, the chain rule ($d\vec{v}^2/dt = 2\ \vec{v}\ d\vec{v}/dt$) is applied in reverse ($\vec{v}\ d\vec{v}/dt = \frac{1}{2}\ d\vec{v}^2/dt$), giving

$$\frac{1}{2}\ m \frac{dv^2}{dt} = m\ \vec{g}\ \frac{d\vec{x}}{dt} - \int\limits_{\partial\Omega} p\ \vec{n}\ dA\ \frac{d\vec{x}}{dt} - \vec{F}_F\ \frac{d\vec{x}}{dt}. \tag{1.49}$$

Multiplication of the velocity with the velocity of the system's center of gravity yields the scalar of the squared velocity on the left side of Eq. (1.49). The dot product of $\vec{g}$ and the position vector $\vec{x}$ yields the gravitational acceleration g multiplied by the z-component of $\vec{x}$ as a scalar. The z-component of $\vec{g}$ is oriented inverse to the z-direction. Integration of Eq. (1.49) over the time t from t_1 to t_2 gives

$$\frac{1}{2}\ m\left(v_2^2 - v_1^2\right) = -m\ g\left(z_2 - z_1\right) - \int\limits_{t_1}^{t_2} \int\limits_{\partial\Omega} p\ \vec{n}\ dA\ \frac{d\vec{x}}{dt}\ dt - \int\limits_{t_1}^{t_2} \vec{F}_F\ \frac{d\vec{x}}{dt}\ dt. \tag{1.50}$$

Applying the Gauss theorem to the pressure term, Eq. (1.50) gives

$$\frac{1}{2}\ m\left(v_2^2 - v_1^2\right) = -m\ g\left(z_2 - z_1\right) - \int\limits_{t_1}^{t_2} \int\limits_{\Omega} \nabla p\ d\Omega\ \frac{d\vec{x}}{dt}\ dt - \int\limits_{t_1}^{t_2} \vec{F}_F\ \frac{d\vec{x}}{dt}\ dt. \tag{1.51}$$

For an infinitesimally small control volume Ω, the integration over the control volume Ω can be substituted by the multiplication with the volume V. In addition, the pressure is constant over the entire

control volume Ω. With the substitution rule applied to the integration of the time derivative over time, the integrals of the pressure and the friction term change, and Eq. (1.51) gives

$$\frac{1}{2}\, m \left(v_2^2 - v_1^2\right) = -m\, g\, (z_2 - z_1) - V \int_{x_1}^{x_2} \nabla p \, d\vec{x} - \int_{x_1}^{x_2} \vec{F}_F \, d\vec{x} \tag{1.52}$$

The integral of the pressure term represents the fundamental theorem of calculus. By evaluating both integrals and sorting by the indices of Eq. (1.52), the energy conservation principle is obtained

$$\frac{1}{2}\, m\, v_1^2 + m\, g\, z_1 + V\, p_1 = \frac{1}{2}\, m\, v_2^2 + m\, g\, z_2 + V\, p_2 - F_F(x_2 - x_1). \tag{1.53}$$

Since it is practically impossible to track and consider individual fluid particles, the energy balance, as per Eq. (1.53) is referred to a fluid volume element V. Therefore, Eq. (1.53) is divided by the volume V, which gives the specific energy, or in other words, the pressure p, and finally results in the Bernoulli principle in its common shape

$$\frac{1}{2}\, \varrho\, v_1^2 + \varrho\, g\, z_1 + p_1 = \frac{1}{2}\, \varrho\, v_2^2 + \varrho\, g\, z_2 + p_2 + \varrho\, g\, h_{loss} \tag{1.54}$$

Here, $x_1 - x_2$ is substituted by the loss of pressure head h_{loss} since the pressure loss due to friction has been obtained by comparing the fluid column height of manometers in former times. Since friction increasingly dissipates energy with increasing flow length for a flow from 1 to 2, the loss of pressure due to friction adds to the total pressure at location 2 to balance the equation.
The transition from Eq. (1.48) to Eq. (1.54) shows that the so-called Bernoulli principle is not autonomous since it solely represents the conservation of energy along a streamline. Therefore, the term principle is misleading in the proper sense but is established in the literature and thus will be used in the present work as well - even though the term Bernoulli equation appears to be the appropriate denomination.
In conclusion, Eq. (1.54) is obtained for an infinitesimal fluid volume moving with the flow. This means that the Bernoulli principle is solely applied adequately when considering the same fluid particle at different times, which represents the Lagrangian description. For a moving fluid particle, different times also mean different locations. The track a fluid particle moves on is called streamline, which must be known in advance before the Bernoulli principle can be adequately applied to it.

The Bernoulli principle can also be derived from the Euler equations assuming ideal frictionless flow. In case the Bernoulli principle shall be applicable between streamlines, a flow without rotation must be assumed additionally. This so-called irrotational flow presumes the absence of vorticity. The viscosity of a fluid induces vorticity between fluid particles of different velocities, especially in the vicinity of walls at turbulent flow. But for a cylinder rotating in a viscous fluid, an irrotational vortex is generated even though viscous effects are present (see Kundu [12] for detailed explanations). This means that viscous stresses can be present, but without net viscous forces, a flow is irrotational. Although the majority of practical flows cannot be assumed to be irrotational, since all fluids are viscous and most applications go beyond a rotating cylinder, it is fair to say that almost every real flow will induce vorticity. However, the absence of viscous effects in the main flow region can be considered a more or less reasonable approximation, so the Bernoulli principle applies. However, viscous effects are dominant in the boundary layer, which means that the Bernoulli principle cannot be applied within the boundary layer.

An informative display on how hydraulic problems and the flow through orifices, in particular, have been approached in former times is given by Miller [22]. Miller derives equations based on the Bernoulli principle that require certain assumptions but are not capable of predicting the actual flow quantities with satisfactory precision in consequence. As a result, coefficients are introduced to close the gap between the theory and the experiment. These coefficients can be obtained by the examination of experimental results, physical considerations, or a blend of both methods leading to different approaches and equations. For practical use, the coefficients elect are equated for a set of parameters resulting in large sets of tables, as shown in Refs. [22, 23].

In contrast to the empirical correction coefficients associated with the Bernoulli principle, the required coefficients for the momentum balance replace integral by averaged expressions and are, therefore, physically well-defined. These coefficients can be obtained by numerical simulations and parametrized to get applicable analytical formulas based on the momentum balance. The numerical method and the general numerical model employed for every simulation of this thesis are described in the following chapter.

2 No CFD Without Momentum / The Numerical Model

2.1 The CFX-Module of ANSYS

The governing equations employed for numerical simulations are the continuity equation, the three momentum equations, and the energy equation in the case of a non-isothermal simulation. These equations, as derived in Chap. 1.4, represent the mathematical model of the CFX module and the Fluent module of ANSYS. Since both modules are not capable of performing direct numerical simulations (DNS), the differential Navier-Stokes equations have to be transformed into the so-called Reynolds-Averaged Navier-Stokes (RANS) equations. This transformation is based on the idea that turbulence eddies and vortices do not need to be resolved for practical applications. Only the effects of turbulence on the flow must be considered for an accurate result. The transformation of the Navier-Stokes equations to the RANS equations can be found in almost every book about numerical simulations and will, therefore, solely be described briefly.
The main idea is to avoid simulating the time-dependent fluctuations of the pressure p and the velocity components u, v, w. Therefore, the so-called Reynolds decomposition is applied to the mentioned variables. For the velocity u, the Reynolds decomposition gives $u = \overline{u} + u'$ with $\overline{u}$ as the average flow velocity in the x-direction and u' representing its fluctuations. This is schematically shown in Fig. 2.1 for a steady and unsteady flow. The local velocity $u = \overline{u} + u'$ represents the values used for DNS, but $\overline{u}$ the values used for RANS simulations. Equation 2.1 shows the result of averaging a product of two velocity components u and v as occurring in the advection term of the Navier-Stokes equations in conservation form as per Eq. (1.31).

$$\overline{u\,v} = \overline{(\overline{u} + u')\;(\overline{v} + v')} = \overline{\overline{u}\,\overline{v} + \overline{u}\,v' + u'\,\overline{v} + u'\,v'} = \overline{u}\,\overline{v} + \overline{u'\,v'} \tag{2.1}$$

The above definition follows the rule that the average of an averaged quantity remains the average $\overline{\overline{u}} = \overline{u}$. But the product of an average and the average of a fluctuation is zero since averaging fluctuations gives zero $\overline{u'} = 0$. In contrast, the average of the product of two fluctuating quantities must not necessarily result in zero. The product $\overline{u'\,v'}$ can result in zero when u' and v' are uncorrelated but result in a value different from zero when u' and v' are correlated. In the end, the Reynolds-averaging generates additional correlation terms. For the momentum in the x-direction, Eq. (1.31) gives:

$$\frac{\partial \overline{u}}{\partial t} + \frac{\partial\,(\overline{u}\,\overline{u} + u'\,u')}{\partial x} + \frac{\partial\,(\overline{u}\,\overline{v} + u'\,v')}{\partial y} + \frac{\partial\,(\overline{u}\,\overline{w} + u'\,w')}{\partial z} = g_x - \frac{1}{\varrho}\,\frac{\partial \overline{p}}{\partial x} + \nu\left(\frac{\partial^2 \overline{u}}{\partial x^2} + \frac{\partial^2 \overline{u}}{\partial y^2} + \frac{\partial^2 \overline{u}}{\partial z^2}\right) \tag{2.2}$$

and with the fluctuation terms rearranged to the right side

$$\frac{\partial \overline{u}}{\partial t}+\frac{\partial \overline{u}\,\overline{u}}{\partial x}+\frac{\partial \overline{u}\,\overline{v}}{\partial y}+\frac{\partial \overline{u}\,\overline{w}}{\partial z}=g_x-\frac{1}{\varrho}\frac{\partial \overline{p}}{\partial x}+\nu\left(\frac{\partial^2 \overline{u}}{\partial x^2}+\frac{\partial^2 \overline{u}}{\partial y^2}+\frac{\partial^2 \overline{u}}{\partial z^2}\right)-\left(\frac{\partial u'\,u'}{\partial x}+\frac{\partial u'\,v'}{\partial y}+\frac{\partial u'\,w'}{\partial z}\right) \quad (2.3)$$

representing the x-component of the so-called Reynolds-averaged Navier-Stokes (RANS) equation. Considering the fluctuation terms in the y- and z-direction additionally, all fluctuation terms combined give the Reynolds stress tensor $\mathbf{R}$. Since every spatial direction adds three unknown fluctuation quantities, the time-averaging adds no new equations but nine new unknowns. In analogy to the viscous stress tensor $\boldsymbol{\tau}$, $\mathbf{R}$ also exhibits symmetry, which means the number of additional unknowns reduces to six. With still four equations, now a total of 10 unknowns must be solved. This means that the system is not closed and additional equations must be found to close the equation system. Besides, this is the reason turbulence is often referred to as the “closure problem”. In summary, the RANS equations contain non-linear correlations of the velocity components and their unknown fluctuations in addition. According to Ref. [24], exact equations for these fluctuation correlations introduce more complex correlation terms containing unknown variables that can not be determined from the variables appearing in the Navier-Stokes equations. But to employ the RANS equations without evaluating the exact values of the fluctuation terms, the turbulent (or eddy) viscosity ν_t is introduced, substituting ν. The trick is to account for the effects of the fluctuation correlation terms by an artificially increased viscosity ν_t so the fluctuation terms can be disregarded. As a result, the turbulent viscosity remains the only unknown that must be modeled by turbulence models being discussed in the following chapter.

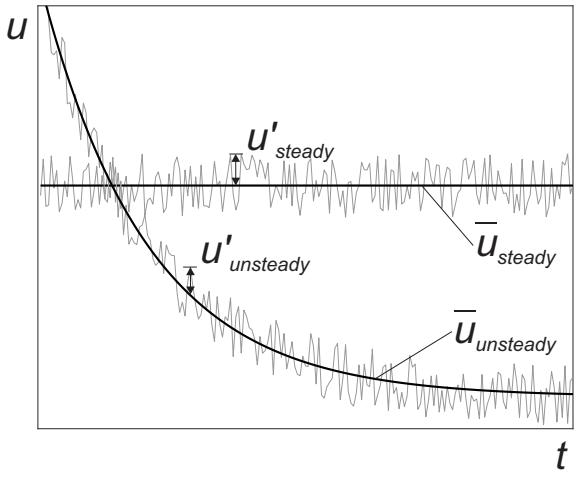

Figure 2.1: Time-averaging of the velocity u for a steady and unsteady flow. The fluctuations u' and the ensemble-averaged $\overline{u}_{unsteady}$ are functions of the time t.

Now the mathematical model must be applied to a simulation domain to approximate the differential equations by discrete functions for the flow quantities. The process of determining the discrete locations in space and time where the continuous differential equations are solved is called discretization. In CFX and Fluent, the finite volume method (FVM) is applied for the discretization of the simulation domain. This method uses the integral conservation equations (see Eqs. (1.4,1.31)) being applied to control volumes. Control volumes can be understood as subdivisions of the simulation domain resulting from the discretization. For the FVM, the computational node where the flow variables are calculated is the centroid of each control volume in most cases (see Ref. [24] for other methods). To obtain

the values of the flow variables at the surfaces of the control volume as well, the flow quantities are interpolated between the centroid values. Since the surface flux leaving one control volume is equal to the surface flux of the adjacent control volume(s), this method is conservative by construction. When all flux approximations and source terms are summed up for one centroid of a control volume, the resulting algebraic equations for the flow quantities relate to the ones of the adjacent control volumes. Therefore, the number of algebraic equations and the number of unknown variables both balance the number of the control volumes of the whole simulation domain, which means the system of equations is well-posed.

The main difference between CFX and Fluent is related to the solution of the resulting algebraic equation system. CFX exclusively employs a direct method for a simultaneous solution, whereas Fluent calculates the equations of the flow variables u, v, w, p sequentially. This requires a pressure-velocity-coupling algorithm in addition. In the later versions of Fluent, the direct method is also integrated, even though Fluent is focused on the indirect method. The workflow diagram of both methods is shown in Fig. 2.2. A direct method means that a coupled solver is used to solve the momentum and continuity equations simultaneously for the whole simulation domain. Therefore, this method is also called the simultaneous or monolithic method since all algebraic equations are considered as a monolithic (non-decouplable) part of the simulation system. Detailed information about the calculation procedure of the direct method can be found in Pascau et al. [25]. The indirect (or iterative) method, as applied by Fluent, solves the algebraic equation system with a segregated solver. In this case, the momentum equations are solved sequentially (one after another) with estimated values for the pressure obtained by a pressure-velocity coupling algorithm. From the process of decoupling or segregation of the governing equations, the name segregated solver is deduced. But in general, the calculated velocities violate the continuity equation. Therefore, the velocities must be iteratively calculated to obtain a velocity field without divergence. This process is called inner iteration. After completing the inner iterations, the coupling of the updated variables with the pressure is performed which are the outer iterations. Then the solution advances to the next cycle with an enhanced pressure estimate. This dual iteration cycle results in an increased number of calculations making the indirect method computationally more demanding than the direct method. In addition, the pressure-velocity coupling reduces the solver stability compared with the direct method. Therefore, various pressure-velocity coupling algorithms are available in Fluent (Simple, Simplec, Piso, and Fractional-Step Method), see Ref. [26]. A suitable algorithm must be chosen for a specific simulation case because every algorithm is designed for different applications. This is necessary since not every pressure-velocity coupling algorithm works properly for every simulation setup. For example, the solver stability depends on a proper selection of the pressure-velocity coupling algorithm to a large extent. However, the ANSYS Fluent Theory Guide [26] provides more information about the algorithms as well as recommendations for employment.

According to Burns et al. [27], the direct method increases the solver robustness and fewer iterations are required to achieve convergence. This is also confirmed by Pascau et al. [25], examining the performance of different solution methods. But the direct method produces larger equation systems and the matrices exhibit a more complex pattern as considerably more non-zero diagonals occur compared with segregated solvers, see Ref. [25]. In conclusion, the major asset of the indirect method is less memory demand at the expense of higher computational demand for more iterations. Otherwise, the direct method shows higher robustness and superior performance compared with the indirect method but at the expense of 1.5 - 2 times higher memory demand, according to Ref. [26]. Last but not least, a highly practical asset of the direct method is that the choice of a proper pressure-velocity coupling algorithm can be omitted.

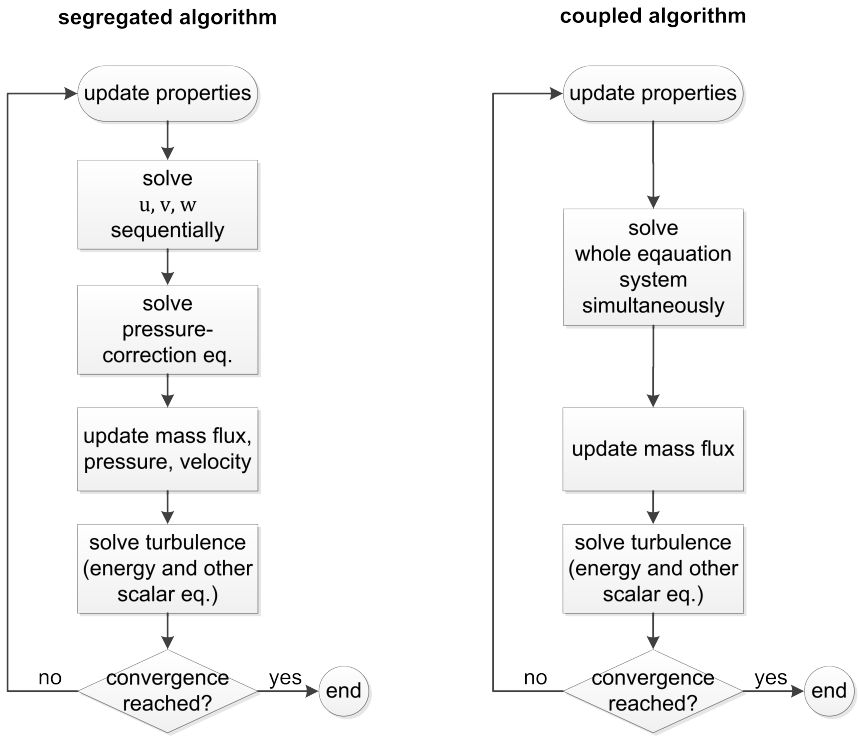

Figure 2.2: Workflow of the solving process for an indirect (left side) and direct method (right side).

Although the choice of a pressure-velocity coupling algorithm can be circumvented by using the direct method, a proper turbulence model to approximate the artificial parameter ν_t must be selected either way.

2.2 Choosing a Proper Turbulence Model

2.2.1 Opening Remarks

To substitute the velocity fluctuation correlation terms, the turbulent viscosity ν_t is introduced to the RANS equations, see Eq. (2.3). In contrast to the molecular viscosity ν, which is a property of the fluid, ν_t is a property of the flow. The turbulent viscosity ν_t artificially increases the viscosity of the flow in such a way that the resulting flow behavior without considering the velocity fluctuations corresponds to the real flow. Therefore, turbulence models must be employed. All turbulence models have the common purpose to calculate or compute a proper value for ν_t at the given flow conditions. In general, RANS-based turbulence models can be divided into three groups, namely linear turbulence models, non-linear turbulence models, and Reynolds stress (transport) models. CFX and Fluent provide all three groups of models. Linear turbulence models relate the Reynolds stresses linearly to the mean flow field. These models are classified by the number of partial differential equations representing the transport equations to be solved for computing ν_t. There are zero-equation or algebraic models and one- and two-equation models. A non-linear turbulence model relates ν_t to the velocity field by a non-linear relationship. The Reynolds-Stress models employ second-order equations to calculate the Reynolds-Stress tensor $\mathbf{R}$ directly without assuming isotropic eddy-viscosity in contrast to linear turbulence models. According to Refs. [26, 28], the Reynolds-Stress model is the most elaborated

RANS-turbulence model, but practice shows that it is often not superior to two-equations models, at least for industrial flows. That is also confirmed by Jin and Herwig [29], assessing the performance of RANS simulations compared with Direct Numerical Simulations (DNS).
However, since a large variety of literature on turbulence modeling is available (Refs. [30, 31, 32]), only the two-equation model employed for the performed numerical simulations is described in detail in the following.

2.2.2 kω-SST Turbulence Model

Various investigations indicate that the kω-SST turbulence model shows the best overall performance when it comes down to the simulation of practical (industrial) applications. The abbreviation SST stands for shear stress transport. The investigation of Jin and Herwig [29] reveals that RANS simulations employing the kω-SST turbulence model exhibit the highest agreement with DNS results and even outperform Reynolds stress models for flows in rough channels. The authors' evaluation is based on the high correlation of the general shape of the turbulence eddy dissipation ε in the near-wall region compared with DNS results. All other examined turbulence models do not show a proper agreement. In addition, the trend of the friction coefficient λ is also only reproduced appropriately by the kω-SST turbulence model, although its results deviate around 20% from the DNS results.
A similar conclusion is drawn by Bardina et al. [32], evaluating the performance of several turbulence models. The authors recommend using the kω-SST turbulence model for simple and complex flows.
Another assessment of commonly used turbulence models by Rodriguez [30] yields the same result, which leads Rodriguez to recommend using the kω-SST turbulence model. The ANSYS CFX Solver Theory Guide [28] strongly recommends this turbulence model for general-purpose simulations as well. Ultimately, the kω-SST turbulence model might not be the best choice for every flow configuration but employing this turbulence model is a good choice not to go wrong seriously in the first place.
The application of the kω-SST turbulence also most closely matches the results of the referenced experimental investigations of the discussed flow structures. Therefore, the application of the kω-SST turbulence model will be validated for every flow structure in the respective chapter.

The kω-SST turbulence model is a two-equation turbulence model, physically based on the kω turbulence model. ω-based turbulence models solve the transport equations for the turbulence kinetic energy k and the specific turbulence dissipation rate ω, which can be understood as the rate of turbulence kinetic energy being converted into thermal energy. Menter [33] devised the turbulence model, in hindsight named the kω-SST turbulence model, as a combination of the kω [31] and the kε turbulence model [34] (named "standard kε" or SKE model). ε represents the turbulence eddy dissipation as a rate for the dissipation of velocity fluctuations. This means that the kω-SST turbulence model combines the assets of the kε and the kω model. By the time the kω-SST turbulence model was devised, the kε model approximated the free stream flow reasonably but failed for modeling separated flows or the boundary layer. In contrast, the kω model showed superior performance in the near-wall region and for separated flows but exhibited high sensitivity for free stream boundary conditions, see Ref. [30]. It shall be mentioned that the latest version of the kω turbulence model [31] is disposed of the flaws that were present during the time the kω-SST turbulence model was devised. But the use of the standard kε turbulence model shall be avoided (Refs. [30, 32]) due to the advent of improved kε turbulence models.

As an explanatory parenthesis to the turbulence quantities k, ε, and ω, the interaction of the turbu-

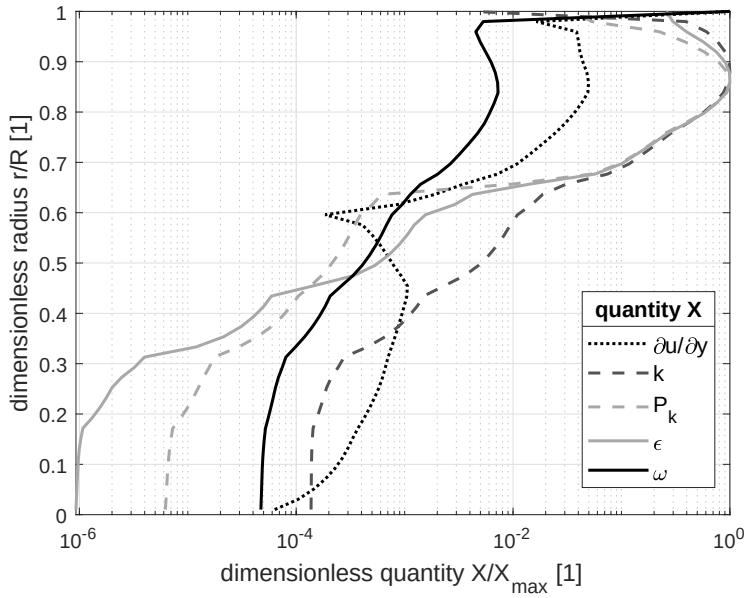

Figure 2.3: Radial distribution of turbulence quantities in the vena contracta divided by the respective maximum value for normalized visualization over the normalized pipe radius with swapped axes.

lence quantities is presented now for better comprehension. Figure 2.3 shows the gradient of the axial velocity over the radius $\partial u/\partial y$, the turbulence kinetic energy k, the production of the turbulence kinetic energy P_k, the turbulence eddy dissipation ε, and the turbulence dissipation rate ω for a cross-section in the vena contracta downstream of a sudden contraction. The velocity gradient $\partial u/\partial y$ represents the major velocity difference and is therefore selected as the reference. For an equally-scaled visualization, all quantities are normalized by the respective maximum value and shown on a semi-logarithmic scale with the y-axis representing the normalized pipe radius r/R. The gradient of the axial velocity in the radial direction $\partial u/\partial y$ is shown by its norm since the gradient only takes positive values in the range of $0.6 < r/R < 0.98$ for the chosen part of the cross-sectional line. Consequently, the gradient's maximum is reached around $0.84R$. Physically speaking, the velocity difference of neighboring fluid particles in the axial direction is maximum at around $0.84R$, leading to large velocity fluctuations u'. As a result, the production of turbulence kinetic energy P_k is also maximum in this region, as well as the turbulence kinetic energy k itself. When k is large, the potential to dissipate turbulence kinetic energy k into thermal energy is also larger, resulting in the maximum turbulence (eddy) dissipation ε in the same region. The same explanation applies to the turbulence dissipation rate ω, disregarding the near-wall region $r/R > 0.98$. In summary, Fig. 2.3 shows that turbulence originates from velocity differences and all turbulence quantities are connected, whereby the common basic definition of the turbulence dissipation rate ω: $\omega = \varepsilon/k$ is reasoned (depending on the reference, ε/k can be multiplied by a factor).
The presented quantities are obtained with the verified numerical model and the kω-SST turbulence model for the sudden contraction, discussed in detail in Chap. 3.1.4.

However, the kω-SST turbulence model is obtained by transforming the differential equations of the kε turbulence model to the kω formulation. Besides different modeling constants, an additional term occurs in the ω-equation representing the cross-diffusion, which is then multiplied by the blending function $(1 - F_1)$ giving

$$\frac{\partial(\varrho k)}{\partial t} + \frac{\partial(\varrho u_j k)}{\partial x_j} = P_k - D_k + \frac{\partial}{\partial x_j}\left((\mu + \sigma_k \mu_t)\frac{\partial k}{\partial x_j}\right) \tag{2.4}$$

$$\frac{\partial(\varrho \omega)}{\partial t} + \frac{\partial(\varrho u_j \omega)}{\partial x_j} = P_\omega - D_\omega + \frac{\partial}{\partial x_j}\left((\mu + \sigma_\omega \mu_t)\frac{\partial \omega}{\partial x_j}\right) + 2(1 - F_1)\frac{\varrho \sigma_{\omega 2}}{\omega}\frac{\partial k}{\partial x_j}\frac{\partial \omega}{\partial x_j} \tag{2.5}$$

Here, u represents the local velocity, μ_t the eddy viscosity or turbulent viscosity, $P_{k;\omega}$ the production and $D_{k;\omega}$ the destruction or dissipation term, and σ the respective closure coefficients. The above-mentioned transformation of the kε to the kω formulation results in the additional last term of Eq. (2.5) with the blending function F_1 to merge both models with a smooth transition. F_1 is a hyperbolic tangent function of the distance to the nearest wall. Approaching the wall, the blending function F_1 gradually changes from zero in the turbulent layer and the overlap layer (represented by the yellow and light green area in Fig. 2.4) to unity in the viscous sublayer (represented by the dark green area in Fig. 2.4). This means that in the viscous sublayer, the kω turbulence model is applied, whereas the kε turbulence model comes into effect in the free-stream region. A schematic profile of F_1 is also shown in Fig. 2.5 in Chap. 2.2.3.
Figure 2.4 shows a flow over a flat plate with the alteration of an ideal and fully developed velocity distribution (indicated by u_∞) and the emerging boundary layer. After the leading edge of the plate is passed, a laminar boundary layer of short height comes into existence where the flow near the plate surface is well-arranged, showing no turbulences. Within a certain flow distance, small oscillations in the near-wall flow (curved lines) increasingly resonate, leading to small swirls. Therefore, the boundary layer height δ (indicated by the bold red line) in the so-called transition layer increases accompanied by a decreasing gradient of the velocity profile. In the turbulent region, the boundary layer height approaches its final value and the flow is completely turbulent except for the viscous sublayer. Here, the laminar flow behavior persists. The blue bold line indicates the momentum thickness θ, which will be briefly outlined at this point. The momentum thickness θ represents the distance between a reference plane (e.g. a wall) and the specific plane, where the current total momentum of the flow is equal to the total momentum of the flow without a boundary layer. In other words, θ quantifies the distance a plane must be displaced to a wall so that the total momentum of the sheared velocity profile is equal to the total momentum of a uniform velocity profile. According to Fig. 2.4, the momentum thickness is the distance from the wall up to the plane where both blue-shaded sections of the velocity distribution are of equal area.

The indication shall be provided that Menter [33] used the Lagrangian derivative, which is not the standard form used by Menter later on or in the literature. Here, both equations are written in the conservative form (see Ref. [35]) to be consistent with the kω equations of Wilcox [31]. A detailed description of the evolution of the kω-SST turbulence model, in particular, the refinement of the expressions for the production P and dissipation D, is given in Ref. [30].

Another substantial asset of the kω-SST turbulence model is that it can also be applied to flows where the transition from laminar to turbulent flow or in the reverse direction - from turbulent to laminar occurs. Therefore, the kω-SST turbulence model can be augmented by a transition model solving two additional local transport equations. A detailed description of the transition model can be found in Ref. [36].

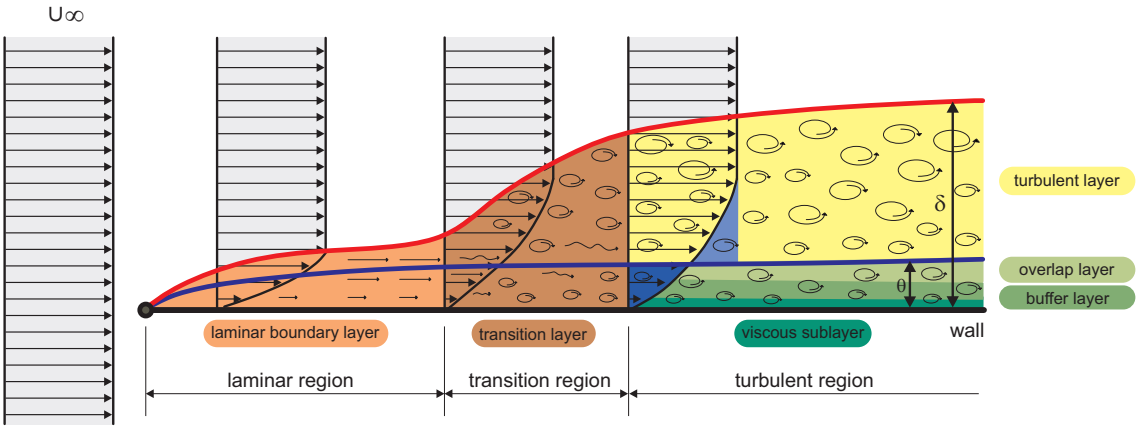

Figure 2.4: Sketch of the momentum thickness θ in a flow over a plate with the boundary layer or displacement thickness δ and the development of the boundary layer. When a uniform laminar or low intense turbulent flow is approaching a wall's leading edge, the boundary layer is laminar, then merges to turbulent (transitional), and finally turns to turbulent completely.

2.2.3 The Flow Near a Wall

Although a proper turbulence model is chosen, the region near the walls deserves closer attention. Since a zero flow velocity at a wall (or a closed boundary) results in high gradients of the flow variables in the immediate vicinity of the wall (the boundary layer), viscous effects strongly affect the flow behavior in the boundary layer. As a result, the flow variables are changing rapidly in the boundary layer. Figure 2.5 shows the dimensionless velocity u^+ vs. the dimensionless wall distance y^+ on a semilogarithmic scale in the near-wall region by the dashed lines. The function consists of two formulations representing the so-called law of the wall, which is universally valid for any (smooth) surface. This profile was mathematically described first by von Kármán [37] in 1930, confirming Prandtl's mixing length approach. The profile can be subdivided into two zones. Within the viscous sublayer $y^+ \leq 5$, the flow shows laminar behavior since the molecular viscosity is dominant. Therefore, u^+ is equal to y^+ in the viscous sublayer. Starting at a dimensionless wall distance y^+ of 30, turbulent effects are dominating, represented by the logarithmic law layer. In this region, u^+ can be calculated via $ln(y^+)/\kappa + 5.1$ with the von-Kármán constant $\kappa = 0.41$. The region between the viscous sublayer and the logarithmic law layer is called the buffer layer. The buffer layer is the transition region where neither the effects of molecular viscosity nor turbulence are dominant, so both have an influence on the mixing or exchange of flow characteristics (e.g. velocity, heat, concentration). In the buffer layer, none of the formulations for the dimensionless velocity u^+ apply completely. According to Wilcox [31], the logarithmic law layer ends at $y^+ = 500$ followed by the defect layer indicating the border between the inner and outer boundary layer. Hence, the logarithmic law layer is also called the overlap layer since it represents the region the outer boundary layer merges the inner boundary layer.

Applying RANS simulations, the boundary layer can be modeled in two different ways, as shown schematically in Fig. 2.6.
Using the near-wall model approach, a very fine mesh is generated close to the walls to resolve the boundary layer. This method is also known as the so-called low Reynolds number method. Therefore, the turbulence model is modified to capture the rapid variations of the flow variables in the near-wall region down to the wall. 'Low' Reynolds number means that this method correctly approximates the

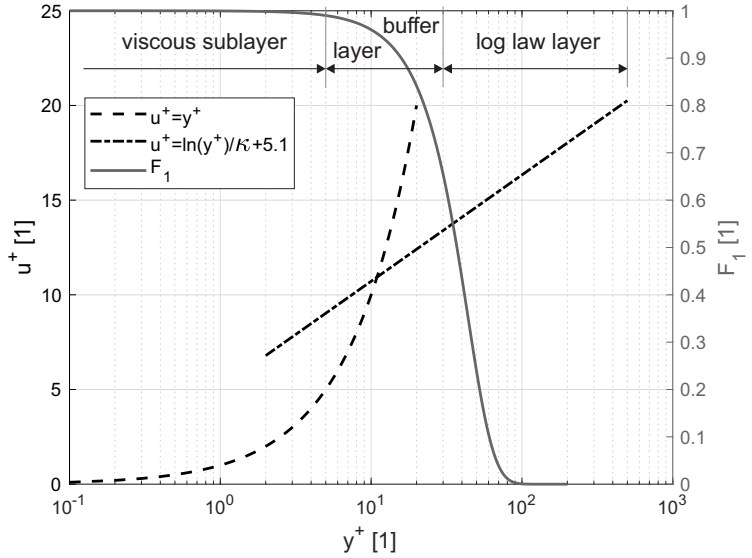

Figure 2.5: Wall function of the dimensionless velocity u^+ and the blending function F_1 of the kω-SST turbulence model vs. the dimensionless wall distance y^+

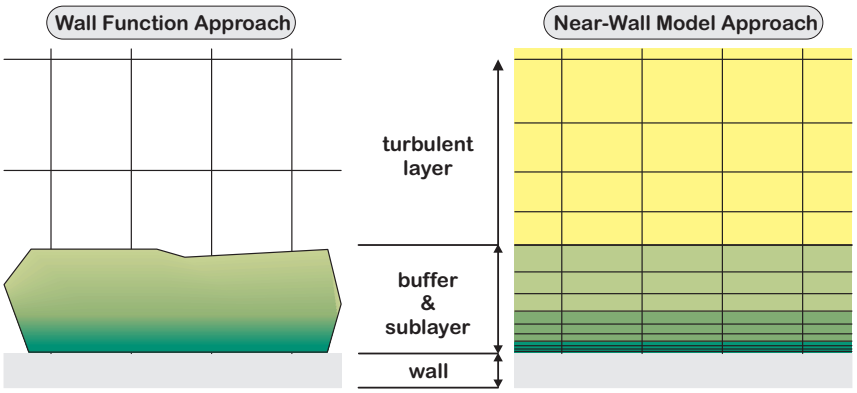

Figure 2.6: Wall treatment approaches in ANSYS

Reynolds number also in the near-wall region or for *low* length scales to the wall, where viscosity primarily affects the flow. But the low Reynolds number method requires a fine mesh that takes a high computational demand. In addition, the mesh within the boundary layer is subject to certain requirements and restrictions. The ANSYS Fluent Theory Guide [26, p. 134] and the ANSYS CFX Solver Theory Guide [28] recommend resolving the near-wall region by 10 to 20 mesh layers to accurately predict the flow variables in the boundary layer. Whereas ensuring certain values of the dimensionless wall distance y^+ is considered less important. In addition, the total thickness of all mesh layers within the boundary layer (named prism layers due to the shape of the mesh elements) must be larger than the boundary layer thickness. Otherwise, the boundary layer can be confined by the prism layers. A calculation procedure for an initial estimate of the layer heights and the boundary layer thickness is given in the following chapter. Whether the near-wall mesh refinement (the prism layers) covers the boundary layer height can be checked after the first solution is obtained. Since the turbulent viscosity ν_t exhibits a maximum in the middle of the boundary layer, the distance of the maximum ν_t to the wall gives an initial indication of the boundary layer thickness δ, see Ref. [26, p. 134].

Another method is the so-called wall function approach to model the viscosity-affected viscous sublayer and buffer layer by applying semi-empirical formulas called wall functions. Wall functions link the viscosity-affected region to the fully-turbulent boundary layer region to ensure suitable conditions for calculating the flow variables. In essence, the flow variables are calculated by functions being applied to the vicinity of the wall. The main asset of the wall function method is that fewer mesh elements are required in the near-wall region, and consequently, the computational demand is reduced. But in regions where the flow is detached, wall functions yield wrong results since a void velocity profile is presumed.
For an accurate computation regardless of the mesh, the CFX module of ANSYS offers an option called automatic wall treatment to switch between both methods depending on the mesh resolution [38]. In Fluent, this option is called y^+-insensitive wall treatment ω-equation. For the ε-based turbulence models, scalable wall functions are employed. However, for the ω-based turbulence models, the automatic near-wall treatment method is used. For flows with flow separation, the employment of the kω (see Ref. [31]) or the kω-SST turbulence model (see Ref. [35]) is strongly recommended. Since flow separation occurs for all applications subject to this investigation, a turbulence model based on the ω-equation is employed for all numerical simulations. Therefore, solely the automatic wall treatment is explained. Wilcox's kω turbulence model [31] employs an analytical expression for ω in the viscous sublayer that is used for switching automatically from wall functions to the low Reynolds number method when the mesh is refined. Therefore, the wall value for ω is blended between the formulations of both methods. In conclusion, the automatic wall treatment guarantees consistent results for mesh refinements from coarse meshes not resolving the viscous sublayer to fine meshes resolving the viscous sublayer by multiple layers.
The ANSYS CFX-Solver Modeling Guide [38] strongly recommends using the kω-SST turbulence model with an automatic wall function for examining details of the boundary layer if a sufficiently fine mesh is produced. Therefore, the boundary layer should consist of at least 15 elements to reduce errors, see Ref. [38]. But as shown by Menter [35], the deviation of the wall shear stress employing a mesh with the first prism layer height $y^+ = 2$ or $y^+ = 100$ is almost negligible for industrial applications. Even for a coarser near-wall mesh resolution, the velocity profiles follow the profile of the logarithmic law. The effect of the wall mesh resolution is therefore reduced if a near-wall treatment is applied. According to Carlson et al. [39], wall functions can be applied up to a first prism layer height of $y^+ = 250$. But especially for heat transfer simulations, it is strongly recommended that the first layer of cells is defined for a dimensionless wall distance y^+ of 1 so the quantities of the near-wall cells are calculated directly [28].

2.2.4 Initial Estimates of the Near Wall Mesh Parameters

The ANSYS CFX-Solver Modeling Guide [38] proposes a guideline to calculate the minimum spacing and the minimum number of mesh layers in the boundary layer to initially set the near-wall mesh parameters. It can be used for an assessment of the near-wall mesh quality as well.
The minimum spacing of the mesh Δy represents the height of the first mesh layer to the wall and depends on the turbulence model and the wall treatment method applied. The dimensionless wall distance y^+ and the wall distance y represent the distance normal to the wall. First, the so-called wall shear stress coefficient or friction coefficient C_f is estimated by

$$C_f = 0.0791\ Re^{-1/4} \tag{2.6}$$

for internal flows with the Reynolds number Re based on correlations for a pipe. Equation 2.6 is obtained by Blasius [40] for smooth pipes with regard to the Weisbach friction factor λ, which can be transferred to the employed Fanning friction factor C_f via $C_f = \lambda/4$. The dimensionless wall distance y^+ can be calculated as follows:

$$\Delta y^+ = \frac{\Delta y \, u_*}{\nu} \tag{2.7}$$

The space between the mesh layer and the wall is represented by Δy. The Fanning friction coefficient in an alternative formulation yields

$$C_f = 2\frac{\tau_w}{\varrho \, u^2}. \tag{2.8}$$

With the definition of the wall shear stress $\tau_w = u_*^2 \, \varrho$ and Eq. (2.8) flipped to the friction velocity u_*, u_* can be eliminated in Eq. (2.7). Therefore, the differential wall distance Δy gives

$$\Delta y = \Delta y^+ \sqrt{\frac{2}{C_f}} \frac{\nu}{u} \tag{2.9}$$

with u as the characteristic velocity used for calculating the Reynolds number. C_f can now be substituted by Eq. (2.6). Equation (2.9) allows targeting a desired y^+ value to obtain the mesh spacing in the boundary layer.

The number of mesh layers can be calculated subsequently by estimating the boundary layer thickness δ by

$$\delta = 0.035 \, d_{Hyd} \, Re^{-\frac{1}{7}} \tag{2.10}$$

It appears that the calculation of δ as per Eq. (2.10) underestimates the final boundary layer thickness δ more or less by a factor of 1.5 compared with the turbulent viscosity profile, as discussed in the previous section.
Finally, the refined near-wall mesh can be checked if the distance of the last mesh layer to the wall is larger than the Boundary layer height δ.

Additionally, it is recommended that the transition from the refined wall mesh to the outer mesh is smooth by limiting the aspect ratio of the cell height between these two layers to a value of 2 or 3 at maximum. This means that the last near-wall layer should be 0.33 or 0.5 times as high as the adjacent cell of the outer mesh in the free stream region.

2.3 Estimation of the Uncertainty in CFD Results

A unified approach to calculating and reporting the uncertainty of numerical results is presented by Roache [41] named the Grid Convergence Index GCI. It is based on the generalized Richardson extrapolation first described in 1910. The GCI indicates the deviation of the actual computed solution from the asymptotic numerical value the simulation can approach at best, which is named the exact value by Roache [41]. The Grid Convergence Index, therefore, represents a measure of how much the solution changes, further refining the mesh. Hence, a preferably low GCI is desired since it also indicates that the simulation results are within the asymptotic range of the numerical values. In contrast to the Richardson Extrapolation, the approach of Roache [41] can also be applied to meshes with discontinuities of the geometry (e.g. sudden contractions and expansion, orifices). It is the basis of the

procedure proposed by Celik et al. [42] on the estimation of discretization uncertainties in numerical simulations. In contrast to Roache [41], the method of Celik et al. [42] is unrestrictedly valid for unstructured meshes and, thus, the procedure elect. First, a representative mesh size s must be defined. Therefore, Eq. (2.11) must be applied for three-dimensional simulations if integral quantities (like the pressure coefficient c_P or the reattachment length of the flow) are considered and the mesh is not equally sized.

$$s = \left(\frac{1}{N} \sum_{i=1}^{N} (\Delta V_i) \right)^{\frac{1}{3}} \tag{2.11}$$

Here, N is the total number of mesh elements and ΔV_i the volume of the ith mesh element. For equally sized meshes or field variables like the pressure along the streamline, the representative mesh size can be substituted by the local mesh size. In the second step, the key variables f of the simulation must be determined, and the simulation must be performed with three different meshes. This results in different values of the key variables. In the present studies, the momentum coefficients β and the pressure coefficients c_P are defined as the key variables since these are the crucial coefficients for the calculation. In Ref. [42], a mesh refinement factor $S = s_{coarser}/s_{finer}$ of at least 1.3 is highly recommended. It shall be mentioned that the recommended value of S is purely based on the authors' experience. Now the mesh refinement factors can be determined, considering the intermediate and the fine mesh S_{if} plus the coarse and the intermediate mesh S_{ci}. The method's apparent order o can be iteratively calculated via

$$o = \frac{1}{ln\left(S_{if}\right)} \left| ln\left(\left| \frac{\left(f_c - f_{int}\right)}{\left(f_{int} - f_f\right)} \right| \right) + ln\left(\frac{S_{if}^o - 1 \cdot sign\left(\left(f_c - f_{int}\right) / \left(f_{int} - f_f\right)\right)}{S_{ci}^o - 1 \cdot sign\left(\left(f_c - f_{int}\right) / \left(f_{int} - f_f\right)\right)} \right) \right|. \tag{2.12}$$

The apparent order o of the method indicates that the meshes are in the asymptotic range if the value is close to the simulation scheme's formal order. For all performed numerical investigations in this thesis, solution schemes of the second order are employed. But values of o differing from the formal order of the solution scheme must not inevitably indicate inadequate simulation results (Ref. [42]). It just means that the results exhibit oscillatory convergence or the mesh is not within the asymptotic range to the converging value of the particular quantity. Celik et al. [42] draw attention to the fact that the proposed procedure fails for $(f_c - f_{int})$ or $(f_{int} - f_f)$ "very close" to zero. Unfortunately, the authors give no quantification of "very close". However, $(f_c - f_{int})$ or $(f_{int} - f_f) \rightarrow 0$ indicates oscillatory convergence or that the exact solution is attained. In these cases, an additional mesh refinement should be performed. The extrapolated values of the key variables f_{ext} (named exact value by Roache) can now be calculated from

$$f_{ext,if} = \frac{S_{if}^o \cdot f_f - f_{int}}{S_{if}^o - 1} \tag{2.13}$$

and similarly for $f_{ext,ci}$. In the last step, the error estimates can be calculated. The approximate relative error e_a is obtained by

$$e_{a,if} = \left| \frac{f_f - f_{int}}{f_f} \right| \tag{2.14}$$

and the extrapolated relative error e_{ext} by

$$e_{ext,if} = \left| \frac{f_{ext,if} - f_f}{f_{ext,if}} \right|. \tag{2.15}$$

Finally, the grid convergence index GCI of the fine mesh can be calculated from

$$GCI_{if} = \frac{1.25\, e_{a,if}}{S_{if}^o - 1} \tag{2.16}$$

with 1.25 as a safety factor considering the 95% confidence bound on the approximate relative error e_a. This experience-based safety factor depends on the number of meshes used for the convergence study, see Ref. [41].
Finally, it shall be mentioned that a comparison of experimental results with numerical results may not be an appropriate substitution for a GCI and a proper validation of the simulation model. According to Roache [41], four out of seven experimental results show a better agreement to simulation results obtained with coarse meshes than to the ones obtained with finer meshes. This is shown by Zingg [43] performing grid studies of flow fields around airfoils. Zingg found out that the agreement of experimentally obtained drag coefficients with drag coefficients computed with coarser meshes is higher than the agreement with drag coefficients computed with finer meshes. This can result in a misleading accuracy estimate of the simulation model. Therefore, even with an experimental reference to validate the numerical model, a mesh convergence study should always be performed.

2.4 Universal Settings

Besides the turbulence model, additional settings and options are applied to all numerical simulation models and will therefore be discussed jointly.
According to the ANSYS CFX-Solver Theory Guide [28], applying a second-order solution scheme as the solver setting is recommended for reliable RANS simulations. Therefore, the option of high resolution is applied to the advection scheme and the turbulence numerics for all numerical simulations. The high-resolution option employs a blended method of the first-order upwind scheme and the second-order central differences scheme. In detail, the governing equations and turbulence model equations are solved second-order accurate in the general flow-flied but solved first-order accurate near discontinuities. According to the ANSYS CFX-Solver Theory Guide [28], this method is considered second-order accurate. For a detailed description of the principles of the high-resolution advection scheme, see Barth and Jespersen [44].

An important general inlet boundary condition represents the turbulence intensity J, which is defined as

$$J = \frac{\sqrt{\frac{1}{3}\left(u'^2 + v'^2 + w'^2\right)}}{\sqrt{\overline{u}^2 + \overline{v}^2 + \overline{w}^2}} \tag{2.17}$$

The velocity fluctuations in all three spatial directions are represented by u', v', w' and the mean flow velocity by $\overline{u}$, $\overline{v}$, $\overline{w}$. The turbulence intensity J can be described as the upstream history of the flow. In ANSYS, J can be set to low ($\leq 1\%$), medium ($1\% < J \leq 10\%$), and high ($> 10\%$). A low turbulence intensity occurs for non-developed or undisturbed flows, see Ref. [28].
The ANSYS CFX-Solver Theory Guide [28] proposes an empirical equation for pipe flows to estimate the turbulence intensity as the average over the whole cross-section:

$$J = 0.16\ Re^{-\frac{1}{8}} \tag{2.18}$$

where Re is the pipe Reynolds number. Since no reference or explanation is given about the origin of Eq. (2.18), Russo and Basse [45] investigated the turbulence intensity obtaining

$$J = 0.14\ Re^{-0.079} \tag{2.19}$$

from simulations of incompressible pipe flows. Equation (2.19) gives the turbulence intensity as the average over the pipe cross-section. The authors' investigations also show that the maximum turbulence intensity is reached at the walls, which is more pronounced for incompressible flows. However, Eq. (2.18) and Eq. (2.19) can be used to estimate the turbulence intensity for the Reynolds numbers applied to the simulation. It appears that medium intensity is a good approximation in general since the turbulence intensity varies between 7% for $Re = 5000$ and 5% for $Re = 4.1 \cdot 10^5$, according to Eq. (2.19). But J varies between 5.5% for $Re = 5000$ and 3% for $Re = 4.1 \cdot 10^5$, according to Eq. (2.18). Changing the turbulence intensity between low and medium in combination with the kω-SST turbulence model is not influencing the results. This might be reasoned by a sufficiently long flow length between the inlet and the region of interest for the flow to fully develop. For all investigated hydraulic structures applies that the differential pressure plus the momentum coefficients remain constant, regardless of low or medium turbulence intensity. Solely the downstream pressure coefficients change negligibly at the fourth decimal point. In consequence, medium turbulence intensity is always applied to the inlet boundaries of the described numerical models.

An optimal compromise between accuracy and efficiency proved to define the stop criterion for the iterations when all residuals are below $1 \cdot 10^{-4}$. Since the change of the flow quantities is negligible with a further decreased residual value, the solutions are considered fully converged for all residuals falling below $1 \cdot 10^{-4}$.

3 Application of the Momentum Balance to Practical Hydraulics

3.1 The Sudden Contraction

Extracts of the findings presented in this section have been published in the Journal of Fluids Engineering, January 2021. The manuscript can be found at https://doi.org/10.1115/1.4048286.

3.1.1 Retrospective / State of the Art

At first glance, the pressure drop over a sudden contraction appears to be easy to describe and calculate hydraulically. But this fundamental flow structure turned out to baffle many researchers since the effect causing the pressure drop was ambiguous for a long time. Johann Bernoulli [46], as an example, assumed the pressure drop to originate from an eddy in front of the contraction, see Fig. 3.1 of Ref. [46]. Investigating flow structures in detail, Julius Weisbach [19] revealed the flow pattern of a sudden contraction very precisely, as shown in Fig. 3.2. According to Weisbach, the pressure drop is induced due to the contracting flow but also due to the expansion of the flow downstream of the sudden contraction. The contraction of the flow also affects the downstream region of the sudden contraction up to the vena contracta, where the flow is maximally converged, as shown by plane E in Fig. 3.2. Therefore, the vena contracta is included in many theories, which will be shown throughout the next chapters.

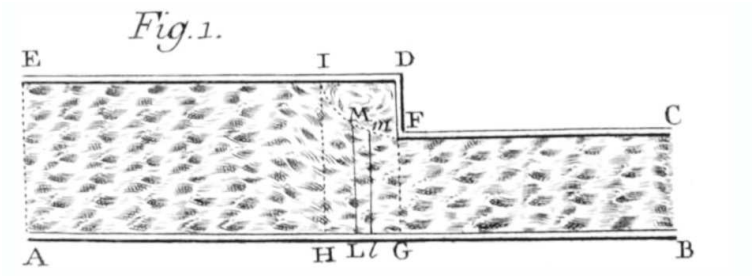

Figure 3.1: Sketch of a flow field for a sudden contraction from Johann Bernoulli's Opera Omnia (1742). Bernoulli assumed the pressure drop to originate from an eddy in front of the sudden contraction.

In addition to the existing ambiguity, Borda [47] derived a formulation for the pressure change of a sudden expansion based on the momentum balance in 1766. It appeared that the formulation yields the pressure change with a high agreement. Due to a revision of Lazare Carnot [48], this formula is now called the Borda-Carnot loss. But for the sudden contraction, a satisfying description or derivation of the pressure drop remained an enigma.

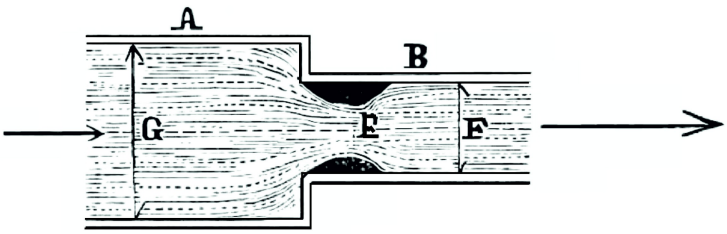

Figure 3.2: Wood engraving of a flow through a sudden contraction from Julius Weisbach's Die Experimental-Hydraulik (1855).

However, the hydraulic description of the sudden contraction started with Johann Bernoulli [46]. Bernoulli derived a formulation for the so-called resistance force of a sudden contraction. These days, the formula is obtained employing Bernoulli's energy conservation principle by balancing the energy of a fluid element on a streamline. Therefore, Eq. (1.54) for a horizontally oriented streamline $z_1 = z_2$ and the absence of frictional losses $h_{loss} = 0$ gives

$$p_1 + \frac{\varrho}{2} v_1^2 = p_2 + \frac{\varrho}{2} v_2^2 \tag{3.1}$$

With the continuity equation flipped to the upstream average velocity v_1

$$v_1 = v_2 \frac{A_2}{A_1} \tag{3.2}$$

the pressure drop of a sudden contraction yields

$$p_1 - p_2 = \frac{1}{2} \varrho \, v_2^2 \left(1 - \frac{A_2^2}{A_1^2} \right) \tag{3.3}$$

where v_2 represents the average velocity downstream of the contraction, $A_{1;2}$ the respective cross-sectional areas, and $p_{1;2}$ the respective pressures. But Eq. (3.3) underestimates the pressure drop in a sudden contraction considerably.
Therefore, Weisbach [19] added an additional term to Eq. (3.3), accounting for sudden losses by the so-called sudden loss coefficient k. Weisbach justified the additional term by the development of a vena contracta downstream of the sudden contraction, causing an increased effect on the pressure drop, see Fig. 3.2.

$$p_1 - p_2 = \frac{1}{2} \varrho \, v_2^2 \left(1 - \frac{A_2^2}{A_1^2} \right) + \underbrace{\frac{1}{2} k \, \varrho \, v_2^2}_{p_{loss}} . \tag{3.4}$$

For practical applications, the introduction of a pressure loss coefficient K directly into Eq. (3.3), as shown by Kays [49], prevailed

$$\Delta p = p_1 - p_2 = \frac{1}{2} K \, \varrho \, v_2^2 \tag{3.5}$$

The loss coefficient K accounts for the sudden pressure loss p_{loss} as well as the dependency on the contraction ratio $\left(1 - \frac{A_2^2}{A_1^2} \right)$ into one coefficient.
The pressures p_1 and p_2 in the formulations of Eqs. (3.4,3.5) represent the extrapolation of the linear pressure gradients of the fully developed flow regions upstream and downstream of the contraction up to the contraction plane, see Fester et al. [50] or Sanchez et al. [51]. This means that frictional

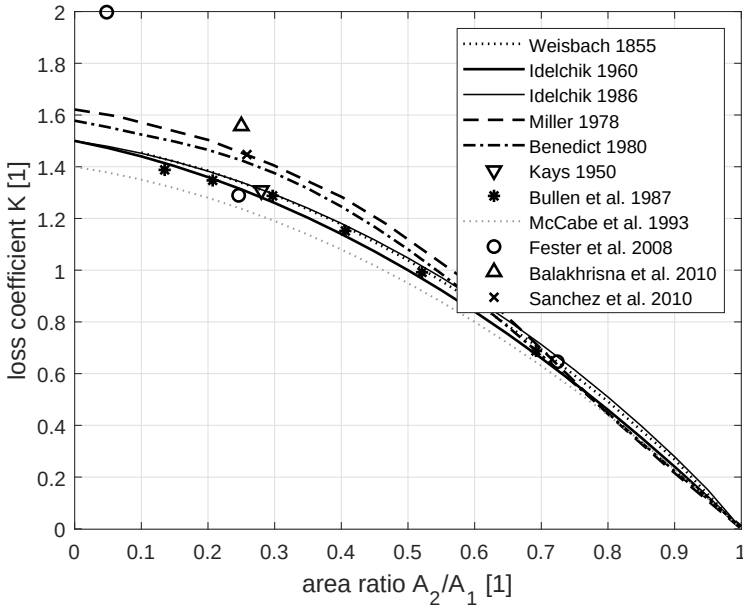

Figure 3.3: Loss coefficient K of a sudden contraction versus the area ratio A_2/A_1 of different references.

effects are excluded and solely the pressure drop induced by the sudden contraction is considered. Furthermore, the pressure share originating from the geodetical height difference $z_1 - z_2$ between the inflow and the outflow cross-section is considered negligible compared with the other pressure shares.

The loss coefficient K can be converted into the sudden loss coefficient k and vice versa by using Eq. (3.4) into Eq. (3.5) and solving for K or k

$$K = k + 1 - \frac{A_2^2}{A_1^2} \tag{3.6}$$

$$k = K - 1 + \frac{A_2^2}{A_1^2}. \tag{3.7}$$

Since there is, up to now, no physical derivation of the pressure drop of a sudden contraction available, the theory was fine-tuned to the experimental results by the (sudden) loss coefficients k and K. In consequence, literature provides a lot of investigations on these coefficients with different values and parametrizations, as shown in Fig. 3.3. Both coefficients are generally related to the dependency of the contraction ratio, but also numerous publications can be found which investigate the dependency of the loss coefficient from the Reynolds number, see Refs. [50, 52, 53, 54].

The loss coefficients K for turbulent flow are plotted as the average value if K is obtained as a function of the Reynolds number. Figure 3.3 shows the spread of loss coefficients K and parametrizations for the sudden contraction. The scatter proves that most of the experimental studies disagree with each other since most of the loss coefficients are obtained for a specific experimental setup. Therefore, the verification of the momentum-based approach must be performed with own data and the classical parametrization of the sudden loss coefficient k by Idelchik [55] as a reference.

Nevertheless, some approaches employing the momentum balance to predict the pressure drop of

a sudden contraction are reported by the literature. Benedict et al. [56] first attempted to apply the momentum balance to the sudden contraction. But the authors noticed that, in contrast to sudden expansions, an explicit analytic formula for the loss coefficient of a sudden contraction could not be obtained. By that time, it was impossible to describe the flow pattern in the vena contracta analytically.

In the book Fundamentals of Pipe Flow, Benedict [57] presented the application of the momentum balance to orifices. The control volume contains the complete inflow cross-section upstream of the orifice and the contracting jet up to the vena contracta. Benedict accounted for the pressure forces in the inflow and outflow cross-sections as well as on the upstream-facing orifice wall as a counteracting force. Due to the definition of the control volume, the downstream-facing orifice wall is excluded from the considerations. The author also took into account the non-uniform pressure distribution over the orifice wall radius. Therefore, an integral coefficient for the counteracting force is introduced, replacing the pressure distribution integral over the upstream-facing orifice wall. Unfortunately, Benedict assumed the velocity distribution over the inlet and outlet cross-section to be uniform and equal. As a result, no momentum coefficients are taken into account as the approach is presented as an idealized solution. The major issue with Benedict's approach appears to be the definition of the downstream part of the control volume. Since it only comprises the jet leaving the orifice up to the vena contracta, the diameter of the vena contracta must be considered. But still, no satisfactory universal definition for the diameter of the vena contracta or the contraction coefficient has been obtained. Therefore, the momentum-based approach is not further pursued by Benedict as an alternative to the Bernoulli principle.

Besides a properly defined control volume, another problem in the application of the momentum balance was the determination of the momentum coefficients β. The problem is that the momentum balance is very sensitive to changes in the velocity distributions. For evaluating the momentum coefficient of a specific cross-section, detailed information on the velocity distribution is required.
Back in the time when no high-fidelity numerical simulations or measurement techniques were available, the real velocity profile could only be approximated. Therefore, variations of the velocity profile over the flow length have often been assumed or calculated, as shown by Glück [58].
Experimental studies about the change of the velocity profile over the flow length have been conducted by Durst and Loy [59] in 1985. Durst and Loy investigated laminar flows through a sudden contraction experimentally and numerically. The authors examined the change of the flow pattern upstream and downstream of a contraction using a Laser-Doppler-Anemometry (LDA) measuring system. Durst and Loy found out that the upstream flow pattern changes from laminar to turbulent and re-develops to laminar downstream of the contraction. In addition, the lengths upstream and downstream of the contraction where flow changes have also been obtained experimentally. Durst and Loy also investigated the dimensions of the upstream dead water and the downstream recirculation zone. An important finding of Durst and Loy [59] is a characteristic overshoot of the radial velocity profile upstream of the contraction. It vanishes in the contraction plane but immediately redevelops downstream. With the presented numerical simulation, the authors obtain a high agreement with the measurement results for the axial and radial velocity components over the flow length.

The investigation of Durst and Loy [59] shows the immense effort to measure the velocity distribution at that time. Nowadays, the velocity distribution over any cross-section is easily-obtainable by sophisticated measurement and simulation techniques.

3.1.2 Applying the Momentum Balance

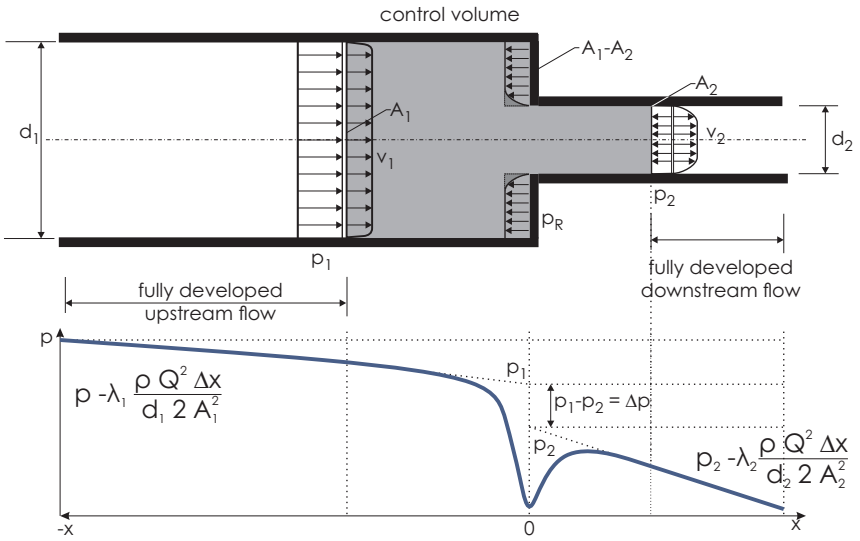

Figure 3.4: Definition of the control volume, pressures, and flow velocities

A control volume of the sudden contraction is shown in Fig. 3.4 by the grey area, jointly with axial pressure distribution along the center line. The control volume comprises the full cross-sections upstream and downstream of the sudden contraction. The inlet and the outlet should be placed in the region where the flow is fully developed and not influenced by the sudden contraction.
The pressure drop of the sudden contraction Δp is defined by the extrapolated linear pressure gradients, which means Δp is adjusted by frictional effects. The methodology is shown in the lower part of Fig. 3.4. Therefore, frictional forces F_F cancel out when Eq. (1.46) is applied to the control volume of a sudden contraction. In addition, the gravitational force term can be neglected because the flow through a sudden contraction is usually defined in the horizontal direction. Besides, for practical applications, the share of the gravitational force is small compared with the other forces involved.

$$0 = -\sum_i \varrho\, \beta_i\, v_i\, \vec{v}_i \cdot \vec{n}_i\, A_i - \sum_i p_i\, \vec{n}_i \cdot \vec{n}_v\, A_i \tag{3.8}$$

As shown by the control volume in Fig. 3.4, three pressure terms have to be considered, which are the inlet pressure p_1, the outlet pressure p_2, and the reacting pressure p_R of the contraction wall $(A_1 - A_2)$. With the normal unit vectors defined as $\vec{n}_v = [1;0]$, $\vec{n}_1 = [-1;0]$, and $\vec{n}_2 = [1;0]$, Eq. (3.8) gives

$$0 = -\sum_i \varrho\, \beta_i\, v_i\, \vec{v}_i \cdot \vec{n}_i\, A_i + p_1\, A_1 - p_2\, A_2 - p_R\, (A_1 - A_2) \tag{3.9}$$

The pressure force term considering the reacting pressure of the contraction wall p_R is negative since the normal unit vector of the contraction wall is equal to $\vec{n}_2$.
The momentum fluxes can be defined for the inlet and outlet cross-section, so Eq. (3.9) is expanded by the momentum fluxes entering and leaving the control volume.

$$0 = \varrho \left(\beta_1 \frac{Q^2}{A_1} - \beta_2 \frac{Q^2}{A_2} \right) + p_1\, A_1 - p_2\, A_2 - p_R\, (A_1 - A_2)\,. \tag{3.10}$$

Since the fluid is considered incompressible and only one inlet and outlet are present, the volumetric flow rate Q is independent of the cross-section: $Q = Q_1 = Q_2$.

As found by Benedict [57] and also shown by the numerical simulations discussed in the following, the reacting pressure p_R is not uniformly distributed over the contraction wall. Therefore, an analytical expression must be found for the counteracting pressure p_R considering the non-uniform distribution of the effective pressure. The effective pressure acting on the contraction wall is a function of the contraction wall radius $p(r)$ thus, p_R is defined as the average of the effective pressure $p(r)$. With the integration of the effective pressure over the contraction wall divided by the area of the contraction wall $(A_1 - A_2)$, p_R gives

$$p_R = \frac{1}{A_1 - A_2} \int_{R_2}^{R_1} 2\,\pi\,r\,p(r)dr \tag{3.11}$$

Here, r represents the contraction wall radius, R_1 the outer and R_2 the inner radius of the contraction wall. Figure 3.5 shows the normalized effective pressure $p(r)^* = (p_1 - p(r))/p_1$ over the normalized wall radius $r^* = (r - R_2)/(R_1 - R_2)$ $(R_1 \geq r \geq R_2)$ on the right-hand side. One can see that the pressure at the outer radius of the upstream pipe $p(R_1)$ is equal to the inlet pressure p_1. Starting at R_1, $p(r)$ remains constant up to the point where the radial flow attaches to the contraction wall. The radial flow is induced by the sudden contraction causing the whole flow field to converge in the contraction. From the attachment point to the inner radius R_2, the effective pressure $p(r)$ decreases due to the increasing radial velocity. This is shown on the left-hand side of Fig. 3.5. Here, the so-called convergence zone is illustrated by two converging lines and extends up to $r^* = 0.48$ for $\sigma = A_2/A_1 = 0.184$. For greater values of r^*, a dead water zone exists, which is illustrated by a circular arrow. Similar findings have been obtained by DeOtte et al. [60] conducting three-dimensional laser Doppler anemometry measurements of flow fields near an orifice plate. For an area ratio σ of 0.25, the resulting vector field shows that the flow attaches to the upstream orifice plate at around $r^* = 0.5$, confirming the simulation results. In the following chapters, it will be reasoned that it is justified to compare the upstream flow field of a sudden contraction with the one of an orifice.
According to the simulation results, the dead water zone extends to the whole contraction wall for $\sigma > 0.75$. In this case, the reacting pressure p_R is equal to p_1.

Because the pressure $p(r)$ is not constant over the contraction wall, Eq. (3.11) is parameterized by

$$p_R = p_1 - c_P \frac{\varrho}{2} \frac{Q^2}{A_1^2}, \tag{3.12}$$

with the pressure coefficient c_P, introducing the dependency of the pressure integral on the contraction ratio. In consequence, Eq. (3.12) is valid for any area ratio σ or flow rate because c_P takes into account the pressure distribution over the contraction wall.

Using Eq. (3.12) into Eq. (3.10), the pressure drop $\Delta p_I = p_1 - p_2$ of a sudden contraction gives:

$$\Delta p_I = \varrho \frac{Q^2}{{A_2}^2} \left(\beta_2 - \beta_1 \frac{A_2}{A_1} - \frac{c_P}{2} \frac{A_2}{A_1} + \frac{c_P}{2} \frac{A_2^2}{A_1^2} \right). \tag{3.13}$$

Alternative application of the momentum balance

As an alternative to the control volume covering the full cross-sections, a second approach with a different definition of the control volume is presented in Fig. 3.6. Here, the control volume is defined as a centric cylinder of the downstream pipe diameter d_2 in the upstream pipe. This means the control volume can be understood as an extension of the small pipe into the large pipe. The control volume

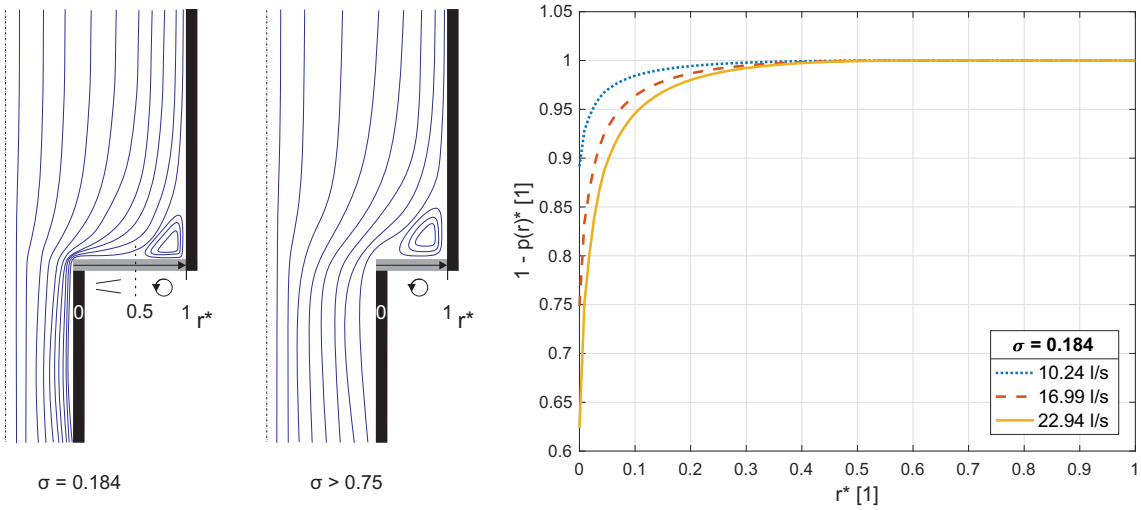

Figure 3.5: Illustration of the dead water and convergence zone at the contraction wall plus a chart of the normalized effective pressure versus the normalized contraction wall radius for different flow rates

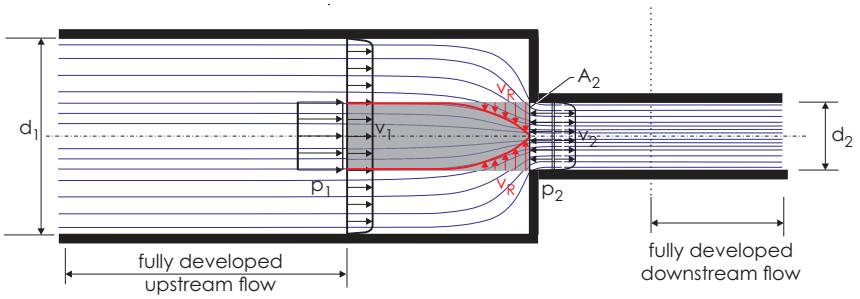

Figure 3.6: Definition of the control volume for the second approach

starts at a point where the flow is not influenced by the contraction and ends at the contraction plane. Starting with Eq. (3.9), the counteracting pressure term p_R is omitted as the contraction wall is not included in the control volume, which gives

$$0 = -\sum_i \varrho\, \beta_i\, v_i\, \vec{v}_i \cdot \vec{n}_i\, A_i + p_1 A_2 - p_2 A_2. \tag{3.14}$$

In Eq. (3.14), the inlet pressure p_1 is only acting on the area A_2. The pressure of the cylinder's shell surface is acting in the normal direction to the flow direction and, therefore, not contributing to the change of the axial momentum. The momentum flux terms apply analogously to the latter approach. But in this case, momentum can enter the control volume through the cylinder's front and shell surface. Nevertheless, the flow entering the control volume must also cross the pipe's cross-sectional area. The only difference in the influx terms between both approaches refers to the momentum coefficient being discussed in Chap. 3.1.4. Equation 3.14 yields

$$0 = p_1 A_2 - p_2 A_2 + \varrho \left(\beta_0 \frac{Q^2}{A_1} - \beta_{cont} \frac{Q^2}{A_2} \right) \tag{3.15}$$

The momentum coefficient of the influx term β_0 considers the influx through the shell and front surface of the control volume. This results in a different computation of the momentum coefficient, now named β_0 instead of β_1. The momentum coefficient at the outlet (contraction plane) is renamed to β_{cont}.

Flipped to $\Delta p_{II} = p_1 - p_2$, Eq. (3.15) gives the pressure drop of a sudden contraction for the second approach.

$$\Delta p_{II} = \varrho \frac{Q^2}{{A_2}^2} \left(\beta_{cont} - \frac{A_2}{A_1} \beta_0 \right) \tag{3.16}$$

Both approaches require physical coefficients originating from the substitution of integral by averaged expressions. These coefficients can be obtained from multiple measurements that are used to find parametrizations for the coefficients. Apart from that, a less laborious option is to conduct a set of numerical simulations to obtain the parametrizations. Therefore, only a few highly sophisticated measurements are required as a reference to verify and calibrate the numerical model. When a satisfactory agreement is obtained, the numerical model can be employed for further simulations.

3.1.3 Experimental Investigations

Setup

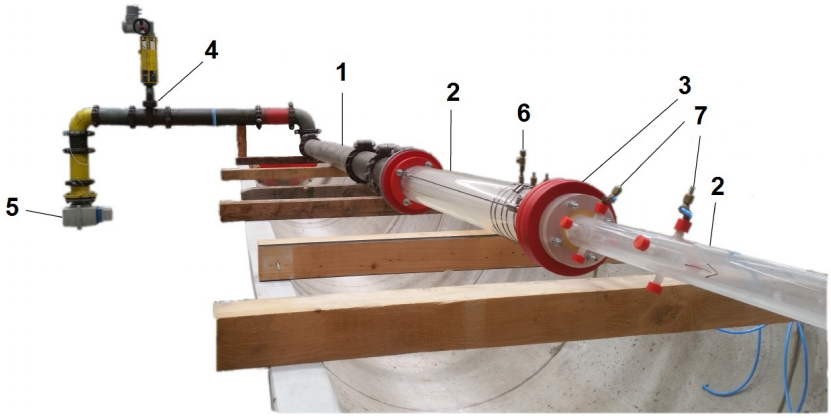

Figure 3.7: Sudden contraction test facility

Figure 3.7 shows the test bench built up in the hydraulic engineering laboratory for the verification of the numerical simulation from the outlet side. Water at temperatures around 20 °C is used for the experimental investigations. The experimental setup's main components are numbered in Fig. 3.7. To supply the sudden contraction with water, a steel piping (1) of the nominal diameter (DN) 150 connects the test bench with the laboratory's water supply system. A flow straightener is installed at the end of the steel piping to minimize eddies and turbulences before the fluid enters the region of interest. The mounted flow straightener consists of a bundle of pipes with a smaller diameter inserted into the last steel pipe before the acryl glass pipe. The purpose of the flow straightener is to homogenize the flow field by splitting the flow into various flow fields, which leads to a uniform flow pattern when the flow field is re-united.

The connected acryl glass section (2) comprises a pipe of DN 140 upstream, a pipe of DN 60 downstream of the sudden contraction, and the sudden contraction (3) itself. A control valve (4) operated in open loop to adjust the volume flow is installed within the steel piping. Therefore, sufficient distance to the region of interest is maintained to ensure a flow field undisturbed by the valve. A non-invasive volumetric flow sensor (5) is used to measure the volume flow. It is based on the electromagnetic measuring principle, specifically Faraday's law of induction. The sensor generates a magnetic field the conductive fluid moves through. The motion of the conductive fluid through the magnetic field induces

a voltage to be measured, which exhibits a linear proportionality to the flow rate, see Ref. [61]. To ensure an undisturbed flow pattern for the volumetric flow sensor, the sensor is mounted upstream of the control valve in a vertical piping section with sufficient free flow lengths. The measurement range reaches from 12 to 600 m^3/h at a maximum measurement error of $\pm$0.4% of the measured value.
To obtain the pressure drop over the sudden contraction, the upstream (6) and the downstream pressure tapping point (7) are connected to a differential pressure gauge. The differential pressure gauge covers a measurement range of 60 to 600 mbar possessing a maximum measurement error of $\pm$0.2% full scale. The pressure values gathered are wall static pressures. The downstream measuring position can be switched between three pressure tapping points at a flow distance of 103, 383, and 1027 mm downstream of the sudden contraction. All downstream pressure tapping points are connected to a valve block allowing to change between the measurement points without adapting the configuration. The upstream pressure tapping point is 275 mm distant from the sudden contraction. The control valve, the volumetric flow sensor, and the differential pressure gauge are connected to a data acquisition and control system. It allows to manually set the demanded flow rate and record the gathered values. The schematic of the test setup is shown in Fig. 3.8.

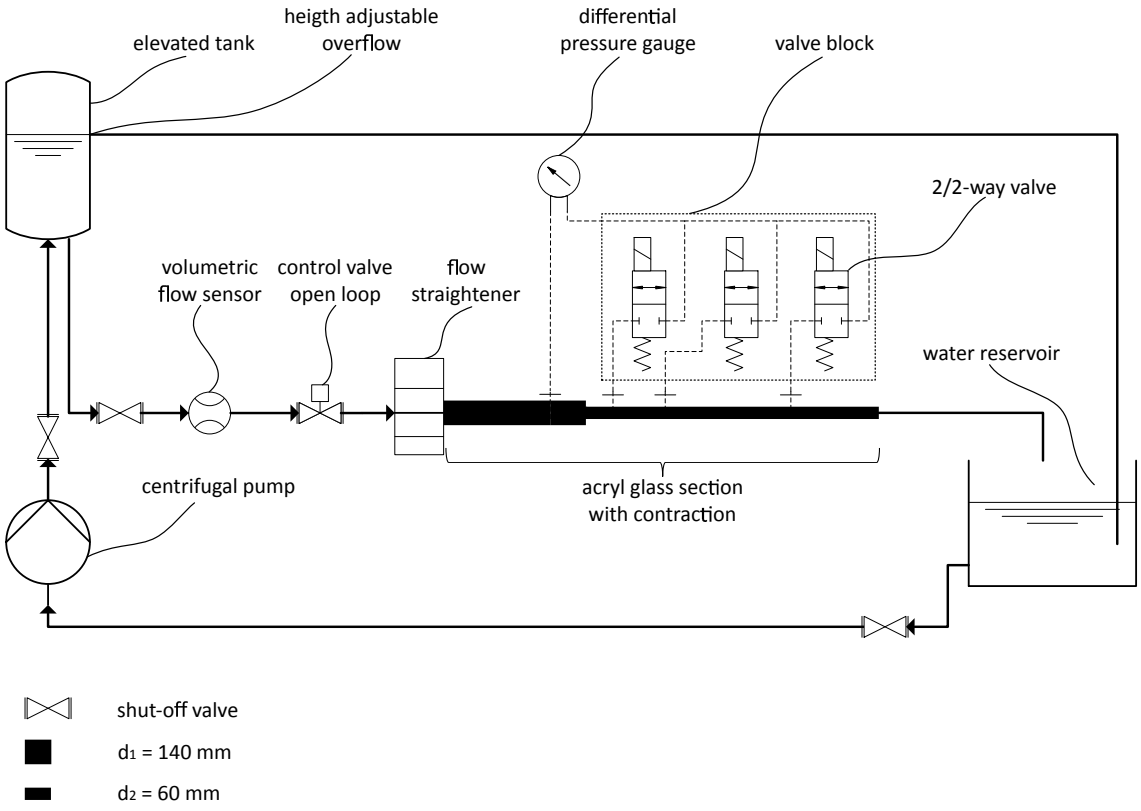

Figure 3.8: Schematic of the sudden contraction test facility

It is well known that the sharpness of the contraction edge strongly affects the pressure drop of a sudden contraction, as shown by Bullen et al. [52]. Therefore, the contraction edge is machined as sharp as possible but without burrs or roundings. To avoid flow disturbing steps between the downstream pipe and the sudden contraction, both parts are assembled flush and centric before connecting to the upstream pipe. A circular groove is machined into the sudden contraction part, ensuring a proper centric fit of the upstream pipe. The contraction ratio $\sigma = {d_2}^2/{d_1}^2$ of 0.184 is obtained by averaging the diameters of five measurements spread over the specific circumference (d_1 = 140.92 mm, d_2 =

60.43 mm). To ensure a fully developed flow field at the beginning of the region of interest, the length of the piping between the last bend and the sudden contraction amounts to about 40 times the diameter d_1. This free flow length includes the flow straightener and a flow length of 9 times the diameter d_1 solely in the acryl glass pipe. Therefore, it can be assumed in a good approximation that the flow field at the upstream pressure tapping point is fully developed. In addition, the elevated tank with the overflow minimizes pulsations induced by the pumps and guarantees a flow rate to be considered constant. Since gravitational effects are neglected in the derivation of the momentum balance, the acryl glass pipe is mounted horizontally. The deviation from the horizontal plane amounts to a maximum of $\pm 0.1\,^{\circ}$. Table 3.1 provides the investigated volumetric flow rates Q and the corresponding Reynolds numbers $Re_1,\ Re_2$.

Table 3.1: Volume flow rate converted to Reynolds numbers

volume flow rate Q [l/s]	Reynolds number upstream Re_1 [1]	Reynolds number downstream Re_2 [1]
10.24	92 556	215 820
11.85	107 111	249 759
15.35	138 693	323 401
16.99	153 490	357 906
20.12	181 801	423 920
22.12	199 893	466 106
22.94	207 270	483 307

Procedure

The large upstream pipe diameter results in large run-off distances upstream and downstream of the contraction. Two of the pressure tapping points downstream of the contraction are in the region of non-fully developed flow, as indicated by the performed numerical simulations detailed in Chap. 3.1.4. This allows proving the applicability of the momentum-based approach in a non-fully developed flow region as well.
The average values of the differential pressure and the corresponding volumetric flow rate are obtained by nine independent measurements. To further reduce random precision errors, the measured values of every measurement are averaged over 10 seconds, each at a measuring frequency of 10 Hz.
The pressure drop of a sudden contraction must be determined regardless of the wall roughness. Therefore, frictional effects have to be excluded from the experimental results, which means the wall roughness ks of the acryl glass pipes must be determined experimentally. For more accurate values, the wall roughness value is measured instead of using literature numbers. The friction factor λ can be determined using the Weisbach equation:

$$p_F = \lambda \, \frac{\varrho \, L \, Q^2}{2 \, d_{hyd} \, A^2}. \tag{3.17}$$

where p_F represents the frictional pressure loss, d_{hyd} the hydraulic diameter, and L the flow length of the pipe. With Eq. (3.17) flipped to λ, the wall roughness ks can be determined by introducing the friction factor λ into the Haaland equation [62]:

$$\frac{1}{\sqrt{\lambda}} = -1.8 \log_{10}\left(\frac{6.9}{Re} + \left(\frac{ks}{3.75\, d_{hyd}}\right)^{\frac{10}{9}}\right). \tag{3.18}$$

For the acryl glass section used in the experiments, a wall roughness in the range of $ks = 7.1 \cdot 10^{-5}...8.8 \cdot 10^{-5}\ m$ is determined with $ks = 7.8 \cdot 10^{-5}\ m$ as the mean value of all performed roughness measurements. The obtained wall roughness is larger than the range given in Ref. [63] for similar plastics: $ks = 1.5 \cdot 10^{-6}...6 \cdot 10^{-6}\ m$. With the wall roughness ks quantified, the frictional pressure loss p_F of both pipes can be calculated by Eq. (3.17) and subtracted from the measured differential pressures. The result yields the pressure drop Δp solely caused by the contraction, as shown in the lower part of Fig. 3.4. Therefore, the experimental results are directly comparable to the literature.

Error Analysis

For the evaluation of the measurement, it is mandatory to make a statement on the quality of the performed experiment to consider whether “precise” results have been obtained. It also answers the question if the planned experiment can meet the required accuracy when the result must be known within a certain range. To give a bold example: Two physical theories shall be compared against experimental results. Both theories are based on different approaches and correlate equally but not ideally with the experimental results. One can now argue which theory compares best with the experimental data. If the experimental results are known within 4%, it would be a pointless dispute if both theories compare within 2%.
The preceding example illustrates the importance of the estimation of the inaccuracy relating to measurements. Since it is impossible to perform ideal measurements, every measured value contains errors to be evaluated. Combining all (the significant) errors of the measurement results in the uncertainty of a measurement, which is obtained by an uncertainty analysis. Succinctly, an uncertainty analysis replies to the key question in experimentation: how are the uncertainties of the measured variables propagating to the result?

The uncertainty U of a result or measurement consists of systematic or fixed errors, called bias errors and random or variable errors, called precision errors. Bias errors can be reduced via calibration but can not be calculated directly. In contrast, precision errors can only be reduced by multiple measurements and readings. Every measured variable contains bias errors as well as precision errors. The quantification of all bias or precision errors regarding one measured variable amounts to the bias limit or precision limit, respectively. That is why a quantified error is called a limit. The combination of the bias limit and the precision limit yields the uncertainty U.

Coleman and Steele [64] describe methods for the general uncertainty analysis and detailed uncertainty analysis. A general uncertainty analysis is used in the planning phase of an experiment to consider the uncertainty in all measured variables. Here, the uncertainty is not subdivided into bias and precision errors. The general uncertainty analysis is rather used to survey if the planned experiment and especially the selected instrumentation can yield the desired information within the required tolerance. It is also used to identify the most critical measurements or measurement methods regard-

ing uncertainty. All contributors to the uncertainty are considered random in this case, see Ref. [64]. For each measured variable X_i, $B_i = 0$ which results in $U_i = P_i$ where B_i is the bias error and P_i the precision error. Therefore, the uncertainty of an experimental result Y as a function of i variables X_i can be calculated by:

$$U_Y = \left[\left(\frac{\partial Y}{\partial X_1} U_1 \right)^2 + \left(\frac{\partial Y}{\partial X_2} U_2 \right)^2 + \left(\frac{\partial Y}{\partial X_i} U_i \right)^2 \right]^{\frac{1}{2}} \tag{3.19}$$

A detailed uncertainty analysis is used to investigate the bias errors and precision errors and their propagation into the result separately. Here, the uncertainty of the result U_Y is expressed as a combination of the result's bias limit B_Y and precision limit P_Y:

$$U_Y = \left[B_Y^2 + P_Y^2 \right]^{\frac{1}{2}} \tag{3.20}$$

In general, the calibration determines the bias errors of measuring devices. As a consequence, one could suppose that when it can be determined, the bias error can also be eliminated. But the "true" value of a measured variable is never known, so calibration can only reduce the bias errors to a certain amount. This is because the bias error of the calibration device or standard used for the calibration remains in the output of the calibrated measurement device. Hence, all remaining bias errors are unknown and have to be estimated. It shall be emphasized that the computational resolution and curve fits also contribute to the bias error, although they are of minor influence. The bias limit B_Y is calculated as follows:

$$B_Y = \left[\left(\frac{\partial Y}{\partial X_1} B_1 \right)^2 + \left(\frac{\partial Y}{\partial X_2} B_2 \right)^2 + \left(\frac{\partial Y}{\partial X_i} B_i \right)^2 \right]^{\frac{1}{2}} \tag{3.21}$$

A significant difference between the estimation of bias and precision errors is that the bias limit of measured variables can be dependent on each other. This is the case when two variables are measured with the same device (e.g. the diameter of two pipes of one experimental setup) or when transducers are calibrated against the same reference. Then the bias limits of these measured variables are correlated, which results in additional terms in Eq. (3.21).

$$\begin{aligned} B_Y^2 = &\left(\frac{\partial Y}{\partial X_1} B_1 \right)^2 + \left(\frac{\partial Y}{\partial X_2} B_2 \right)^2 + \left(\frac{\partial Y}{\partial X_i} B_i \right)^2 \\ &+ 2 \frac{\partial Y}{\partial X_1} \frac{\partial Y}{\partial X_2} \, \phi_{12} \, B_1 \, B_2 + 2 \frac{\partial Y}{\partial X_1} \frac{\partial Y}{\partial X_i} \, \phi_{1i} \, B_1 \, B_i + 2 \frac{\partial Y}{\partial X_2} \frac{\partial Y}{\partial X_i} \, \phi_{2i} \, B_2 \, B_i \end{aligned} \tag{3.22}$$

Equation (3.22) represents the case when all variables are correlated with each other with ϕ as the correlation coefficient between the bias of two measured variables and $\phi_{xy} = \phi_{yx}$. The correlation coefficient represents the degree of correlation that can take values between minus unity and unity. In brief, unity stands for perfect correlation, minus unity for perfect inverse correlation, and zero for no correlation. According to Ref. [64], the correlation coefficient is set to unity in practice, but B_x must then be taken into detailed consideration. Therefore, $\hat{B}_x$ is introduced as the portion of the bias error B_x that originates from the joint error source (e.g. the calibration). For the sake of simplicity, if ϕ_{1i} and ϕ_{2i} are assumed zero Eq. (3.22) gives:

$$B_Y^2 = \left(\frac{\partial Y}{\partial X_1} B_1\right)^2 + \left(\frac{\partial Y}{\partial X_2} B_2\right)^2 + \left(\frac{\partial Y}{\partial X_i} B_i\right)^2 + 2\frac{\partial Y}{\partial X_1}\frac{\partial Y}{\partial X_2}\, 1\, \hat{B}_1\, \hat{B}_2 \tag{3.23}$$

In general, the estimation of $\hat{B}_x$ requires detailed knowledge about the calibration process, shown exemplarily in Coleman and Steele [64] (example 4.1). According to Coleman and Steele, it is possible to obtain information about the bias errors B_x in the following ways: by comparing the results of independent measurements depending on different physical principles, by an independent calibration of the installed transducers, by comparing the results with known values, or by the manufacturer's specifications. The authors propose that the calibration should always be performed with the complete employed measurement system or at least a configuration as close as possible to the final measurement system. This guarantees the consideration of all bias errors contributed by the entire experiment's measuring chain. The bias error of the measuring chain can therefore be reduced up to the bias error of the calibration reference. In the following, $\hat{B}_x$ is assumed to completely originate from the calibration against the same standard and, therefore, is set equal to B_x.

The result's precision limit P_Y can be calculated as follows:

$$P_Y^2 = \left(\frac{\partial Y}{\partial X_1} P_1\right)^2 + \left(\frac{\partial Y}{\partial X_2} P_2\right)^2 + \left(\frac{\partial Y}{\partial X_i} P_i\right)^2 \tag{3.24}$$

Equation (3.24) does not take correlation terms into account in contrast to the bias limit, see Eq. (3.22). The reason is that the precision limit is based on random errors of a measurement, which can be seen as statistical effects. Therefore, the precision limits of measured variables are independent of each other. It shall be mentioned that the partial derivatives $\partial Y/\partial X_i$ are equal to the ones determined for the bias limit. The precision limit P can be determined statistically by evaluating multiple results measured with the same transducer. Another source to obtain resilient estimates for the precision limit is the manufacturer's specification, where a certain measuring tolerance is provided. Using the specified measuring tolerances for the estimation of the precision limit also represents the worst case for which the uncertainty is not underestimated with high probability. In summary, assuming the sensor's measuring tolerance as its precision limit can, therefore, be justified as the most conservative estimate for the precision limit P_Y.

The previous considerations are now transferred to the estimation of the uncertainty $U_{\Delta p}$ associated with the calculation of the pressure drop Δp. Therefore, the share of the pressure drop Δp_I as per Eq. (3.13) plus the shares of the frictional pressure loss Δp_F of both pipes, according to Eq. (3.17), have to be taken into consideration. The measured quantities (Δp, Q, L_1, L_2, d_1, and d_2), as well as universal parameters (in this case: ϱ and ν), contain bias and precision errors. It can be assumed in a good approximation that the universal parameters have been determined with much greater accuracy than the measured quantities of the performed experiment. Consequentially, the errors regarding the universal parameters are neglected. The detailed uncertainty analysis described by Coleman and Steele [64] is used to estimate the bias limit ($B_{\Delta p}$) and the precision limit ($P_{\Delta p}$), resulting in the uncertainty ${U_{\Delta p}}^2 = {P_{\Delta p}}^2 + {B_{\Delta p}}^2$.

Equation (3.13) with the introduced values $c_P = c_P(0.184)$, $\beta_1 = 1.03$, and $\beta_2 = 1.03$ (discussed in the following chapter) is used to calculate the uncertainty of the measured differential pressure.

$$\Delta p_I = \varrho Q^2 \left(0.705\frac{16}{\pi^2 d_2^4} + 0.245\frac{16}{\pi^2 d_1^2 d_2^2} - 1.575\frac{16}{d_1^4 \pi^2} + 0.625\frac{16 d_2^6}{d_1^6 d_2^4 \pi^2}\right) - \frac{\varrho \lambda_1 L_1 Q^2}{2 d_1 \frac{\pi^2}{16} d_1^4} - \frac{\varrho \lambda_2 L_2 Q^2}{2 d_2 \frac{\pi^2}{16} d_2^4}. \tag{3.25}$$

The results of the numerical simulation are assumed to have much higher accuracy compared with the measured quantities. Therefore, the associated numerical uncertainties are neglected. Equation (3.25) is used for the derivations of Δp concerning the measured variables. The partial derivatives are:

$$\frac{\partial \Delta p}{\partial Q} = 2\varrho Q\left(0.705\frac{16}{\pi^2 d_2^4} + 0.245\frac{16}{\pi^2 d_1^2 d_2^2} - 1.575\frac{16}{d_1^4\pi^2} + 0.625\frac{16 d_2^6}{d_1^6 d_2^4 \pi^2}\right) - 2Q\frac{8\varrho\lambda_1 L_1}{\pi^2 d_1^5} - 2Q\frac{8\varrho\lambda_2 L_2}{\pi^2 d_2^5} \tag{3.26}$$

$$\frac{\partial \Delta p}{\partial d_1} = \varrho Q^2\left(-0.245\frac{32}{\pi^2 d_1^3 d_2^2} + 1.575\frac{64}{\pi^2 d_1^5} - 0.625\frac{96 d_2^2}{d_1^7\pi^2}\right) + \frac{40\varrho\lambda_1 L_1 Q^2}{d_1^6\pi^2} \tag{3.27}$$

$$\frac{\partial \Delta p}{\partial d_2} = \varrho Q^2\left(-0.705\frac{64}{\pi^2 d_2^5} - 0.245\frac{32}{\pi^2 d_1^2 d_2^3} + 0.625\frac{32 d_2}{d_1^6\pi^2}\right) + \frac{40\varrho\lambda_2 L_2 Q^2}{d_2^6\pi^2} \tag{3.28}$$

$$\frac{\partial \Delta p}{\partial L_1} = -\frac{8\varrho\lambda_1 Q^2}{d_1\pi^2 d_1^4} \tag{3.29}$$

$$\frac{\partial \Delta p}{\partial L_2} = -\frac{8\varrho\lambda_2 Q^2}{d_2\pi^2 d_2^4} \tag{3.30}$$

$$\frac{\partial \Delta p}{\partial \lambda_1} = -\frac{8\varrho L_1 Q^2}{d_1\pi^2 d_1^4} \tag{3.31}$$

$$\frac{\partial \Delta p}{\partial \lambda_2} = -\frac{8\varrho L_2 Q^2}{d_2\pi^2 d_2^4} \tag{3.32}$$

According to the calculation of the bias limit $B_{\Delta p}$ (Eq. (3.23)) and the precision limit $P_{\Delta p}$ (Eq. (3.24)), the bias and precision errors of all measured quantities have to be quantified. As mentioned, these values can not be obtained by repetitive measurements as the volume flow rate is not perfectly constant during the experiments. Therefore, the calibration standards or calibration devices have to be taken into consideration for the estimation of all bias limits. In contrast, the data sheets of the used measuring devices provide information about the precision limit.

The bias limit of the final equation calculating the pressure drop (Eq. (3.25)) $B_{\Delta p}$ gives:

$$\begin{aligned} B_{\Delta p}^2 = &\left(\frac{\partial \Delta p}{\partial Q}B_Q\right)^2 + \left(\frac{\partial \Delta p}{\partial d_1}B_{d1}\right)^2 + \left(\frac{\partial \Delta p}{\partial d_2}B_{d2}\right)^2 + \left(\frac{\partial \Delta p}{\partial L_1}B_{L1}\right)^2 + \left(\frac{\partial \Delta p}{\partial L_2}B_{L2}\right)^2 + \\ &\left(\frac{\partial \Delta p}{\partial \lambda_1}B_{\lambda 1}\right)^2 + \left(\frac{\partial \Delta p}{\partial \lambda_2}B_{\lambda 2}\right)^2 + 2\frac{\partial \Delta p}{\partial d_1}\frac{\partial \Delta p}{\partial d_2}\,1\,B'_{d1}\,B'_{d2} + 2\frac{\partial \Delta p}{\partial L_1}\frac{\partial \Delta p}{\partial L_2}\,1\,B'_{L1}\,B'_{L2} + \\ &2\frac{\partial \Delta p}{\partial \lambda_1}\frac{\partial \Delta p}{\partial \lambda_2}\,1\,B'_{\lambda 1}\,B'_{\lambda 2}, \end{aligned} \tag{3.33}$$

and the precision limit:

$$\begin{aligned} P_{\Delta p}^2 = &\left(\frac{\partial \Delta p}{\partial Q}P_Q\right)^2 + \left(\frac{\partial \Delta p}{\partial d_1}P_{d1}\right)^2 + \left(\frac{\partial \Delta p}{\partial d_2}P_{d2}\right)^2 + \left(\frac{\partial \Delta p}{\partial L_1}P_{L1}\right)^2 + \left(\frac{\partial \Delta p}{\partial L_2}P_{L2}\right)^2 + \\ &\left(\frac{\partial \Delta p}{\partial \lambda_1}P_{\lambda 1}\right)^2 + \left(\frac{\partial \Delta p}{\partial \lambda_2}P_{\lambda 2}\right)^2. \end{aligned} \tag{3.34}$$

Equation 3.33 includes correlation terms for the diameter and the length since the diameters d_1 and d_2 and the pipe lengths L_1 and L_2 have been measured with the same measuring device. The correlation term for the friction factor λ is explained subsequently. According to Eqs. (3.23) and (3.24), the bias and the precision error of every measured variable have to be quantified. The values for the bias and the precision limit and their sources are given in Tab. 3.2 for Δp, Q, d_1, d_2, L_1, L_2, λ_1, λ_2.

The bias and the precision limit of the friction factor λ are determined by an uncertainty analysis described in the following. The friction factor has been experimentally determined by measuring the pressure drop over a defined flow length L for two flow rates $Q = 22\ l/s$ and $Q = 27\ l/s$. The wall roughness ks was then determined by the Colebrook-White equation [20] (Eq. (3.35)) solved for ks, see Eq. (3.36). As the wall roughness ks obtained is negligibly dependent on the flow rate Q or the Reynolds number Re, ks can be applied to all investigated flow rates.

$$\frac{1}{\sqrt{\lambda}} = -2\ \log_{10}\left(\frac{2.51}{Re\sqrt{\lambda}} + \frac{k_s}{3.7\ d_{hyd}}\right). \tag{3.35}$$

$$ks = \left(10^{\frac{-1}{\sqrt{\lambda_2}}} - \frac{2.51}{Re\sqrt{\lambda}}\right) 3.7\ d_{hyd} \tag{3.36}$$

Equation (3.36) yields a wall roughness ks of $7.089 \cdot 10^{-5}\ m$ ($\lambda = 0.0208$) for $Q = 27\ l/s$ and $8.718 \cdot 10^{-5}\ m$ ($\lambda = 0.0219$) for $Q = 22\ l/s$. It is obvious that the implicit Colebrook-White equation (Eq. (3.35)) can not be used to substitute λ in the final pressure drop equation (3.25).

Following the approach of Coleman and Steele [64] for the calculation of the uncertainty straightforwardly, the bias and the precision limit for the friction factor λ must be obtained by applying the uncertainty analysis to the measurement of the friction factor, respectively, the wall roughness ks. The uncertainty of the friction factor (U_λ) is calculated from the friction measurements. Here, the final equation is obtained by solving the Weisbach equation [19] (Eq. (3.17)) for λ.

$$\lambda = \frac{\Delta p\ d_2^5\ \pi^2}{8\ \varrho\ Q^2\ L} \tag{3.37}$$

The partial derivatives of Eq. (3.37) are:

$$\frac{\partial \lambda}{\partial \Delta p} = \frac{d_2^5\ \pi^2}{8\ \varrho\ Q^2\ L} \tag{3.38}$$

$$\frac{\partial \lambda}{\partial d_2} = \frac{5\ \Delta p\ d_2^4\ \pi^2}{8\ \varrho\ Q^2\ L} \tag{3.39}$$

$$\frac{\partial \lambda}{\partial Q} = -\frac{2\ \Delta p\ d_2^5\ \pi^2}{8\ \varrho\ Q^3\ L} \tag{3.40}$$

$$\frac{\partial \lambda}{\partial L} = -\frac{\Delta p\ d_2^5\ \pi^2}{8\ \varrho\ Q^2\ L^2} \tag{3.41}$$

With the values of all bias and precision limits, given in Tab. 3.2, the bias limit of the friction factor can be obtained by applying Eq. (3.23), which results in

$$B_\lambda^2 = \left(\frac{\partial \lambda}{\partial \Delta p} B_{\Delta p}\right)^2 + \left(\frac{\partial \lambda}{\partial d} B_{d_2}\right)^2 + \left(\frac{\partial \lambda}{\partial Q} B_Q\right)^2 + \left(\frac{\partial \lambda}{\partial L} B_{L_2}\right)^2 \tag{3.42}$$

and for the precision limit by applying Eq. (3.24)

$$P_\lambda^2 = \left(\frac{\partial \lambda}{\partial \Delta p} P_{\Delta p}\right)^2 + \left(\frac{\partial \lambda}{\partial d} P_{d_2}\right)^2 + \left(\frac{\partial \lambda}{\partial Q} P_Q\right)^2 + \left(\frac{\partial \lambda}{\partial L} P_{L_2}\right)^2. \tag{3.43}$$

For the uncertainty of the friction factor,

$$U_\lambda = \left[B_\lambda^2 + P_\lambda^2\right]^{\frac{1}{2}} \tag{3.44}$$

Table 3.2: Bias and precision limits of measured quantities with the respective sources

quantity X	bias limit B_X	precision limit P_X
differential pressure Δp	$B_{\Delta p} = 20\ Pa$ [65]	$P_{\Delta p} = 108\ Pa$ [66]
flow rate Q	$B_Q = 0.0006\ Q$ [67]	$P_Q = 0.04\ Q + 0.0002\ Q_{max}$ [68]
diameter upstream pipe d_1	$B_{d1} = 5 \cdot 10^{-5}\ m$ [69]	$P_{d1} = 5 \cdot 10^{-5}\ m$ (1/2 scale division)
diameter downstream pipe d_2	$B_{d2} = 5 \cdot 10^{-5}\ m$ [69]	$P_{d2} = 5 \cdot 10^{-5}\ m$ (1/2 scale division)
flow length upstream L_1	$B_{L1} = 1 \cdot 10^{-3}\ m$ [70]	$P_{L1} = 5 \cdot 10^{-4}\ m$ (1/2 scale division)
flow length downstream L_2	$B_{L2} = 1.4 \cdot 10^{-3}\ m$ [70]	$P_{L2} = 5 \cdot 10^{-4}\ m$ (1/2 scale division)
friction factor upstream λ_1	$B_{\lambda 1} = 1.4545 \cdot 10^{-4}$	$P_{\lambda 1} = 4.6412 \cdot 10^{-4}$
friction factor downstream λ_2	$B_{\lambda 2} = 1.4545 \cdot 10^{-4}$	$P_{\lambda 2} = 4.6412 \cdot 10^{-4}$

Eq. (3.44) gives $U_{\lambda,22} = \pm 2.22\%$ for $Q = 22\ l/s$ and $U_{\lambda,27} = \pm 1.9\%$ for $Q = 27\ l/s$. It shall be emphasized that in Tab. 3.2, the maximum values of B_λ and P_λ are given, as obtained from the uncertainty analysis of the friction measurements.

For the sake of simplicity, with the upper and lower limit of λ determined, ks can be calculated by Eq. (3.36) for both limits. As a result, the maximum and minimum values of the wall roughness ks are obtained. It shall be mentioned that this method neglects the errors of the measured variables in Eq. (3.36) but simplifies the calculation considerably. Coleman and Steele [64] proposed the method of substituting the derivatives $\partial Y/\partial X$ by differences $\Delta Y/\Delta X$. Explained in simple words: the difference between the upper and lower λ results in a difference of ks, which can be assumed as the uncertainty of the wall roughness U_{ks}. This simplification can be justified by examining the range of ks depending on the volume flow rate Q. The spread of the friction factor λ between different volume flow rates is much higher (around $\pm 5\%$) than the uncertainty $U_{\lambda,22} = \pm 2.22\%$.

With all bias limits and precision limits defined, the uncertainty of the pressure drop $U_{\Delta p}$ can be estimated by applying Eq. (3.33) and Eq. (3.34) to Eq. (3.20):

$$U_{\Delta p} = \left[B_{\Delta p}^2 + P_{\Delta p}^2\right]^{\frac{1}{2}}. \tag{3.45}$$

Ultimately, the maximum uncertainty is obtained for $Q = 10\ l/s$ and amounts to $U_{\Delta p_{I,10}} = \pm 1.26\%$, whereas the minimum uncertainty is obtained for $Q = 23\ l/s$ and amounts to $U_{\Delta p_{I,23}} = \pm 1.06\%$.

For the second approach regarding the momentum coefficient β_0, the uncertainty analysis is performed in the same way. Equation (3.16) with the introduced results of the numerical simulation $\beta_{cont} = 1$ and $\beta_0(0.184) = 1.8363$ gives

$$\Delta p_{II} = \varrho Q^2 \left(\frac{16}{\pi^2\, d_2^4} - 1.8363 \frac{16}{\pi^2 d_1^2 d_2^2}\right) - \frac{8\varrho\lambda_1 L_1 Q^2}{\pi^2 d_1^5} - \frac{8\varrho\lambda_2 L_2 Q^2}{\pi^2 d_2^5} \tag{3.46}$$

Only the partial derivatives $\partial\Delta p/\partial Q$, $\partial\Delta p/\partial d_1$, and $\partial\Delta p/\partial d_2$ as per Eqs. (3.26,3.27,3.28) change as follows:

$$\frac{\partial \Delta p_{II}}{\partial Q} = 2\varrho Q \left(\frac{16}{\pi^2\, d_2^4} - 1.8363 \frac{16}{\pi^2 d_1^2\, d_2^2}\right) - 2Q \frac{8\varrho\lambda_1 L_1}{\pi^2 d_1^5} - 2Q \frac{8\varrho\lambda_2 L_2}{\pi^2 d_2^5} \tag{3.47}$$

$$\frac{\partial \Delta p_{II}}{\partial d_1} = \varrho Q^2 \left(3.6726 \frac{16}{\pi^2 d_1^3 d_2^2} \right) + \frac{40 \varrho \lambda_1 L_1 Q^2}{d_1^6 \pi^2} \tag{3.48}$$

$$\frac{\partial \Delta p_{II}}{\partial d_2} = \varrho Q^2 \left(-\frac{64}{\pi^2 d_2^5} + 3.6726 \frac{16}{\pi^2 d_1^2 d_2^3} \right) + \frac{40 \varrho \lambda_2 L_2 Q^2}{d_2^6 \pi^2} \tag{3.49}$$

By solely substituting Eqs. (3.26,3.27,3.28) with Eqs. (3.47,3.48,3.49) in the calculation procedure of the presented detailed uncertainty analysis, the uncertainty according to the second momentum-based approach is obtained. The uncertainty is maximum for $Q = 10\ l/s$ again and amounts to $U_{\Delta p_{II,10}} = \pm 1.28\%$. The minimum uncertainty is obtained for $Q = 23\ l/s$ in analogy to the first approach and amounts to $U_{\Delta p_{II,23}} = \pm 1.09\%$.

For the sake of the identifiability of the data sets, the error bars of the measurement results are not displayed in the graphs since the result's marker size is approximately two to three times bigger than the error bars.

3.1.4 Numerical Modelling

To obtain the momentum coefficients β and the pressure coefficient c_P closing the presented momentum-based approaches, numerical simulations have to be performed. Thus, a steady-state three-dimensional simulation using the CFX-Tool of ANSYS is employed. Although the rotational symmetry of the axisymmetric contraction could be used for a two-dimensional simulation with polar coordinates, the simulation is performed in three dimensions to allow for capturing flow effects in all three spatial dimensions. The simulation domain covers a region starting $10d_1$ upstream of the contraction up to the outlet at $14d_1$ ($\simeq 33d_2$) downstream of the contraction. The upstream flow length ensures that the flow is fully developed, entering the region of interest. A flow is considered fully developed when β is constant up to the third decimal point over a flow length of at least 2 d_1. However, increasing the inflow length further does not influence the results of the upstream momentum coefficient β considerably. Otherwise, the downstream momentum coefficient is strongly affected by the contracting flow and, therefore, influenced irrelevantly by the upstream flow.
An unstructured mesh of tetrahedral elements is applied to the whole simulation domain, see Fig. 3.9. An unstructured mesh is chosen due to a smooth transition to the refined mesh of the contraction wall, detailed in the following. The mesh quality parameters like the skewness and aspect ratio, as proposed by Rodriguez [30], maintain values closer to the optimum when an unstructured mesh is employed. The tetrahedral element edge length is set to 3 mm. At the pipe walls, the mesh is refined by 25 prism layers. The thickness of every prism layer is increasing by a factor of 1.2 toward the pipe inside. Hence, several prism layers cover the boundary layer's buffer zone since the highest investigated flow rate together with the target value of the dimensionless wall distance $y^+ = 5$ is used to calculate the first layer height $\Delta y_1 \approx 1.45 \cdot 10^{-5}\, m$, see Eq. (2.9). The maximum thickness of the boundary layer is estimated at 1 mm at the upstream pipe walls and 0.4 mm at the downstream pipe walls, according to Eq. (2.10). The total height of the prism layers amounts to 1.4 mm for the given growth rate and the number of layers. An inflated total thickness of the prism layers beyond the boundary layer thickness proves beneficial for the flow since the tendency of flow oscillations is significantly reduced in the downstream pipe. Another advantage of an extended region of the increased mesh resolution in the near-wall region comes into effect for the computation of the momentum coefficient β as it shows a high sensitivity to the rapidly changing velocity profile in the near-wall region. In fact, no significant change of the momentum coefficient β can be observed when changing the wall layers, whereas an

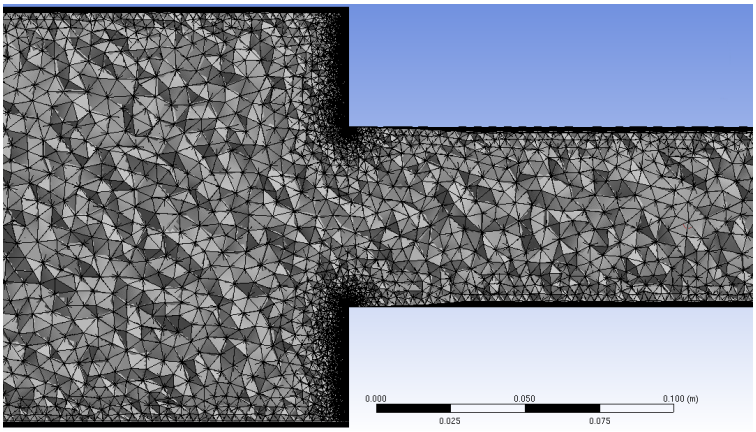

Figure 3.9: Sectional view of the mesh around the sudden contraction

absence of wall layers results in notable errors of β.
The pressure over the contraction wall is an important quantity in computing the pressure coefficient c_P. Therefore, the mesh resolution at the contraction wall is increased additionally, as shown in Fig. 3.9. The initial element edge length at the contraction wall amounts to 0.5 mm and increases smoothly to 3 mm towards the inside. This mesh has proven to be the best compromise between accuracy and efficiency, which will be shown in a subsequent paragraph discussing numerical independency.

A mass flow inlet with a defined mass flow rate is applied as the inlet boundary condition. At the outlet, a pressure outlet is selected as the boundary type with the options average static pressure and pressure averaging over the whole outlet. At the outlet, the gauge pressure is set to 0 Pa. The reference pressure of the simulation domain is defined as 101 325 Pa, which is the standard pressure. A wall with the experimentally determined wall roughness $ks = 7.8 \cdot 10^{-5}\ m$ is applied to all closed boundaries of the simulation domain.

To justify the choice of a proper turbulence model, the pressure profiles simulated with three common turbulence models (kϵ, kω, kω-SST) are compared with the measured differential pressure in the pressure recovery zone. Figure 3.10 shows the measured pressure by markers and the simulation results of the turbulence models by lines. The kω-SST turbulence model [33] shows the best correlation with the experimental results and is therefore considered the most appropriate choice. For the sudden contraction, the ω-based turbulence models can show their assets since these turbulence models are able to predict flow separation and adverse pressure gradients physically reasonably, which both occur in the vena contracta region. But the kω and kω-SST turbulence models also yield reliable results for the flow variables in near-wall regions. For example, the pressure coefficient c_P computed with the kϵ turbulence model deviates approximately 6% from the value obtained by the kω-SST turbulence model. Whereas the deviation between the kω and the kω-SST turbulence model only amounts to under 1% for c_P. Using the results of β and especially c_P obtained with the k-ϵ turbulence model results in an additional 2% deviation of the theory as per Eq. (3.13) from the measurement.

Employing the kω-SST turbulence model [33] with the automatic wall function and the roughness $ks = 7.8 \cdot 10^{-5}\ m$, the simulated pressure drops match the measured ones within -2.3% to +1.3% deviation. Table 3.3 shows the deviation of the measured to the simulated differential pressure. Additionally, the deviation of the simulated differential pressure using the kϵ and the kω turbulence model to the measured differential pressure is also included in Tab. 3.3. For the experimentally investigated case, the results of the simulated pressure drop Δp_{sim} change around 1% applying the kϵ or the kω

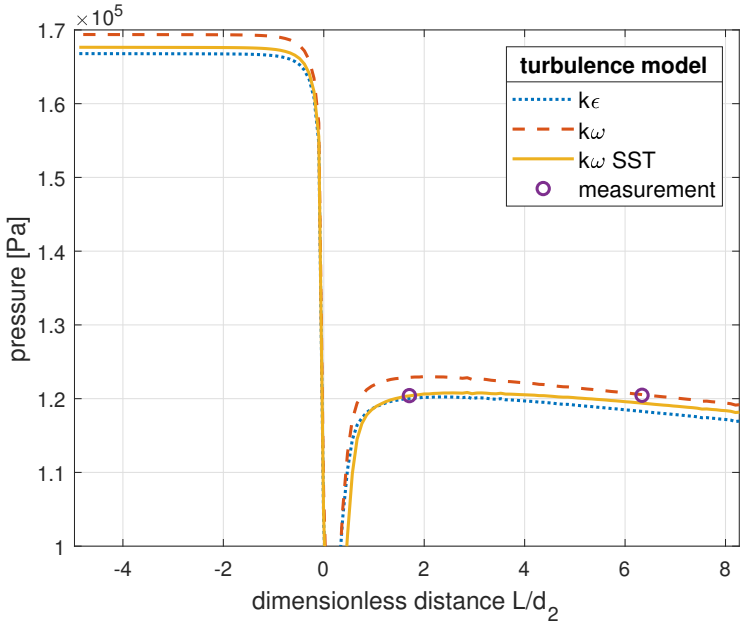

Figure 3.10: Measured differential pressure in the recovery zone together with the pressure profiles obtained with different turbulence models

Table 3.3: Comparison of measured and simulated pressures for 22.94 l/s with kω-SST, kϵ, and kω turbulence model

pressure tapping point	differential pressure measured Δp_{meas} [Pa]	differential pressure simulated Δp_{sim} [Pa]	deviation $1 - \frac{\Delta p_{sim}}{\Delta p_{meas}}$	deviation with kϵ	deviation with kω
1	47 232	47 262	-0.001	0.01	0.016
2	47 184	48 287	-0.023	-0.028	-0.034
3	55 987	55 238	0.013	0.013	-0.003

turbulence model compared with the kω-SST turbulence model. Figure 3.11 shows the simulated axial wall pressure distribution and the measured differential pressures over the dimensionless distance from the contraction L/d_2. The employed turbulence model captures the measured values with high accuracy. Applying a wall roughness $ks = 7.1 \cdot 10^{-5}\ m$ or $ks = 8.8 \cdot 10^{-5}\ m$ to the numerical model that both represent the boundaries of the experimentally determined range for ks causes a negligible change of the pressure drop Δp of under 0.8% at maximum. Therefore, the exact value of the equivalent wall roughness ks is of subordinate importance to the numerical model's accuracy.

The numerical simulation indicates the axial pressure distribution deviating from a linear profile within the region from approximately $0.5d_1$ or 70 mm upstream of the contraction to approximately $18d_2$ or 1080 mm downstream of the contraction. The linear pressure profile is shown by the dashed line in Fig. 3.11. It also shows that the computed pressure profile is in line with the results obtained by Fester et al. [50]. The authors found out that the flow is fully re-developed after approximately $20d_2$, as well as a dependency of the flow redevelopment distance on the contraction ratio. These effects are also reproduced in good accordance with the performed numerical simulation.

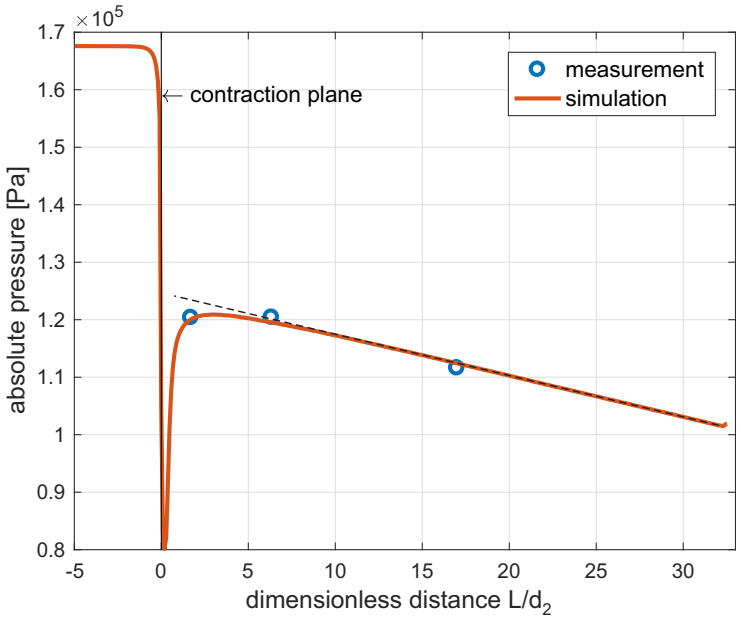

Figure 3.11: Profile of the simulated pressure at the wall in comparison with the measured differential pressure

Comparing the results of the numerical model with the performed experiments justifies the employment of the kω-SST turbulence model. As an additional assessment of the turbulence model, the results of the numerical model can be compared with external measurements. Bullen et al. [71] experimentally investigated turbulent flows through a sudden contraction with a laser Doppler anemometer. Pipes with an upstream diameter of 110.17 mm and a downstream diameter of 63.46 mm are used for the experiments. The measurements are conducted at a Reynolds number of $1.538{\cdot}10^5$ based on the upstream pipe diameter and at different axial locations. More detailed evaluations of the investigated flow field can be found in Bullen et al. [72]. However, the measured radial distributions of the turbulence intensity J are compared with the results of the presented numerical model employing different turbulence models. Therefore, the measurement data of Bullen et al. at four different axial locations is shown in Fig. 3.12 by grey markers, together with the numerical results of the kε, the kω, and the kω-SST turbulence model. The vertical axis represents the radius r, normalized by the respective pipe radius R and the horizontal axis the turbulence intensity J, calculated via $J = \sqrt{2/3\,k}/(Q/A)$ with k representing the turbulence kinetic energy. The axial location is given in multiples of the upstream pipe diameter d_1 with negative values indicating upstream locations.

Figure 3.12 shows that all turbulence models yield very similar results in the downstream region, even though the measurement results are not captured in all detail. This is because the specific deficiencies of the turbulence models are not coming into full effect for a sudden contraction flow, in contrast to the sudden expansion and the metering orifice as shown in the following sections. However, the kω-SST turbulence model shows the best agreement with the data in the downstream region, especially in the region near the wall ($r/R = 1$). Pairs of data at equal radii indicate a deviation of the measurement over the diameter, probably due to an asymmetric flow pattern. At the upstream location, all turbulence models fail to reproduce the measured data precisely. But the general trend of the experimental results is captured most accurately by the kω-SST turbulence model.
An important issue is a non-physical behavior of J near the wall obtained by the kε turbulence model.

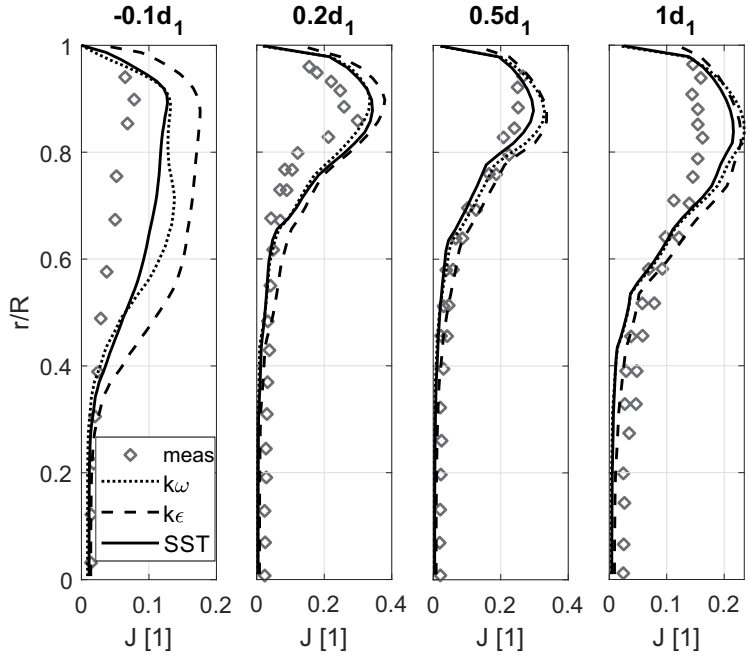

Figure 3.12: Normalized pipe radius r vs. the radial turbulence intensity J distribution of the simulated results compared with the measurements of Bullen et al. [71]

Here, the turbulence intensity is not diminished to zero or values close to zero as calculated by the ω-based turbulence models. In addition, the kε turbulence model strongly overestimates the turbulence intensity in the upstream region close to the contraction. A reason might be the contracting flow towards the center, causing adverse pressure gradients in the vicinity of the contraction wall. Modeling adverse pressure gradients is one of the main flaws of the kε turbulence model, according to Rodriguez [30] and Wilcox [31].
In conclusion, the kω-SST turbulence model also shows the best agreement compared with the (scarce) measurement data for turbulence quantities. Therefore, the use of the kω-SST turbulence model is finally justified.

Since the setup of the numerical model is complete, a mesh independence study can be conducted to prove the convergence of the simulation results by refining the mesh.
This study is performed, according to Celik et al. [42] with three different meshes: a coarse mesh with 4 088 879 elements, an intermediate mesh with 9 428 829 elements, and a fine mesh with 21 392 571 elements. The intermediate mesh is obtained by applying the previously described meshing settings. In contrast, the coarse mesh is obtained by setting the element edge length to 4.5 mm for the main mesh and 0.75 mm for the contraction wall mesh, whereas the fine mesh is obtained by setting 2 mm for the main mesh and 0.33 mm for the contraction wall mesh. This gives a mesh refinement ratio S for the intermediate to the fine mesh $S_{if} = 1.31$ and for the coarse to intermediate mesh $S_{ci} = 1.32$ according to Celik et al. [42].
The axial pressure profile along the centerline for the coarse (dotted line), intermediate, and fine mesh (dashed line) is shown in Fig. 3.13. Here, a mass flow rate $\dot{m}$ of 20.06 kg/s at an area ratio σ of 0.184 is chosen. The maximum deviation between the pressure profiles of the fine and intermediate mesh amounts to 2% at maximum. In contrast, the maximum deviation between the pressure profile

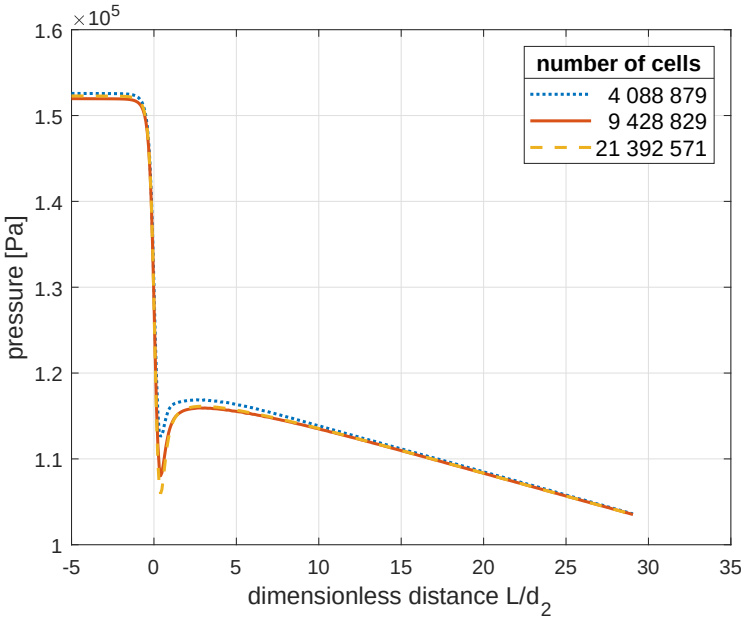

Figure 3.13: Profile of the simulated axial pressure along the centerline for three different meshes

of the intermediate and coarse mesh gives 4%. In both cases, the maximum deviation is obtained for the lowest pressure value downstream of the contraction within the vena contracta. Downstream of the vena contracta, the deviation between the intermediate mesh and the fine mesh pressure profile is negligible in good approximation.

The values of the estimation of the discretization uncertainty are given in Tab. 3.4. β_0, β_1, β_2 and c_P are selected as the relevant key variables f for the sudden contraction the uncertainty estimation is applied to. Index f represents the fine mesh, int the intermediate, and c the coarse mesh.

Table 3.4: Calculation of the discretization uncertainty

	β_0	β_1	β_2	c_P
f_f [1]	2.1865	1.0173	1.0301	1.7885
f_{int} [1]	2.1467	1.017	1.0286	1.8223
f_c [1]	2.0924	1.0168	1.0226	1.8713
o [1]	1.0539	0.6429	5.0416	1.2728
$f_{ext,ci}$ [1]	2.3058	1.0183	1.0306	1.7072
$f_{ext,if}$ [1]	2.3058	1.0188	1.0306	1.7072
$e_{a,if}$ [%]	1.82	0.03	0.14	1.89
$e_{ext,if}$ [%]	5.18	0.14	0.05	4.76
GCI_{if} [%]	6.82	0.18	0.06	5.68

Table 3.4 shows the apparent order o of the calculation of β_1 and β_2 differing significantly from the formal order of the solution scheme, which is two, as discussed in Chap. 2. But as previously explained, the converse must not necessarily indicate unsatisfactory calculations shown by the following

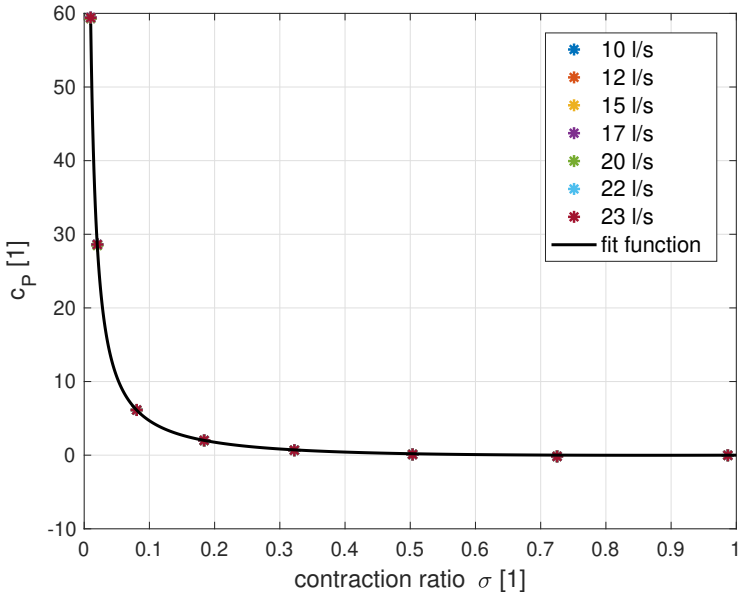

Figure 3.14: Pressure coefficient c_P versus contraction area ratio σ for all investigated flow rates, together with the fit function

calculation results. With the values of the fine and the intermediate mesh, the extrapolated value of the key variables $f_{ext,if}$ is obtained. With reference to Celik et al. [42], the extrapolated key variables obtained with the fine and intermediate mesh $f_{ext,if}$ shall be almost equal to the extrapolated key variables obtained with the intermediate and coarse mesh $f_{ext,ci}$. In the present case, the agreement between $f_{ext,if}$ and $f_{ext,ci}$ is excellent. However, the approximated relative error between the fine and the intermediate mesh results $e_{a,if}$ amounts to 1.9% at maximum for c_P. In contrast, the error for the momentum coefficients is less than 0.2% except for β_0, which is 1.8%. The approximated relative error to the extrapolated result $e_{ext,if}$ exhibits a maximum of 5.18% for β_0, but a minimum for β_2 with 0.05%. As a result, the GCI is also highest for β_0 with 6.8%. However, calculating the pressure drop over a sudden contraction with the extrapolated values and the intermediate mesh values as per Eq. (3.13) or Eq. (3.16) results in a deviation that is lower than the calculated measurement uncertainty (detailed in Chap. 3.1.3). Therefore, the mesh is considered sufficiently fine.

Eventually, the numerical simulation can be used as a verified base for further numerical investigations since it shows a high agreement with various experimental references.

With the validated and verified numerical model, the momentum coefficients β and the pressure coefficient c_P can be determined for a set of different contraction ratios σ and flow rates Q. According to the experimental investigations, the diameter of the upstream pipe d_1 is chosen at 140.92 mm for the simulation domain. The downstream pipe diameter d_2 is variable and defined as 14, 20, 40, 60.43, 80, 100, 120, and 140 mm, corresponding to the contraction ratios $\sigma = 0.010$, 0.020, 0.081, 0.184, 0.322, 0.504, 0.725, and 0.987. For every contraction ratio, seven different volumetric flow rates (Tab. 3.1) are investigated to obtain the dependency of the required coefficients as functions of the contraction ratio σ and flow rate Q.

Figure 3.14 shows the simulation results of the pressure coefficient c_P over the contraction ratio σ. It appears that the pressure coefficient c_P is no function of the flow rate Q since the results of c_P for

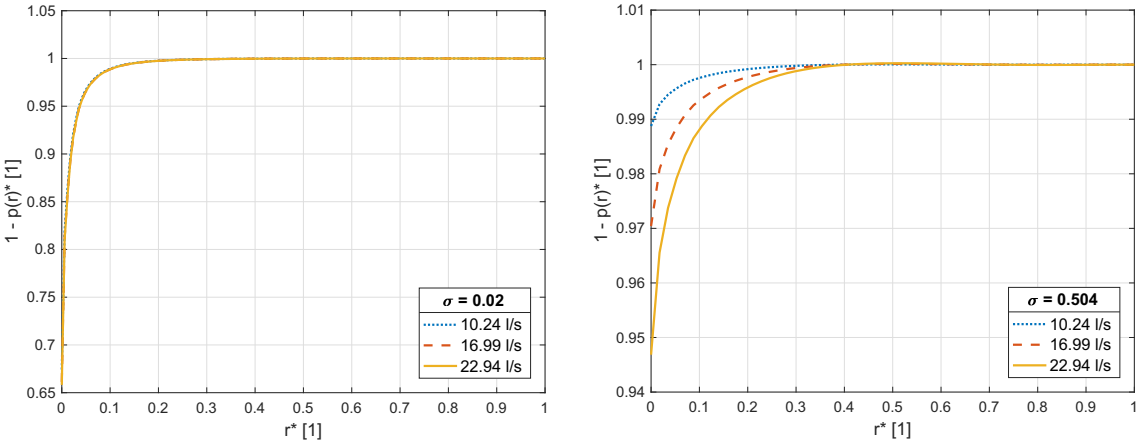

Figure 3.15: Radial distribution of the normalized effective pressure $p(r)^*$ over the contraction wall for different contraction ratios σ and flow rates Q versus the normalized contraction wall radius r^*

different flow rates lie on top of each other. However, a function in the shape of

$$c_P\left(\sigma\right) \;=\; -1.9 + 0.65\,\frac{1}{\sigma} + 1.25\,\sigma. \tag{3.50}$$

describes the dependency of c_P on the contraction ratio extremely well. For contraction ratios approaching zero, the fit function, as per Eq. (3.50), asymptotically approaches infinity. Contrasting, for increasing contraction ratios, c_P approaches zero but slightly undercuts the zero line for $\sigma > 0.5$. For $\sigma \leq 0.5$, c_P gives positive values, which means the inlet pressure p_1 is larger than the counteracting pressure p_R, see Eq. (3.12). This effect increases for smaller contraction ratios. Inversely, the pressure coefficient is negative for contraction ratios $0.5 < \sigma < 1$, which means the inlet pressure p_1 is lower than p_R.

In addition, the numerical simulation also indicates that for contraction ratios $\sigma > 0.75$, the dead water zone extends to the whole contraction wall, as shown in Fig. 3.5. This means the radial flow is not touching the contraction wall diminishing the effective pressure. For $\sigma = 1$, which represents a uniform pipe, Eq. (3.50) gives zero. Therefore, the discussed findings indicate that the stagnation pressure in front of a sudden contraction is highly dependent on the contraction ratio σ. Figure 3.15 additionally shows the radial distribution of the dimensionless effective pressure $p(r)^*$ over the dimensionless contraction wall radius r^* for two more contraction ratios σ. For both area ratios, the pressure starts to decrease at a similar r^* independent of the volume flow rate. In contrast, the minimum pressure at the contraction edge for $\sigma = 0.504$ strongly depends on the contraction ratio. But the lowest effective pressure appears to be no function of the volume flow rate for $\sigma = 0.02$.

Momentum coefficients represent the velocity distribution over a specific plane and, therefore, quantify the velocity profile for every cross-section upstream and downstream of the contraction. The axial distribution of the momentum coefficient for different area ratios σ over the dimensionless distance to the contraction L/d_1 is shown in Fig. 3.16. In the background, the velocity distribution is visualized with the color mapping quantifying the magnitude of the velocity for $\sigma = 0.184$ as a representative example. The dead water zone and the recirculation zone outside of the vena contracta are shown by blank areas.

Upstream of the sudden contraction, the momentum coefficients β all amount to $\simeq 1.03$, representing fully turbulent flow. The constant profiles indicate a fully developed flow with a homogeneous velocity distribution over the cross-section. Around an upstream distance to the contraction plane of

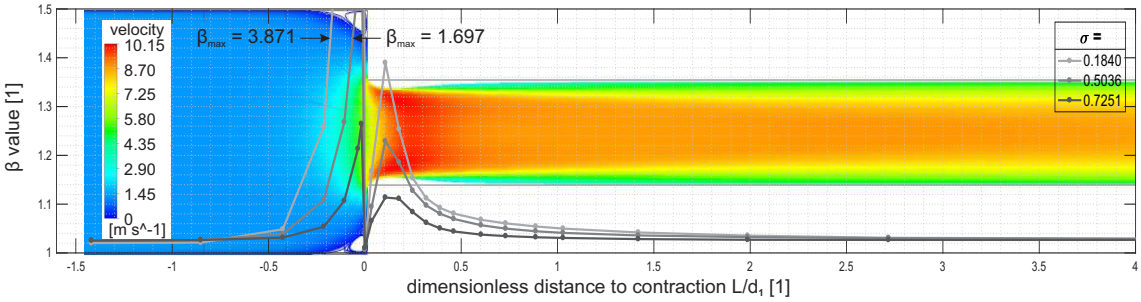

Figure 3.16: Profile of the momentum coefficient β over the non-dimensionalized distance to the contraction $L/d1$ with the velocity distribution and the magnitude of the velocity of the center cross-sectional plane

$0.5d_1$, the upstream momentum coefficient β sharply increases to its maximum value near the contraction plane caused by the radial flow towards the pipe's center. Directly in the contraction plane, the momentum coefficient is equal to unity, which is in line with the experimental findings of Durst and Loy [59] for laminar flow. The downstream momentum coefficient reaches its maximum value shortly downstream of the contraction plane at different distances to the contraction, depending on the contraction ratio σ. This maximum is caused by the vena contracta since the velocity is zero in the dead water zones at the pipe's wall. To satisfy the principle of the conservation of mass, the velocity must increase in the center of the pipe. Downstream of the vena contracta, the momentum coefficients are re-approaching values close to fully turbulent ones but slightly differ from each other. This is due to the different downstream pipe diameters causing slightly variant velocity profiles. No vena contracta is found for a contraction ratio σ of 0.987.

Evaluating the integral momentum balance for the defined control volume, the momentum coefficients in the inflow and the outflow cross-sections have to be obtained. In both cross-sections, $\beta = 1.03$ is chosen in good accordance with the numerical simulation, which corresponds to the velocity profile of a fully developed turbulent pipe flow, see Refs. [73, 10, 58].

Now that the parametrization for the pressure coefficient c_P (Eq. (3.50)) is obtained and the momentum coefficient values $\beta_1 = \beta_2 = 1.03$ are numerically determined, the presented momentum-based approach as per Eq. (3.13) is complete. With Eq. (3.50) and the findings for the momentum coefficients introduced in Eq. (3.13), the final formula for the first approach gives:

$$\Delta p_I = \varrho \frac{Q^2}{{A_2}^2} \left(0.7050 + 0.245 \frac{A_2}{A_1} - 1.575 \frac{A_2^2}{A_1^2} + 0.625 \frac{A_2^3}{A_1^3} \right) \tag{3.51}$$

The momentum-based loss coefficient of the first approach $K_{M,I}$ is represented by the bracketed term of Eq. (3.51), yielding

$$K_{M,I} = 0.7050 + 0.245 \frac{A_2}{A_1} - 1.575 \frac{A_2^2}{A_1^2} + 0.625 \frac{A_2^3}{A_1^3} \tag{3.52}$$

Concluding, $K_{M,I}$ represents the physically derived momentum-based pressure loss coefficient. In contrast to pressure loss formulations provided by the literature, $K_{M,I}$ is purely based on physical correlations but not on empirical results.

As shown in Fig. 3.16, the momentum coefficient at the contraction plane β_{cont} appears to be nearly independent of the investigated flow rates. For the present contraction ratio $\sigma = 0.184$, the momentum

coefficient amounts to 1.008. The spread of the momentum coefficient β_{cont} for all investigated flow rates Q is less than 0.5% at every investigated contraction ratio σ. However, assuming $\beta_{cont} = 1.01$ results in a maximum deviation from the pressure drop calculated with $\beta_{cont} = 1.008$ of 0.3%, which is a negligibly small deviation. Therefore, β_{cont} can be assumed 1.01 in a good approximation. In contrast, the deviation increases to 1.2%, setting β_{cont} equal to unity, which shows the sensitivity of the momentum balance to the velocity distribution. The numerical results for β_{cont} are justified by the findings of Durst and Loy [59]. The authors' experimental investigation of laminar flow also yields a velocity profile in the contraction plane corresponding to values of β very close to unity. The reason is that no flow length is present for a velocity profile to develop in the contraction plane.
The momentum coefficient β_0 is computed by considering the axial flow through the front surface and the radial flow through the shell surface into the control volume. Therefore, the computation of β_0 is performed via:

$$\beta_0 = \frac{\int\limits_{A_{front}} v_1^2 \, dA + \int\limits_{A_{shell}} v_{rad}^2 \, dA}{\frac{Q^2}{A_1^2} \, A_1}, \tag{3.53}$$

where A_{front} is the control volume's front surface, A_{shell} the shell surface, and v_{rad} the radial velocity at the shell surface. As mentioned above, the flow entering the control volume must cross the pipe's cross-section as well, so the denominator is related to the cross-section of the pipe A_1 and the average velocity Q/A_1. The nominator comprises the axial velocity integral over the front surface and the radial velocity integral over the shell surface, see control volume in Fig. 3.6. The computation is performed with the aid of numerical simulations to obtain an applicable value for β_0.

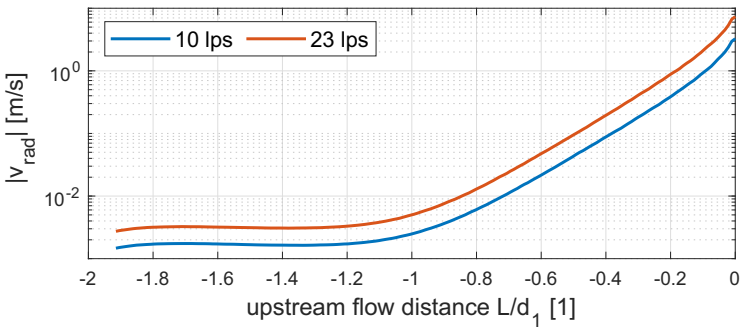

Figure 3.17: Radial velocity along the shell surface of the cylindric control volume versus the distance to the contraction

The control volume of the second approach also represents the computation domain of β_0 and extends up to an upstream distance to the contraction, where the flow is not yet influenced by the contraction itself. For the present investigation, this distance is at approximately $1.2d_1$ upstream of the contraction. From this distance, the radial velocity profile starts to increase due to the contracting flow. The radial velocity along an axial line at a radius of 30.22 mm ($d_2/2$) versus the flow distance up to the contraction is shown in Fig. 3.17 for flow rates of 10 l/s and 23 l/s. The distance of the beginning increase of v_{rad} appears to be independent of the flow rate around $1.2d_1$. The only difference between the two graphs is an offset with an almost equal gap on a logarithmic scale. Figure 3.18 shows the simulation results of β_0 together with the mathematical function on a semi-logarithmic scale. Analogous to c_P, the momentum coefficient β_0 is not dependent on the flow rate Q. The dependency of the

contraction ratio σ is well described by the mathematical function

$$\beta_0(\sigma) = -0.1894 + 0.3429\,\frac{1}{\sigma} + 0.8769\,\sigma, \tag{3.54}$$

which is valid for sudden contraction configurations at turbulent flow. The fitted function Eq. (3.54) asymptotically approaches infinity for contraction ratios approaching zero. With an increasing contraction ratio the momentum coefficient decreases, reaching values slightly lower than unity for $\sigma > 0.4$ and re-approaching unity for contraction ratios $\sigma > 0.75$. For $\sigma = 1$, which represents a uniform pipe, β_0 is 1.03. This is in good agreement with the computed values of β_2, discussed in the preceding paragraphs.

With the mathematical function for the momentum coefficient β_0 Eq. (3.54) and the momentum coefficient value $\beta_{cont} = 1.01$ determined numerically, the presented approach with the integral momentum balance for the alternative control volume as per Eq. (3.16) is completed. This alternative approach can be applied to calculate the pressure drop caused by a sudden contraction as well. Using Eq. (3.54)

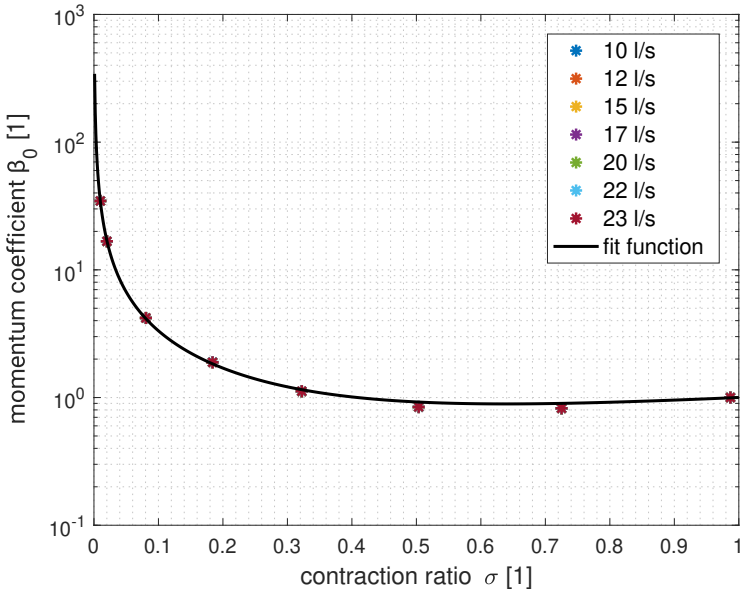

Figure 3.18: momentum coefficient β_0 versus contraction ratio

into Eq. (3.16), the final formula of the second approach gives:

$$\Delta p_{II} = \varrho \frac{Q^2}{{A_2}^2} \left(0.6671 + 0.1894 \frac{A_2}{A_1} - 0.8769 \frac{A_2^2}{A_1^2} \right) \tag{3.55}$$

In consequence, the momentum-based loss coefficient $K_{M,II}$ as per Eq. (3.55) results

$$K_{M,II} = 0.6671 + 0.1894 \frac{A_2}{A_1} - 0.8769 \frac{A_2^2}{A_1^2}. \tag{3.56}$$

3.1.5 Results

Finally, the proposed momentum-based approaches require validation against the obtained experimental results and literature numbers. Since the theory is also applied to locations where the downstream velocity profile is not fully re-developed, the momentum coefficient β_2 needs to be adapted for the first approach.

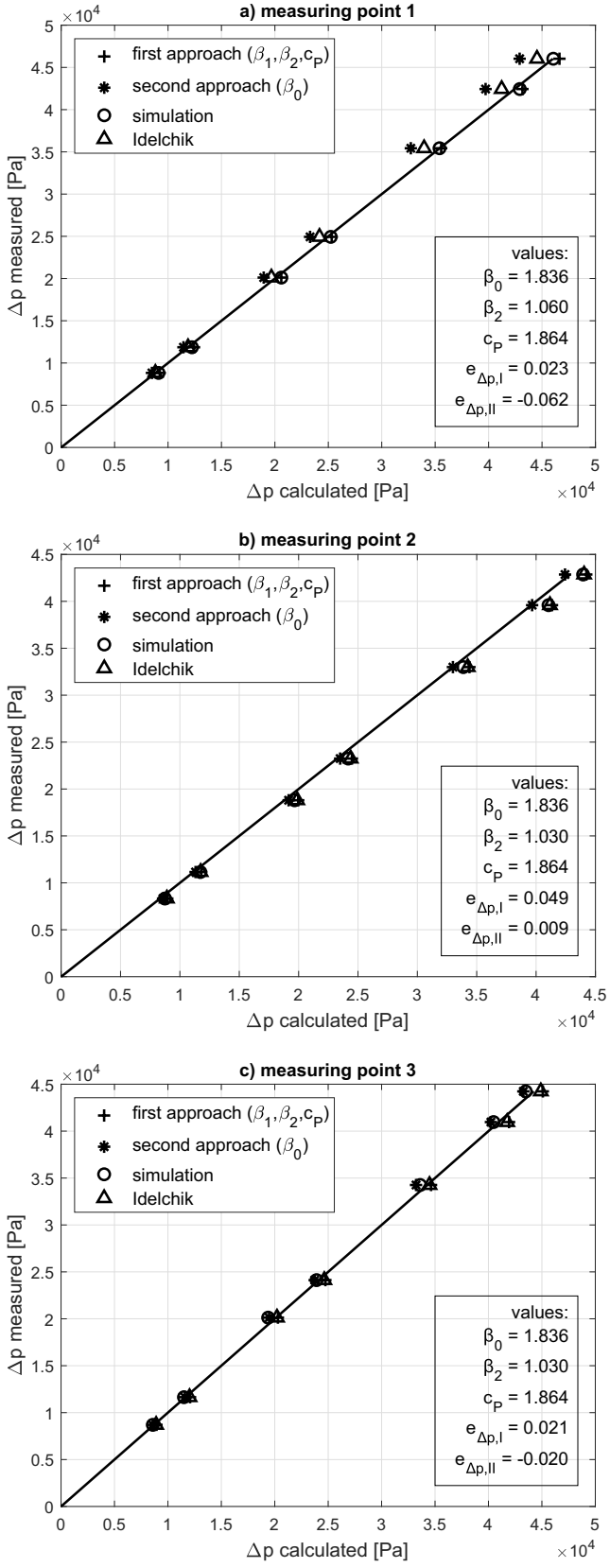

Figure 3.19: 45-degree plot of the results for every measuring position

Thus, Fig. 3.19 shows the results of the Bernoulli principle with the Idelchik sudden loss coefficient k_{Idel}, the momentum-based, and the simulated differential pressure represented by markers in the 45-degree plots for all measuring positions and investigated flow rates Q (see Tab. 3.1). The vertical axis represents the measured differential pressure and the horizontal axis represents the calculated or simulated one. Equal values on both axes are indicated by lines, visualizing the gradients of unity, which means a zero deviation. Hence, the closer results match the lines, the more accurately the calculated or simulated differential pressure represents the measured pressure. The results of the first momentum approach are obtained by applying Eq. (3.51), the second momentum approach by Eq. (3.55), and the Bernoulli principle by Eq. (3.5) with the Idelchik loss coefficient K_{Idel} as per Eq. (3.58). The text boxes in every figure indicate the computed values of β_0, β_2, c_P, and the average deviation $e_{\Delta p}$ for the differential pressures of both momentum-based approaches, calculated as follows:

$$e_{\Delta p} = 1 - \frac{1}{n} \sum_{i=1}^{n} \frac{\Delta p_{meas_i}}{\Delta p_{calc_i}} \tag{3.57}$$

Here, Δp_{meas} is the measured and Δp_{calc} the calculated differential pressure. To calculate the deviation of the simulated pressure drop $e_{\Delta p,sim}$ by Eq. (3.57), Δp_{calc} can be substituted by Δp_{sim}. Figure 3.19 shows that the general deviation of the proposed approaches to the measurements is within 5%, except for the second momentum approach (Eq. (3.55)) at the first measuring point. The problem lies in the second momentum-based approach, solely considering the upstream flow pattern but not the downstream flow conditions. Therefore, a high correlation to the measured results and references is only obtained for regions of (almost) fully developed flow downstream of the contraction where the momentum coefficient is closer to unity, as specified for β_{cont}. This is the case for the second and third measuring points since the downstream momentum coefficient β_2 amounts to ≈ 1.03. The agreement between the first momentum approach and the established Bernoulli principle with the Idelchick correction coefficient K_{Idel} is excellent for the second and third measuring points. For the first measuring point, the agreement of the first momentum approach to the simulation and measurement results is excellent. It proves that this approach is also applicable to non-developed flow regions since the downstream velocity distribution is considered appropriately. Eventually, the comparison shows that the presented momentum-based approaches correlate highly with the measurements and the reference. Figure 3.19 also shows the results of the Bernoulli principle together with the sudden loss coefficient of Idelchik k_{Idel}, given in Ref. [55]. In accordance with the momentum approaches as per Eqs. (3.51) and (3.55), the Idelchik sudden loss coefficient k_{Idel} is formulated in the shape of the pressure loss coefficient K_{Idel} as

$$K_{Idel} = 1 - \frac{A_2^2}{A_1^2} + \underbrace{\frac{1}{2}\left(1 - \frac{A_2}{A_1}\right)^{\frac{3}{4}}}_{k_{Idel}}. \tag{3.58}$$

The agreement between the Bernoulli principle with the loss coefficient of Idelchik and the measured data is very high. But Idelchik determined the parametrization of the loss coefficient semi-experimentally by fitting a mathematical function to various data sets. In contrast, the presented momentum-based approaches are based solely on physics without requiring empirically determined correction coefficients.

Figure 3.20 shows the pressure loss coefficients K_M and K_{Idel} plus the simulated one K_{sim} over the contraction ratio σ on a semi-logarithmic scale. The simulated pressure loss coefficient K_{sim} is calculated by flipping Eq. (3.51) or Eq. (3.55) to the bracketed term, representing K_M and introducing

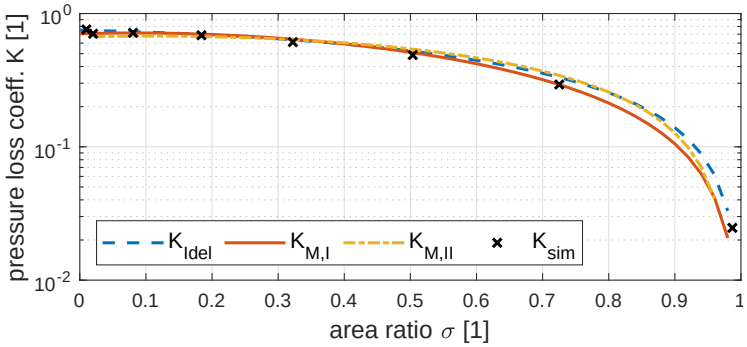

Figure 3.20: Pressure loss coefficient K versus the area ratio σ according to Idelchik K_{Idel}, the momentum-based approaches K_M, and the numerical result K_{sim}

the simulated differential pressure obtained in fully developed flow regions minus frictional pressure losses p_F, see Eq. (3.17). Consequently, the results of K_{sim} are no function of the flow rate Q. Over the whole range of investigated contraction ratios, the deviation between $K_{M,I}$ and K_{Idel} amounts to 5.5% at maximum. Just for the largest contraction ratio $\sigma = 0.987$, the deviation of $K_{M,I}$ and $K_{M,II}$ increases significantly since the loss coefficients approach values close to zero. The loss coefficient $K_{M,II}$ deviates around 7% at maximum from K_{Idel} but up to 10% for $\sigma = 0.01$ and $\sigma = 0.02$. Contraction ratios of 0.01, 0.02, and 0.987 solely represent academic cases since these contraction ratios are of no practical use. Additionally, the frictional pressure loss p_F outnumbers the pressure drop Δp by far for very large contraction ratios. Therefore, the results for contraction area ratios larger than 0.504 are highly dependent on friction but less dependent on the pressure drop induced by the contraction. Figure 3.20 shows a high correlation between the Idelchik pressure loss coefficient K_{Idel} and the numerical result of the pressure loss coefficient K_{sim}. Nevertheless, the correlation between the momentum-based pressure loss coefficients K_M and K_{sim} is generally higher, except for extreme contraction ratios $\sigma = 0.01$ and $\sigma = 0.987$. This speaks for the validity of the proposed method of applying the momentum balance with computed physical coefficients. Therefore, the present investigation represents the physical validation for the empirical Idelchik coefficient k_{Idel}.

Figures 3.19 and 3.20 indicate that the calculation results correlate highly with the experimental data. In addition, a very high correlation with the classical formulation of Idelchik is achieved as well. In summary, the applicability of the momentum-based approach calculating the pressure drop of a sudden contraction is proved.

3.2 The Sudden Expansion

The relevant findings discussed in this section have been presented at the ASME 2021 Fluids Engineering Division Summer Meeting, August 10-12 2021 and published in the Proceedings of the ASME 2021 Fluids Engineering Division Summer Meeting. The manuscript can be found at https://doi.org/10.1115/FEDSM2021-65703.

3.2.1 Retrospective / State of the Art

With the phenomena of a contracting flow investigated and the momentum balance successfully applied to the flow through a sudden contraction, the expanding flow of a sudden expansion is now investigated in detail. In scientific history, the pressure change due to a sudden expansion or enlargement of a cross-section is also called shock loss (Idelchik [18]). It originates from the mathematical solution that is derived by applying the theory of an inelastic shock to the sudden expansion. This derivation dates back to the Frenchman Borda, who published the theory as a part of a more involved problem of the filling of submerged vessels in 1766, see Ref. [47]. In the Version of Lazare Carnot, Borda's theory is named the Borda-Carnot equation, presented in the following.
Assuming a constant pressure and velocity distribution over the cross-sections, the Energy conservation in the shape of the Bernoulli principle as per Eq. (1.54) yields

$$g\,z_1 + \frac{1}{\varrho}p_1 + \frac{1}{2}v_1^2 = g\,z_2 + \frac{1}{\varrho}p_2 + \frac{\varrho}{2}v_2^2 \tag{3.59}$$

for a fluid particle on a streamline. Here, index 1 indicates the expansion plane and index 2 the downstream region. Losses due to friction in the downstream pipe are neglected since Eq. (3.59) is set up in the region where flow is not re-attached to the wall. Since the considered region is of short reach, the height difference $z_1 - z_2$ is usually neglected. This means that even for a vertically orientated expansion the other pressure shares involved have a superior impact. However, for a horizontally orientated sudden expansion $z_1 = z_2$ applies, so Eq. (3.59) gives

$$p_2 - p_1 = \frac{\varrho}{2}\left(v_1^2 - v_2^2\right) \tag{3.60}$$

For flows through increasing cross-sections, the downstream pressure p_2 is higher than the pressure in the expansion plane p_1. It turns out that Eq. (3.60) can not appropriately predict the pressure change of a flow through a sudden expansion. Therefore, an additional loss term p_{loss} is introduced to Eq. (3.59), according to Weisbach [19]

$$p_1 + \frac{\varrho}{2}v_1^2 = p_2 + \frac{\varrho}{2}v_2^2 + p_{loss} \tag{3.61}$$

Solving Eq. (3.61) for the pressure loss p_{loss} gives

$$p_{loss} = p_1 - p_2 + \frac{\varrho}{2}v_1^2 - \frac{\varrho}{2}v_2^2. \tag{3.62}$$

To substitute the unknown pressure loss p_{loss} in Eq. (3.62), the stationary momentum balance is applied to a control volume in the downstream pipe, starting at the expansion plane and reaching downstream up to that point where the pressure p_2 reaches the maximum value. Again, losses due to friction are neglected. The derivation of the momentum balance is given in detail in the following chapter. However, the result as obtained by Borda [47] in the version of Lazare Carnot [48] is known

as the Borda-Carnot equation:

$$p_{loss} = \varrho\, v_2^2 - \varrho\, v_2^2\, \frac{A_2}{A_1} + \frac{\varrho}{2} v_2^2 \frac{A_2^2}{A_1^2} - \frac{\varrho}{2} v_2^2 = \frac{\varrho}{2} v_2^2 \left(\frac{A_2}{A_1} - 1 \right)^2 . \tag{3.63}$$

Since the velocity v_1 is higher than v_2, the bracketed term gives a positive value if arranged as per Eq. (3.63).
It is important to mention that Eq. (3.63) yields the only sudden loss coefficient $k = (A_2/A_1 - 1)^2$ derived physically. In contrast, the loss coefficient of any other hydraulic structure is obtained experimentally. As a marginal note, it appears like irony of history that Borda leveraged the Bernoulli principle since it is discussed and improved in a memoir of Borda, according to Gillispie and Pisano [74, p. 98]. However, to transform the sudden loss coefficient k into a loss coefficient K, achieving compliance with the momentum equation, Eq. (3.63) is used in Eq. (3.62) and solved for $p_2 - p_1$ giving:

$$p_2 - p_1 = \varrho\, v_2^2 \left(\frac{A_2}{A_1} - 1 \right) . \tag{3.64}$$

Here, the loss coefficient K is represented by the bracketed term. But the same result, as given by Eq. (3.64), can be obtained by applying the (idealized) momentum balance straightforwardly. In the following chapter, it is shown that solely applying the momentum balance also yields Eq. (3.64) but with fewer calculation steps.

Despite its physically conclusive derivation, some investigations reveal a gap between the results obtained with the Borda-Carnot equation and experimental results.
Bear [75] conducted experiments on the pressure change of flows through a vertically orientated sudden expansion. The author aims to assess to what extent the Borda-Carnot equation is capable of predicting the energy loss (the historical term 'energy loss' physically means energy dissipation). The Borda-Carnot equation (Eq. (3.63)) is based on the assumption that the energy loss induced by the change of the velocity from v_1 to v_2 equals the energy loss of an inelastic shock. This assumption presupposes that the pressure over the expansion wall p_R is evenly distributed and equal to p_1. For the evaluation of the experimental results, Baer defines the threshold the experimental results must lie within. The upper limit represents the term obtained by solely applying the Bernoulli principle $(v_1^2 - v_2^2)$ as the loss if the excess energy is completely dissipated to turbulence. The lower limit represents the Borda-Carnot loss $(v_1 - v_2)^2$ as an ideal inelastic shock. The experimental results of Baer all lie in between both limits. It turns out that the results approach the upper limit the lower the velocities and the smaller the expansion area ratio. But for higher velocities and larger expansion area ratios, the obtained loss approaches the lower limit (Borda-Carnot loss). The author concludes that for velocities $v_1 > 3\ m/s$ and expansion area ratios $\sigma_{inv} > 1/3$, the Borda-Carnot loss predicts the actual loss with sufficient accuracy.

In 1913, Archer [76] investigated the pressure change of flows through a sudden expansion in circular pipes for multiple area ratios. The experimental results show that the maximum pressure p_2 is reached around $7d_2$ downstream of the expansion depending on the area ratio. This point represents the location where the pressure is recovered to its maximum. With increasing flow length, the pressure is solely decreasing due to pipe friction. Archer presented a formula to calculate the distance between the expansion and the point of maximum p_2. The author's results also show that for small expansion area ratios A_1/A_2, the minimum pressure is reached shortly downstream of the expansion. Just for

a large area ratio of approx. 0.7, the pressure recovery starts immediately after the expansion. In addition, Archer proposes a modified formula for the loss term given by the Borda-Carnot equation (Eq. (3.63)) that is based on the author's measurement results.

$$p_{loss} = \frac{\varrho}{2}\, 1.098 \left(\frac{v_2\, A_2}{A_1}\right)^{1.919} \left(1 - \frac{A_1}{A_2}\right)^{1.919} \tag{3.65}$$

This relation can also be expressed by introducing an additional correction coefficient ζ into Eq. (3.63)

$$p_{loss} = \frac{\varrho}{2} v_2^2\, \zeta \left(\frac{A_2}{A_1} - 1\right)^2 \tag{3.66}$$

For the results of Archer, ζ is a function of the velocity and the expansion area ratio $\sigma_{inv} = A_1/A_2$. It appears that the correlation between the pressure loss according to Eq. (3.65) of Archer [76] and the results of other investigations is very low for small expansion area ratios. But for expansion area ratios $A_1/A_2 \geq 0.3$, the correlation increases to nearly unity. Archer recognized that the Borda-Carnot equation underrates the pressure change for small expansion area ratios σ_{inv}. But Archer's equation overrates the pressure change for small σ_{inv} compared with the simulation results, which are explained in more detail in the following chapters.
The experimental results of Gibson [77] also show a deviation from the classical Borda-Carnot loss of up to 11% for high flow rates. The author's results indicate that the sudden loss coefficient k is dependent on the flow rate Q. Gibson [78] proposes the following formula for the coefficient ζ, which is valid for $0.08 \geq \sigma_{inv} \leq 0.5$ and an upstream pipe diameter d_1 between 12.7 mm (0.5 in) and 152.4 mm (6 in)

$$p_{loss} = \frac{\varrho}{2} v_2^2 \underbrace{\frac{102.5 + 0.25\frac{A_2}{A_1} - 2d_1}{100}}_{\zeta} \left(\frac{A_2}{A_1} - 1\right)^2 \tag{3.67}$$

Applying Eq. (3.67) as the pressure loss term, the obtained results deviate 4% at maximum from Gibson's experimental results within the given scope.
In contrast to the findings of Gibson [77, 78], Kays [49] obtained a sudden loss coefficient that appears to be no function of the flow rate in the fully turbulent flow regime. For the investigated expansion area ratio, Kays' results confirm the Borda-Carnot relation in good approximation.

Such divergent investigations on the applicability of the Borda-Carnot equation to experiments provoked Schütt [79] to conduct experiments in 1929. The author raised doubts about introducing different correction coefficients ζ to the Borda-Carnot loss, see Eq. (3.66). For the experiments, Schütt uses a straight horizontal pipe with an inserted nozzle to contract the flow continuously. After a short straight section at the end of the nozzle, representing the sudden expansion, the contracted flow is released into the pipe. The author emphasizes the special shape of the nozzle to avoid a vena contracta to develop. But no proof is given that no vena contracta is present. In addition, Schütt solely investigates medium expansion area ratios. The obtained experimental results agree very well with the prediction of the Borda-Carnot equation. Further, the author supposes that the introduction of correction coefficients ζ originates from downstream pressure measurements in regions where the pressure is not recovered to the full extent. According to Schütt, this is the case with the experiments of Baer [75]. The investigation also indicates that the assumption of the reacting pressure p_R being equal to p_1 is valid.

Lipstein [80] investigated the pressure change of air flows passing a circular sudden expansion. Here, the sudden expansion is shaped as a pipe insert with a continuous rounded contraction at the inlet side and a sudden area change at the outlet side. The axial wall pressure distribution exhibits a minimum value shortly downstream of the area change, followed by a rise toward the maximum pressure. This characteristic pressure distribution is observed for all investigated area ratios. The author compares the maximum pressure with the Borda-Carnot prediction, see Eq. (3.63), obtaining a high correlation for small expansion area ratios but a steady rising discrepancy for expansion area ratios approaching unity. In addition, Lipstein also measured the radial velocity distribution at different distances downstream of the area change. For every investigated expansion area ratio, the author obtains a flat velocity profile in the downstream pipe's core flow bounded by the radius of the small pipe in good approximation. The persistence of the flat profile strongly depends on the expansion area ratio σ_{inv} since it can be observed at large distances downstream for small σ_{inv} but vanishes shortly downstream for high σ_{inv}. The author's results suggest that the maximum reverse flow velocity is reached in the region where the axial pressure gradient is maximal but not directly downstream of the sudden expansion.

Chaturvedi [81] investigated the flow field downstream of an area change with different expansion angles using hot wires. The investigation confirms previous measurement results of Lipstein [80] that the flow entering the larger pipe forms a core with a flat velocity profile, which means the radial velocity distribution is flat-shaped in the core. But this core dissipates within a few pipe diameters downstream of the expansion. The author's investigation also reveals that after a downstream flow distance of $10d_2$, the velocity distribution remains constant. In contrast, the radial pressure distribution is found to be constant at a flow distance of $6d_2$. This flow distance is not significantly affected by the expansion angle. In addition to this, Chaturvedi identified the pressure profile over the cross-section of the smaller pipe in the expansion plane and over the expansion wall to be flat. As a result, assuming the pressure p_1 to be homogeneously distributed over the inlet cross-section A_1 and the expansion wall $A_2 - A_1$ is confirmed by various investigations (see Refs. [82, 79, 81]).
At this point, a short evaluation of the radial velocity profile according to the performed numerical simulations presented in the following shall be given. The numerical simulations show that the radial velocity distribution in the core flow is not flat but in the shape of a turbulent velocity profile. It appears that it was not possible to resolve the core flow in such resolution and accuracy as to capture the small deviation from a flat profile with former measurement techniques.

Kays [49] considered the non-uniform velocity distribution over the cross-sections by introducing momentum coefficients to the Borda-Carnot equation. The momentum coefficient starts at 1.07 for $Re = 2 \cdot 10^3$ and decreases to 1.04 for $Re = 2 \cdot 10^4$. For momentum coefficients equal to unity, the author's loss coefficient yields the Borda-Carnot relation. It is shown in the following, that for small area ratios the momentum coefficient is of high importance to the predicted pressure change.

Idelchik [18] also considers the impact of a non-uniform velocity distribution on the pressure change. According to the author, a non-uniform velocity distribution increases the pressure loss of flows through sudden expansions. Idelchik considers the additional loss in a loss coefficient dependent on the area ratio and the velocity profile. The impact of the velocity profile is described analytically by coefficients being calculated from representative exponential-law velocity profiles. In addition, Idelchik states that the flow reattaches after 8 to 10 hydraulic (downstream) diameters downstream of the expansion.

Teyssandier and Wilson [83] propose to apply a momentum-based approach for the prediction of the axial downstream pressure distribution and the reattachment length, obtaining a system of ordinary differential equations. The authors' results exhibit a good correlation with the experiments of Lipstein [80] and Chaturvedi [81]. Teyssandier's and Wilson's investigation also shows that the pressure recovery is not completed at the point of reattachment of the flow but several more diameters downstream of that point. Their analysis assumes the wall roughness negligibly affects the pressure gradient up to the reattachment point and, therefore, the wall roughness affects the reattachment length insignificantly. According to Teyssandier and Wilson [83], the reattachment length is strongly dependent on the area ratio reaching from $4.4d_2$ for large area ratios up to $8d_2$ for an expansion area ratio of 0.3. The authors also show that the minimum pressure is reached just slightly downstream of the sudden expansion. But the difference between the minimum pressure to the pressure in the expansion plane p_1 is very small, especially compared with the pressure recovery to the maximum pressure p_2.

Papadopoulos and Ötügen [84] raise doubts about the validity of the Borda-Carnot equation applied to planar (large width-to-height ratio) sudden expansions. It is shown that the predicted loss coefficient deviates strongly from the one obtained by Papadopoulos and Ötügen but also from measurement results for planar expansions of other authors. The authors' experimental results lead to a different formulation of the loss coefficient for such expansions. However, the applicability of the Borda-Carnot equation for axisymmetric and four-sided expansions is confirmed.

As far as the author's research, solely Archer [76], Gibson [78], and Miller [85] propose sudden loss coefficients k for circular sudden expansions that differ from the Borda-Carnot relation. Miller's data is originally given in a diagram and presented in Fig. 3.21 jointly with the data given by Archer [76] (Eq. (3.65)), Gibson [77, 78], Kays [49], and the Borda-Carnot equation Eq. (3.63).

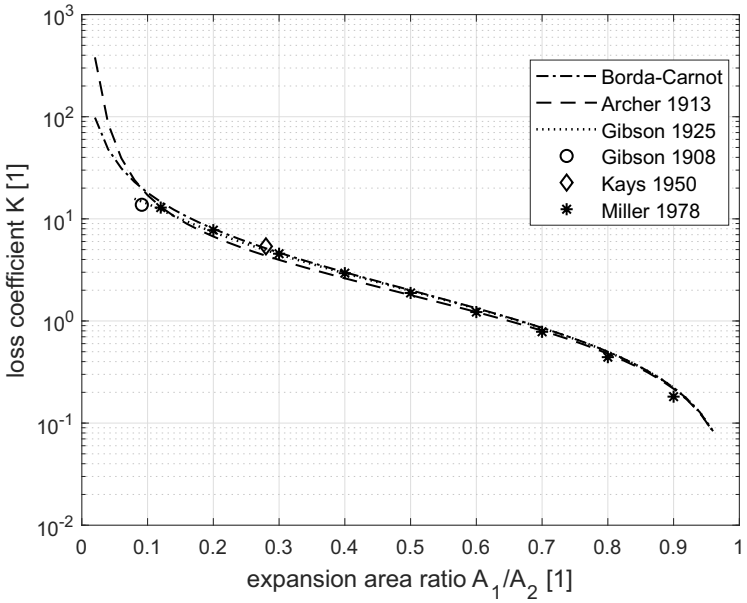

Figure 3.21: Loss coefficient K versus the expansion area ratio σ_{inv} of different investigations

Figure 3.21 shows the loss coefficient K referred to the velocity in the downstream pipe Q/A_2 versus the expansion area ratio σ_{inv}. Almost over the entire range of σ_{inv}, the loss coefficients K exhibit a

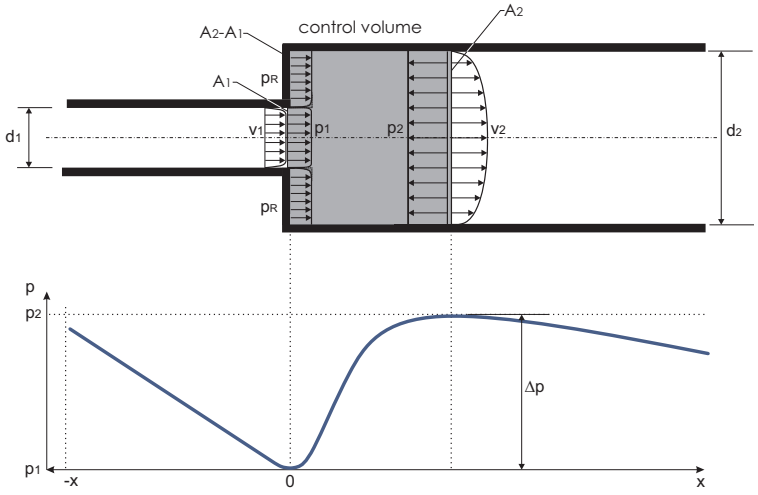

Figure 3.22: Control volume of a sudden expansion and the definitions and radial distributions of the velocity and pressure. The lower part shows the axial pressure distribution.

high correlation among one another. Gibson 1908 (Ref. [77]) obtained a dependency of K on the flow rate, so the data is presented as the mean loss coefficient. For low expansion area ratios, the results of Archer [76] deviate considerably from the ones obtained by Borda-Carnot. But for $\sigma_{inv} > 0.3$, the loss coefficient of Archer approaches the values of Borda-Carnot. The results of Miller [85] exhibit a slight deviation compared with the Borda-Carnot relation over the entire range of expansion area ratios.

In summary, the sudden expansion represents the only hydraulic structure for which the loss coefficient is physically derived but not empirically determined. But the literature review indicates ambiguous results since some investigations confirm the applicability of the Borda-Carnot equation (Refs. [49, 18, 84]). Other investigations, however, raise doubts about the assumptions and simplifications made during the derivation and present adapted formulations for the loss coefficient K (Refs. [75, 76, 77, 80]). Notwithstanding this, the momentum balance will be applied to the sudden expansion in compliance with the sudden contraction.

3.2.2 Applying the Momentum Balance

The stationary momentum balance is applied to a control volume in the downstream pipe, as shown by the grey area in Fig. 3.22, starting at the expansion plane and reaching downstream to that point where the pressure p_2 reaches the maximum value. In contrast to the sudden contraction, Δp is defined by the pressure difference between the maximum downstream pressure and the pressure in or shortly downstream of the expansion, as shown in the lower part of Fig. 3.22. Again, frictional forces F_F cancel out when Eq. (1.46) is applied to the control volume of a sudden expansion since the expanding jet is not re-attaching to the wall within the control volume. In addition, the gravitational force term can be neglected in compliance with the sudden contraction. Therefore, the initial equation

$$0 = -\sum_i \varrho\, \beta_i\, v_i\, \vec{v}_i \cdot \vec{n}_i\, A_i - \sum_i p_i\, \vec{n}_i \cdot \vec{n}_v\, A_i \tag{3.68}$$

can be expanded by the three pressure terms according to the control volume in Fig. 3.22, which are the inlet pressure p_1, the outlet pressure p_2, and the reacting pressure p_R of the expansion wall

$(A_2 - A_1)$. In analogy to the sudden contraction, the normal unit vectors are defined as $\vec{n}_v = [1; 0]$, $\vec{n}_1 = [-1; 0]$, and $\vec{n}_2 = [1; 0]$. As a result, Eq. (3.68) gives

$$0 = -\sum_i \varrho\, \beta_i\, v_i\, \vec{v}_i \cdot \vec{n}_i\, A_i + p_1\, A_1 - p_2\, A_2 + p_R\, (A_2 - A_1) \tag{3.69}$$

But in this case, the pressure force term considering the reacting pressure of the contraction wall p_R is positive since the normal unit vector of the contraction wall is equal to $\vec{n}_1$.
The momentum fluxes are defined for the inlet and outlet cross-section analogously to the sudden contraction, so Eq. (3.69) yields

$$0 = \varrho \left(\beta_1 \frac{Q^2}{A_1} - \beta_2 \frac{Q^2}{A_2} \right) + p_1 A_1 - p_2 A_2 + p_R\, (A_2 - A_1)\,. \tag{3.70}$$

Equation (3.70) also considers the non-uniform velocity distribution over the cross-section by the momentum coefficients $\beta_{1;2}$. At this point, it must be emphasized that Eq. (3.70) is equal to Eq. (3.10) as derived for the sudden contraction.
Schütt [86] conducted experiments proving that the pressure on the expansion wall is equal to the pressure in the pipe of the smaller diameter directly in the expansion plane p_1. Similar results are also obtained by Nusselt [82] in 1940 from experiments with air. Therefore, the reacting pressure p_R is assumed to equal p_1 in the derivation of the classical Borda-Carnot equation. But numerical simulations show that assuming $p_R = p_1$ results in a significant deviation of the simulated pressure change from the one calculated by Eq. (3.63) for small area ratios σ_{inv}. Therefore, analogous to the sudden contraction, the reacting pressure p_R is parametrized by

$$p_R = p_1 - c_P \frac{\varrho}{2} \frac{Q^2}{A_1^2} \tag{3.71}$$

with the pressure coefficient c_P taking into account the non-uniform pressure distribution over the expansion wall $A_2 - A_1$ and the deviation of p_R from p_1. Figure 3.23 shows the normalized effective pressure $p(r)$ over the normalized expansion wall radius $r^* = (r - R_1)/(R_2 - R_1)$ for two different expansion area ratios. Here, r defines the expansion wall radius $R_1 \leq r \leq R_2$, R_1 defines the radius of the upstream pipe, and R_2 defines the radius of the downstream pipe. The effective pressure $p(r)$ declines with decreasing distance to the expansion edge, as shown in both lines of Fig. 3.23. But for small expansion area ratios, the difference between the lowest and highest value of the effective pressure is much larger than for $\sigma_{inv} = 0.184$. In addition, the effective pressure at the outer radius $p(R_2)$ can not be approximated equal to p_1. Whereas for $\sigma_{inv} = 0.184$, $p(r)$ can be assumed constant and equal to p_1 in good approximation.

Using Eq. (3.71) into Eq. (3.70) and solving for the positive pressure change $p_2 - p_1$ yields

$$p_2 - p_1 = \varrho \frac{Q^2}{A_2^2} \left(\frac{A_2}{A_1} \beta_1 - \beta_2 + \frac{c_P}{2} \frac{A_2}{A_1} - \frac{c_P}{2} \frac{A_2^2}{A_1^2} \right). \tag{3.72}$$

The non-idealized loss coefficient K is represented by the bracketed term of Eq. (3.72). For $\beta_1 = \beta_2 = 1$ and $c_P = 0$, Eq. (3.72) is identical to Eq. (3.64) as a combination of the energy conservation principle and the Borda-Carnot equation. In addition, flipping Eq. (3.72) to $p_1 - p_2$ yields the formulation of the momentum-based pressure loss for a sudden contraction, see Eq. (3.13).
Now the momentum coefficients $\beta_{1;2}$ and the pressure coefficient c_P must be obtained by numerical simulations to close the proposed approach.

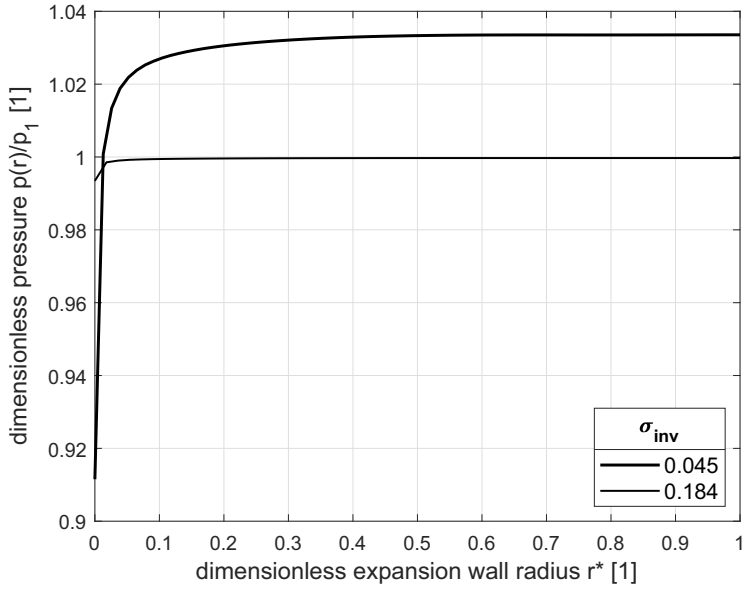

Figure 3.23: Dimensionless pressure distributions $p(r)/p_1$ over dimensionless expansion wall radius r^* for two different expansion area ratios

3.2.3 Numerical Modelling

Since less experimental data is available for the sudden expansion, the validated numerical model of the sudden contraction is employed and adapted for the simulation of the sudden expansion. Therefore, the basic parameters of the simulation model are equal to the numerical model of the sudden contraction, see chap. 3.1.4. An unstructured mesh of tetrahedral elements is applied to the simulation domain with an upstream flow length of $15d_2$ and a downstream flow length of $10d_2$. Here, d_2 represents the downstream pipe diameter, which is approximately 140.92 mm. The upstream flow length ensures that the flow is fully developed before entering the sudden expansion. This is verified by computing the momentum coefficient β in the upstream pipe at different cross-sections. It turns out that β solely changes around one thousandth over a flow length of $2d_2$ after an inlet flow length of $8d_2$, independent of the investigated expansion area ratio. In addition, the sudden expansion already affects the velocity distribution in the expansion plane. According to the literature, the maximum pressure occurs within a downstream flow length of $7d_2$ as obtained by Archer [76] or 5 to $6d_2$ as obtained by Schütt [79] when examining the pressure charts in detail. With a downstream flow length of $10d_2$, the maximum pressure occurs within the simulation domain and an additional flow length of 3 to $4d_2$ is guaranteed before the outlet. The additional flow length ensures that the outlet boundary condition does not affect the maximum pressure p_2. As the inlet boundary condition, the option mass flow rate is applied, and average static pressure as the outlet boundary condition. All closed boundaries are defined as smooth walls to reduce frictional effects but ensure proper development of the wall boundary layer and, consequently, the velocity distribution.

The mesh of the simulation domain consists of tetrahedral elements with an edge length of 3 mm. At the expansion wall and the expansion edge, the mesh is refined by elements of 0.5 mm edge length. A growth rate of 1.2 ensures a smooth transition of the refined mesh at the expansion wall to the mesh with a 3 mm edge length. The radial pipe walls are refined with 20 prism layers of exponentially increasing layer height towards the inner. The first cell height of the prism layers corresponds to a

dimensionless wall distance $y^+ < 5$. This results in a number of 11 148 373 mesh elements. Figure 3.24 shows the generated mesh in the sectional view.

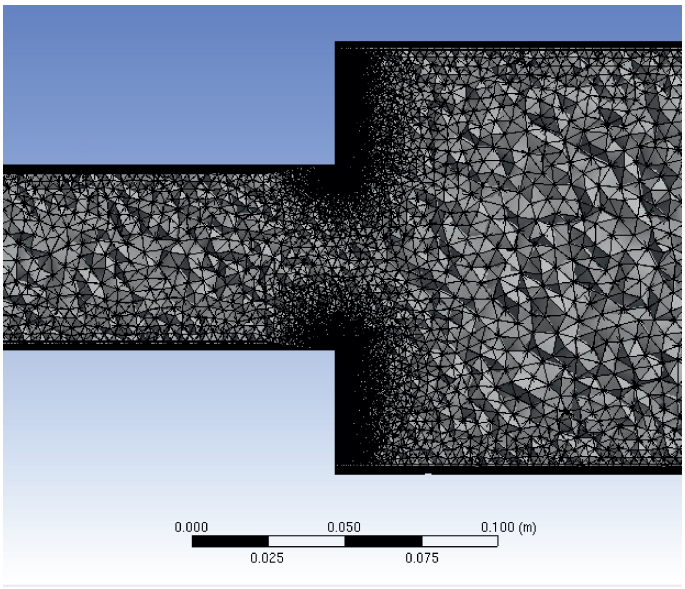

Figure 3.24: Sectional view of the mesh applied to the sudden expansion with boundary layers and refinement at the expansion edge and wall

A detailed examination of the most common turbulence models with the major assets and flaws is given previously. Since the major asset of the kω-SST turbulence model [33, 35] is the modeling of adverse pressure gradients and separated flows (see Ref. [30]), it is applied as the turbulence model. The computation of the momentum coefficients is sensitive to the wall boundary layer since this region affects the coefficients considerably. Therefore, the option automatic wall treatment is enabled for a program-controlled selection of the most suitable method to capture the variations of the flow variables in the near-wall region.
Only very little experimental data is available for sudden expansion flows of water. But the investigation of Khezzar et al. [87] provides measurement data of the turbulence kinetic energy k downstream of the sudden expansion. The turbulence kinetic energy can be calculated from the velocity fluctuations in every spatial direction (u', v', w') via:

$$k = \frac{1}{2}\left(u'^2 + v'^2 + w'^2\right) \tag{3.73}$$

Although the relevant data of Khezzar et al. [87] is presented as a contour plot, a qualitative comparison with the simulation results can be performed to check whether the turbulence models can capture the region of high turbulence kinetic energy adequately. The values are obtained in the mid-plane of the downstream pipe at a Reynolds number of 40 000, referred to the upstream pipe with an upstream pipe diameter of 48 mm and 84 mm for the downstream one. Figure 3.25 shows the simulation results of k normalized by its maximum value k_{max} for the kε, kω, and kω-SST turbulence model as a colored surface, together with an overlay of the experimental results of Khezzar et al. [87] represented by contour lines. Due to symmetry reasons, only half the pipe diameter of the downstream section from the expansion plane up to a flow length of 0.6 m ($\approx 8.5\,R_2$) is shown. In this region, the largest variations in the turbulence kinetic energy k occur. The extent and the magnitude of the measured k show the

best agreement with the numerical results of the kω-SST turbulence model. But the kω turbulence model also shows a good agreement with the measurements of Khezzar et al. [87]. In contrast, the kε turbulence model underestimates the extent of the region of high turbulence kinetic energy. But in comparison with the sudden contraction and the metering orifice, the kε turbulence model shows the highest agreement to the experimental results for this application. Due to its specific asset of properly modeling free-stream regions, it appears that this model also yields reasonable results downstream of a sudden expansion.
The authors report a maximum measured turbulence kinetic energy of $0.025\ m^2/s^2$, which is predicted most precisely by the kω turbulence model with $0.023\ m^2/s^2$. The kω-SST turbulence model predicts a maximum of $0.022\ m^2/s^2$, but the kε turbulence model yields $0.029\ m^2/s^2$. In summary, the ω-based turbulence models again show the best agreement with measurement results. Due to the scarce available data, the standard turbulence models can solely be assessed qualitatively. It is shown that the kω and the kω-SST turbulence model accurately predict the results of Khezzar et al. [87]. It appears that the kω turbulence model predicts the distribution of k more precisely at the downstream side of the maximum region, whereas the kω-SST turbulence model performs better at the upstream side of the maximum region. Nevertheless, applying the kω-SST turbulence model guarantees not to go seriously wrong for the sudden expansion as well.
With the justification of the employed turbulence model, the setup of the numerical model is complete. Now it can be proved that the mesh of the simulation domain is sufficiently fine, so simulation results do not change considerably by further refining the mesh.

A mesh independence study is performed with two additional meshes, according to Celik et al. [42]. The fine mesh consists of 22 718 762 elements with an element size of 2 mm and 0.3 mm at the expansion wall and edge. The coarse mesh consists of 7 486 598 elements of 4 mm and 0.7 mm element size. This results in mesh refinement ratios S of ≈ 1.3 according to Eq. (2.11). The values of the estimation of the discretization uncertainty are given in Tab. 3.5. For the sudden expansion, the parameters β_1, β_2 and c_P are the relevant key variables f the uncertainty estimation is applied to. The apparent order o as per Eq. (2.12) is larger than the order of the numerical solution scheme, which is the desired ideal threshold for o not to fall below. The extrapolated values agree well with the ones obtained for the intermediate mesh. Only for the pressure coefficient c_P, an increased deviation can be noticed due to values very close to zero. The deviation between the key variables of the fine and intermediate mesh is given by the extrapolated absolute error $e_{a,if}$ and to the extrapolated values $f_{ext,if}$ by $e_{ext,if}$. Except for the pressure coefficient, the change can be considered marginal. The extrapolated key variables obtained with the fine and intermediate mesh $f_{ext,if}$ exhibit a very high agreement with the extrapolated key variables obtained with the intermediate and coarse mesh $f_{ext,ci}$. As a result, the grid convergence index amounts to values far below 0.1% for the momentum coefficients β_1 and β_2 but to 4% for c_P. However, a change in value of 4% for c_P results in a negligible change of the calculated pressure change Δp of under 0.1%. The comparably large change in the pressure coefficient c_P between the fine and intermediate mesh can therefore be considered acceptable.
Figure 3.26 shows the pressure profile along the axis for all three meshes over the flow length L in multiples of the downstream pipe diameter d_2. All pressure profiles exhibit an almost equivalent shape except for the upstream region, where pressure profiles decline with different gradients. This results in different pressure values in the expansion plane. For the coarse mesh, the minimum pressure is slightly smaller than predicted by the other meshes. Due to the scale division of the y-axis, the deviation appears larger than the calculated values indicate. The maximum deviation between the pressure values of the fine and the intermediate mesh amounts to 0.1%, but to 0.13% for the coarse to intermediate

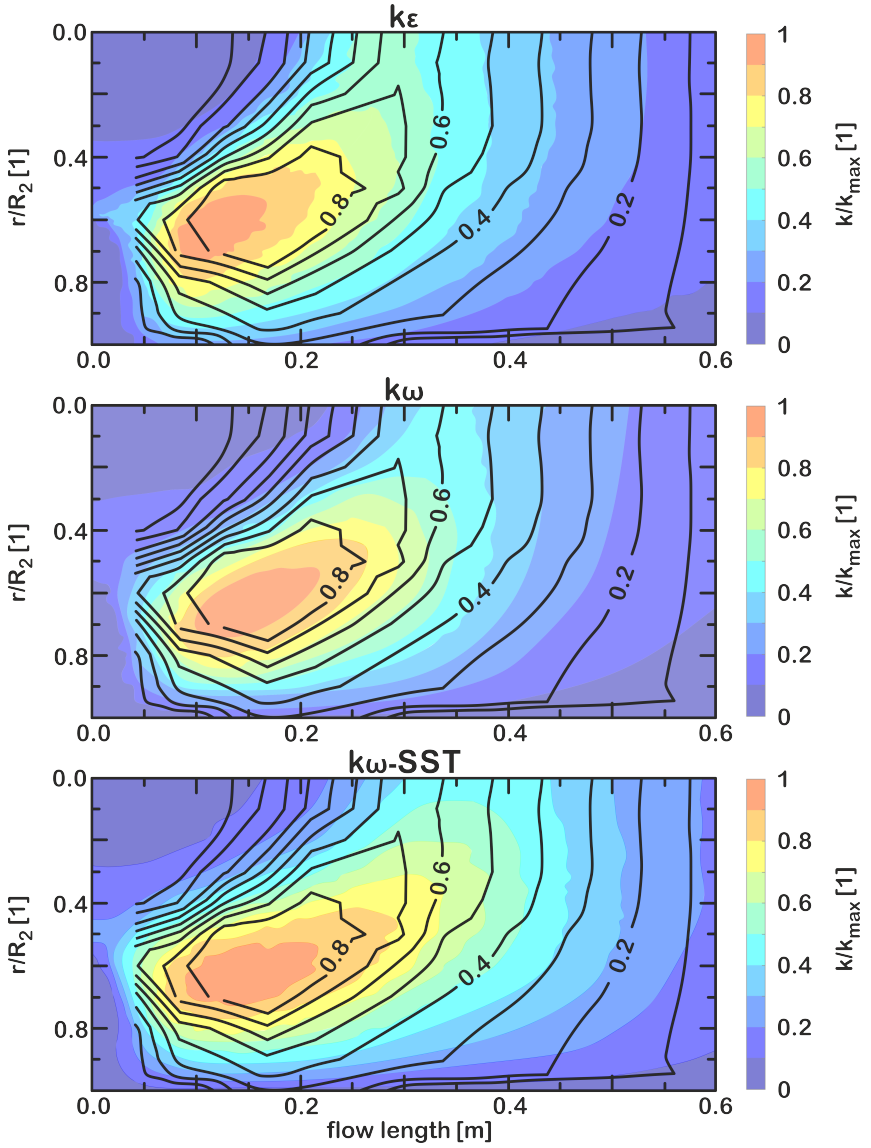

Figure 3.25: Numerical results of k downstream of a sudden expansion obtained with different turbulence models. The experimental results of Khezzar et al. [87] are shown by the contour lines as an overlay.

mesh pressure values. However, all three meshes accordingly predict the location of the maximum pressure at a flow length of around 6.2d_2.
Therefore, the intermediate mesh is considered sufficiently fine.

Now, the numerical model can be employed to investigate the flow through a sudden expansion. For an expansion area ratio σ_{inv} of 0.184, the examination of the pressure recovery zone shows that the pressure reaches its maximum at a downstream flow length of approx. 5.5d_2 for a mass flow rate of 2 kg/s and approx. 6.6d_2 for 20 kg/s. The downstream flow length approaches a final value around 6.8d_2 for the maximum pressure location at mass flow rates $\dot{m} > 20\,kg/s$. Therefore, the control volume is defined starting at the expansion plane and reaching up to the cross-section 6d_2 downstream of the expansion. The maximum deviation of the simulated maximum pressure p_2 and the pressure obtained at 6d_2 amounts to 0.3%, which is negligibly small. But the deviation of the pressure value at

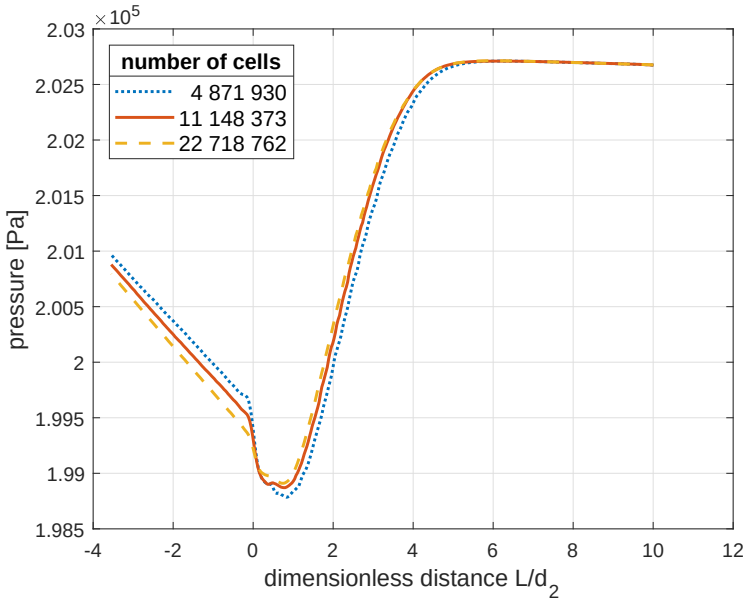

Figure 3.26: Simulation results of the axial pressure profiles along the centerline for three different meshes at a mass flow rate $\dot{m}$ of 14 kg/s.

Table 3.5: Calculation of the discretization uncertainty

	β_1	β_2	c_P
f_f, f_{int}, f_c [1]	1.0171, 1.0166, 1.0149	1.0309, 1.0324, 1.0257	0.00179, 0.00199, 0.00206
o [1]	4.111	5.563	6.679
$f_{ext,ci}$ [1]	1.0174	1.0342	0.0020
$f_{ext,if}$ [1]	1.0174	1.0304	0.0017
$e_{a,if}$ [%]	0.05	0.15	11.81
$e_{ext,if}$ [%]	0.02	0.05	3.14
GCI_{if} [%]	0.04	0.07	3.81

$6d_2$ from the maximum pressure decreases to under 0.1% with increasing flow rate.

To discover dependencies of the coefficients and to find a mathematical function for the parameterization of the coefficients, the simulation is performed with a set of parameters, given in Tab. 3.6. Every combination of the mass flow rate $\dot{m}$ and the expansion area ratio σ_{inv} is solved.

Figure 3.27 shows the momentum coefficient versus the dimensionless distance to the expansion L/d_2 for three different expansion area ratios σ_{inv}. In the background, the velocity distribution over the pipe's central plane is visualized with its magnitude quantified by the color mapping for $\dot{m} = 8\,kg/s$ and $\sigma_{inv} = 0.184$. The dead water zones and the areas where the flow velocity is (almost) zero are represented by the dark blue color. The red color represents the maximum velocity. The profiles of the momentum coefficients start at a dimensionless flow distance L/d_2 of 2 with values indicating fully developed turbulent flow. The momentum coefficient remains constant up to the expansion plane and

Table 3.6: Values of the simulation parameter set for the sudden expansion

parameter	1	2	3	4	5	6
$\dot{m}$ [kg/s]	2.00	5.00	8.00	14.00	20.00	
σ_{inv} [1]	0.020	0.045	0.184	0.322	0.503	0.724

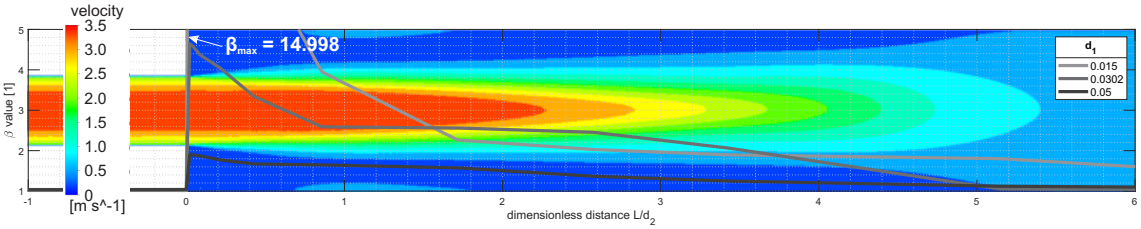

Figure 3.27: Representative axial distribution of the momentum coefficient β vs. the dimensionless flow length L/d_2 for different expansion area ratios σ_{inv} with the color-mapped magnitude of the velocity in the background

soars to its maximum, which is reached around $L/d_2 = 0.02$ downstream of the expansion plane. The maximum value is strongly dependent on the expansion area ratio σ_{inv}. As the jet expands in the downstream pipe, β decreases, re-approaching values around 1.03. But the downstream flow length for β to re-approach fully turbulent numbers strongly depends on σ_{inv}, since for low expansion area ratios, the jet needs to cover a higher radial distance in the downstream pipe up to the wall. Due to the jet, the distance for the flow to fully re-develop is much larger compared with the sudden contraction.

Figure 3.28 shows the momentum coefficient β_1 versus the expansion area ratio for every simulated mass flow rate. Since β_1 is computed in the expansion plane, the flow is highly disturbed, which means β_1 is a function of the mass flow rate $\dot{m}$ and the expansion area ratio. With regard to the mass flow rate $\dot{m}$, the spread around the mean of β_1 is in the range of +2% to -1%. Therefore, the dependency on $\dot{m}$ can be neglected as a first approximation. Averaging the simulation results of β_1 for every σ_{inv} gives the mean of β_1 as a function of σ_{inv}. The mean values are now used to fit a mathematical function:

$$\beta_1 \left(\sigma_{inv}\right) = 0.045 \, \sigma_{inv}^{0.203} + 1 \tag{3.74}$$

represented by the bold line in Fig. 3.28.

The downstream momentum coefficient β_2 is computed for a plane $6d_2$ downstream of the expansion. Despite the flow distance of $6d_2$, the flow is not fully re-developed, but the pressure is recovered to its maximum in this region. The simulation results of the downstream momentum coefficient β_2 versus the expansion area ratio are shown in Fig. 3.29 for every mass flow rate. In analogy to β_1, β_2 is also a function of the expansion area ratio and the mass flow rate. In addition, β_2 reaches the maximum at $\sigma_{inv} = 0.504$ and decreases with further increase of σ_{inv}. With regard to the mass flow rate $\dot{m}$, the spread around the mean of β_2 is in the range of $\pm$3%. This means that the dependency of β_2 on $\dot{m}$ is neglected as a first approximation as well. With the simulation results of β_2 averaged over $\dot{m}$ for every expansion area ratio σ_{inv}, the mean values of β_2 are used to fit a mathematical function

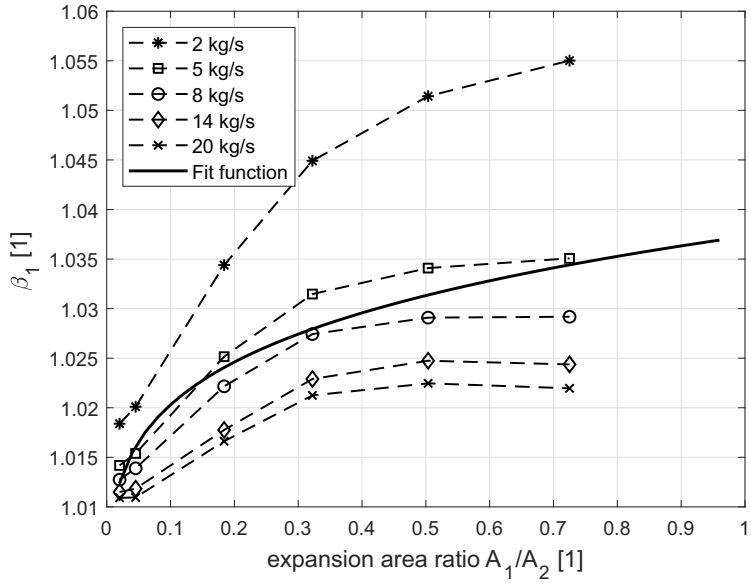

Figure 3.28: Momentum coefficient β_1 versus expansion area ratio for different mass flow rates together with the fit function

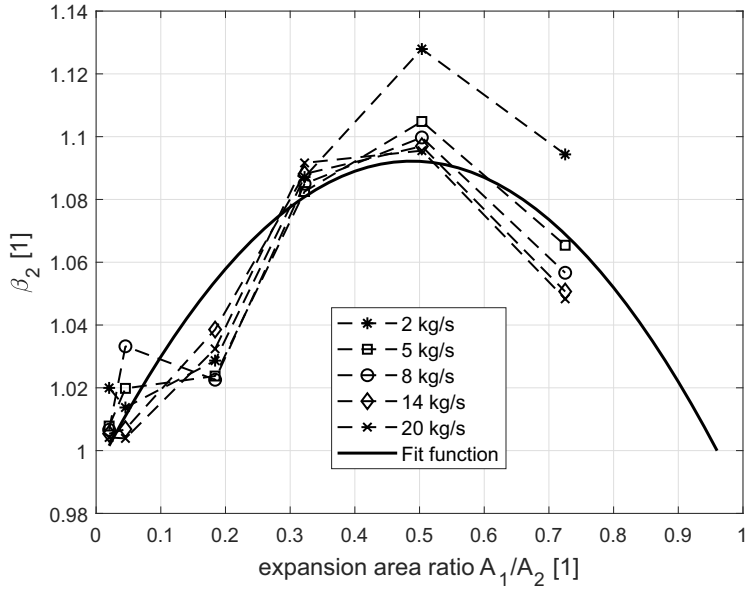

Figure 3.29: Momentum coefficient β_2 versus expansion area ratio for different mass flow rates together with the fit function

$$\beta_2\left(\sigma_{inv}\right) = -0.414\,\sigma_{inv}^2 + 0.404\,\sigma_{inv} + 1 \tag{3.75}$$

Figure 3.30 shows the simulation results of the pressure coefficient c_P versus the expansion area ratio for all simulated mass flow rates. In analogy to the momentum coefficients, c_P exhibits a dependency on the mass flow rate and the expansion area ratio. As a special feature of the c_P profiles, c_P is negative for low expansion area ratios, which means the reacting pressure p_R is higher than the inlet pressure p_1. In accordance with the momentum coefficients, the dependency of c_P on $\dot{m}$ is disregarded

and the obtained mathematical function by using the mean of c_P for every expansion area ratio σ_{inv} yields:

$$c_P\left(\sigma_{inv}\right) = 0.035\ \sigma_{inv}^{0.295} - 0.017 \tag{3.76}$$

The required coefficients β_1, β_2, and c_P can also be parametrized considering the dependency on the expansion area ratio σ_{inv} and the mass flow rate $\dot{m}$. This would result in more complex 2-parameter fit functions. But the agreement between the simulation results Δp_{sim} and the momentum approach Δp as per Eq. (3.72) increases by about 2% (and 3.5% at maximum for the smallest expansion area ratio), which is a disproportional effort for this negligible effect. Parametrizing the mean values of the coefficients is therefore justified as an appropriate simplification.

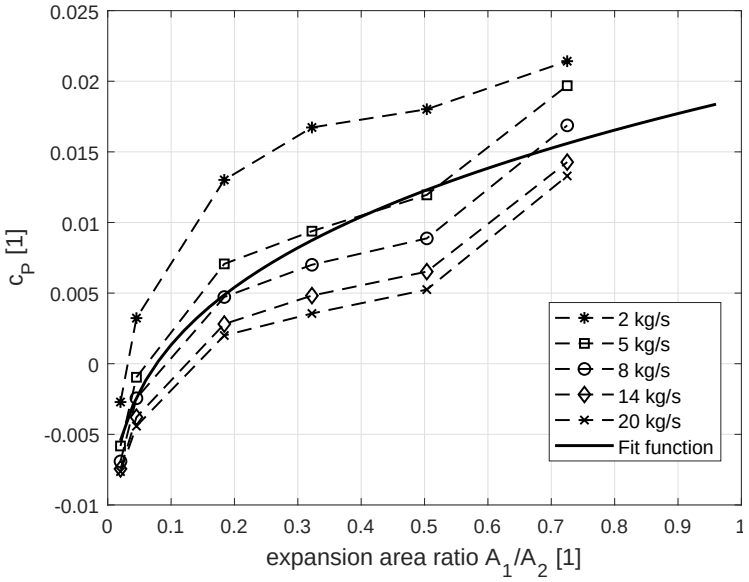

Figure 3.30: Pressure coefficient c_P versus expansion area ratio for different mass flow rates together with the fit function

The deviation of the reacting pressure $p_{R,fit}$ as per Eqs. (3.76) and (3.71) to the simulated reacting pressure $p_{R,sim}$ is within 2%. Just for the smallest expansion area ratio $\sigma_{inv} = 0.02$ at a mass flow rate of 20 kg/s, the deviation increases to approximately 7%. In contrast, the deviation of p_1 to $p_{R,sim}$ is about 80% for $\sigma_{inv} = 0.02$. Figure 3.31 shows the calculated reacting pressure $p_{R,fit}$ and the inlet pressure p_1 divided by the simulated reacting pressure $p_{R,sim}$ on a semi-logarithmic scale versus σ_{inv} for all simulated mass flow rates. It can be seen that for low expansion area ratios the agreement between theory and simulation is significantly improved if p_R is not assumed equal to p_1.

With the obtained fit functions for the momentum coefficients β_1, β_2, and the pressure coefficient c_P, the non-idealized momentum-based approach is complete. Using Eqs. (3.74),(3.75),(3.76) into Eq. (3.72) gives the final formula of the proposed approach. Due to the type of the fit functions, the final formula is bulky and, therefore, not given in the expanded form.

3.2.4 Results

The calculated and simulated pressure change of the sudden expansion must be checked against the literature for validation. Figure 3.32 shows the loss coefficients plotted in Fig. 3.21, extended by the

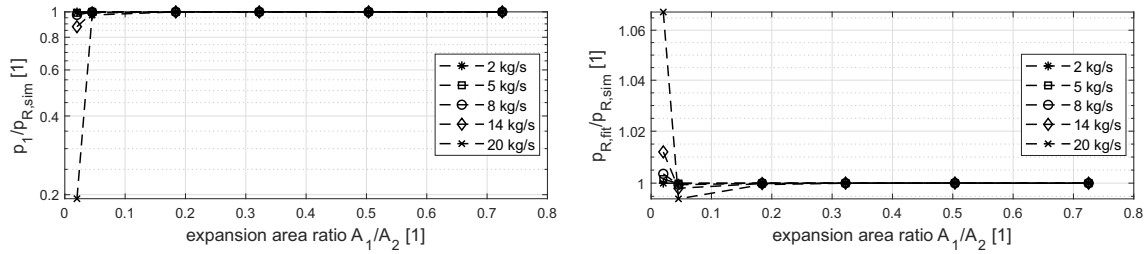

Figure 3.31: Deviation of the calculated reacting pressure $p_{R,fit}$ and the inlet pressure p_1 to the simulated reacting pressure $p_{R,sim}$ versus the expansion area ratio for different mass flow rates

simulation results and the calculation results of Eq. (3.72). The average values of both additional results are displayed for comparison with the literature numbers. The averaging is justified since the spread around the mean of the simulated loss coefficient ranges from -8% to +6% and -6% to +4% for the calculated loss coefficient obtained with the bracketed term of Eq. (3.72). Both results exhibit a high correlation to the Borda-Carnot relation in the shape of the bracketed term of Eq. (3.64). A deviation can be discerned solely for small and large expansion area ratios σ_{inv} since the assumption of the reacting pressure of the expansion wall being equal to the pressure within the expansion p_1 is inappropriate for small σ_{inv}. Therefore, the results of Eq. (3.63) are significantly distorted for small expansion area ratios.

Figure 3.33 shows the agreement of the simulated pressure change Δp_{sim} with the pressure change obtained with the Borda-Carnot equation Δp_{BC} (left-hand side) and the non-idealized approach of Eq. (3.72) Δp (right-hand side). The results obtained for Δp agree very well with the simulation results, even for low expansion area ratios where the deviation to p_{sim} is within 6%. For large expansion area ratios, the deviation increases to 9%. In contrast, the Borda-Carnot relation exhibits acceptable agreement with the simulated pressure change for medium area ratios, whereas the deviation for small and large expansion area ratios considerably increases up to 21%. The values shown in Fig. 3.33 are also given in Tab. 3.7 for $\dot{m} = 14\ kg/s$.

Table 3.7: Values of the pressure change for $\dot{m} = 14\ kg/s$ obtained by the simulation, the non-idealized momentum approach, and the Borda-Carnot relation

σ_{inv} [1]	0.02	0.045	0.184	0.322	0.504	0.725
Δp_{sim} [Pa]	47 938	18 273	3642	1674	738	264
Δp [Pa]	45 226	17 729	3596	1681	765	285
Δp_{BC} [Pa]	39 313	17 024	3585	1699	797	306

Consequently, the integral momentum balance without the simplifications of the Borda-Carnot relation results in a significantly improved accuracy of the predicted pressure difference, especially for extreme expansion area ratios. However, the simplifications of uniform radial velocity distributions and a constant reacting pressure distribution over the entire expansion plane of the Borda-Carnot relation can be assumed appropriate for medium area ratios. It is also proven that the sudden expansion can be hydraulically described by the very same formula as the sudden contraction. Solely the momentum and pressure coefficients change and distinguish between both flow structures.

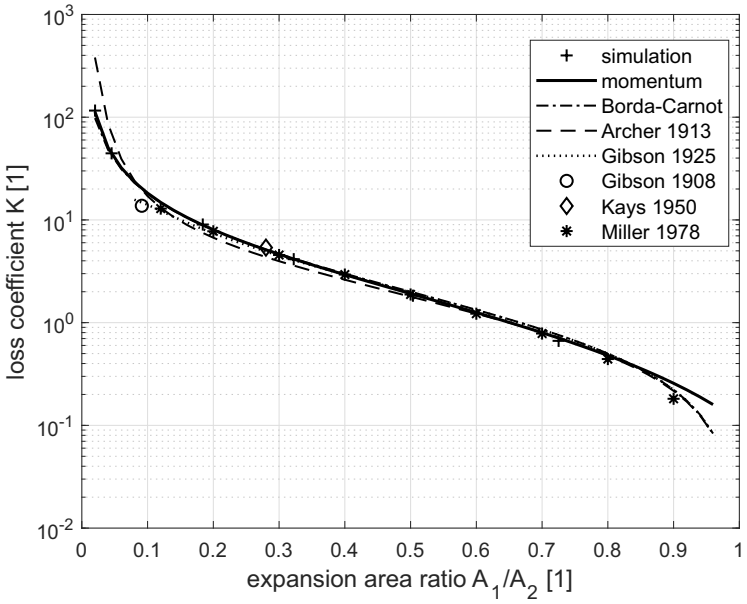

Figure 3.32: Comparison of different loss coefficients K vs. the expansion area ratio σ_{inv} including the non-idealized approach of Eq. (3.72) and the simulation results

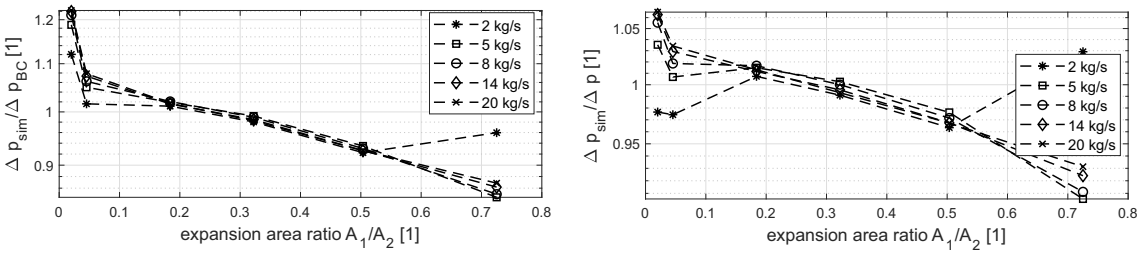

Figure 3.33: Agreement of the simulated pressure change Δp_{sim} with the Borda-Carnot pressure change Δp_{BC} and the non-idealized pressure change Δp over the expansion area ratio

In contrast to the sudden contraction, the proposed non-idealized approach for the sudden expansion requires obtaining the momentum coefficients in regions where the flow is highly disturbed. This means the momentum coefficients exhibit dependencies on the area ratio and the flow rate, unlike the constant values for the sudden contraction. Regarding the flow pattern, the pressure change of the sudden expansion is a more complex problem compared with the sudden contraction.
Since the sudden contraction and the sudden expansion have been successfully described by a unified approach based on the integral momentum balance, the momentum-based approach will now be applied to the orifice as an interconnection of both flow structures.

3.3 The Measuring Orifice

Extracts of the findings presented in this section have been published in the Journal of Fluids Engineering, October 2022. The manuscript can be found at https://doi.org/10.1115/1.4062505.

3.3.1 Retrospective / State of the Art

When a sudden contraction is followed by a sudden expansion, the resulting flow structure represents an orifice from a systemic point of view. But combining the hydrodynamics of both flow structures does not represent the hydrodynamics of an orifice since the sudden contraction and the sudden expansion are treated differently for a hydraulic description. The hydraulics of a sudden contraction are evaluated in regions where the flow is fully (re-)developed, which is not valid for the sudden expansion. In this case, the region is defined by the expansion plane and the location of the maximum pressure. However, an orifice can be used to limit the dynamic pressure, reduce or limit the flow, and also for measuring tasks. In the latter case, the orifice is called a metering orifice.
The metering orifice is a flow structure used in differential-pressure meters to indirectly measure the flow rate of gas, steam, or liquid flows. Due to its reliability, simple handling and installation, the metering orifice is a widely-used device in industrial differential-pressure-based flow meters, especially in the petrochemical and petroleum industry. Despite its simple geometry, the fluid mechanics behind the flow through an orifice are challenging since an orifice affects the flow with high impact and at long distances.
Therefore, the velocity distribution of the center sectional plane obtained by the numerical simulations is shown in Fig. 3.34. The upstream flow is affected just shortly upstream of the orifice, whereas the downstream flow is affected strongly and also at a long downstream distance. In consequence, the downstream flow of an orifice is highly disturbed.

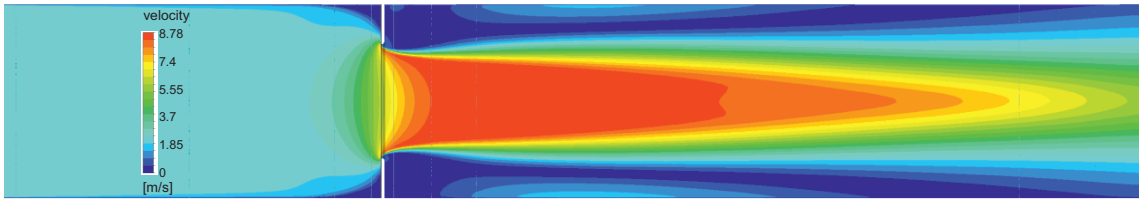

Figure 3.34: Representative velocity distribution of a flow through an orifice.

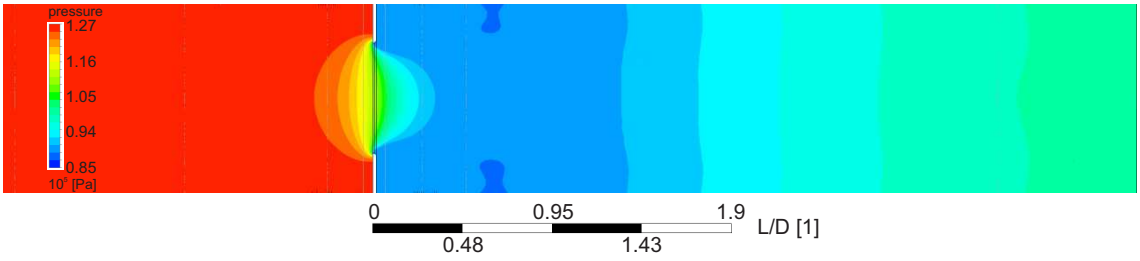

Figure 3.35: Representative pressure distribution of a flow through an orifice.

Even the downstream pressure close to the orifice can not be assumed evenly distributed in the radial direction, which is shown by the colored pressure distribution of the center sectional plane in Fig.

3.35. In fact, this leads to a complex flow in the vicinity of the orifice where the pressure is usually measured for the flow metering.

However, the common calculation method, valid for all differential pressure-based flow meters, is based on the Bernoulli principle applied on a horizontal streamline passing the pipe cross-section upstream and downstream of the flow obstruction. For the present investigation, incompressible fluid with constant density ϱ and at a constant height z is considered. Therefore, the energy balance along a streamline yields

$$p_1 + \frac{\varrho}{2} v_1^2 = p_2 + \frac{\varrho}{2} v_2^2 \tag{3.77}$$

Frictional effects are neglected as well, discussed in the following. Equation (3.77) yields no pressure loss for equal diameters upstream and downstream ($v_1 = v_2$) when the Bernoulli principle would be applied to the whole cross-section instead of a streamline. As a consequence, the downstream point is often referred to as a cross-section that differs from the pipe cross-section (e.g. the vena contracta diameter or the narrowest diameter of a Venturi tube respectively). However, the continuity equation in terms of the mass conservation gives

$$\dot{m} = \varrho v_1 A_1 = \varrho v_2 A_2 = \varrho Q \tag{3.78}$$

Equation (3.78) used into Eq. (3.77) gives

$$\Delta p = \frac{\varrho}{2} \frac{Q^2}{A_1^2} \left(\frac{A_1^2}{A_2^2} - 1 \right) \tag{3.79}$$

where Δp is the differential pressure $p_1 - p_2$. At this point, a distinction must be made concerning the purpose of the approach. For designing hydraulic systems or pumps, the pressure loss or irreversible pressure drop must be obtained. However, for the determination of the flow rate, the differential pressure is the measured quantity used as an input for the prediction of $\dot{m}$. But in this case, the differential pressure contains reversible and irreversible shares.

Formula for the irreversible pressure drop

The irreversible pressure drop is obtained by introducing a loss coefficient K into Eq. (3.79) as previously shown

$$\Delta p = K \frac{\varrho}{2} \frac{Q^2}{A_1^2} \tag{3.80}$$

where K also contains the dependency on the area ratio A_2/A_1. Equation 3.80 presumes a filled pipe. In the literature, K can be referred to the pipe velocity v_1 (Refs. [19, 18, 88]) or the velocity of the narrowest section v_2 (Refs. [23, 63]). But since the vena contracta area, representing the narrowest flow area, can not be determined precisely, the orifice bore area A_O is used instead. As a result, the loss coefficient K additionally accounts for the inconsistency of applying the theory to the vena contracta but using the orifice bore area. As an example, the investigation of Dayev and Kairakbaev [89] on modeling a function for the contraction coefficient to improve the determination of the flow coefficient shows its complexity. The contraction coefficient accounts for the contraction of the effective flow area, which in this case is the vena contracta as a reduction from the orifice bore area. Dayev and Kairakbaev describe the profile of the representative streamline bounding the flow of the vena contracta by a

mathematical function, which is then used to derive a formulation for the contraction coefficient. But the mathematical function used approximates the downstream profile of the streamline only dissatisfyingly accurate since a smooth tangential approach to the wall can not be modeled. However, focusing on the vena contracta region, the authors obtain an elaborate formulation for the contraction coefficient solely depending on the diameter ratio that exhibits high agreement with experimental results. The proposed formulation of Dayev and Kairakbaev [89] is shown in Chap. 3.3.3.

State of the art for the determination of the loss coefficient K is the comparison of the empirically obtained pressure loss with the calculated results. This led to a variety of empirical data for K obtained by different authors investigating the pressure loss of an orifice. In Fig. 3.36, the loss coefficient K referred to the mean velocity of the pipe Q/A_1 versus the area ratio σ is shown. The references shown namely are: Weisbach 1855 [19], Idelchik 1966 [18], Miller 1978 [85], Alvi et al. 1978 [88], Benedict 1980 [57], Benedict 1984 [23], Westaway and Loomis 1984 [90], Rennels and Hudson 2012 [63], and the international standard ISO 5167:2003 [91]. Most of the cited literature refers K to the mean velocity of the orifice bore area but for compliance with the momentum-based approach presented in the following, K is related to Q/A_1.

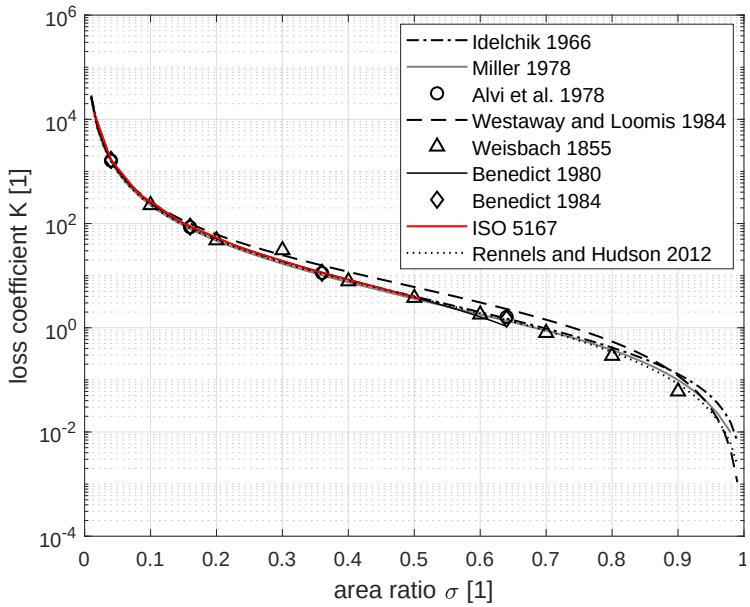

Figure 3.36: Comparison of different loss coefficients K vs. the orifice area ratio σ.

Most of the data presented in Fig. 3.36 agree with one another, except for the data of Westaway and Loomis [90], deviating noticeably from all other results at medium area ratios. The continuous black line represents the expression for the loss coefficient by Benedict 1980 [57] and is only valid for $\sigma \leq 0.6$.

But the loss coefficient K can also be derived from the so-called discharge coefficient C_D as the remaining loss of the pressure drop measured for flow metering, see Refs. [88, 57, 23, 90, 91]. It means that the loss coefficient K only accounts for the gap of the remaining or irreversible drop Δp_{irrev} in the fully (re-)developed flow, whereas C_D accounts for the gap to the actual pressure drop. The diagram of the pipe wall pressure over the flow length in the lower part of Fig. 3.38 shows the definition of Δp_{irrev}. The irreversible pressure drop is obtained by extrapolating the lines of the linear pressure gradients.

However, the differential pressure measured at the defined pressure tapping points (see the upper part of Fig. 3.38) can not be obtained that easily since it contains a reversible share recovering partially with increasing distance to the orifice.

Formula for the flow rate

Differential-pressure flow meters are used to obtain a pressure difference as an input to the calculation of the flow rate. Therefore, Eq. (3.79) is expressed in terms of the mass flow rate $\dot{m}$ with the aid of Eq. (3.78) and referred to the area A_2 where the flow is maximally converged.

$$\dot{m} = \frac{\sqrt{2\,\varrho\,\Delta p}}{\sqrt{1-\left(\frac{A_2}{A_1}\right)^2}} A_2 \tag{3.81}$$

This equation being valid for various differential-pressure flowmeters (Venturi tubes, nozzles, orifices) is now referred to orifice meters exclusively. Applying Eq. (3.81) presumes a completely filled pipe and the absence of additional losses. Using Eq. (3.81) for the orifice, the orifice bore area A_O is referenced as the downstream location as discussed before and shown in Refs. [23, 92]. Equation (3.81) requires the differential pressure Δp as an input. Normally, the pressure is measured at pressure tapping points at the pipe's wall. But the measured pressure value must not necessarily be equal to the pressure in the center of the pipe, in particular for tapping points close to the orifice. Especially for the orifice meter, Reader-Harris [92] claims that the irreversible pressure drop due to the expanding flow downstream of the orifice is significant. To account for these pressure tapping errors, the irreversible pressure drop, and the errors due to inadequate assumptions made, Eq. (3.81) is multiplied by the so-called flow (rate) or discharge coefficient C_D.

$$\dot{m} = C_D \sqrt{\frac{2\,\varrho\,\Delta p}{1-\left(\frac{A_O}{A_1}\right)^2}} A_O \tag{3.82}$$

In general, Eq. (3.80) is used for the determination of the irreversible pressure drop introducing the loss coefficient K, whereas Eq. (3.82) with the discharge coefficient C_D is used for the prediction of the flow rate obtained by the measured differential pressure of an orifice meter. It is common to derive the loss coefficient K from the discharge coefficient C_D since flow metering is the main application of a measuring orifice. Therefore, various investigations have been conducted, see Refs. [23, 57, 88, 90, 91]. Both coefficients can be converted by

$$K = \frac{A^2}{A_O^2\,C_D^2}\left(1-\frac{A_O^2}{A^2}\right) \tag{3.83}$$

which is the result of using Eq. (3.80) into Eq. (3.82). This method is proposed in the literature discussed in the following.

Benedict and Wyler [93] presented their results of the calculation of the flow coefficient of flow meters based on the differential pressure in 1974. By the time, no purely physical formulation was available to satisfactorily predict the experimentally obtained discharge coefficient C_D for orifices - except for a very similar formulation that was previously obtained by Pardoe [94] in 1943 or formulations based on the boundary layer theory. But since no reliable values are given for the required variables necessary to calculate the discharge coefficient, the equation of Pardoe [94] was not applicable at that time. Therefore, Benedict and Wyler investigated nozzle and orifice flow to obtain a generalized coefficient

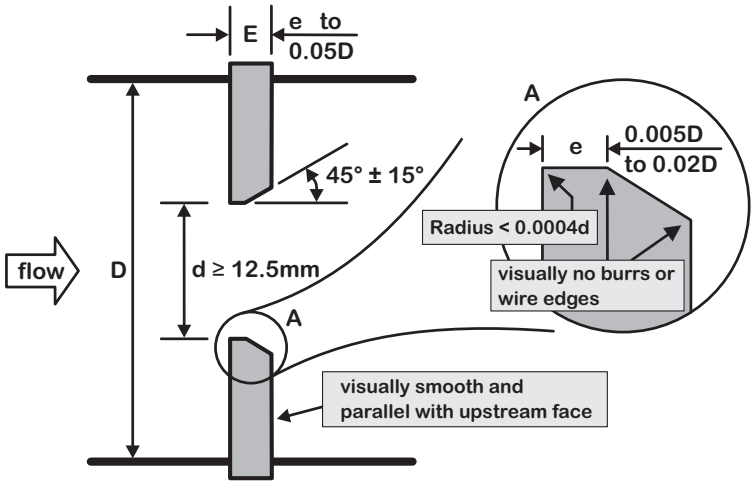

Figure 3.37: Geometric specifications of a metering orifice; the chamfer is not mandatory

capable of being applied to all flow meters based on measuring the differential pressure. The authors define the discharge coefficient C_D as the ratio of the actual mass flow rate to the ideal mass flow rate. The ideal mass flow rate presumes no pressure loss and contraction effects to be involved. The Bernoulli principle is then applied to a fluid particle on a streamline $1D$ upstream and $0.5D$ downstream of the orifice and evaluated for the ideal and actual case. It is important to mention that the author's derivation for the actual case takes into account the non-uniform velocity distribution represented by kinetic energy correction coefficients. The obtained discharge coefficient is applicable to all differential pressure-based flow meters. It includes the dependencies on the diameter ratio, the contraction coefficient, the flow pattern (represented by the kinetic energy correction coefficients), and the Reynolds number Re referred to the orifice. These coefficients are parametrized for every particular flow meter, leading to a generalized function of C_D for flow meters based on measuring the differential pressure. The proposed expression for the discharge coefficient accounts for all impacts and predicts the empirical results with a reasonable agreement plus it can be evaluated analytically straightforwardly, which was not possible beforehand. In addition to this, the authors propose a formulation for the loss coefficient K obtained from the discharge coefficient C_D. But the loss coefficient of Benedict and Wyler deviates strongly from other literature numbers and is therefore not given in Fig. 3.36.
The investigation of Benedict and Wyler [93] is a quantum leap since sets of tables for every variation of the input parameters became obsolete in determining the discharge coefficient, as given in Refs. [22, 23]. But the authors' investigation solely considered the pressure tapping points located $1D$ upstream and $0.5D$ downstream of the orifice. However, for determining the flow rate based on measurements of the differential pressure, the international standard ISO 5167:2003 [91] allows two more pressure tapping point locations. This standard is highly relevant because nearly every commercially manufactured flow meter based on measuring the differential pressure is standardized according to ISO 5167:2003. The standard ISO 5167:2003 is substantially built on the research of Reader-Harris and Gallagher, given to the fullest extent in the book Orifice Plates and Venturi Tubes [92]. It provides the description of the orifice's geometrical shape as shown in Fig. 3.37, the limitations of the application and the calculation method to convert the measured differential pressure into a flow rate. The calculation of the discharge coefficient C_D is given by the Reader-Harris/Gallagher equation [92] (Eq. (3.84)) as the international standard, which also takes into account the permitted pressure tapping point locations.

The Reader-Harris/Gallagher equation requires all diameters and lengths in millimeter

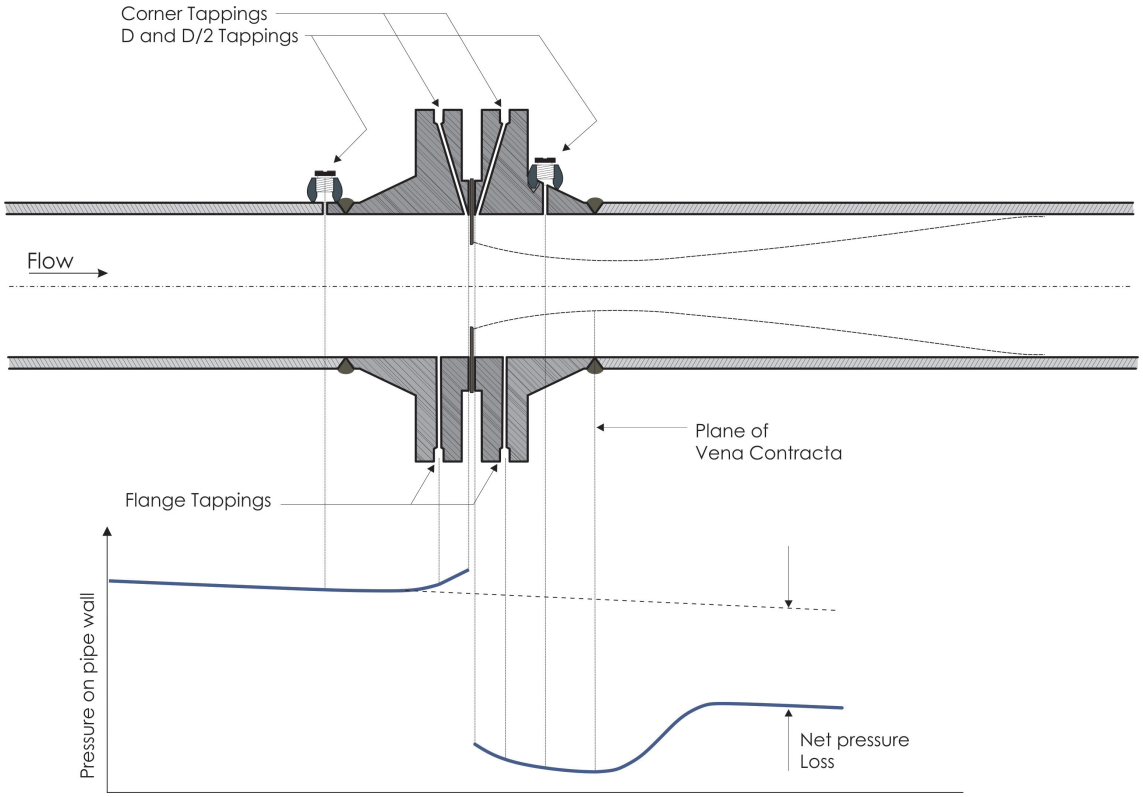

Figure 3.38: Pressure tapping points and qualitative pressure distribution of the flow through an orifice plate following Reader-Harris [92]

$$
\begin{aligned}
C_D = 0.5961 + 0.0261\,\sqrt{\sigma}^{2} - 0.216\,\sqrt{\sigma}^{8} + 0.000521\left(\frac{10^6\,\sqrt{\sigma}}{Re_D}\right)^{0.7} + \\
\left(0.0188 + 0.0063\left(\frac{19\cdot 10^3\,\sqrt{\sigma}}{Re_D}\right)^{0.8}\right)\sqrt{\sigma}^{3.5}\left(\frac{10^6}{Re_D}\right)^{0.3} + \\
\left(0.043 + 0.080e^{-10\,L_1} - 0.123e^{-7\,L_1}\right)\left(1 - 0.11\left(\frac{19\cdot 10^3\,\sqrt{\sigma}}{Re_D}\right)\right)^{0.8}\left(\frac{\sqrt{\sigma}^4}{1-\sqrt{\sigma}^4}\right) - \\
0.031\left(M_2' - 0.8\,M_2'^{1.1}\right)\sqrt{\sigma}^{1.3}
\end{aligned}
\tag{3.84}
$$

and if $D < 71.12\ mm$, the following term must be added to Eq. (3.84)

$$
+0.011\left(0.75 - \sqrt{\sigma}\right)\left(2.8 - \frac{D}{25.4}\right)
$$

Here, $\sqrt{\sigma}(= d/D)$ represents the diameter ratio between the orifice and pipe diameter, Re_D the pipe Reynolds number, L_1 the quotient between the distance of the upstream pressure tapping point to the upstream facing orifice plate's front side and the pipe diameter D. The coefficient M_2' is defined as:

$$
M_2' = \frac{2\,L_2'}{1-\sqrt{\sigma}} \tag{3.85}
$$

where L_2' is the quotient between the distance of the downstream pressure tapping point to the down-

Table 3.8: Length portions L_1 and L_2' depending on the pressure tappings

parameter	corner	flange	D-D/2
L_1	0	$\frac{25.4}{D}$	1
L_2'	0	$\frac{25.4}{D}$	0.47

stream facing orifice plate's front side and the pipe diameter D. Depending on the pressure tapping point locations, the parameters L_1 and L_2' have to be parameterized, as shown in Tab. 3.8.

The standard ISO 5167:2003 specifies the calculation rule. This calculation rule can be assumed well checked against experimental results and, therefore, validated as the reference for the current investigation. As a consequence, own experimental investigations are not necessary while the momentum-based approach is being compared to the results obtained with the standard ISO 5167:2003. These results are also used to validate the numerical simulation. The standard ISO 5167:2003 determines the limits of application for the calculation rule, see Ref. [91] for details. The main relevant limits are:

- the orifice diameter $d \geq 12.5\ mm$,
- the diameter ratio $\sqrt{\sigma}$: $0.10 \leq \sqrt{\sigma} \leq 0.75$,
- the pipe diameter D: $50\ mm \leq D \leq 1000\ mm$,
- and the pipe Reynolds number $Re_D \geq 5000$ (in general).

In addition to this, the pipe's wall roughness must meet specific requirements depending on the diameter ratio $\sqrt{\sigma}$ and the Reynolds number Re_D, see Ref. [91]. The standard ISO 5167:2003 defines three pressure tapping positions, which are the corner tapping points, the flange tapping points, and the D - D/2 tapping points. For the corner tapping points, the pressure is measured directly before and after the orifice plate. The flange tapping points are always 25.4 mm distant from the nearest orifice plate surface. This means the pressure tapping boreholes are placed into the flange. The distance of the D and D/2 tapping points is depending on the pipe diameter D where the upstream tapping point is $1D$ distant to the upstream orifice plate surface and the downstream tapping point is $0.5D$ distant to the upstream orifice plate surface. Any other tapping point arrangements are not admissible. Within the given specifications, a maximum measurement uncertainty of 0.6% is specified for the discharge coefficient C_D according to Ref. [91]. Thereby, all other measured variables are assumed to be determined fault-free. Practically, the measuring uncertainty of flow rate measurements based on measuring orifices is specified within 1% as per Reader-Harris [92], which defines the accuracy the numerical simulation and, consequentially, the momentum-based approach must compete. The standard ISO 5167:2003 [91] also proposes deriving the loss coefficient K from the discharge coefficient C_D with the effect that K is not a constant but dependent on the tapping point couple.

As the literature shows, several authors formed concepts of the calculation of the pressure drop based on the momentum balance. However, approaches employing the momentum balance are almost exclusively applied to determine the irreversible pressure drop but not for the mass flow rate, as shown before.

In 1960, Martin and Pabbi [95] presented their approach to the calibration of an orifice meter for gas flow by comparison with an orifice meter that has been calibrated against an absolute standard. The authors' intention is to reduce the effort of performing large experimental campaigns. Therefore, Martin

and Pabbi use a blend of the momentum balance and the energy balance in the shape of the Bernoulli equation in combination with the mass balance to eliminate unknown variables. The authors' defined control volume is represented by the light red colored area in Fig. 3.39 starting at least $1D$ upstream of the contraction where the flow is not significantly affected by the orifice and reaching up to the vena contracta. This method is quite elaborated due to the following assumptions made by the authors: (1) Friction can be neglected between the upstream plane and the vena contracta since the authors claim the major friction loss occurs in the region of the expanding flow downstream of the vena contracta. (2) More importantly, the pressure in the vena contracta is almost equivalent to the pressure at the downstream-facing side of the orifice plate, which the authors claim is an exact assumption. (3) The pressure the upstream-facing orifice plate exerts on the fluid body is uniformly distributed over the whole plate and equal to the inlet pressure p_1. In the following, this assumption is modified by the authors introducing a coefficient c_{act} to account for the actual force in relation to the idealized force of the plate. The momentum-based approach derived by Martin and Pabbi [95] considers acting and reacting forces as well as momentum fluxes, obtaining

$$\Delta p = \frac{\varrho}{2} v_O^2 \left(\frac{4}{{c_{act}}^2} - \frac{4\, A_O}{c_{act}\, A} \right) \tag{3.86}$$

But the authors do not consider momentum coefficients that account for the non-uniform velocity distribution over the cross-sections and assume a uniform pressure distribution in the vena contracta cross-section. With c_{act} determined experimentally, Eq. (3.86) yields a reasonable correlation with the references.

At the FLOMEKO Conference in 2019, Reader-Harris et al. [96] published current findings on the calculation of the pressure loss ratio of a compressible flow through an orifice plate based on the derivation given in Ref. [92, 62 pp.]. According to Refs. [23, 96], the pressure loss ratio is defined as the ratio of the irreversible pressure drop at the pressure tapping points to the measured one. The authors used the momentum balance to obtain the first portion of a formulation capable of predicting the pressure loss ratio. Therefore, Reader-Harris et al. integrate the equations of motion over the fixed control volume, which is considered only the downstream region. It reaches from the downstream orifice plate surface along the orifice jet edges to the vena contracta cross-section and up to the cross-section $6D$ downstream of the orifice plate. This volume is represented by the light blue area in Fig. 3.39. Reader-Harris et al. assume the pressure over the cross-sections to be uniformly distributed, so the integral pressure terms $\int\limits_{\partial\Omega} p\, dA$ can be simplified to a multiplication of the pressure p and the respective area A. The authors assume the pressure in the vena contracta to be uniform over to the vena contracta cross-section and the downstream orifice plate surface. In addition, the velocity distributions are considered uniformly distributed across the cross-sections as well. But due to the constricting and expanding flow, the momentum coefficients can not be neglected and have to be taken into account.
This approach includes an approximation of the frictional losses since the downstream cross-section is at a distance of $6D$.
The flow between the upstream region $1D$ before the orifice and the vena contracta (light red colored area in Fig. 3.39) as the formulation's second portion is physically modeled via the Bernoulli principle. Consequentially, the presented approach is a blend of momentum and energy conservation to calculate the irreversible pressure drop. The authors obtain a good correlation between the theory and the performed experiments.

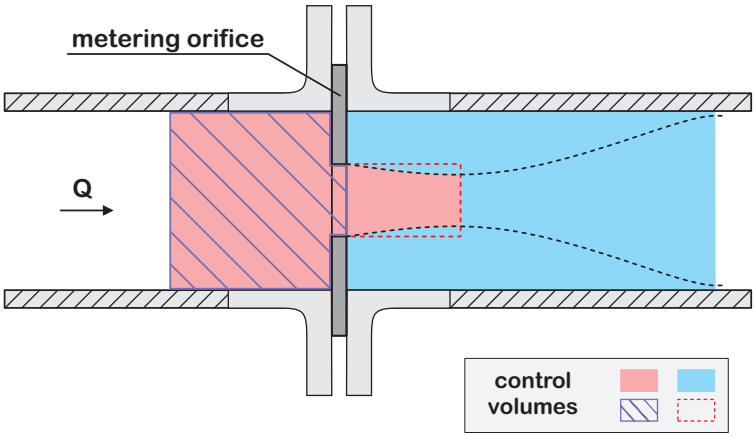

Figure 3.39: Approaches and control volumes used by different authors.

Benedict [57] presented a purely momentum-based approach to calculate the pressure drop of a flow through orifices from an inflow cross-section to the vena contracta downstream of the orifice. This approach is very similar to the one of Martin and Pabbi [95] and illustrated by the cross-hatched area plus the area enclosed by the red dashed line in Fig. 3.39. In contrast to Martin and Pabbi, Benedict took the counteracting force of the upstream-facing orifice plate surface into account as an integral expression. Additionally, the downstream cross-section at the vena contracta extends to the orifice bore area instead of the vena contracta area, as shown by the red dashed line in Fig. 3.39. But the analytic expression that substitutes the integral requires a coefficient depending on the contraction coefficient, which is determined empirically and presumes knowledge of the diameter of the vena contracta. Benedict extrapolated the pressure of the vena contracta cross-section up to a cross-section equal to the orifice bore area. But the author did not consider momentum coefficients and assumed the pressure to be uniformly distributed over the downstream cross-section, which both are strong approximations. It appears that Benedict solely provided the basics as an alternative for the Bernoulli principle because the momentum-based approach is not further pursued.

Nevertheless, some investigations reveal room for improvement in the calculation method and the orifice meter measurements, which shall be presented briefly.
Morrison et al. [97] investigated how the velocity profile upstream of the orifice affects the flow coefficient and the pressure drop, respectively. Therefore, the authors create different velocity profiles upstream of the orifice by special devices, obtaining a deviation of -1 to +6% from the standard value of C_D, dependent on the velocity profile. If swirls are created in the upstream flow the discharge coefficient C_D varies by $\pm$5%. As a result, Morrison et al. [97] propose to use a slotted plate with concentric rings that comprise several radial-orientated slots instead of using an orifice. According to the authors' measurement results, this plate reduces the deviation due to non-fully developed flow or induced swirls to $\pm$0.25% and 2%, respectively. The advantages of the slotted orifice plate mainly are a smaller pressure loss for equivalent area ratios, a discharge coefficient closer to unity, and a faster pressure recovery since the slotted orifice plate acts as a flow straightener as well. The results of Morrison et al. [97] also reveal that the pressure reaches the minimum at $1D$ and is fully recovered around $3.5D$ downstream of the standard orifice. But for the slotted orifice, the pressure recovery is completed after a downstream flow length of $0.5D$.

A refinement of the loss coefficient for larger area ratios is proposed by Urner [98]. The author derives a formula for the loss coefficient of the irreversible pressure drop that is valid for the entire range of the area ratio since existing coefficients give negative results for large area ratios. With this improvement, the pressure loss amounts to zero for an area ratio of unity. Therefore, Urner applies the energy conservation to the upstream region of the orifice since the flow in this region is considered frictionless, as shown by the cross-hatched area in Fig. 3.39. In the downstream region from the orifice plate up to the cross-section where the free-stream is reattached to the wall, Urner applies the momentum balance. But again, momentum coefficients are not taken into account. The improved loss coefficient K is extended by additional factors but remains a function only of the diameter ratio and the discharge coefficient C_D. The resulting loss coefficient can be used outside the scope defined by the standard ISO 5167:2003 and gives reasonable results for every pressure tapping point couple.

Another major flaw of the proposed energy-based or blended methods is that their range of application is limited to specific flow regimes, which means a fully turbulent flow in general. Therefore, investigations have been conducted to extend the range of applicability of the discharge coefficient C_D to transitional and laminar flow.

Ahmed and Ghanem [99] propose a novel formulation for the discharge coefficient C_D for laminar flows at Reynolds numbers referred to the orifice bore area Re_O starting from 0.5 up to 250. The functions are found by parametrizing the results of the numerical study and being compared with the experimental results of other authors. The authors' final formula for C_D at laminar flow regime is divided into two sections with different behavior of C_D. In the range of $0.5 \leq Re_O \leq 10$, the flow coefficient shows a linear dependency on the Reynolds number referred to the orifice bore area Re_O to the power of 0.5: $\sqrt{Re_O}$. On the contrary, in the range of $10 < Re_O \leq 250$, C_D exhibits a non-linear dependency on $\sqrt{Re_O}$. It also appears that C_D converges to a maximum value with increasing Re_O dependent on the diameter ratio. The authors obtain a high correlation between their proposed approach with measured results.

Besides finding better functions for the empirical coefficients K and C_D, literature also provides deeper adaptions to the existing theories or models. Borutzky et al. [100] presented a simulation model to predict the flow through an orifice at laminar and turbulent flow. Based on the profile of C_D vs. $\sqrt{Re_D}$ given in Fig. 3.40, a unified expression to determine the differential pressure for laminar and turbulent flow is obtained. Substitution of C_D in Eq. (3.82) with the formula proposed by Borutzky et al. [100] leads to a sum for the differential pressure that combines a linear share for the laminar and a quadratic share for the turbulent flow. For low flow rates, the quadratic term approaches zero, which means the term representing laminar flow becomes dominant. In the other case, high flow rates diminish the impact of the laminar term since the quadratic term becomes prevalent. This approach is presented as an add-on for existing simulation programs dealing with both laminar and turbulent flow. Eventually, the presented method appears to be capable of describing different flow regimes by a unified approach.

The literature research reveals that no practically applicable approach exists to predict the pressure loss or the flow rate without empirically determined coefficients. However, many approaches employ the momentum balance to consider the downstream region of an orifice and to substitute unknowns in the theory. Up to now, there is no straightforward and complete momentum-based approach. In addition to this, investigations aiming to extend the limited range of application for C_D to laminar and

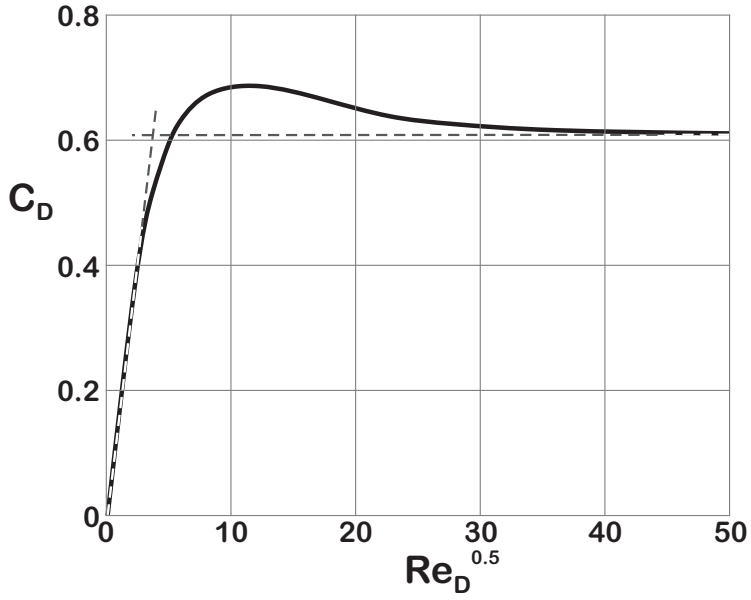

Figure 3.40: Discharge coefficient vs. Reynolds number in the laminar regime as obtained by Merritt [101].

turbulent flow regimes are also reported by the literature. In conclusion, the variety of different approaches shows that the physics behind the flow through an orifice is not completely represented by existing theories. Moreover, some approximations of the derivation of the presented theories are inadequate. Therefore, a purely momentum-based approach is presented in the following chapter.

3.3.2 Applying the Momentum Balance

As the literature research shows, there is no straightforward momentum-based approach for differential pressure-based flow meters. Most approaches combine energy and momentum conservation or are subject to improper or faulty simplifications, like the idealized approach of Benedict [57].
Using the integral momentum balance, proper control volumes have to be chosen. According to the standard ISO 5167:2003 [91], only three different arrangements of the pressure tapping points are allowed: corner, flange, and D-D/2 tapping points. Therefore, the control volume differs for every tapping point position, starting at a cross-section where the center of the upstream tapping point is located and ending where the center of the downstream tapping point is located. For the irreversible pressure drop, the control volume is extended to a distance of at least $1D$ upstream and $6D$ downstream of the orifice plate, where the pressure is assumed fully recovered in accordance with Reader-Harris [92]. Reader-Harris [92, p. 64] states that the pressure is recovered to its maximum extent after $6D$. This is in line with the findings of Müller and Malcherek [102] for the maximum pressure recovery of a sudden expansion. Either way, the control volume comprises the whole fluid body, which is in between both cross-sections as shown by the grey-colored area in Fig. 3.41.

Resuming Eq. (1.47), the viscous pressure loss can be neglected since the control volume is of a short extent ($1.5D$ at maximum), and only low values for the wall roughness are allowed. This simplification is also valid for a control volume covering a reach $1D$ upstream to $6D$ downstream, see Reader-Harris [92]. Reader-Harris states that the pressure loss due to friction within the flow length from $1D$ upstream to $6D$ downstream is significantly less than the pressure loss due to friction in a straight pipe of $7D$ flow length in fully developed flow. For the empirical determination of the systemic

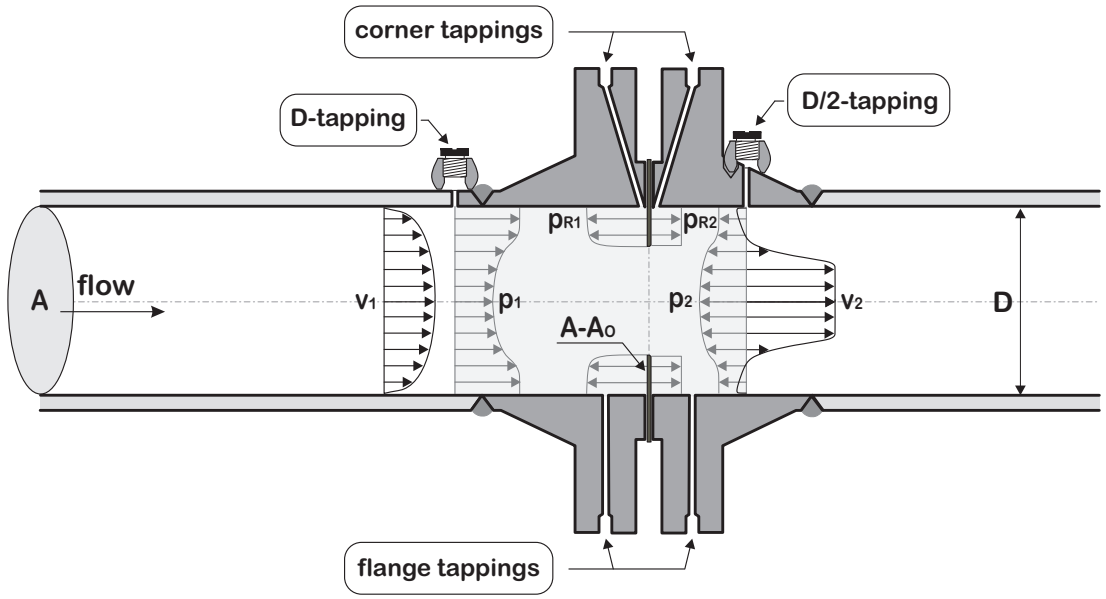

Figure 3.41: Orifice control volume for the D-D/2 pressure tapping points. The radial pressure and velocity distributions are shown for the flange tapping points for lack of space.

or irreversible pressure drop Δp_{irrev}, the gradients of the pressure in the fully developed flow regions upstream and downstream of the orifice can be extrapolated up to the orifice plane, see the lower part in Fig. 3.38. The vertical distance of both lines then yields the irreversible pressure drop. Frictional forces can be evaluated by applying the Weisbach equation (Eq. (1.44)) to the pressure at a certain point in the fully developed flow region upstream and downstream of the orifice. L then represents the distance from that particular point to the orifice plate. With the upstream pressure diminished and the downstream pressure increased by the result of the Weisbach equation, Δp_{irrev} can also be calculated from any point within the fully developed flow region.

The cited standard is not considering the mounting direction of the orifice meter assembly for the calculation of the discharge coefficient C_D, whether the orifice meter is mounted vertically or horizontally. But the pressure resulting from the height difference can be factored in the measured pressure drop Δp. For the sake of simplicity, the orifice meter is thought to be mounted for horizontal flow, so the term considering the gravitational acceleration can be neglected since the dot product of $\vec{g} = [0; -9.81]$ and $\vec{n}_v = [1; 0]$ gives zero. For any other mounting direction besides horizontal flow, the vertical portion of gravitational force is considered by the second element of $\vec{n}_v$. Additional forces $\vec{F}_{add}$ are absent. In setting up the momentum balance for the orifice, the pressure forces of the inflow and outflow cross-section have to be taken into account. But force is also exerted on the fluid by the orifice plate because the orifice plate redirects the flow. In consequence, the reacting pressure forces of the upstream $p_{R,1}$ and the downstream orifice plate face $p_{R,2}$ add to the sum of pressure forces. Together with the momentum fluxes through the inflow and outflow cross-section Eq. (1.46) gives

$$0 = -p_1\ A\ \vec{n}_1 \cdot \vec{n}_v - \ p_2\ A\ \vec{n}_2 \cdot \vec{n}_v - \ (p_{R,1}\ \vec{n}_1 \cdot \vec{n}_v + p_{R,2}\ \vec{n}_2 \cdot \vec{n}_v)\ (A - A_O) \\ - (\beta_1\ \vec{v}_1 \cdot \vec{n}_1 + \beta_2\ \vec{v}_2 \cdot \vec{n}_2)\ \varrho\ A\ \frac{Q}{A} \tag{3.87}$$

with $A - A_O$ representing the orifice plate's surface area perpendicular to the flow direction and the mean velocities $v_1 = v_2 = Q/A$. For a horizontal main flow direction oriented in the direction of the x-axis, the normal unit vectors are $\vec{n}_1 = [-1; 0]$ since $\vec{n}_1$ points outwards of the control volume in the opposite flow direction and $\vec{n}_2 = [1; 0]$, $\vec{n}_v = [1; 0]$ since both vectors point in the positive x-axis direction. Consideration of the normal unit vectors within Eq. (3.87) yields the correct signs of all terms, so Eq. (3.87) reads

$$0 = p_1\ A - \ p_2\ A - \ (p_{R,1} - p_{R,2})\ (A - A_O) + (\beta_1 - \beta_2)\ \varrho\ \frac{Q^2}{A} \tag{3.88}$$

As already shown for the sudden contraction, the upstream reacting pressure $p_{R,1}$ is not constant over the radius of the orifice either. Therefore, $p_{R,1}$ is defined as the average of the effective pressure $p(r)$ acting on the orifice's upstream surface. Integrating the effective pressure over the orifice surface divided by the orifice surface area $(A - A_O)$ yields $p_{R,1}$

$$p_{R,1} = \frac{1}{A - A_O} \int_{R_2}^{R_1} 2\ \pi\ r\ p(r) dr \tag{3.89}$$

with r as the variable radius value. Analogously to the sudden contraction, the pressure at the outer upstream radius of the orifice $p(R)$ is approximately equal to the inlet pressure p_1, see the function named $p_{R,1}$ in Fig. 3.42 as a representative example. Figure 3.42 shows the dimensionless effective pressure $p(r)/p_1$ over the dimensionless orifice plate radius r/R with R representing the pipe radius. Starting from the pipe wall at $r/R = 1$, the effective pressure $p(r)$ is constant until the radial flow touches the orifice surface (here: around $r/R \approx 0.84$). From this point, the effective pressure $p(r)$ decreases to a minimum due to the increasing radial velocity up to the orifice bore edge at $r/R = 0.714$. Within the orifice bore, the effective pressure recovers to almost constant values in the center $p(0)$. The profile of the dimensionless pressure over the dimensionless radius is pronounced stronger for lower area ratios, especially the minimum value and the gap between $p(0)$ and p_1.
Although $p(r)$ is not constant over the radius, Eq. (3.89) is parameterized by

$$p_{R,1} = p_1 - c_{P,1} \frac{\varrho}{2} \frac{Q^2}{A^2}, \tag{3.90}$$

with $c_{P,1}$ as the upstream pressure coefficient that takes into account the non-uniform pressure distribution over the orifice surface. The pressure coefficient $c_{P,1}$ also considers the dependency of the pressure integral on the orifice area ratio σ.

In contrast to the upstream reacting pressure, numerical simulations show that the downstream reacting pressure $p_{R,2}$ is almost constant over the radius, as shown in Fig. 3.42. It appears that $p_{R,2}$ can be approximated very precisely by applying the Bernoulli principle along the pipe's center streamline, which yields

$$p_{R,2} = p_1 + \frac{\varrho}{2} v_1^2 - \frac{\varrho}{2} v_{max}^2 \tag{3.91}$$

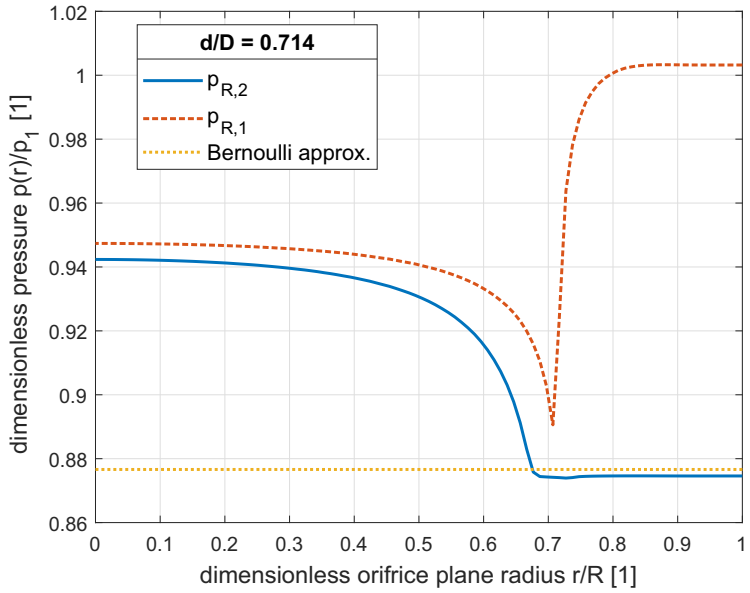

Figure 3.42: Dimensionless pressure distribution $p(r)/p_1$ over dimensionless orifice radius r/R for both orifice sides and the Bernoulli approximation of the downstream orifice pressure

with v_{max} as the maximum axial flow velocity (on the center streamline). Numerical simulations show that $p_{R,2}$ calculated as per Eq. (3.91) perfectly matches the lowest pressure obtained by the simulation. Moreover, the simulations reveal that the lowest pressure extends up to the radial pipe wall and even applies to the whole downstream-facing orifice plate surface, detailed in Chap. 3.3.3. The solution of Eq. (3.91) named 'Bernoulli approx' is also shown in Fig. 3.42 for a diameter ratio $\sqrt{\sigma}$ of 0.714. The deviation of the simulated pressure at the downstream orifice plate surface from the Bernoulli approximation as per Eq. (3.91) amounts to approximately 0.3%, which is a representative value for all investigated area ratios σ (except for very low values of σ). The proposed parametrization of the reacting pressures p_R based on the Bernoulli principle is therefore justified.
Two different approaches solely concerning the downstream reacting pressure $p_{R,2}$ will be discussed in the following.

(I) For turbulent flow, the upstream centerline velocity v_1 can be substituted by the average velocity Q/A, which is a good approximation since the velocity is homogeneously distributed over the whole cross-section in the region of a fully developed flow upstream of the orifice. The maximum velocity v_{max} occurs in the vena contracta, where the flow reaches its maximum convergence. Since the shape and the exact location of the vena contracta are unknown, v_{max} is substituted by Q/A_O assuming the diameter of the vena contracta to be equal to the orifice diameter. However, the vena contracta area is not equal to the orifice bore area A_O, so the orifice bore cross-section must be multiplied by the contraction coefficient c_C, accounting for the reduced flow area: $v_{max} = Q/(c_C\, A_O)$. Introducing the contraction coefficient c_C as a function of the area ratio σ that takes into account the discrepancy between v_{max} and Q/A_O, Eq. (3.91) can be rewritten as

$$p_{R,2} = p_1 + \frac{\varrho}{2}\frac{Q^2}{A^2} - \frac{\varrho}{2}\frac{1}{c_C^2}\frac{Q^2}{A_O^2} \tag{3.92}$$

Anticipating the results of the numerical simulations, the contraction coefficient c_C is not dependent on the flow rate and can be parametrized by

$$c_C = 0.4664\,\sigma^2 - 0.07021\,\sigma + 0.6023 \tag{3.93}$$

as shown in Fig. 3.43 by the continuous line. The point $(c_C = 1;\ \sigma = 1)$ is not simulated but included in the fit function of Eq. (3.93) as a practically valid supporting point. Although out of the applicable range of the area ratio, data is also obtained for $\sigma = 0.666$ and $\sigma = 0.836$ to equally fill the gap and show the validity of the fit function. The parametrization found by Dayev and Kairakbaev [89] and Weisbach [19] is also shown by the dashed lines for comparison purposes. The deviation between the fit function and the parametrization of Dayev and Kairakbaev and Weisbach amounts to 4% at maximum in both cases.

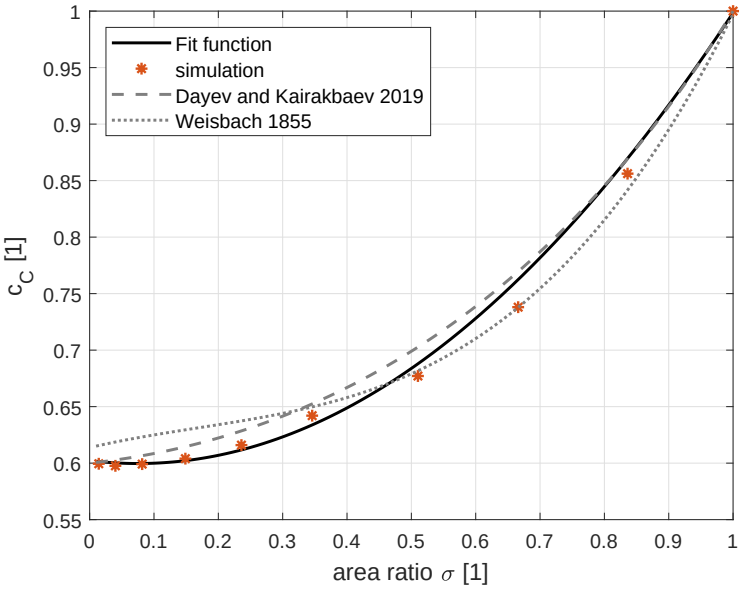

Figure 3.43: Contraction coefficient c_C vs. the area ratio σ.

Using Eqs. (3.90) and (3.92) into Eq. (3.88) flipped to $p_1 - p_2$ gives

$$\Delta p_{irrev,I} = \varrho \frac{Q^2}{A^2}\left(\beta + \frac{1}{2}\left(\frac{A^2}{A_O^2}\frac{1}{c_C^2} - \frac{A}{A_O}\frac{1}{c_C^2} - 1 - c_{P,1}\right)\left(1 - \frac{A_O}{A}\right)\right) \tag{3.94}$$

with the irreversible pressure drop $\Delta p_{irrev,I} = p_1 - p_2$. Additionally, the momentum coefficients β_1 and β_2 are combined to the total momentum coefficient $\beta = \beta_2 - \beta_1$, which reduces the number of variables to be parameterized.

In this case, $c_{P,1}$ is dependent on the control volume applied to the respective pressure tapping points. This means that a mathematical function for $c_{P,1}$ must be found for every control volume when approach (I) is applied to flow measurement control volumes. However, from a hydraulic point of view, the orifice can be seen as a sudden contraction followed by a sudden expansion. Therefore, Eq. (3.50) as found for the sudden contraction can be introduced to Eq. (3.94) substituting the upstream pressure coefficient $c_{P,1}$ for the calculation of the irreversible pressure drop:

$$\Delta p_{irrev,I} = \varrho \frac{Q^2}{A^2} \left(\beta + \frac{1}{2} \left(1.55 - 2.15 \frac{A_O}{A} + 1.25 \frac{A_O^2}{A^2} - \left(0.65 + \frac{1}{c_C^2} \right) \frac{A}{A_O} + \frac{1}{c_C^2} \frac{A^2}{A_O^2} \right) \right) \tag{3.95}$$

The momentum-based loss coefficient of the first approach $K_{M,I}$ is represented by the bracketed term of Eq. (3.95), yielding

$$K_{M,I} = \beta + \frac{1}{2} \left(1.55 - 2.15 \frac{A_O}{A} + 1.25 \frac{A_O^2}{A^2} - \left(0.65 + \frac{1}{c_C^2} \right) \frac{A}{A_O} + \frac{1}{c_C^2} \frac{A^2}{A_O^2} \right) \tag{3.96}$$

Equation (3.95) predicts the pressure loss $\Delta p_{irrev,I}$ of a flow through an orifice very precisely, as shown in the following chapters. But it shall be emphasized that the upstream pressure coefficient $c_{P,1}$ of the sudden contraction, see Eq. (3.50), is derived from a control volume with sufficient distance to the sudden contraction. Thus, the pressure is homogeneously distributed over the inlet cross-section. In consequence, Eq. (3.95) can not be applied to control volumes used for volume flow determination since the inlet pressure p_1 depends on the control volume. In this case, a parameterization of $c_{P,1}$ for every tapping point couple must be obtained and used within Eq. (3.94).

(II) To avoid an additional parameterization of $c_{P,1}$ and to keep the equation for the pressure drop well-arranged, the second approach consists of parameterizing $p_{R,2}$ similarly to $p_{R,1}$ with reference to the upstream pressure p_1 and the upstream average velocity Q/A

$$p_{R,2} = p_1 - c_{P,2} \frac{\varrho}{2} \frac{Q^2}{A^2}. \tag{3.97}$$

Here, the downstream pressure coefficient $c_{P,2}$ takes into account the deviation of the effective pressure from the inlet pressure p_1. According to Eqs. (3.90) and (3.97), both reacting pressures have the same structure and will therefore be combined into one expression, namely the differential reacting pressure Δp_R

$$\Delta p_R = p_{R,1} - p_{R,2} = c_P \frac{\varrho}{2} \frac{Q^2}{A^2} \tag{3.98}$$

Using Eqs. (3.90) and (3.97) into Eq. (3.98) and with the definition $c_P = -c_{P,1} + c_{P,2}$, the inlet pressure p_1 is canceled out. This substitution enjoys the advantage that the pressure coefficient c_P is not any more dependent on the control volume or the pressure tapping point, respectively. Using Eq. (3.98) into Eq. (3.88) and flipped to $p_1 - p_2$ gives

$$p_1 - p_2 = \left(c_P \frac{\varrho}{2} \frac{Q^2}{A^2} \right) \left(1 - \frac{A_O}{A} \right) + \varrho \frac{Q^2}{A^2} \beta_2 - \varrho \frac{Q^2}{A^2} \beta_1 \tag{3.99}$$

The momentum coefficients β_1 and β_2 are combined to the total momentum coefficient $\beta = \beta_2 - \beta_1$. After some rearrangement of Eq. (3.99), the formula of the irreversible pressure drop $\Delta p_{irrev,II} = p_1 - p_2$ over an orifice for the second approach is obtained

$$\Delta p_{irrev,II} = \varrho \frac{Q^2}{A^2} \left(\beta + \frac{c_P}{2} \left(1 - \frac{A_O}{A} \right) \right) \tag{3.100}$$

The momentum-based loss coefficient of the second approach $K_{M,II}$ is again represented by the

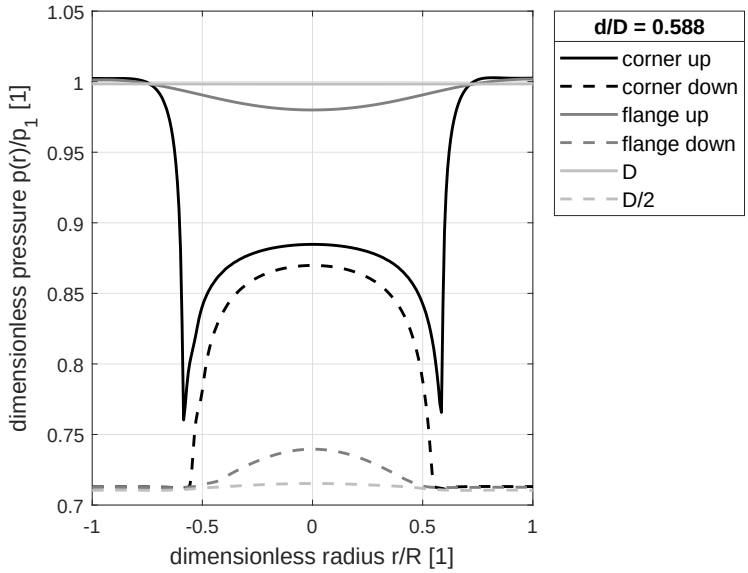

Figure 3.44: Dimensionless radial pressure distribution $p(r)/p_1$ over dimensionless radius r/R for all pressure tapping planes

bracketed term of Eq. (3.100):

$$K_{M,II} = \beta + \frac{c_P}{2}\left(1 - \frac{A_O}{A}\right) \tag{3.101}$$

Equations (3.95) and (3.100) are valid for control volumes with sufficient distance to the orifice, so the pressure is uniformly distributed over the cross-section as assumed in the derivation of the momentum balance. Figure 3.44 shows the pressure distribution for a diameter ratio $d/D = 0.588$ versus the cross-sectional plane radius at every pressure tapping point. Continuous lines represent the upstream and dashed lines the downstream region. The graphs in Fig. 3.44 reveal that the pressure is not uniformly distributed over the cross-section since it is diminished in the upstream core flow but increased in the downstream core flow. Only for the D-D/2 tapping points the pressure distribution can be assumed uniformly distributed in good approximation. But for the flange tapping points and the corner tapping points, in particular, the pressure distribution differs significantly from a uniform one.

As a consequence, Eqs. (3.95) and (3.100) directly predict the irreversible pressure drop of a flow through an orifice when the control volume reaches up to an inlet and outlet cross-section with homogeneous pressure distribution. If the control volume is extended up to a downstream cross-section where the flow is fully re-developed ($\beta_2 = \beta_1$), the total momentum coefficient β equals zero.

Due to the simplified approach with the combined pressure coefficient c_P, Eq. (3.100) is applied to the given tapping point locations determining the mass flow rate. Therefore, the control volume only covers the volume between the cross-sections of the respective pressure tapping point couple. Such a control volume is shown in Fig. 3.41 by the grey-shaded area. This means that the velocity distribution is not uniform over the inlet and the outlet cross-sections, so both momentum coefficients have to be taken into account. Since the differential pressures are obtained at the pipe wall, numerical simulations indicate that the pressure at the pipe wall is not equal to the average pressure over the whole cross-section as shown in Fig. 3.44. As a result, the pressure over the cross-section can not be considered equally distributed as assumed in the derivation of the momentum balance. Conversely,

the exact pressure must be taken into account, which is represented by the integral of the pressure over the area. This means that the left side of Eq. (3.100) is substituted by the integral expressions of the pressure over the area:

$$\frac{2\pi}{\pi R^2}\int_0^R rp_1(r)dr - \frac{2\pi}{\pi R^2}\int_0^R rp_2(r)dr = \varrho\frac{Q^2}{A^2}\left(\beta + \frac{c_P}{2}\left(1 - \frac{A_O}{A}\right)\right) \tag{3.102}$$

But the pressure integrals must be replaced by the pressure as obtained at the pressure tapping points at the wall for an analytically evaluable approach. In consequence, an additional coefficient must be taken into consideration, accounting for the deviation of the pressure of the respective cross-section from the pressure obtained at the wall Δp:

$$\frac{2}{R^2}\int_0^R r\left(p_1(r) - p_2(r)\right)dr := \frac{\Delta p}{\gamma} \tag{3.103}$$

Therefore, the pressure exaggeration coefficient γ relates the differential wall pressure to the average differential pressure for every pressure tapping point couple. Here, the average differential pressure is the equivalent to Δp. With the pressure exaggeration coefficient γ included,

Equation (3.100) gives

$$\frac{\Delta p}{\gamma} = \varrho\,\frac{Q^2}{A^2}\left(\beta + \frac{c_P}{2}\left(1 - \frac{A_O}{A}\right)\right) \tag{3.104}$$

Flipping Eq. (3.104) to the volume flow rate Q, the final formula for the flow rate through orifices gives

$$Q = \sqrt{\frac{1}{\gamma\left(\beta + \frac{c_P}{2}\left(1 - \frac{A_O}{A}\right)\right)}} \cdot \sqrt{\frac{\Delta p}{\varrho}}\,A \tag{3.105}$$

which is completely momentum-based and requires no empirical coefficients. For a closed momentum-based approach, the required coefficients β, γ, and c_P must be parametrized with the aid of numerical simulations, which are presented in the following. The momentum coefficient β, as well as the pressure exaggeration coefficient γ, have to be obtained for every pressure tapping point couple. Only the pressure coefficient c_P is generally valid since c_P is independent of the applied control volume.

3.3.3 Numerical Modelling

Validation of the Numerical Model

The three-dimensional numerical simulation is performed with the CFX module of ANSYS 20 and the general settings, as discussed in Chap. 2.

The size of the simulation domain must ensure that fully developed flow enters the region of interest, which starts $1D$ upstream and ends $6D$ downstream of the orifice plate for the prediction of the irreversible pressure drop as proposed by Reader-Harris [92]. In addition, the downstream boundary must be placed sufficiently distant from the region of interest to ensure no interaction with the outlet boundary condition. Reader-Harris et al. [96] used an inlet flow length of $30D$ for numerical investigations of compressible flow. This is a sound definition since the investigation of Morrison et al. [97] shows that achieving fully developed flow upstream of the orifice is important to the determination of the discharge coefficient C_D. Although the velocity profile is strongly affected by the orifice in the region of the orifice meter's pressure tapping points, Morrison et al. show that the upstream flow condition is of significant

importance as detailed in Chap. 3.3.1.
Therefore, the simulation domain of the present numerical model includes an upstream flow length of $11D$ and a downstream length of $8D$. As a result, the defined simulation domain ensures fully developed flow to enter the orifice-affected flow region since the momentum coefficient β solely changes in the third decimal point over a flow length of $2D$ before entering the control volume at $1D$. In addition, the outlet at $8D$ downstream of the orifice prevents the outlet boundary conditions from diffusing into the region of interest at $6D$.
To approach the final settings of the numerical simulation and to perform the mesh convergence study, the pipe diameter D is set to 105 mm, the orifice bore diameter d to 61.75 mm, and the orifice plate thickness to 2.1 mm. Both diameters comply with the numerical model of Lebedev et al. [103], whose results are used as an additional verification of the employed numerical model. The final numerical simulations are performed for water at a temperature of $25\,^{\circ}C$.

Generally, an unstructured mesh of tetrahedrons with an edge length of 2 mm and a growth rate of 1.2 is applied to the whole simulation domain. The edge length of the mesh elements automatically reduces smoothly to 0.5 mm with decreasing distance to the edges or faces of the simulation domain. The mesh in the vicinity of the pipe walls is additionally refined by layers of mesh elements with increasing height towards the interior pipe. Therefore, the first layer height y_1 is calculated as per Eq. (2.9) for the maximum flow rate to be investigated and a dimensionless wall distance $y^+ < 5$. The total thickness of the boundary layer δ is estimated initially as per Eq. (2.10), where the growth rate of the layer height can be deduced to maintain a resolution of the boundary layer by 10-15 element layers. Setting up the near-wall mesh in ANSYS, the option 'first layer thickness' with the value $2.5{\cdot}10^{-5}$ m is applied, which is slightly lower than the calculated value as per Eq. (2.9). With the calculated boundary layer thickness $\delta \approx 0.6$ mm, the number of layers is extended to 15, which results in a total layer height of approximately 1 mm to account for potential locally increased boundary layer thicknesses.

According to the standard ISO 5167:2003 [91], the orifice inlet edge must be sharp, which means its radius must not be greater than $4d/10\,000$. For setting up the simulation model, the mesh element size around the inlet edge, as well as the outlet edge, is set to a value not greater than $4d/10\,000$ with a smooth increase of the element size towards the inner simulation domain. Erdal and Andersson [104] investigated the effect of different settings of a two-dimensional simulation model on the resulting pressure drop of a metering orifice. The authors' investigation revealed that the pressure drop of an orifice is very sensitive to the mesh size in the vicinity of the orifice edges but not to the mesh size of the entire domain. Erdal and Andersson showed that the pressure drop is strongly dependent on the edge radius and appears to converge towards a fixed value of the pressure drop for radii less than $0.0005d$. Another outcome of Erdal and Andersson [104] is that the refinement of the mesh in certain areas of the domain is more important than the total number of cells. Therefore, the orifice bore edges are refined by elements of a maximum edge length of $4d/10\,000$ with d as the lowest investigated orifice bore diameter of the further numerical studies at a growth rate of 1.1. The orifice plate faces are refined with elements of 0.5 mm edge length at maximum and at a growth rate of 1.1 since both surfaces are crucial for the determination of the pressure coefficient c_P. Both local mesh refinements plus the near-wall mesh refinement prove beneficial for a symmetrical flow downstream of the orifice as the tendency of oscillations is significantly reduced. The employment of an unstructured mesh proves beneficial for the mesh quality.
Erdal and Andersson [104] also found out that the main flow velocity gradient in the boundary layer is in the radial direction, which means that the radial resolution of the mesh must be higher than its axial resolution. This effect is covered by the described near-wall mesh refinement. The described mesh in

the vicinity of the orifice is shown in Fig. 3.45.

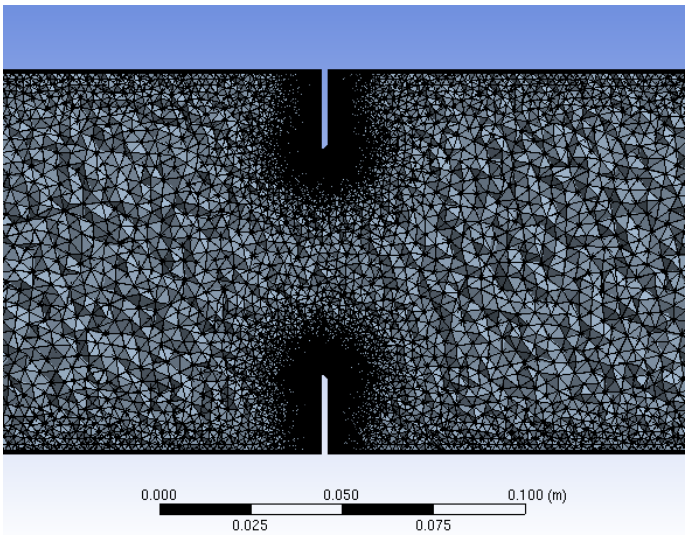

Figure 3.45: Sectional view of the applied mesh in the vicinity of the orifice with refined mesh around the orifice plate and pipe wall region

It shall be mentioned that employing a mesh resolving the boundary layer is strongly recommended by Erdal and Andersson [104]. By that time, the authors revealed that the application of wall functions in the downstream region from the orifice plate up to $10D$ results in considerable deviations of the computed turbulence kinetic energy from measured values. Nowadays, well-checked and highly sophisticated wall functions are available. Therefore, the ANSYS CFX Solver Theory Guide [28] recommends employing wall functions for general-purpose simulations for the sake of efficiency, see Chap. 2.2.3.
Besides, the geometrical shape of the orifice, the range of the Reynolds number, and the pipe roughness are of major importance in setting up the numerical model. According to the standard ISO 5167:2003 [91], for a diameter ratio $\sqrt{\sigma}$ of 0.59 and a Reynolds number range of $6 \cdot 10^4$ to $1 \cdot 10^6$, ks must be within the range of 0 to 0.0105 mm. Therefore, the sand-grain roughness ks for all closed boundaries of the simulation domain is set to $1 \cdot 10^{-5}\, m$ since this is a more practical relevant value than assuming a hydraulically smooth pipe. But the standard ISO 5167:2003 states that the downstream wall roughness is of subordinate importance to meeting the defined uncertainty of the calculation results.

The kω-SST turbulence model again shows the best agreement with measurement data of turbulence quantities and is therefore selected for the numerical model of the metering orifice. Since the assessment of turbulence models is extensive for the metering orifice as shown in the following section, the mesh convergence study is prefixed for the sake of greater clarity in this chapter.
The mesh convergence is proven by the method proposed by Celik et al. [42] and performed for an orifice bore diameter d of 61.75 mm and a mass flow rate $\dot{m}$ of 16.44 kg/s. The combined momentum coefficient β, the pressure exaggeration coefficient γ, and the pressure coefficient c_P are the relevant quantities chosen to quantify the mesh convergence. The chosen parameters are obtained at the corner tapping points (represented by the subscript corner) since the parameters in the region very close to the orifice appear to be most sensitive to mesh adaptions - except for the pressure coefficient c_P,

which is independent of the pressure tapping point. Table 3.9 shows the results of the quantities used for the evaluation of the mesh convergence as obtained for the three different mesh types.
The intermediate mesh represents the described mesh settings, resulting in a total number of 18 550 778 mesh elements. The coarse mesh is obtained by setting the element edge length of the main mesh to 4 mm, the orifice wall to 0.8 mm, and the orifice edge to 0.2 mm, resulting in 5 392 079 mesh elements. The fine mesh is obtained by setting the element edge length of the main mesh to 1.5 mm, the orifice wall to 0.4 mm, and the orifice edge to 0.05 mm, resulting in 37 385 726 mesh elements. Comparing the results of the three meshes, the change in the relevant quantities amounts to values around 1% to be considered negligible. But β and γ appear to exhibit oscillatory convergence. Since c_P changes insignificantly, the apparent order o is strongly increased to 22 in comparison with the solution method's apparent order of 2. According to Celik et al. [42], the high value of the apparent order can be explained because c_P almost converged to the final value. However, the numerical uncertainty of the coefficients is represented by the grid convergence index GCI for the fine grid, represented by GCI_{if} in Tab. 3.9. The maximum of GCI_{if} amounts to 2.1% for γ_{corner} but is below 0.01 % for c_P compared with the respective values for the medium mesh. Since there is no objective criterion for when the GCI is sufficiently small, the evaluation of the GCI remains a task of the user. Therefore, the pressure profiles are compared as an additional justification.

Table 3.9: Results of the mesh convergence study with $d = 61.75\,mm$ and a mass flow rate $\dot{m}$ of $16.44\,kg/s$

	β_{corner}	γ_{corner}	c_P
f_f, f_{int}, f_c [1]	0.4769, 0.481, 0.4732	1.4585, 1.4488, 1.4647	-19.3577, -19.2105, -19.1694
o [1]	1.8538	1.4269	22.0069
$f_{ext,ci}$ [1]	0.4878	1.4290	-19.2105
$f_{ext,if}$ [1]	0.4694	1.4831	-19.3586
$e_{a,if}$ [%]	0.85	0.67	0.76
$e_{ext,if}$ [%]	1.6	1.66	<0.01
GCI_{if} [%]	1.97	2.11	0.01

In addition to the GCI, Fig. 3.46 shows the axial pressure profile along the pipe wall for the coarse (dotted line), medium (dashed line), and fine mesh (continuous line). All pressure profiles show a very high correlation, especially upstream of the orifice and resuming at $2D$ downstream. Around the minimum value, the profiles of the pressure exhibit an apparent deviation for all meshes. But the location of the minimum pressure is predicted at almost the same flow length, and the maximum pressure recovery is predicted at a downstream flow length of approximately $6D$ by all mesh configurations at a very similar magnitude. It is, therefore, justified to confirm the finding of Erdal and Andersson [104] that the mesh in the vicinity of the orifice is the decisive part since the flow is highly disturbed in the initial downstream region. In contrast, the mesh in the upstream region and after a downstream flow distance of $6D$ is of subordinate importance. However, the maximum deviation of the pressure profile reaches 2% for the medium mesh compared with the coarse mesh. But the deviation between the medium and the fine mesh amounts to less than 1% at maximum occurring around $0.5D$. As a result, it is proven that the medium mesh provides sufficient accuracy. Hence, the medium mesh with the

described parameters will be used for the following numerical simulations.

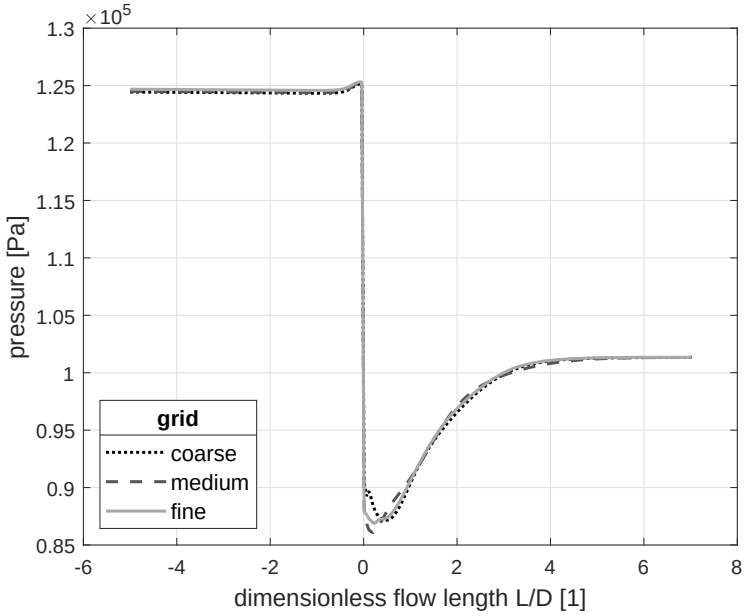

Figure 3.46: Axial pressure distribution along the wall for the coarse, medium, and fine mesh

Assessment of Turbulence Models

Own investigations of the orifice reveal that the deviation of the computed differential pressure from the one obtained with the ISO 5167:2003 decreases from 2-3% with the kϵ to 0.6-1.6% with the kω-SST turbulence model. In the following, it will be justified that this turbulence model, once more, is the best option by comparing the numerical results to measured data.

The numerical investigation of Imada et al. [105] of flows through orifices shows that better agreement with the results of standard ISO 5167:2003 [91] is achieved by applying the kω-SST turbulence model instead of the kε turbulence model. Nevertheless, the deviation of the numerical results obtained by Imada et al. from the standard results amounts to 4.9%, which appears somewhat large.

With regard to comparing the numerical results with the literature numbers, the described numerical model and especially the mesh setting can now be used to evaluate the turbulence model performance. Therefore, the mesh is scaled to the applied pipe diameters of the specific investigation to maintain an almost constant mesh density over the radius. A streamlined mesh convergence study (not presented) confirms this practical execution.

Erdal and Andersson [104] assessed the performance of different kε turbulence models predicting the flow through an orifice. It turned out that the turbulence kinetic energy k is more sensitive to mesh adaptions than the velocities, so k is used in their assessment. The numerical results of k are compared with the measured results of other authors. Erdal and Andersson [104] reveal that the flow behavior can not be predicted in detail with the kε turbulence model where only the general trend in the flow field is provided. Especially the turbulence kinetic energy k near the wall is not predicted physically correct using the kε turbulence model. This finding is in compliance with the obtained results for the turbulence intensity J for the sudden contraction, see Chap. 3.1.4. Erdal and Andersson [104]

propose to avoid the use of the kε turbulence model due to its specific deficiencies, which come into full effect for an orifice flow. The authors' assertion is examined by comparing the results of own numerical simulations with the measured results presented in Erdal and Andersson [104]. Unfortunately, the raw data set is not available so the numerical results can only be compared with Ref. [104] based on the charts. Figure 3.47 shows the dimensionless pipe radius r/R with $R = D/2$ at the vertical axis versus the turbulence kinetic energy k normalized by the squared mean velocity Q/A at the horizontal axis for an intuitive graphical representation. A dimensionless pipe radius r/R of minus unity represents the pipe wall and zero the center line. The measured profile of the results presented in Ref. [104] for a downstream flow distance of 2.5D and 5D is given by markers, whereas the numerical results of different turbulence models are shown by lines.

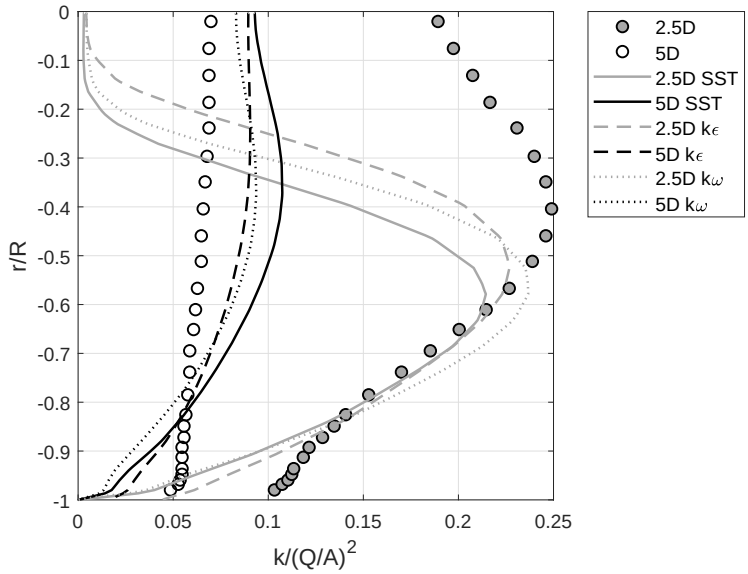

Figure 3.47: Normalized pipe radius r vs. the dimensionless radial normalized turbulence kinetic energy k distribution of simulated and measured results of Erdal and Andersson [104]

Figure 3.47 shows that the profile of the measured k can not be reproduced by the numerical models. This is in line with the numerical results of Erdal and Andersson [104]. Especially the strong decrease of k with r approaching the centerline ($r = 0$) as predicted by all numerical results for 2.5D is not observed in the referenced measurements. In the near-wall region where r/R approaches minus unity, the profiles of the measured and the computed results exhibit a significant deviation. Specifically, the kε turbulence model (dashed line in Fig. 3.47) shows its deficiencies in the near-wall region since k is not zero at the wall. This is physically not valid because the velocity and, therefore, its fluctuations are zero at the wall. But the general trend for the measured profile at 5D is predicted slightly more precisely with the kε turbulence model. The kω (dotted line) and the kω-SST turbulence model correctly capture the real physics of k in the near-wall region. Both ω-based models exhibit a very similar shape, although they also fail to reproduce the measured magnitude of k and its location. The kω-SST turbulence model predicts lower values of k compared with the kε and the kω turbulence model, which can be explained by the employed production limiter P_k in the kω-SST turbulence model by default, see Menter et al. [35]. But ANSYS provides optional production limiters for P_k also for the kε and the kω turbulence model. The ANSYS CFX Solver Theory Guide [28] recommends its use to avoid excessive values in stagnation regions, which means that the production limiter is disabled for the current

simulation with the kε and the kω turbulence model.
In conclusion, the measured profiles of the turbulence kinetic energy k, as presented by Erdal and Andersson [104], can not be reproduced by the investigated turbulence models. But the ω-based turbulence models show a more physical behavior of k in the near-wall region. Based on the current investigation, it is justified that the use of the kε turbulence model shall be avoided when simulating the flow through an orifice. Furthermore, it is not possible to give a recommendation for the kω-SST or the kω turbulence model based on the present measurement data of k.

Shan et al. [106] investigated the flow field downstream of an orifice with the aid of particle image velocimetry (PIV) for a diameter ratio d/D of 0.62. The authors also derived the turbulence kinetic energy k from the velocity fluctuations of the PIV measurements. The distribution of k over the radius r is given in Fig. 3.48 at four different positions, indicated as multiples of the pipe radius R. The vertical axis represents the dimensionless pipe radius r/R and the horizontal axis the turbulence kinetic energy k normalized by the squared maximum flow velocity v_{max} at the centerline. The measurement results are represented by the square markers whereas the numerical results of Shan et al. are shown by the grey line. The authors employed a Reynolds stress model (RSM), which directly computes the stresses of the Reynolds stress tensor $\mathbf{R}$ (see fluctuation terms in Eq. (2.3)). Thus the RSM directly accounts for interactions in the turbulent flow, see Ref. [28]. Reynolds stress models are more elaborated models and therefore considered the most complete turbulence models applicable to RANS simulations. However, the results of Shan et al. in Fig. 3.48 are extended by the results of the own numerical model with the kε, the kω, and the kω-SST turbulence model.

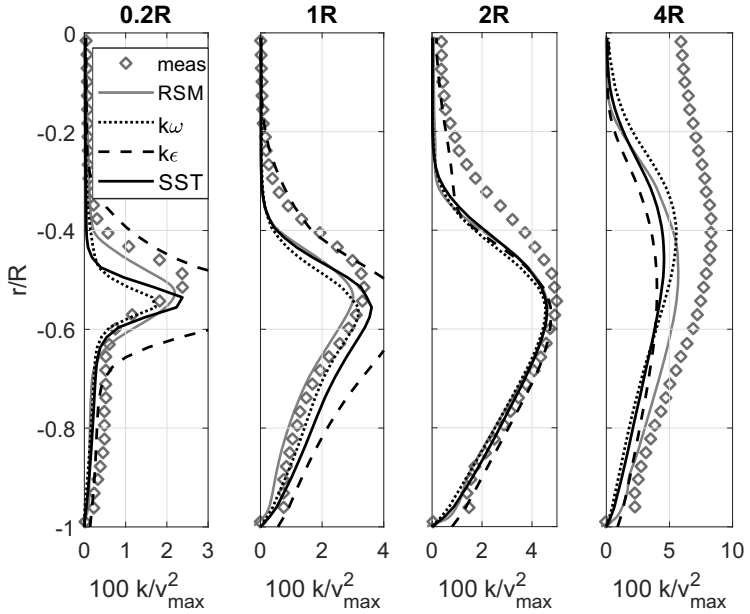

Figure 3.48: Normalized pipe radius r vs. the dimensionless radial normalized turbulence kinetic energy k distribution of simulated and measured results of Shan et al. [106]

For flow distances of $0.2R$, $1R$, and $2R$, the RSM and the ω-based turbulence model results show reasonable agreement with the measurement results. Only the kε turbulence model deviates considerably and exhibits excessive maximum values at $0.2R$ and $1R$. It also fails to reproduce the development of k from the wall into the center flow field. At a flow distance of $2R$, all models show a high correlation

with one another but the models' deviation from the measured results between the peak value and the core flow region increases. However, the location of the maximum k is predicted most precisely by the ω-based turbulence models. According to DeOtte et al. [60], turbulence is produced maximally in the region where the flow is decelerated, resulting in strong interactions of shear layers. Therefore, the sharp increase of the turbulence kinetic energy initially starts at the orifice edge ($r/R = 0.62$) but the peak is dissipated rapidly throughout the flow field with increasing flow length. Due to the contracting flow, the shear region is found at values lower than the diameter ratio of 0.62 for 0.2R. At 4R, all turbulence models fail to reproduce the profile of k, which is in analogy to the findings of Erdal and Andersson [104] in Fig. 3.47 for larger flow distances. Shan et al. conclude that the increasing discrepancy with increasing flow length originates from emerging vortex interaction mechanisms. Such unsteady motions can not be predicted by RANS models. In summary, the kω-SST turbulence model overall shows the best correlation to the RSM, which again justifies the use of this two-equation turbulence model.

Another investigation can be used to evaluate the performance of the present numerical model for a different fluid. Lebedev et al. [103] numerically investigated the impact of manufacturing tolerances and non-compliance with the requirements of an orifice meter installation on the deviation of the loss coefficient. This study is conducted with the previously given diameters ($D = 105\,mm$ and $d = 61.75\,mm$), but cooling water is used as the operating fluid at a temperature of 70 $^\circ C$ with a density ϱ of 986 kg/m^3 and a dynamic viscosity μ of 4.09·10^{-4} Pa·s. The numerical simulations performed by Lebedev et al. take advantage of the simulation domain's axial symmetry, which means the authors employed a two-dimensional axisymmetric simulation domain. Nonetheless, the numerical solutions of Lebedev et al. are compared with the present three-dimensional numerical simulation. Lebedev et al. used the Spalart-Allmaras turbulence model [107] and the kε turbulence model as a reference. The Spalart-Allmaras turbulence model is a one-equation model designed and optimized specifically for aeronautic applications, see Ref. [107] for details. The authors' numerical results exhibit the highest agreement with the results of the standard ISO 5167:2003 using the Spalart-Allmaras turbulence model. For all investigated parameters, the deviation to the results of the standard ISO 5167:2003 is less compared with the kε turbulence model.
Therefore, the Spalart-Allmaras turbulence model is also applied to the present numerical model with the medium mesh and cooling water as the operating fluid. In its original formulation, the Spalart-Allmaras turbulence model is a low Reynolds number model, which means that the mesh in the near-wall region must be highly resolved for proper modeling of the boundary layer. But in recent ANSYS releases, the Spalart-Allmaras turbulence model is enhanced with a wall treatment approach, allowing the application of a near-wall mesh without the boundary layer highly resolved. But according to Wilcox [31], the Spalart-Allmaras turbulence model exhibits some flaws if free shear regions like the jet region downstream of the orifice are present in the simulation domain. Table 3.10 shows the obtained numerical results for the Spalart-Allmaras turbulence model Δp_{SA} and the kω-SST turbulence model Δp_{SST}. For comparison, Tab. 3.10 also includes the results of Lebedev et al. $\Delta p_{Lebedev}$ and the standard ISO 5167:2003 Δp_{ISO}. All differential pressures refer to the D-D/2 pressure tapping points.

Table 3.10 shows that the results of Lebedev et al. $\Delta p_{Lebedev}$ deviate around 4% from the results obtained with the Spalart-Allmaras turbulence model Δp_{SA}. Applying the kω-SST turbulence model, the deviation of the simulation results Δp_{SST} to the results of Lebedev et al. and the standard ISO 5167:2003 is significantly diminished to 1.3% at maximum. These results are in contrast to the findings of Lebedev et al. where the Spalart-Allmaras turbulence model shows very high agreement with the

Table 3.10: Results of the differential pressure vs. the mass flow rate of different approaches.

$\dot{m}\ [kg/s]$	4.11	10.96	16.44	17.26
$\Delta p_{ISO}\ [kPa]$	2.256	16.17	36.46	40.20
$\Delta p_{Lebedev}\ [kPa]$	2.261	16.20	36.53	40.27
$\Delta p_{SA}\ [kPa]$	2.229	16.30	37.27	38.75
$\Delta p_{SST}\ [kPa]$	2.227	15.99	36.17	39.77

calculated results Δp_{ISO}. An explanation for the diverging agreement might be that the one-equation Spalart-Allmaras turbulence model shows better performance in two-dimensional flows since its major flaw of inaccurately modeling jet spreading rates (see Ref. [31]) is coming into full effect for three-dimensional flows. However, the presented results justify, once more, that the kω-SST turbulence model is an appropriate choice for modeling the metering orifice as well.

Simulations of the Orifice

Since the pre-investigations verified the employed numerical model, the computed results can now be checked against the results of the standard ISO 5167:2003 [91] for a set of parameters, presented in Tab. 3.11. Therefore, the deviation of the calculated pressure difference according to the standard ISO 5167:2003 [91] Δp_{ISO} from the simulated pressure difference Δp_{sim} is used as the quality criterion to finally validate the simulation. A deviation of the pressure difference of less than 1% as obtained for the flange (25.4 mm), the D and D/2, and corner tapping points compared to the standard is the desired accuracy of the simulation results.
The lower absolute applicability limit of the standard ISO 5167:2003 is indicated by an orifice bore diameter d of 12.5 mm, whereas the relative upper applicability limit for d is 78.75 mm due to the pipe diameter D of 105 mm in accordance with Lebedev et al. [103]. The simulated differential pressure Δp_{sim} of every combination of the mass flow rate $\dot{m}$ and the area ratio d^2/D^2 is used as the final verification of the numerical model. Solely the differential pressure values at the pressure tapping points are used for this purpose since these values are most crucial to proving the applicability of the proposed approach.

Table 3.11: Parameter set used for the numerical simulation

parameter	1	2	3	4	5	6	7
$d\ [mm]$	12.5	21	30	40.5	51	61.75	75
$\dot{m}\ [kg/s]$		2	4.11	10.96	16.44	17.26	20
Re_D		27 253	56 004	149 340	224 020	235 190	272 525

The range of the parameter set for Re_D (Tab. 3.11) is very narrow, compared with the applicability limits given by the standard ISO 5167:2003 [91]. It is shown in the following that the parametrization of the coefficients and the resulting fit functions are very sensitive to low Reynolds numbers. On the contrary, the functions' progress is almost constant for Reynolds numbers higher than given in Tab.

3.11. Therefore, the flow rate values employed by Lebedev et al. [103] mainly will also be used for the present numerical study. Although the simulations are only performed for water at a temperature of 25 $°C$ to obtain the results, the evaluation is referred to the pipe Reynolds number Re_D instead of the flow rate $\dot{m}$ for the sake of comparability with the literature.

Employing the presented numerical models, the simulated differential pressures match the calculated differential pressures as per standard ISO 5167:2003 within -1% to +0.8% deviation for the whole set of parameters as shown in Fig. 3.49. Only the outliers for an orifice diameter d of 75 mm at the corner tapping points exceed the deviation to -1.6%. However, when referring to the measurement uncertainty for the discharge coefficient C_D given by the standard ISO 5167:2003 [91] to the differential pressure, the simulated results are perfectly within the specified range. A mean deviation of approx. 0.13% is achieved for all differential pressures and the maximum deviation amounts to 1.6%. Generally speaking, the differential pressure computed for the corner tapping points deviates most from the standard results, whereas the computed results deviate least for the D-D/2 tapping points. Figure 3.49 also shows a decreasing deviation with an increasing mass flow rate for all tapping points. It can therefore be concluded that the employed numerical model is capable of reproducing the results of the standard ISO 5167:2003 as well as the results of Lebedev et al. [103] within a reasonably small deviation range. As a result, the numerical model is entirely verified to be used for detailed investigations of flows through an orifice and to determine the required coefficients.

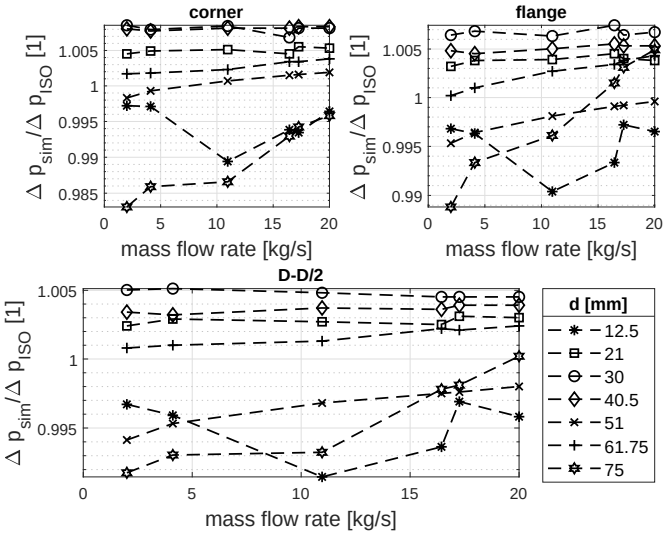

Figure 3.49: Correlation between simulated differential pressure Δp_{sim} and calculation result according to ISO 5167:2003 Δp_{ISO}

Now, the pressure coefficient c_P, the momentum coefficients β, and the pressure exaggeration coefficients γ are determined for every area ratio $\sigma = d^2/D^2$ and mass flow rate given in Tab. 3.11. With a pipe diameter D of 105 mm, the area ratio σ corresponds to 0.0142, 0.0400, 0.0816, 0.1488, 0.2359, 0.3459, and 0.5102. For every area ratio, the mass flow rates $\dot{m}$ as per Tab. 3.11 are investigated to obtain the dependency of c_P, β, and γ as functions of the area ratio σ and the mass flow rate $\dot{m}$.

The total pressure coefficient c_P as a function of the pipe Reynolds number Re_D for an area ratio σ of 0.3459 (d/D=0.588) is shown in Fig. 3.50 as a representative example for all area ratios. Due

to the definition of Eq. (3.98), the total pressure coefficient is negative, which means the pressure on the upstream orifice wall is larger than the pressure downstream. With increasing Re_D, c_P appears to approach a value around -19.5. A fit function in the shape of $f(Re_D) = a_1\, {Re_D}^{a_2} + a_3$ approximates the results with very high agreement but only for a single area ratio. To obtain an expression including the dependency on the area ratio as well, the fit coefficients a_1 and a_3 are expressed as functions of the area ratio with the aid of the parameter set. The same fit function $f(\sigma) = a_4\, \sigma^{a_5} + a_6$ is applied to a_1 and a_3 to account for the area ratio dependency. This leads to a two-parameter fit function of the total pressure coefficient c_P given as a function of the pipe Reynolds number Re_D and the diameter ratio $d/D = \sqrt{\sigma}$ for better practical applicability.

$$c_P\left(Re_D, d/D\right) = \left(25.1\left(\frac{d}{D}\right)^{-2.96} + 23\right) Re_D^{-0.5} + \left(-2.63\left(\frac{d}{D}\right)^{-4.03} + 2.66\right) \tag{3.106}$$

Equation (3.106) reproduces the numerical results with a mean deviation of less than 1% at a maximum deviation of 2%. This confirms the capability and suitability of the proposed simple fit function. Figure 3.51 shows the fit function as per Eq. (3.106) and the numerical results in a three-dimensional plot with the z-axis in a logarithmic scale.

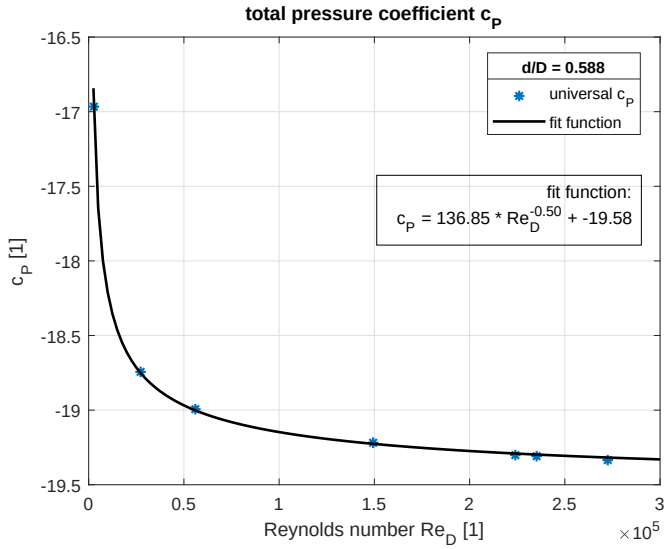

Figure 3.50: Numerical results of the total pressure coefficient c_P vs. the pipe Reynolds number Re_D represented by markers and the fit function for $d/D = 0.588$

The momentum coefficient can be evaluated for every cross-section upstream and downstream of the orifice. Figure 3.52 shows the momentum coefficient versus the dimensionless distance to the orifice L/D for various pipe Reynolds numbers Re_D at $d/D = 0.588$. In the background, the velocity distribution over the pipe's central plane is visualized with its magnitude quantified by the color mapping. The dead water zones and the areas where the flow velocity is (almost) zero are represented by the dark blue color. An upstream and downstream recirculation zone can be identified, whose shape and extent are in good accordance with the experimental results of DeOtte et al. [60], justifying once more that the upstream flow pattern of an orifice exhibits apparent similarities to a sudden contraction. The red color represents the maximum velocity. The profiles of the momentum coefficients start at a

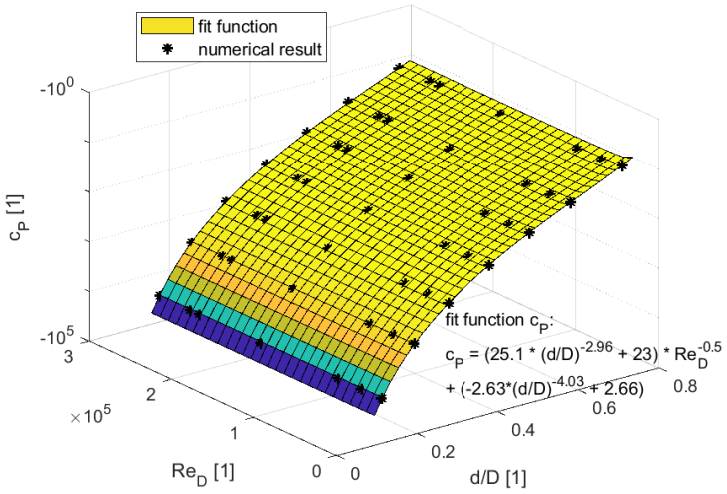

Figure 3.51: Numerical results of the total pressure coefficient c_P vs. the pipe Reynolds number Re_D and vs. the diameter ratio d/D represented by markers and the two-parameter fit function represented by the colored surface

dimensionless flow distance L/D of 2 with values ≈ 1.03, which indicates a homogeneous velocity distribution over the cross-section in a turbulent flow, see Refs. [10, 73]. Around $1D$ before the orifice, a slight increase of β can be noticed, changing to a non-linear increase around $0.2D$ reinforcing up to the upstream-facing orifice wall. Here, the upstream maximum is reached. Within the orifice where the flow is contracting to the orifice bore area, β decreases to values lower than 1.1 but higher than 1.03. Shortly downstream of the orifice, β jumps to its maximum value around a downstream flow length of $0.6D$, independent of the flow rate. This is due to the interaction of the beginning recirculation at the walls and the vena contracta indicated by large values of β. It shows that the numerical results are in good agreement with the experimental results of Shan et al. [106]. The authors found that the vena contracta is located independent of the flow rate at around $0.5D$ downstream of the orifice. With further increasing flow length, β decreases and re-approaches a value of 1.03 for a sufficient downstream flow length. Due to the free stream, the distance for the flow to fully re-develop is much larger compared with the sudden contraction, but in line with the finding for the sudden expansion since it takes roughly $6D$ for the flow to reattach to the wall. But in the case of a sudden expansion, no vena contracta can be found since the upstream flow is not converging and, thus, contains no relevant radial velocity component.

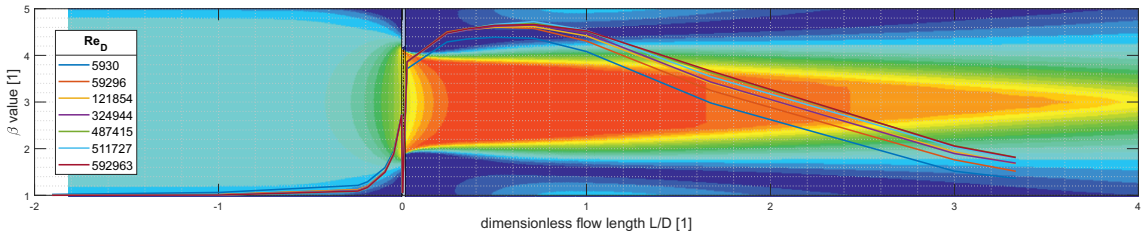

Figure 3.52: Representative axial distribution of the momentum coefficient β vs. the dimensionless flow length L/D with the color-mapped magnitude of the velocity in the background

Figure 3.52 also shows that all pressure tapping points are in a region where the flow is highly disturbed. This means that the required momentum coefficients are not constant, as shown by the numerical simulation. Since the upstream momentum coefficient β_1 and the downstream momentum coefficient β_2 must be obtained for every pressure tapping point couple, the combined momentum coefficient $\beta_{tp} = \beta_{2,tp} - \beta_{1,tp}$ is parametrized with the subscript tp representing the respective tapping point couple: corner, flange, or D-D/2. A representative example of the combined momentum coefficient β_{tp} as a function of the pipe Reynolds number Re_D is shown in Fig. 3.53 for the area ratio σ of 0.3459 (d/D=0.588). For increasing flow rates, β_{tp} increases and approaches a final value, depending on the tapping point couple. This is because the difference between the downstream and the upstream momentum coefficient becomes constant for flow rates to increase further. Only for very small flow rates, the difference decreases. As expected, the lowest values are obtained for β_{corner} where the flow represents the conditions within the orifice since no flow length is covered in the pipe. The deviation between the flange β_{flange} and the D-D/2 momentum coefficient $\beta_{D-D/2}$ is significantly reduced compared with β_{corner}. However, β_{tp} shows a dependency on the flow rate regardless of the tapping point couple. In analogy to c_P, a fit function in the shape of $f(Re_D) = a_1\, {Re_D}^{a_2} + a_3$ can be employed to approximate the results for every β_{tp} with high agreement at the given area ratio. Analogously to the total pressure coefficient c_P, the fit coefficients a_1 and a_3 are expressed as functions of the area ratio as well since β_{tp} is also a function of the area ratio ($\sigma = d^2/D^2$). The fit coefficients' dependency on the area ratio is also approximated very well by the same fit function $f(\sigma) = a_4\, \sigma^{a_5} + a_6$. Eventually, the final fit functions accounting for the dependency on the flow rate and the diameter ratio are obtained for the momentum coefficient of every tapping point couple, shown for β_{corner} in Fig. 3.54.

$$\beta_{corner}\left(Re_D, d/D\right) = \left(-2.54\left(\frac{d}{D}\right)^{-1.57} - 0.08\right) Re_D^{-0.5} + \left(0.15\left(\frac{d}{D}\right)^{-2.59} - 0.12\right) \quad (3.107)$$

$$\beta_{flange}\left(Re_D, d/D\right) = \left(-0.73\left(\frac{d}{D}\right)^{-3.34} - 19.65\right) Re_D^{-0.5} + \left(1.56\left(\frac{d}{D}\right)^{-2.08} - 1.32\right) \quad (3.108)$$

$$\beta_{D-D/2}\left(Re_D, d/D\right) = \left(-0.84\left(\frac{d}{D}\right)^{-3.42} - 19.18\right) Re_D^{-0.5} + \left(1.61\left(\frac{d}{D}\right)^{-2.09} - 1.26\right) \quad (3.109)$$

The last parameter required to complete the momentum-based approach is the pressure exaggeration coefficient γ. Figure 3.44 shows that the deviation of the radial pressure profile from the respective average radial pressure is almost 0 for the D-D/2 tapping points but strongly increases for the flange and especially the corner tapping points. Therefore, the pressure exaggeration coefficient varies with the tapping point couple as well as the combined momentum coefficient β_{tp}. The numerical simulation shows that γ can be assumed independent of the flow rate for every tapping point couple since the spread around the mean of γ_{tp} for all flow rates at a single area ratio is less than 0.1%. But the pressure exaggeration coefficient γ_{tp} exhibits a dependency on the area ratio. In Fig. 3.55, the numerical results of γ_{tp} for all tapping point couples are shown by markers together with the fit functions. For d/D approaching zero γ approaches unity since $d/D = 0$ means no orifice opening, thus no flow. For d/D approaching unity, which represents a straight pipe, γ should approach unity as well, but this case is not covered by the present approach as it exceeds the limits of d/D given by the standard ISO 5167:2003 [91]. The value for $\gamma_{D-D/2}$ at $d/D = 0.588$ is regarded as an outlier and therefore excluded from the current considerations, knowing that the deviation of the radial pressure distribution

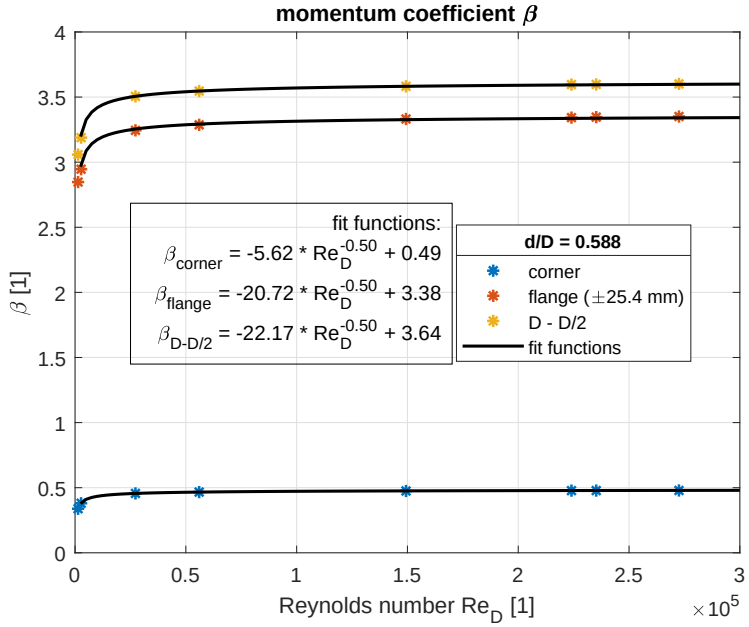

Figure 3.53: Numerical results of the combined momentum coefficient β_{tp} vs. the pipe Reynolds number Re_D represented by markers together with the fit function for $d/D = 0.588$

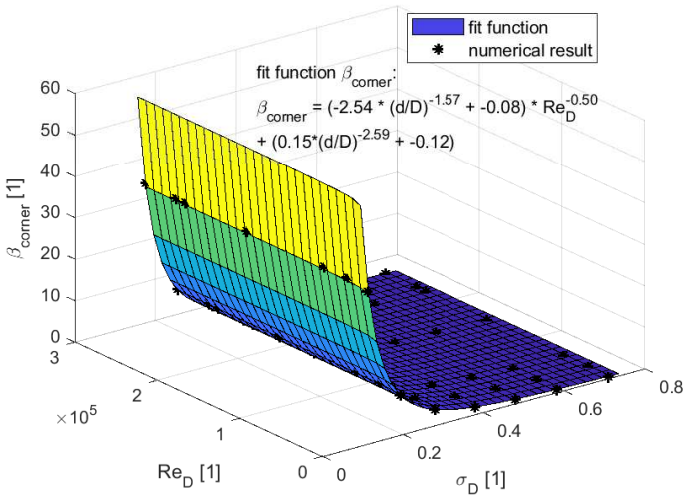

Figure 3.54: Numerical results of the combined corner tapping point momentum coefficient β_{corner} vs. the pipe Reynolds number Re_D and the diameter ratio d/D represented by markers and the two-parameter fit function represented by the colored surface

for $d/D = 0.588$ is also 0 at the D-D/2 tapping points. In analogy to the total pressure coefficient c_P and the combined momentum coefficient β_{tp}, the same fit function can be employed, parametrizing the results with a very high agreement. In the case of the D-D/2 tapping points, the flow length upstream and downstream of the orifice is sufficient for the pressure to be distributed uniformly over the radius, which means the pressure at the wall is equal to the pressure at any point over the radius - resulting in $\gamma_{D-D/2} = 1$. The following fit functions are obtained for γ_{corner} and γ_{flange}.

$$\gamma_{corner}\,(d/D) \;=\; 2.40\left(\frac{d}{D}\right)^{3.05} + 1 \tag{3.110}$$

$$\gamma_{flange}\,(d/D) \;=\; 0.27\left(\frac{d}{D}\right)^{3.95} + 1 \tag{3.111}$$

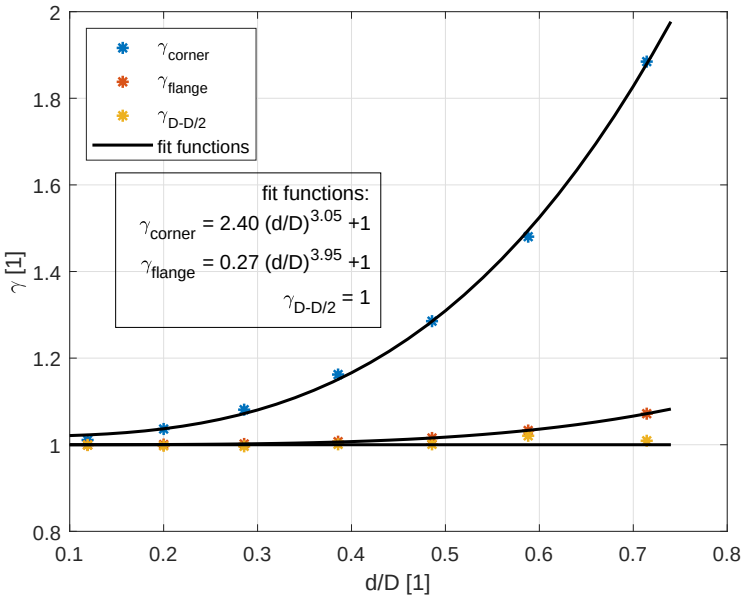

Figure 3.55: Numerical results of the pressure exaggeration coefficient γ_{tp} vs. diameter ratio d/D represented by markers together with the fit functions

Now that all required coefficients are parametrized by a simple analytic function, the pressure difference for every tapping point couple can be calculated by a completely momentum-based approach without any empirical coefficient. With the volume flow rate Q substituted by $\dot{m} = \varrho\, Q$, Eq. (3.105) gives

$$\dot{m} = \sqrt{\frac{\Delta p\;\varrho}{\gamma\left(\beta + \frac{c_P}{2}\left(1 - \frac{A_O}{A}\right)\right)}}\;A \tag{3.112}$$

The mass flow rate can now be determined for a given pressure difference at a specific tapping point couple. The momentum-based approach for flow metering is completed using c_P as per Eq. (3.106), β_{tp} as per Eqs. (3.107,3.108,3.109), and γ_{tp} as per Eqs. (3.110,3.111) into Eq. (3.112).

3.3.4 Results

The momentum-based loss coefficients for the pressure loss of an orifice $K_{M,I}$ as per Eq.(3.96) and $K_{M,II}$ as per Eq.(3.101) must be multiplied by two for direct comparison with the literature numbers obtained via the Bernoulli principle. Figure 3.56 shows the parametrizations of $K_{M,I}$ and $K_{M,II}$ compared with literature numbers. All coefficients are referred to the pipe velocity Q/A. In contrast to the sudden contraction (see: Fig. 3.3), the loss coefficients scatter less and most of the investigations agree with one another. It is shown in Fig. 3.3 that the parametrization of $K_{M,II}$ for a Reynolds number of $1 \cdot 10^6$ (chosen in compliance with the graph of the ISO 5167:2003) is almost equivalent to $K_{M,I}$. Since the standard ISO 5167:2003 [91] defines the upper applicability limit of σ as 0.56, the increased

deviation of $K_{M,II}$ to the literature numbers and to $K_{M,I}$ for area ratios greater than 0.7 is negligible. In contrast, $K_{M,I}$ correlates very well with the loss coefficients obtained by other authors over the entire range of area ratios. Due to the assumption of a mean value $C_D = 0.61$ for all area ratios, the results of Westaway and Loomis [90] show a noticeable deviation from other results. The results of Benedict [57] (represented by the line named 'Benedict 1980') are only valid for area ratios $\sigma \leq 0.6$.

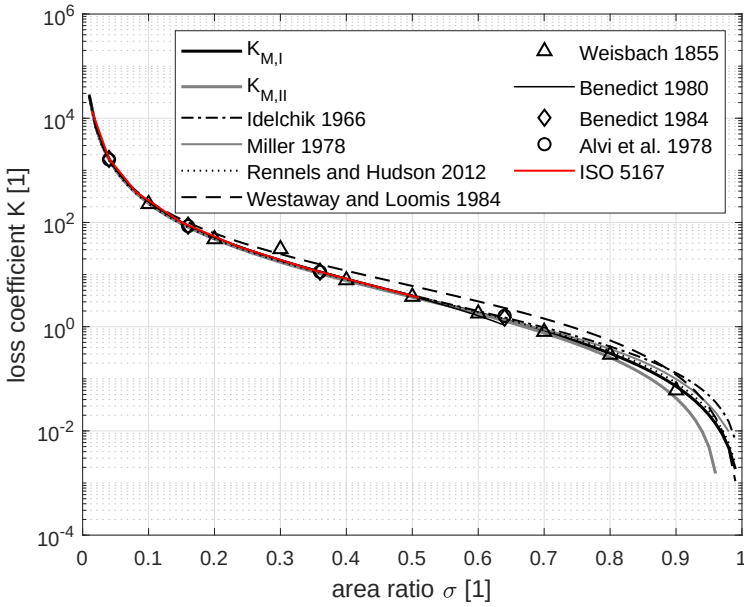

Figure 3.56: Loss coefficient K versus area ratio σ

In summary, the proposed momentum approach distinguishes between the irreversible pressure drop or the pressure drop at the pressure tapping point locations solely by the choice of the control volume. Different coefficients, such as the empirical discharge coefficient C_D or the loss coefficient K, are not necessary for the unified momentum approach.

As mentioned in Chap. 3.3.1, the investigation is solely focusing on devices and the calculation method provided by the standard ISO 5167-2:2003 for orifices [91] since this standard is the benchmark in differential pressure-based flow rate measurement.

It shall be mentioned that the proposed approach is also applicable to laminar flows without any adaption. However, the numerical model mentioned is only valid for turbulent flows. In addition, the standard [91] explicitly claims Reynolds numbers representing fully turbulent flow. Since laminar flows are of little practical use in engineering applications and very little experimental data is available, the irreversible pressure drop obtained by the momentum balance is only compared with the irreversible pressure drop as per ISO 5167:2003 $\Delta p_{ISO,irrev}$ in brief.

Figure 3.57 shows the ratio of both momentum-based irreversible pressure drop calculations $\Delta p_{irrev,I}$ and $\Delta p_{irrev,II}$ to the reference pressure loss $\Delta p_{ISO,irrev}$ according to the standard ISO 5167:2003 [91] vs. the mass flow rate $\dot{m}$. The deviation is within 2% for all investigated mass flow rates and area ratios except for an orifice diameter d of 75 mm. In this case, the deviation increases to approximately 6% due to the small pressure loss. Nevertheless, Fig. 3.57 shows that both approaches of the momentum balance are also capable of accurately predicting the irreversible pressure drop of a flow through an orifice.

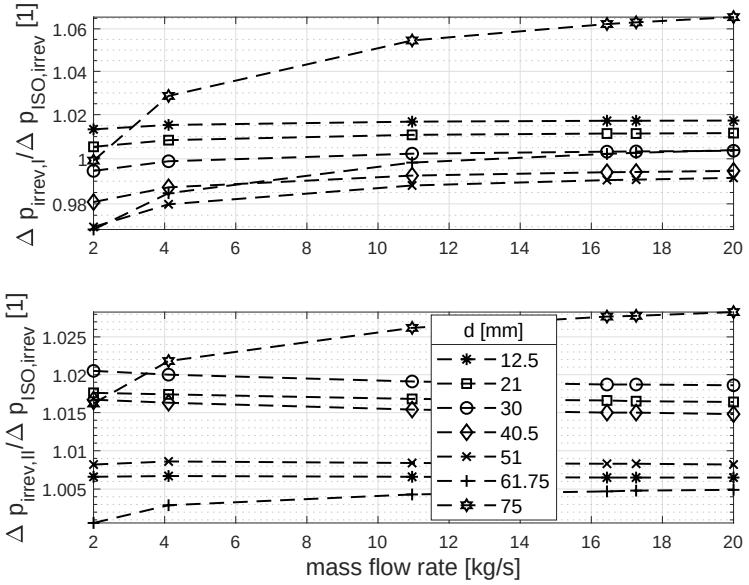

Figure 3.57: Correlation between calculated differential pressure losses $\Delta p_{irrev,I}$ and $\Delta p_{irrev,II}$ with the parametrized coefficients and calculation result according to ISO 5167:2003 $\Delta p_{ISO,irrev}$

The standard ISO 5167:2003 specifies a range of approximately $\pm$0.6% for the uncertainty of the discharge coefficient C_D as per Eq. (3.84) for metering the mass flow rate $\dot{m}$ (Eq. (3.82)). Figure 3.58 shows the momentum-based mass flow rate $\dot{m}$ divided by the mass flow rate as obtained by applying the ISO 5167:2003 $\dot{m}_{ISO}$ vs. the mass flow rate used as the inlet boundary condition for the numerical simulation.

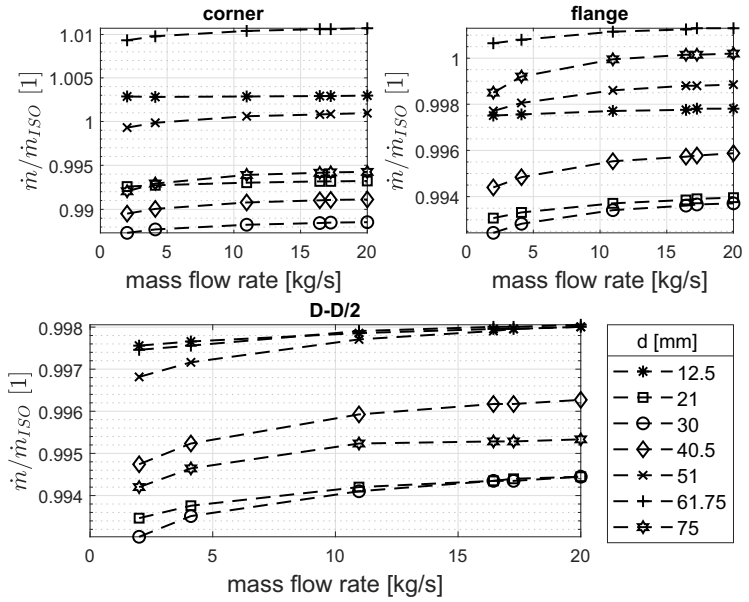

Figure 3.58: Correlation between the calculated mass flow rate $\dot{m}$ and the calculation result according to ISO 5167:2003 $\dot{m}_{ISO}$ for all tapping point couples

Figure 3.58 confirms that the results of the momentum-based approach are within the specified

uncertainty range of $\pm$0.6%. Only at the corner tapping points, the deviation increases to $\pm$1%, which is still in line with the uncertainty range given by Reader-Harris [92], see Chap.3.3.1. In conclusion, the proposed momentum-based approach predicts the flow rate of water for a measured differential pressure as precisely as the standard approach given in Ref. [91]. The main asset of the proposed approach is that no empirical coefficient is required but solely physically founded coefficients to account for a non-uniform pressure or velocity distribution over specific cross-sections or walls.
As previously mentioned, the range of the investigated flow rates (and corresponding pipe Reynolds numbers Re_D) is very limited compared with the range of applicability defined by the standard ISO 5167:2003 [91]. To confirm the validity of the proposed approach for the whole range of Re_D, the calculation of the mass flow rate $\dot{m}$ is extended up to $Re_D \approx 2.3 \cdot 10^7$ employing the given parametrizations. It appears that the deviation for all tapping point couples is reduced with increasing mass flow rate, as already indicated by the profiles of the correlation in Fig. 3.58. For $\dot{m} > 20\ kg/s$, the predicted mass flow rates for all pressure tapping point couples converge to deviation values within a range of $\pm$0.6%.

In summary, it is proven that the mass flow rate and the irreversible pressure drop of a flow through a metering orifice can be predicted with a very high agreement by employing an approach based on the momentum balance. Analogies to the sudden contraction and the sudden expansion are also drawn that outline the similarities of the mentioned hydraulic structures, as well as the modularity of the momentum balance. The present investigation is solely focused on water to demonstrate the proposed method and its applicability. The practicality of the proposed method for different fluids like oil and compressible fluids needs to be examined in subsequent investigations.

4 No Hydraulics Without Momentum / Conclusion

Describing flow quantities like the pressure change or the volume flow rate by the Bernoulli principle requires empirical loss or discharge coefficients to close the gap between the theory and empirical results. This is a result of non-compliance with the restrictions that the Bernoulli principle is subject to. Bernoulli's approach requires an irrotational flow field (absence of friction) or is only valid on a streamline, among other things.
However, the integral momentum balance is valid for the whole defined control volume but needs physical coefficients to substitute integral expressions with averaged ones. The inlet and outlet velocity distributions and pressure distributions are obtained by numerical simulations yielding the coefficient's parametrizations. The numerical simulations are performed with ANSYS, solving the RANS equations. An assessment of the most commonly used turbulence models with the literature of all investigated flow structures shows that the kω-SST turbulence model performs best. As references, the turbulence kinetic energy and the turbulence intensity are employed.
Besides, the integral momentum balance also links hydraulics and numerical simulations (CFD) since CFD is mostly based on the differential form of the momentum balance, better known as the Navier-Stokes equations.

The sudden contraction has been intensively studied over the years. As a result, a vast variety of investigations with different findings for the loss coefficient is available. But most of the parametrizations and coefficient numbers disagree with one another, especially when obtained by different authors. Describing the pressure drop of a sudden contraction with the momentum balance, the momentum coefficients and the pressure coefficient of the contraction wall are required. Since the literature research reveals a vast range of loss coefficients, own measurements are conducted to compare the results with the momentum-based approach. The obtained momentum-based formulas for the pressure drop maximally deviate 6% from the author's measurement results and, therefore, physically confirm the classical formulation of Idelchick, which was chosen as the reference. In addition, a closer examination of the flow pattern in the vicinity of the contraction revealed a better understanding of the pressure coefficient due to the interaction of the contracting flow and the pressure at the contraction wall.

The sudden expansion represents the only hydraulic structure where the loss coefficient is directly derived from momentum considerations. Although the so-called Borda-Carnot loss is purely based on the momentum balance, some simplifications and assumptions are inadequate. Application of the non-idealized integral momentum balance to the sudden expansion yields the same formula as for the sudden contraction. Both structures are solely distinguished by the parametrization of the momentum and pressure coefficients. This is in contrast to the Bernoulli principle where it is necessary to introduce an empirical coefficient for the sudden contraction but a momentum-based coefficient for the sudden expansion. Consequently, the Bernoulli principle can not describe both structures by a unified

approach. It turns out that the flow of a sudden expansion is a more complex problem compared with a sudden contraction due to the jet expanding into the larger pipe. In addition, the coefficients for the sudden expansion exhibit an additional dependency on the mass flow rate. Compared with the Borda-Carnot relation, the proposed non-idealized approach shows a higher correlation to the simulation results.

Combining the sudden contraction and the sudden expansion from hydraulic aspects results in an orifice. Although some (incomplete) approaches to applying the momentum balance to the orifice are reported by the literature, the established methods of calculating the pressure drop and, more important, the flow rate are mainly based on the Bernoulli principle. Metering orifices are widely used to induce a specific pressure drop in the flow that can be measured and used to calculate the flow rate. Since the sole application of the Bernoulli principle to the metering orifice leads to inaccurate results, the so-called discharge coefficient is introduced as a correction factor for the calculated flow rate. The discharge coefficient accounts for inadequate simplifications and deviations of the flow from the ideally assumed one, the dependency of the Reynold number plus the diameter ratio, and the pressure tapping points. However, with the empirical discharge coefficient, the calculation results are calibrated to obtain a very high agreement with the measurement within an uncertainty range of 0.6%. Applying the momentum balance to the metering orifice, the same average deviation can be maintained without any empirical coefficient. The momentum-based approach accounts for the inhomogeneous velocity and pressure distributions over the cross-sections and the orifice walls by separate coefficients. The employed coefficients capture the relevant physical effects since these coefficients arise from physically founded substitutions. Parametrizations of the required coefficients are obtained with the aid of numerical simulations and result in simple analytical fit functions. Consequently, a very high agreement between the empirical formulation as per standard ISO 5167:2003 and the formulation of the momentum-based approach is achieved.

In addition to the flow rate, the irreversible pressure drop of an orifice can be calculated via the same approach simply by dropping two coefficients. The derivation of the momentum balance for the orifice revealed various analogies to the derivations for the sudden contraction and the sudden expansion. Some findings on the flow pattern of the sudden expansion and sudden contraction, as well as the pressure coefficient of the sudden contraction, can be adopted for the orifice. This speaks for the universality and applicability of the momentum balance describing hydraulic structures.

Therefore, every fundamental hydraulic structure should be described by the integral momentum balance instead of the Bernoulli principle. Hereby, better insights into the actual flow are gained, leading to new fundamental hydraulic formulations without artificial parameters. This may ultimately result in a unified theory for all hydraulic structures, which no longer requires the distinction of whether the aircraft flies inverted or not.

5 What is Next? / Outlook

The momentum balance is already successfully applied to flows of open channel structures, namely the overflow over a weir [6] and the flow under a sluice gate [7], which is detailed further by Steppert et al. [108]. In both cases, the obtained formulas combined with physical coefficients confirm the empirical relations required for the Bernoulli principle.
But the momentum balance is also capable of describing the outflow problem [109]. With the aid of an ingeniously defined control volume, the momentum balance automatically accounts for the correct outflow coefficient for a rounded or sharp outflow geometry. Again, the momentum-based approach unifies different problems and supersedes empirical correction coefficients.

Even though it is proven that the momentum balance applies to additional flow structures, a sheer endless number of research issues await exploration. To mention a few suggestions from the author:

- The derived momentum-based formulas are also valid for laminar and transitional flows since the effects of a different flow pattern are covered by the physical coefficients. It is therefore promising to extend the applicability to all flow conditions, although the practical relevance appears to be minor for laminar flow.
- All considerations of the present thesis refer to water. Especially concerning the practically important application of the metering orifice, the momentum balance can be applied to compressible fluids as well.
- Hydraulic structures with continuous changes in the cross-section are another research object to investigate. Such structures represent the standard shape since exhibiting a beneficial pressure drop compared with the pressure drop of the discussed sudden changes.
- A common feature of all investigated structures is the (local) change in the cross-section. But changes in the flow direction at a constant cross-section also induce pressure losses, for example, in a pipe bend. It is expectable that applying the proposed approach to a structure changing the flow direction reveals comprehensive insights into the physics of such flows.

And if this is not enough, Idelchik [18] published a remarkable book on the loss coefficient for almost every hydraulic structure that waits to be compared with the physical coefficients as obtained by the momentum balance.

Nomenclature

Abbreviations

abbreviation	explanation
CFD	Computational Fluid Dynamics
DN	Nominal Diameter
DNS	Direct Numerical Simulation
FVM	Finite Volume Method
GCI	Grid Convergence Index
ISO	International Standard Organisation (International Organization for Standardization)
LDA	Laser Doppler Anemometry
PIV	Particle Image Velocimetry
RANS	Reynolds-Averaged Navier-Stokes
RSM	Reynolds Stress Model
SKE	Standard kε
SST	Shear Stress Transport

Latin Letters

symbol	denomination	unit
A	area	m^2
$a_1,\ a_2,\ a_3,\ a_4,\ a_5,\ a_6$	fit parameter	1
B	bias limit	Pa
C_D	discharge coefficient	1
C_f	Fanning friction factor	1
c	coefficient	1
D	diameter	m
D_k	destruction of turbulence kinetic energy	$kg\ m^{-1}\ s^{-3}$
D_ω	destruction of turbulence dissipation	$kg\ m^{-3}\ s^{-2}$
d	(pipe-)diameter	m
e	deviation, error	1
F	force	N
F_1	blending function	1
f	key variable	1
GCI	Grid Convergence Index	1
I	momentum	$kg\ m\ s^{-1}$
J	turbulence intensity	1
g	gravitational acceleration	$m\ s^{-2}$
h	height	m
K	pressure loss coefficient	1
k	turbulence kinetic energy	$m^2\ s^{-2}$
k	sudden loss coefficient	1
ks	wall roughness	m
L	flow length	m
L_1, L_2'	orifice length portions	1
m	mass	kg
$\dot{m}$	mass flow rate	$kg\ s^{-1}$
N	total number of mesh elements	1
n	normal unit vector (indicated by $\vec{}$)	1
n	number of samples	1
o	apparent order	1

Latin Letters Continuation

symbol	denomination	unit
P	precision limit	Pa
P_k	production of turbulence kinetic energy	$kg\ m^{-1}\ s^{-3}$
P_ω	production of turbulence dissipation	$kg\ m^{-3}\ s^{-2}$
p	pressure	Pa
$\mathbf{p}$	pressure tensor	Pa
Q	volume flow rate	$m^3\ s^{-1}$
q	variable for the velocity profile according to Idelchik	1
R	total radius	m
$\mathbf{R}$	Reynolds stress tensor	Pa
r	radius	m
Re	Reynolds number	1
S	mesh refinement factor	1
s	mesh size	m
t	time	s
U	uncertainty	1
u	velocity in x-direction	$m\ s^{-1}$
u_*	friction velocity	$m\ s^{-1}$
V	volume	m^3
v	velocity	$m\ s^{-1}$
v	velocity in y-direction	$m\ s^{-1}$
w	velocity in z-direction	$m\ s^{-1}$
X	measured variable	
x	length	m
x	x-coordinate	1
Y	result	Pa
y	distance from the wall	m
y	y-coordinate	1
z	height	m
z	z-coordinate	1

Greek Letters

symbol	denomination	unit
β	momentum coefficient	1
Δ	difference	1
δ	boundary layer thickness	m
γ	pressure exaggeration coefficient	1
ε	turbulence dissipation	$m^2\ s^{-3}$
$\boldsymbol{\varepsilon}$	strain rate tensor	s^{-1}
ζ	correction coefficient for the sudden expansion	1
θ	momentum thickness	m
κ	von-Kármán constant	1
λ	friction factor	1
μ	dynamic viscosity	$kg\ m^{-1}\ s^{-1}$
ν	kinematic viscosity	$m^2\ s^{-1}$
ϕ	correlation coefficient	1
ξ	second viscosity coefficient	$kg\ m^{-1}\ s^{-1}$
ϱ	density	$kg\ m^{-3}$
σ	area ratio	1
σ	stress (in combination with two indices)	Pa
$\boldsymbol{\sigma}$	stress tensor	Pa
$\sigma_k,\ \sigma_\omega,\ \sigma_{\omega 2}$	closure coefficients of the kω-SST turbulence model	1
Ω	control volume	m^3
ω	specific turbulence dissipation rate	s^{-1}
τ	shear stress	Pa
$\boldsymbol{\tau}$	shear stress tensor	Pa
$\partial\Omega$	boundary surface of control volume	m^2

Subscripts or Superscripts

symbol	denomination
$+$	dimensionless
$*$	dimensionless
0	cylindric control volume
1	upstream
2	downstream
a	absolute
act	actual
add	additional
BC	Borda-Carnot
b	body
C	contraction
c	coarse
$calc$	calculated
ci	coarse to intermediate
$cont$	contraction plane
D	pipe diameter
ext	extrapolated
F	friction
f	fine
$front$	front surface
g	gravitational
hyd	hydraulic
$Idel$	Idelchik
if	intermediate to fine
int	intermediate
inv	inverted
ISO	ISO 5167:2003 [91]
$irrev$	irreversible
$Lebedev$	Lebedev et al. [103]
$loss$	loss
M	momentum

Subscripts or Superscripts Continuation

symbol	denomination
max	maximum
$meas$	measurement
O	orifice
R	reacting
r	relative
rad	radial
s	surface
SA	Spalart-Allmaras
$shell$	shell surface
sim	simulation
SST	Shear Stress Transport
sys	system
t	turbulent
V	velocity
v	flow direction
w	wall
x	x-direction
y	y-direction
z	z-direction
$\bar{}$	mean
$\hat{}$	joint error source
$'$	fluctuation
Δp	pressure drop
I	first approach
II	second approach

List of Figures

List of Tables

Bibliography

[1] Regis, E. “The Enigma of Aerodynamic Lift - No One Can Explain Why Planes Stay in the Air”. In: *Scientific American* 322.2 (Feb. 2020), pp. 44–51. DOI: 10.1038/scientificamerican0220-44.

[2] Babinsky, H. “How do wings work?” In: *Physics Education* 38.6 (Nov. 2003), pp. 497–503. ISSN: 0031-9120. DOI: 10.1088/0031-9120/38/6/001.

[3] Epple, P. et al. “On How the Generation of Lift Can Be Explained in a Closed Form Based on the Fundamental Conservation Equations”. In: *Proceedings of the ASME 2020 Fluids Engineering Division Summer Meeting collocated with the ASME 2020 Heat Transfer Summer Conference and the ASME 2020 18th International Conference on Nanochannels, Microchannels, and Minichannels. Volume 2: Fluid Mechanics; Multiphase Flows*. Virtual, Online, July 2020. DOI: 10.1115/FEDSM2020-20261.

[4] Bernoulli, D. *Hydrodynamica, Sive De Viribus Et Motibus Fluidorum Commentarii*. Latin. Basel: Typis Joh. Henr. Deckeri, Typographi Basiliensis, 1738.

[5] Malcherek, A. “History of the Torricelli Principle and a New Outflow Theory”. In: *Journal of Hydraulic Engineering* 142.11 (Nov. 2016), pp. 02516004–1 –7. DOI: 10.1061/(ASCE)HY.1943-7900.0001232.

[6] Malcherek, A. “300 Years ‘de Motu Aquae Mixto’: What Poleni Really Wrote and a New Overflow Theory Based on Momentum Balance”. In: *7th International Symposium on Hydraulic Structures*. Aachen, Germany, May 2018, pp. 78–88. ISBN: 978-0-692-13277-7. DOI: 10.15142/T3693F.

[7] Malcherek, A. “A new theory for the sluice gate hydraulics basing on the momentum balance -A discussion paper”. German. In: *WasserWirtschaft* 108.5 (May 2018), pp. 40–44. ISSN: 0043-0978. DOI: 10.1007/s35147-018-0062-7.

[8] Anderson, J. D. *Computational fluid dynamics: the basics with applications*. 1. ed. New York, London: McGraw-Hill, 1995. ISBN: 978-0-07-113210-7.

[9] Newton, I. *Mathematische Principien der Naturlehre von Isaac Newton übersetzt von Jakob Philipp Wolfers*. Oppenheim, Berlin: Verlag von Robert Oppenheim, 1872.

[10] Cengel, Y. and Cimbala, J. *Fluid Mechanics: Fundamentals and Applications*. 4th ed. New York: McGraw-Hill Education, Feb. 2017. ISBN: 978-1-259-69653-4.

[11] Rieutord, M. *Fluid Dynamics: An Introduction*. Graduate Texts in Physics. Cham: Springer International Publishing, 2015. ISBN: 978-3-319-09350-5. DOI: 10.1007/978-3-319-09351-2.

[12] Kundu, P. K. et al. *Fluid Mechanics*. 6th ed. Amsterdam ; Boston: Academic Press, June 2015. ISBN: 978-0-12-405935-1.

[13] Stokes, G. G. “On the Theories of the Internal friction of Fluids in Motion, and of the Equilibrium and Motion of Elastic Solids”. In: *Transactions of the Cambridge Philosophical Society* 8.3 (1845), pp. 287–319.

[14] Navier, C. L. M. “Sur les Lois des mouvemens des fluides, en ayant égard à l’adhésion des molécules”. French. In: *Annales de chimie et de physique* 19 (1821), pp. 244–260.

[15] Euler, L. “Principes généraux du mouvement des fluides”. French. In: *Mémoires de l’académie des sciences de Berlin* 11 (1757), pp. 274–315.

[16] Stokes, G. G. “On Some Cases of Fluid Motion”. In: *Transactions of the Cambridge Philosophical Society*. Cambridge Library Collection - Mathematics 8.1 (1843), pp. 105–137. DOI: 10.1017/CBO9780511702242.

[17] Boussinesq, J. *Essai sur la théorie des eaux courantes*. French. Paris: Imprimerie nationale, 1877.

[18] Idelchik, I. E. *Handbook of hydraulic resistance*. 1. ed. Washington, D.C.: US Atomic Energy Commission, 1966. ISBN: 978-3-540-15962-9.

[19] Weisbach, J. *Die Experimental-Hydraulik*. German. Freiberg: J. G. Engelhardt, 1855.

[20] Colebrook, C. F. “Turbulent flow in pipes, with particular reference to the transition region between the smooth and rough pipe laws.” In: *Journal of the Institution of Civil Engineers* 11.4 (Feb. 1939), pp. 133–156. DOI: 10.1680/ijoti.1939.13150.

[21] Colebrook, C. F. et al. “Experiments with fluid friction in roughened pipes”. In: *Proceedings of the Royal Society of London. Series A - Mathematical and Physical Sciences* 161.906 (Aug. 1937), pp. 367–381. DOI: 10.1098/rspa.1937.0150.

[22] Miller, R. W. *Flow measurement engineering handbook*. 1st ed. New York: McGraw-Hill, 1983. ISBN: 978-0-07-042045-8.

[23] Benedict, R. P. *Fundamentals of Temperature, Pressure, and Flow Measurements*. 3rd ed. New York: John Wiley & Sons, Inc., 1984. ISBN: 978-0-471-89383-7.

[24] Ferziger, J. H. et al. *Computational Methods for Fluid Dynamics*. 4th ed. Cham: Springer International Publishing, 2020. ISBN: 978-3-319-99693-6. DOI: 10.1007/978-3-319-99693-6_1.

[25] Pascau, A. et al. “A comparison of segregated and coupled methods for the solution of the incompressible Navier-Stokes equations”. In: *Communications in Numerical Methods in Engineering* 12.10 (1996), pp. 617–630. ISSN: 1099-0887. DOI: 10.1002/(SICI)1099-0887(199610)12:10<617::AID-CNM10>3.0.CO;2-J.

[26] ANSYS Inc. *ANSYS Fluent Theory Guide*. Instruction manual ANSYS Fluent Release 19.3. Canonsburg, 2019.

[27] Burns, A et al. “Application of coupled solver technology to CFD modeling of multiphase flows with CFX”. In: *WIT Transactions on Engineering Sciences* 30 (2001), pp. 53–64. ISSN: 1743-3533. DOI: 10.2495/MPF010051.

[28] ANSYS Inc. *ANSYS CFX-Solver Theory Guide*. Instruction manual ANSYS CFX Release 19.3. Canonsburg, 2019.

[29] Jin, Y. and Herwig, H. “Turbulent flow in rough wall channels: Validation of RANS models”. In: *Computers & Fluids* 122 (Nov. 2015), pp. 34–46. ISSN: 0045-7930. DOI: 10.1016/j.compfluid.2015.08.005.

[30] Rodriguez, S. *Applied Computational Fluid Dynamics and Turbulence Modeling: Practical Tools, Tips and Techniques*. Cham, Switzerland: Springer International Publishing, 2019. ISBN: 978-3-030-28690-3. DOI: 10.1007/978-3-030-28691-0.

[31] Wilcox, D. C. *Turbulence modeling for CFD*. 3. La Cañada, Calif.: DCW Industries, 2006. ISBN: 978-1-928729-08-2.

[32] Bardina, J. E. et al. *Turbulence Modeling Validation, Testing, and Development*. Technical Report NASA-TM-110446. Moffett Field, CA: National Aeronautics and Space Administration, Apr. 1997.

[33] Menter, F. R. "Two-equation eddy-viscosity turbulence models for engineering applications". In: *AIAA Journal* 32.8 (Aug. 1994), pp. 1598–1605. ISSN: 0001-1452. DOI: 10.2514/3.12149.

[34] Launder, B. E. and Sharma, B. I. "Application of the energy-dissipation model of turbulence to the calculation of flow near a spinning disc". In: *Letters in Heat and Mass Transfer* 1.2 (Nov. 1974), pp. 131–137. ISSN: 0094-4548. DOI: 10.1016/0094-4548(74)90150-7.

[35] Menter, F. R. et al. "Ten years of industrial experience with the SST turbulence model". In: *Proceedings of the Fourth International Symposium on Turbulence, Heat and Mass Transfer*. Antalya: Begell House, Oct. 2003, pp. 625–632. ISBN: 978-1-56700-196-9.

[36] Langtry, R. B. and Menter, F. R. "Correlation-Based Transition Modeling for Unstructured Parallelized Computational Fluid Dynamics Codes". In: *AIAA Journal* 47.12 (Dec. 2009). DOI: 10.2514/1.42362.

[37] Kármán, T. v. "Mechanische Aehnlichkeit und Turbulenz". German. In: *Nachrichten von der Gesellschaft der Wissenschaften zu Göttingen, Mathematisch-Physikalische Klasse* 1930 (1930), pp. 58–76.

[38] ANSYS Inc. *ANSYS CFX-Solver Modeling Guide*. Instruction manual ANSYS CFX Release 19.3. Canonsburg, 2019.

[39] Carlson, J.-R. et al. "Node-Centered Wall Function Models for the Unstructured FLow Code Fun3D". In: *22nd AIAA Computational Fluid Dynamics Conference*. Dallas, TX: American Institute of Aeronautics and Astronautics, June 2015. ISBN: 978-1-62410-366-7. DOI: 10.2514/6.2015-2758.

[40] Blasius, H. "Das Aehnlichkeitsgesetz bei Reibungsvorgängen in Flüssigkeiten". German. In: *Mitteilungen über Forschungsarbeiten auf dem Gebiete des Ingenieurwesens: insbesondere aus den Laboratorien der technischen Hochschulen*. Berlin, Heidelberg: Springer, 1913, pp. 1–41. ISBN: 978-3-662-02239-9. DOI: 10.1007/978-3-662-02239-9_1.

[41] Roache, P. J. "Perspective: A Method for Uniform Reporting of Grid Refinement Studies". In: *Journal of Fluids Engineering* 116.3 (Sept. 1994), pp. 405–413. ISSN: 0098-2202. DOI: 10.1115/1.2910291.

[42] Celik, I. B. et al. "Procedure for Estimation and Reporting of Uncertainty Due to Discretization in CFD Applications". In: *Journal of Fluids Engineering* 130.078001 (July 2008). ISSN: 0098-2202. DOI: 10.1115/1.2960953.

[43] Zingg, D. "Grid studies for thin-layer Navier-Stokes computations of airfoil flowfields". In: *AIAA Meeting Paper*. Aerospace Sciences Meetings. Reno, Nevada: American Institute of Aeronautics and Astronautics, Jan. 1992. DOI: 10.2514/6.1992-184.

[44] Barth, T. and Jespersen, D. “The design and application of upwind schemes on unstructured meshes”. In: *27th Aerospace Sciences Meeting*. Aerospace Sciences Meetings. Reno, Nevada, Jan. 1989. DOI: 10.2514/6.1989-366.

[45] Russo, F. and Basse, N. T. “Scaling of turbulence intensity for low-speed flow in smooth pipes”. In: *Flow Measurement and Instrumentation* 52 (Dec. 2016), pp. 101–114. ISSN: 0955-5986. DOI: 10.1016/j.flowmeasinst.2016.09.012.

[46] Bernoulli, J. *Opera omnia*. Latin. Lausanne, Geneve: Marci-Michaelis Bousquet & sociorum, 1742.

[47] Borda, J.-C. “Memoire sur l’ecoulement des Fluides par les Orifices des Vases”. French. In: *Histoire de l’Academie royale des sciences* 1 (1766).

[48] Carnot, L. N. M. *Principes fondamentaux de l’équilibre et du mouvement*. French. Paris: Crapelet, 1803.

[49] Kays, W. “Loss coefficients for abrupt changes in flow cross section with low reynolds number flow in single and multiple tube systems”. In: *Transactions of the ASME* 72.8 (1950), pp. 1067–1074.

[50] Fester, V. et al. “Energy losses of non-Newtonian fluids in sudden pipe contractions”. In: *Chemical Engineering Journal* 145.1 (Dec. 2008), pp. 57–63. ISSN: 1385-8947. DOI: 10.1016/j.cej.2008.03.003.

[51] Sanchez, F. P. et al. “Experimental and numerical study of turbulent newtonian flow through an axisymmetric sudden contraction”. In: *Proceedings of ENCIT 2010*. Uberlandia, Brazil: ABCM Associação Brasileira de Engenharia e Ciências Mecânicas, Dec. 2010. DOI: ENC10-0572.

[52] Bullen, P. R. et al. “The determination of pipe contraction pressure loss coefficients for incompressible turbulent flow”. In: *International Journal of Heat and Fluid Flow* 8.2 (June 1987), pp. 111–118. ISSN: 0142-727X. DOI: 10.1016/0142-727X(87)90008-7.

[53] Astarita, G. and Greco, G. “Excess Pressure Drop in Laminar Flow through Sudden Contraction. Newtonian Liquids”. In: *Industrial & Engineering Chemistry Fundamentals* 7.1 (Feb. 1968), pp. 27–31. ISSN: 0196-4313. DOI: 10.1021/i160025a005.

[54] Edwards, M. et al. “Head Loss in Pipe Fittings at Low Reynolds Number”. In: *Chemical Engineering Research and Design* 63.1 (Jan. 1985), pp. 43–50. ISSN: 02638762.

[55] Idelchik, I. E. “Some refinements of the contraction and resistance coefficients in the case of a sudden contraction of the flow”. In: *Hydrotechnical Construction* 20.10 (Oct. 1986), pp. 591–594. ISSN: 0018-8220, 1570-1468. DOI: 10.1007/BF01427247.

[56] Benedict, R. P. et al. “Flow Losses in Abrupt Enlargements and Contractions”. In: *Journal of Engineering for Power* 88.1 (Jan. 1966), pp. 73–81. ISSN: 0742-4795. DOI: 10.1115/1.3678482.

[57] Benedict, R. P. *Fundamentals of pipe flow*. New York: John Wiley & Sons, Inc., 1980. ISBN: 978-0-471-03375-2.

[58] Glück, B. *Hydrodynamische und gasdynamische Rohrströmung*. German. 1st ed. Bausteine der Heizungstechnik 2. Berlin: Verl. für Bauwesen, 1988. ISBN: 3-345-00222-1.

[59] Durst, F. and Loy, T. “Investigations of laminar flow in a pipe with sudden contraction of cross sectional area”. In: *Computers & Fluids* 13.1 (Jan. 1985), pp. 15–36. ISSN: 0045-7930. DOI: 10.1016/0045-7930(85)90030-1.

[60] DeOtte, R. E. et al. “3-D laser Doppler anemometry measurements of the axisymmetric flow field near an orifice plate”. In: *Flow Measurement and Instrumentation* 2.2 (Apr. 1991), pp. 115–123. ISSN: 0955-5986. DOI: 10.1016/0955-5986(91)90019-N.

[61] ABB Automation Products GmbH. *ProcessMaster FEP300, FEP500, HygienicMaster FEH300, FEH500 Magnetisch-induktiver Durchflussmesser*. Operating instruction. Göttingen, Germany, Aug. 2019.

[62] Haaland, S. E. “Simple and Explicit Formulas for the Friction Factor in Turbulent Pipe Flow”. In: *Journal of Fluids Engineering* 105.1 (Mar. 1983), pp. 89–90. ISSN: 0098-2202. DOI: 10.1115/1.3240948.

[63] Rennels, D. C. and Hudson, H. M. *Pipe Flow: A Practical and Comprehensive Guide*. Hoboken: John Wiley & Sons, Inc., May 2012. ISBN: 978-1-118-27527-6 978-0-470-90102-1. DOI: 10.1002/9781118275276.

[64] Coleman, H. W. and Steele, G. W. *Experimentation and uncertainty analysis for engineers*. 2nd. A Wiley-interscience publication. New York: Wiley, 1989. ISBN: 978-0-471-63517-8.

[65] Altlas Copco Tools Central Europe GmbH. *Calibration Certificate DPI 603*. Calibration certificate W17113041. Wetzlar, Germany, Nov. 2017.

[66] Siemens AG. *Messumformer SITRANS P für Differenzdruck und Durchfluß*. Operating instruction C73000-B5600-C75-5. Karlsruhe, Germany, 1994, pp. 1–12.

[67] ABB Automation Products GmbH. *Kalibrierzertifikat FEP311*. Calibration certificate 241567761 X005_080812. Goettingen, Germany, Aug. 2012, p. 1.

[68] ABB Automation Products GmbH. *ProcessMaster FEP300 Magnetisch-induktiver Durchflussmesser*. Data sheet DS/FEP300-DE. Alzenau, Germany, 2012, pp. 1–72.

[69] Deutsches Institut für Normung e.V. *DIN 862:2015-03, Geometrical product specifications (GPS) - Callipers - Maximum permissible errors*. Tech. rep. Berlin: Beuth Verlag GmbH, Mar. 2015.

[70] The European Parliament and the Council of the European Union. *Directive 2014/32/EU of the European Parliament and of the Council of 26 February 2014 on the harmonisation of the laws of the Member States relating to the making available on the market of measuring instruments (recast) Text with EEA relevance*. Mar. 2014.

[71] Bullen, P. R. et al. “A study of Turbulent Flow in Pipe Contractions”. In: *Proceedings of the Institution of Mechanical Engineers, Part E: Journal of Process Mechanical Engineering* 210.3 (Oct. 1996), pp. 171–180. ISSN: 0954-4089. DOI: 10.1243/PIME_PROC_1996_210_312_02.

[72] Bullen, P. R. et al. “Laser Doppler Anemometry Measurements of Flow through a Sudden Pipe Contraction and Comparison with Computer Predictions”. In: *Laser Anemometry: Advances and Applications : Proceedings of the 3rd International Conference*. Swansea: BHRA Information Services, Sept. 1989, pp. 567–576. ISBN: 978-0-387-51924-1.

[73] White, F. M. *Fluid Mechanics*. 7th ed. New York: McGraw Hill, 2011. ISBN: 978-0-07-352934-9.

[74] Gillispie, C. C. and Pisano, R. *Lazare and Sadi Carnot: A Scientific and Filial Relationship*. Vol. 19. History of Mechanism and Machine Science. Dordrecht: Springer Netherlands, 2014. ISBN: 978-94-017-8010-0. DOI: 10.1007/978-94-017-8011-7.

[75] Baer, H. “Versuche über hydraulische Stoßverluste”. German. In: *Polytechnisches Journal* 322 (Mar. 1907), pp. 177–179.

[76] Archer, W. H. “Experimental Determination of Loss of Head Due to Sudden Enlargement in Circular Pipes”. In: *Transactions of the American Society of Civil Engineers* 76.1 (1913), pp. 999–1026.

[77] Gibson, A. H. *Hydraulics and its applications*. London: A. Constable & Co., ltd., 1908.

[78] Gibson, A. H. *Hydraulics and its applications*. 3. New York: D. Van Nostrand company, 1925.

[79] Schuett, H. “Losses of Pressure Head Due to Sudden Enlargement of a Flow Cross-Section”. In: *Transactions of the ASME* 51 (1929), pp. 83–87.

[80] Lipstein, N. J. “Low velocity sudden expansion pipe flow”. In: *American Society of Heating, Refrigerating and Air- Conditioning Engineers Journal* 4.7 (1962), pp. 43–47.

[81] Chaturvedi, M. C. “Flow Characteristics of Axisymmetric Expansions”. In: *Journal of the Hydraulics Division, Proceedings of the American Society of Civil Engineers* 89.HY3 (1963), pp. 61–92.

[82] Nusselt, W. “Der Druck im Ringquerschnitt von Rohren mit plötzlicher Erweiterung beim Durchfluß von Luft mit hoher Geschwindigkeit”. German. In: *Forschung auf dem Gebiet des Ingenieurwesens* 11.5 (Sept. 1940), pp. 250–255. ISSN: 1434-0860. DOI: 10.1007/BF02584891.

[83] Teyssandier, R. G. and Wilson, M. P. “An analysis of flow through sudden enlargements in pipes”. In: *Journal of Fluid Mechanics* 64.1 (June 1974), pp. 85–95. ISSN: 1469-7645, 0022-1120. DOI: 10.1017/S0022112074002011.

[84] Papadopoulos, G. and Ötügen, M. V. “A Modified Borda-Carnot Relation for the Prediction of Maximum Recovery Pressure in Planar Sudden Expansions Flows”. In: *Journal of Fluids Engineering* 120.2 (June 1998), pp. 400–402. ISSN: 0098-2202. DOI: 10.1115/1.2820662.

[85] Miller, D. S. *Internal flow systems*. 1st ed. Vol. 5. British Hydromechanics Research Association. Fluid engineering. Series engineering. 4. Cranfield: BHRA Fluid Engineering, 1978. ISBN: 978-0-900983-78-7.

[86] Schütt, H. “Versuche zur Bestimmung der Energieverluste bei plötzlicher Rohrerweiterung”. German. In: *Mitteilungen des Hydraulischen Instituts der Hochschule München* 1 (1926), pp. 42–58.

[87] Khezzar, L. and Whitelaw, J. H. “Flows Through Round Sudden Contractions”. In: *Proceedings of the Institution of Mechanical Engineers, Part C: Journal of Mechanical Engineering Science* 202.4 (July 1988), pp. 295–300. ISSN: 0954-4062. DOI: 10.1243/PIME_PROC_1988_202_122_02.

[88] Alvi, S. H. et al. “Loss Characteristics of Orifices and Nozzles”. In: *Journal of Fluids Engineering* 100.3 (Sept. 1978), pp. 299–307. ISSN: 0098-2202. DOI: 10.1115/1.3448670.

[89] Dayev, Z. A. and Kairakbaev, A. K. “Modeling of coefficient of contraction of differential pressure flowmeters”. In: *Flow Measurement and Instrumentation* 66 (Apr. 2019), pp. 128–131. ISSN: 0955-5986. DOI: 10.1016/j.flowmeasinst.2019.02.009.

[90] Westaway, C. R. and Loomis, A. W. *Cameron hydraulic data: a handy reference on the subject of hydraulics and steam*. 16. Woodcliff Lake, N.J.: Ingersoll-Rand Company, 1984.

[91] International Organization for Standardization. *ISO 5167-2:2003-03 Measurement of fluid flow by means of pressure differential devices inserted in circular cross-section conduits running full - Part 2: Orifice plates*. Tech. rep. Geneva: Beuth Verlag GmbH, Mar. 2003.

[92] Reader-Harris, M. *Orifice Plates and Venturi Tubes*. Experimental Fluid Mechanics. Cham, Switzerland: Springer International Publishing, 2015. ISBN: 978-3-319-16879-1. DOI: 10.1007/978-3-319-16880-7.

[93] Benedict, R. P. and Wyler, J. S. "A Generalized Discharge Coefficient for Differential Pressure Type Fluid Meters". In: *Journal of Engineering for Power* 96.4 (Oct. 1974). Publisher: American Society of Mechanical Engineers Digital Collection, pp. 440–448. ISSN: 0022-0825. DOI: 10.1115/1.3445873.

[94] Pardoe, W. S. "The Effect of Installation on the Coefficient of Venturi Meters". In: *Transactions of the ASME* 65 (1943), p. 337.

[95] Martin, J. J. and Pabbi, V. R. "Use of momentum balance in calibrating orifices for flow of gases". In: *AIChE Journal* 6.2 (1960), pp. 318–321. ISSN: 1547-5905. DOI: 10.1002/aic.690060228.

[96] Reader-Harris, M. et al. "Orifice plate pressure loss ratio: theoretical work in compressible flow and experimental work in CO2". In: *Proceedings of the FLOMEKO2019*. Lisbon, 2019, pp. 120–125.

[97] Morrison, G. L. et al. "Comparison of orifice and slotted plate flowmeters". In: *Flow Measurement and Instrumentation* 5.2 (Apr. 1994), pp. 71–77. ISSN: 0955-5986. DOI: 10.1016/0955-5986(94)90039-6.

[98] Urner, G. "Pressure loss of orifice plates according to ISO 5167-1". In: *Flow Measurement and Instrumentation* 8.1 (Mar. 1997), pp. 39–41. ISSN: 0955-5986. DOI: 10.1016/S0955-5986(97)00014-9.

[99] Ahmed, E. N. and Ghanem, A. A. "A novel comprehensive correlation for discharge coefficient of square-edged concentric orifice plate at low Reynolds numbers". In: *Flow Measurement and Instrumentation* 73 (June 2020), p. 101751. ISSN: 0955-5986. DOI: 10.1016/j.flowmeasinst.2020.101751.

[100] Borutzky, W. et al. "An orifice flow model for laminar and turbulent conditions". In: *Simulation Modelling Practice and Theory* 10.3 (Nov. 2002), pp. 141–152. ISSN: 1569-190X. DOI: 10.1016/S1569-190X(02)00092-8.

[101] Merritt, H. E. *Hydraulic Control Systems*. New York: John Wiley & Sons, Inc., 1967. ISBN: 978-0-471-59617-2.

[102] Müller, S. and Malcherek, A. "A Unified Theory for the Pressure Change of Sudden Expansions and Contractions Based on the Momentum Balance". In: *Proceedings of the ASME 2021 Fluids Engineering Division Summer Meeting*. Vol. 2: Fluid Applications and Systems; Fluid Measurement and Instrumentation. Virtual, Online: American Society of Mechanical Engineers Digital Collection, Aug. 2021. DOI: 10.1115/FEDSM2021-65703.

[103] Lebedev, M. E. et al. "Achieving better accuracy of determining liquid flowrate in pipelines at a nuclear power station using flow metering orifices". In: *Thermal Engineering* 59.3 (Mar. 2012), pp. 228–230. ISSN: 1555-6301. DOI: 10.1134/S0040601512030081.

[104] Erdal, A. and Andersson, H. I. "Numerical aspects of flow computation through orifices". In: *Flow Measurement and Instrumentation* 8.1 (Mar. 1997), pp. 27–37. ISSN: 0955-5986. DOI: 10.1016/S0955-5986(97)00017-4.

[105] Imada, F. H. J. et al. “Numerical Determination of Discharge Coefficients of Orifice Plates and Nozzels”. In: *Proceedings of the 22nd International Congress of Mechanical Engineering COBEM 2013*. Ribeirão Preto, Brazil, Nov. 2013, p. 6. ISBN: 2176-5480.

[106] Shan, F. et al. “Particle image velocimetry measurements of flow field behind a circular square-edged orifice in a round pipe”. In: *Experiments in Fluids* 54.6 (June 2013), p. 1553. ISSN: 0723-4864, 1432-1114. DOI: 10.1007/s00348-013-1553-z.

[107] Spalart, P. and Allmaras, S. “A one-equation turbulence model for aerodynamic flows”. In: Aerospace Sciences Meetings. Reno, U.S.A., Jan. 1992, AIAA–92–0439. DOI: 10.2514/6.1992-439.

[108] Steppert, M. et al. “Sluice Gate Discharge From Momentum Balance”. In: *Journal of Fluids Engineering* 144.4 (Feb. 2022). ISSN: 0098-2202. DOI: 10.1115/1.4053351.

[109] Malcherek, A. “A General Outflow Theory Based on Momentum Balance”. In: *Journal of Fluids Engineering* 144.1 (July 2021). ISSN: 0098-2202. DOI: 10.1115/1.4051579.